Coulomb explosion imaging of polyatomic molecules after photoionization with X-rays and strong laser fields

by

Utuq Ablikim

B.S., Harbin Institute of Technology, 2009

M.S., Kansas State University, 2015

AN ABSTRACT OF A DISSERTATION

submitted in partial fulfillment of the
requirements for the degree

DOCTOR OF PHILOSOPHY

Department of Physics
College of Arts and Sciences

KANSAS STATE UNIVERSITY
Manhattan, Kansas

2017

Abstract

Imaging the structures of molecules, understanding the molecular dynamics in ionization and dissociation processes and, most importantly, observing chemical reactions, i.e. the making and breaking of chemical bonds in real time, have become some of the most exciting topics in the atomic and molecular physics. The rapid advances of experimental tools such as synchrotron radiation light sources, free-electron lasers and continuing advances of table-top femtosecond ultrashort lasers that provide laser pulses at a variety of wavelengths have opened new avenues for understanding the structure of matter and the dynamics of the chemical interactions. In addition, significant improvements in computational techniques and molecular dynamic simulations have provided complementary theoretical predictions on structures and chemical dynamics.

The Coulomb explosion imaging method, which has been developed and applied in many studies in the last three decades, is a powerful way to study molecular structures. The method has mostly been applied to small diatomic molecules and to simple polyatomic molecules. In this thesis, Coulomb explosion imaging is applied to study the structure of isomers, molecules that have the same chemical formula but different chemical structures. Specifically, by taking inner-shell photoionization as well as strong-field ionization approaches to ionize and fragment the molecules and by using coincidence electron-ion-ion momentum imaging techniques to obtain the three-dimensional momentum of fragment ions, structures of isomers are distinguished by using the correlations among product ion momentum vectors.

At first, the study aims to understand if the Coulomb explosion imaging of geometrical isomers can identify and separate *cis* and *trans* structures. Secondly, in order to extend the application of the Coulomb explosion imaging method to larger organic molecules to test the feasibility of the method for identifying structural isomers, photoionization studies

of 2,6- and 3,5-difluoroiodobenzene have been conducted. In addition, using the full three-dimensional kinematic information of multi-fold coincidence channels, breakup dynamics of both *cis*/*trans* geometric isomers and structural isomers, and in particular, sequential fragmentation dynamics of the difluoroiodobenzene isomers are studied. Furthermore, for each study, Coulomb explosion model simulations are conducted to complement the experimental results.

The results of the Coulomb explosion imaging reseach in this thesis paves the way for future time-resolved Coulomb explosion imaging experiments aiming to understand the transient molecular dynamics such as photoinduced ring opening reactions and *cis*/*trans* isomerization processes in gas-phase molecules.

Coulomb explosion imaging of polyatomic molecules after photoionization with X-rays and strong laser fields

by

Utuq Ablikim

B.S., Harbin Institute of Technology, 2009

M.S., Kansas State University, 2015

A DISSERTATION

submitted in partial fulfillment of the
requirements for the degree

DOCTOR OF PHILOSOPHY

Department of Physics
College of Arts and Sciences

KANSAS STATE UNIVERSITY
Manhattan, Kansas

2017

Approved by:

Major Professor
Daniel Rolles

Copyright

Abstract

Imaging the structures of molecules, understanding the molecular dynamics in ionization and dissociation processes and, most importantly, observing chemical reactions, i.e. the making and breaking of chemical bonds in real time, have become some of the most exciting topics in the atomic and molecular physics. The rapid advances of experimental tools such as synchrotron radiation light sources, free-electron lasers and continuing advances of table-top femtosecond ultrashort lasers that provide laser pulses at a variety of wavelengths have opened new avenues for understanding the structure of matter and the dynamics of the chemical interactions. In addition, significant improvements in computational techniques and molecular dynamic simulations have provided complementary theoretical predictions on structures and chemical dynamics.

The Coulomb explosion imaging method, which has been developed and applied in many studies in the last three decades, is a powerful way to study molecular structures. The method has mostly been applied to small diatomic molecules and to simple polyatomic molecules. In this thesis, Coulomb explosion imaging is applied to study the structure of isomers, molecules that have the same chemical formula but different chemical structures. Specifically, by taking inner-shell photoionization as well as strong-field ionization approaches to ionize and fragment the molecules and by using coincidence electron-ion-ion momentum imaging techniques to obtain the three-dimensional momentum of fragment ions, structures of isomers are distinguished by using the correlations among product ion momentum vectors.

At first, the study aims to understand if the Coulomb explosion imaging of geometrical isomers can identify and separate *cis* and *trans* structures. Secondly, in order to extend the application of the Coulomb explosion imaging method to larger organic molecules to test the feasibility of the method for identifying structural isomers, photoionization studies

of 2,6- and 3,5-difluoroiodobenzene have been conducted. In addition, using the full three-dimensional kinematic information of multi-fold coincidence channels, breakup dynamics of both *cis*/*trans* geometric isomers and structural isomers, and in particular, sequential fragmentation dynamics of the difluoroiodobenzene isomers are studied. Furthermore, for each study, Coulomb explosion model simulations are conducted to complement the experimental results.

The results of the Coulomb explosion imaging reseach in this thesis paves the way for future time-resolved Coulomb explosion imaging experiments aiming to understand the transient molecular dynamics such as photoinduced ring opening reactions and *cis*/*trans* isomerization processes in gas-phase molecules.

Contents

List of Figures xi

Acknowledgements xv

Dedication xvii

1 Introduction 1

1.1 What are Isomers? 4

1.2 Synopsis of Thesis 6

2 Photoionization and Coulomb Explosion Imaging of Molecular Isomers 8

2.1 Photoionization 8

2.1.1 Single-Photon Ionization with X-rays 10

2.1.1.1 Inner-shell Photoionization and Auger Decay 12

2.1.2 Strong-Field Ionization 15

2.2 Coulomb Explosion Imaging 18

2.2.1 Numerical Coulomb Explosion Simulations 21

3 Experimental Methods 24

3.1 X-ray Synchrotron Beams 25

3.2 Ultrafast Femtosecond Lasers 27

3.2.1 Oscillator 28

3.2.2 Multipass Amplifier 28

3.2.3 Spectrometers for Electron-Ion Coincidence Measurements 28

3.2.3.1 Double-sided Coincidence VMI 28

3.2.3.2 COLTRIMS . . . 32
3.2.4 Microchannel Plates (MCP) . . . 33
3.2.5 Delay-line Detectors . . . 35
3.2.6 Coincidence Detection . . . 37
3.2.7 Coincidence Maps: PIPICO and PIPIPICO/TRIPICO . . . 38
3.2.8 Momentum Calibration: Double-sided VMI . . . 40
3.2.8.1 Transverse Momentum: p_x and p_y . . . 40
3.2.8.2 Longitudinal Momentum: p_z . . . 42
3.2.9 Calibration of Ion-ion Coincidence Measurements . . . 43
3.2.10 Coincidence Electron Spectra . . . 45
3.2.10.1 Electron Detector Calibration with Neon $2s$, $2p$ Lines . . . 45
3.2.11 Momentum Calibration: COLTRIMS . . . 48
3.3 Supersonic Molecular Jet and Vacuum System . . . 49
3.4 VUV Synchrotron Measurement of Ionization Potentials . . . 51

4 Identification of *cis-trans* Isomers via Coulomb Explosion Imaging . . . 54
4.1 Introduction . . . 54
4.2 Coulomb Explosion Imaging of *cis* and *trans* 1,2-dibromoethene . . . 56
4.2.1 X-ray Synchrotron Studies: 1,2-$C_2H_2Br_2$ . . . 56
4.2.2 Photo- and Auger-electron spectra of 1,2-$C_2H_2Br_2$ . . . 66
4.2.3 Strong-Field Laser Studies: 1,2-$C_2H_2Br_2$ . . . 70
4.3 Coulomb Explosion Imaging of *cis* and *trans* 1,2-dichloroethene . . . 77
4.3.1 X-ray Synchrotron Studies: 1,2-$C_2H_2Cl_2$ . . . 77
4.3.2 Photo- and Auger-electron spectra of 1,2-$C_2H_2Cl_2$ . . . 81
4.3.3 Strong-Field Laser Studies: 1,2-$C_2H_2Cl_2$ . . . 84
4.3.4 Conclusion . . . 88

5 X-ray and Laser-Induced Fragmentation of 2,6- and 3,5-Difluoroiodobenze . . . 90

5.1 Introduction . . . 90
5.2 Soft X-ray induced fragmentation of 2,6- and 3,5-DFIB . . . 92
5.2.1 $C_6H_3F_2^+ + I^+$ and $C_6H_3F_2^{++} + I^+$ two-body fragmentation channels 98
5.2.2 Sequential breaking of C-I and C-C bonds . . . 102
5.2.3 Identification of molecular isomers via fragment-ion momentum correlations in three-body fragmentation channels . . . 109
5.3 Ultrafast femtosecond laser induced fragmentation of 2,6- and 3,5-DFIB . . . 116
5.3.1 $C_6H_3F_2^+ + I^+$ and $C_6H_3F_2^{++} + I^+$ two-body fragmentation channels 119
5.3.2 Sequential fragmentation in strong laser field . . . 121

6 Summary and Future Perspectives . . . 126

Bibliography . . . 131

A TOF jitter correction in the VMI experiments . . . 145

B VMI image circularization method . . . 148

C VMI Spectrometer Voltages . . . 151

D Coulomb Explosion Model Simulation Matlab Scripts . . . 153
D.1 Coulomb explosion simulation: 2-body . . . 154
D.2 Coulomb explosion simulation: 3-body . . . 156

List of Figures

1.1 Electromagnetic wavelength and photon energy spectrum 2

1.2 Diagram of isomer types 5

2.1 Single photon ionization diagram; $2s$, $2p$ electrons of Neon after photoionization by 100 eV photon 11

2.2 Partial cross section of Neon $2s$ $2p$ shells 12

2.3 Energy level diagram of Xenon photoionization 14

2.4 Schematic of Auger decay mechanism 14

2.5 Strong-field ionization regimes 16

2.6 Coulomb explosion process 19

2.7 Coulomb explosion simulation for the fragmentation of a CH_3I molecule . . . 23

3.1 Picture of the ALS and floor diagram 25

3.2 ALS beamline 10.0.1 spectral resolution measurement 26

3.3 Schematic diagram of the VMI spectrometer 29

3.4 Ion, electron SIMION trajectories 30

3.5 Neon $2s$ and $2p$ position spectrum; Ne^+ ion position distribution 31

3.6 Schematic of a COLTRIMS apparatus 32

3.7 Schematic of MCP channel tubes 34

3.8 Quad and Hex delay-line detectors 35

3.9 Time-sum distribution of delay-line wires 37

3.10 PIPICO and TRIPICO diagrams 39

3.11 SIMION simulation of ions flying parallel to the detector 40

3.12 H^+ TOF distribution; Final ion TOF vs. initial kinetic energy 42

3.13 PIPICO of N_2 molecules; N^++N^+ channel kinetic energy release 44
3.14 Doppler-free kinetic energy release for N^++N^+ channel 45
3.15 Neon $2s$, $2p$ electron distribution 46
3.16 Inverted electron spectrum of Neon $2s$, $2p$ electrons 47
3.17 Neon $2p$ β parameter; e^- detector radius to energy conversion. 47
3.18 Schematic diagram of the VMI system and vacuum system. 50
3.19 Molecular beam machine with VUV synchrotron 51
3.20 Photoionization yield of molecules in VUV beam 52

4.1 Schematic of the double-sided coincidence VMI setup; Molecular structure of 1,2-dibromoethene; TRIPICO spectrum of 1,2-dibromoethene; Ion TOF spectrum of 1,2-dibromoethene 57
4.2 Momentum correlation ($\cos\theta$) of $C_2H_2^+$ + Br^+ + Br^+ channel in synchrotron measurement 59
4.3 Kinetic energy distribution of $C_2H_2^+$ + Br^+ + Br^+ channel in synchrotron measurement 60
4.4 Newton plot of $C_2H_2^+$ + Br^+ + Br^+ in synchrotron measurement 61
4.5 Momentum correlation vs. kinetic energy sum of two Br^+; Yield of $C_2H_2^+$ + Br^+ + Br^+ channel as function of kinetic energy of one Br^+ vs. another Br^+ ion; 62
4.6 Overview of stretching/bending modes in 1,2-$C_2H_2Br_2$ isomers 65
4.7 Photoionization cross sections for bromine subshells 66
4.8 1,2-$C_2H_2Br_2$ raw electron position spectrum in synchrotron measurement . . 67
4.9 1,2-$C_2H_2Br_2$ valence electron position and energy spectra in synchrotron measurement 68
4.10 Raw and inverted position spectra of coincidence electrons for: Br^+,CBr^+,$C_2H_2Br^+$ ions and $C_2H_2Br^+$+Br^+, $C_2H_2^+$+Br^++Br^+ channels 69
4.11 Ion TOF spectrum after strong-field ionization of 1,2-$C_2H_2Br_2$ 71

4.12 PIPICO spectrum of 1,2-$C_2H_2Br_2$ after strong-field ionization 72
4.13 TRIPICO spectrum showing $C_2H_2^+$+Br^++Br^+ channel of 1,2-$C_2H_2Br_2$ after strong-field ionization 73
4.14 Momentum sum of p_x, p_y and p_z components in $C_2H_2^+$+$^{81}Br^+$+$^{81}Br^+$ channel in strong-field measurement 73
4.15 Momentum correlation ($\cos\theta$) of $C_2H_2^+$ + Br^+ + Br^+ channel in strong-field measurement 74
4.16 Kinetic energy distribution of $C_2H_2^+$ + Br^+ + Br^+ channel in synchrotron measurement; Schematic figure of C-Br bond stretching at different electronic states. 75
4.17 Newton plot of the $C_2H_2^+$ + Br^+ + Br^+ channel in strong-field measurement 76
4.18 Ion TOF spectrum of 1,2-dichloroethene in synchrotron measurement 78
4.19 Momentum correlation ($\cos\theta$) of $C_2H_2^+$ + Cl^+ + Cl^+ channel in synchrotron measurement 79
4.20 Newton plot of $C_2H_2^+$ + Cl^+ + Cl^+ channel in synchrotron measurement . . 80
4.21 Kinetic energy distribution of $C_2H_2^+$ + Cl^+ + Cl^+ channel in synchrotron measurement 80
4.22 *cis* 1,2-$C_2H_2Cl_2$: Raw and inverted position spectra of coincidence electrons for: Cl^+,CCl^+,$C_2H_2Cl^+$ ions and $C_2H_2Cl^+$+Cl^+, $C_2H_2^+$+Cl^++Cl^+ channels . 82
4.23 *trans* 1,2-$C_2H_2Cl_2$: Raw and inverted position spectra of coincidence electrons for: Cl^+,CCl^+,$C_2H_2Cl^+$ ions and $C_2H_2Cl^+$+Cl^+, $C_2H_2^+$+Cl^++Cl^+ channels . 83
4.24 Ion TOF spectra of *cis* and *trans* 1,2-$C_2H_2Cl_2$ isomers after strong-field ionization 84
4.25 Momentum correlation ($\cos\theta$) of $C_2H_2^+$ + Cl^+ + Cl^+ channel in strong-field measurement 86
4.26 Newton plot of $C_2H_2^+$ + Cl^+ + Cl^+ in synchrotron measurement 87

4.27 Kinetic energy distribution of $C_2H_2^+$ + Cl^+ + Cl^+ channel in strong-field measurement 87

5.1 Ion TOF spectra of 2,6- and 3,5-DFIB and their normalized difference spectrum 93

5.2 Ion TOF vs. x-position distribution 94

5.3 PIPICO maps for 2,6- and 3,5-DFIB 96

5.4 PIPIPICO maps for 2,6- and 3,5-DFIB 97

5.5 Coincidence electron position and energy spectra for 2,6- and 3,5-DFIB . . . 99

5.6 Kinetic energies of two-body channels of 2,6- and 3,5-DFIB 100

5.7 Ratio of F^+ and I^+ ion yields in 2,6- and 3,5-DFIB. 102

5.8 Kinetic energy spectrum of CF^+ and $C_5H_3F^+$ ions 103

5.9 Kinetic energies of sequential fragmentation channels 104

5.10 Newton diagrams of sequential fragmentation channels 105

5.11 Dalitz plot of CF^++$C_5H_3F^+$+I^+ channel 106

5.12 Schematic cartoon for sequential fragmentation for 2,6-DFIB 107

5.13 Second-step kinetic energy release in sequential breakup channels 108

5.14 Newton plot for F^+ + C_6HF^+ + I^+ channel 110

5.15 Kinetic energy and momentum vector correlation for F^++C_6HF^++I^+ channel 111

5.16 Numerical simulation for sequential fragmentation of 2,6-DFIB 113

5.17 Kinetic energy and momentum vector correlation for F^+ + $C_6H_2{}^+$ + I^+ channel115

5.18 Momentum vector correlation for all F^+ and I^+ ions 116

5.19 TOF mass spectrum for laser fragmentation of 2,6- and 3,5-DFIB 117

5.20 TOF mass spectrum vs. X position of 2,6- and 3,5-DFIB 118

5.21 PIPICO maps for laser fragmentation of 2,6- and 3,5-DFIB 119

5.22 Kinetic energy spectra for laser-induced two-body fragmentation channels . . 120

5.23 PIPIPICO maps from laser fragmentation of 2,6- and 3,5-DFIB 122

5.24 Kinetic energy spectra for laser-induced sequential fragmentation channels . 123

5.25 Newton diagrams for laser-induced sequential fragmentation channels 123

5.26 Second-step kinetic energy release in laser-induced sequential breakup channels 124

6.1 Energy diagram of 1,2-$C_2H_2Br_2$ molecule 128

6.2 Energy diagram of C_4H_4SO molecule 130

A.1 A PIPICO map with & without jitter correction 146

B.1 Neon position spectrum 149

B.2 Neon radius vs. phi angle spectrum 149

C.1 Picture of the universal power supply system 151

C.2 The schematic of double-sided VMI spectrometer 152

D.1 2-body ion Coulomb explosion simulation Matlab script 155

D.2 2-body ion Coulomb explosion simulation; Numerical integration function . . 155

D.3 3-body ion Coulomb explosion simulation Matlab script 157

D.4 3-body ion Coulomb explosion simulation; Numerical integration function . . 158

Acknowledgments

Graduate school may mean different things for lots of us. Some of us will remember the period of time more as an advancement of career, learning of new knowledge or just getting a credential for the next steps of academic life. For me, it is more than that, i learnt great deal of lessons in graduate school, those lessons are both academic lessons and life lessons. The experiences in graduate school helped me shape a deterministic mind-set and have a lasting perseverance. It is not only a period of time for an intellectual growth, but also a time period of self discovery. It is a period of time that i will look back in 10 or 20 years and be thankful for the people who taught me the important lessons and created chances for me and helped me to pursue what i always loved to do.

I owe a great deal of gratitude and respect for my advisor Daniel Rolles. What I learned and continually learning from him are not just the physics research described in this thesis and beyond, but also the optimism, an open and accepting attitude toward different circumstances, being able to work productively and efficiently with many physicists and chemists from all across the world in a friendly and professional way. I know that the curiosity and passion in what one is doing is the most valuable and important things in order to be able to succeed. I am very lucky that during the time of working as Daniel's student, he has been encouraging me and always have been giving me feedbacks in a way that positively influences me and drives me to be more passionate about the future of our research. The essence of encouragement goes beyond scientific research and having an optimistic and passionate view of the future and encouraging people who are working together with you is very important in any field.

I am also thankful to professor Chi-Dong Lin who supported me during my graduate school. I am grateful for not only the AMO courses that i took from him in the starting years of the graduate school but also his support and help that lead me to the new opportunities of research and, of course, lead to the final steps of my PhD life.

Our experimental research is conducted in collaboration with professor Nora Berrah's group. Professor Berrah has been very helpful and supporting for our experiments and giving us useful advices for our research papers. I am grateful for her help and her group's help in our experimental research at the Advanced Light Source, LBNL.

During graduate school, i got to work with many colleagues, some of whom that i became very good friends with. They helped me in experiments and analysis both in the J.R.M lab in Kansas State University and the Advanced Light Source in Lawrence Berkeley Lab. I thank my group-mate Farzaneh Ziaee, who did many experiments together with me and conducted some parts of the laser experiment for my project while I was in Berkeley. I hope her hard work and endless passion for science will lead her to success. I also thank Cédric Bomme, a former postdoc of my PhD advisor, for introducing me to the new double-sided VMI apparatus and helped me with the initial steps of data analysis.

I thank my PhD program commitee members, Dr. Chi-Dong Lin, Dr. Vinod Kumarapan, Dr. Viktor Chikan and the outside chair Dr. Jodi Mcgill. I thank their time and effort into my PhD study. During the last year of my graduate school, I was fortunate to get the Advanced Light Source Doctoral fellowship from the Lawrence Berkeley National Lab. I am extremely grateful for the people at the Berkeley lab to create this opportunity for me. It is an encouragement, an opportunity and an advancement in my career. I thank my primary advisor Musahid Ahmed from the Chemical Dynamics division at the Berkeley lab, and my colleagues who taught me new skills and introduced me to new tools to probe chemical targets.

Last but not least, without the support of my family, my wife Gulnaz Rexit and my little son Arslan Ogen, I would not be able to conduct my PhD research. I thank my wife for her patience and continuing love no matter ups and downs of my life. I thank my parents who have been the source of encouragement for pursuing scientific research from the beginning.

Dedication

This work is dedicated to my family. To my wife, Gulnaz Rexit and my adorable son Arslan Utuq Ogen. Without their support, this work would not be accomplished. The work is also dedicated to my father, my role model Ablikim Hasan, and to my caring and loving mother Turnisa Niyaz. Without their encouragement, I wouldnt be what I am and where I am today.

Chapter 1

Introduction

Over the course of the last few decades, the imaging of molecular structures and dynamics have been a crucial subject of interest. The advancement of spectroscopic techniques together with the progress in the generation of accelerator-based X-ray synchrotron light sources as well as tabletop ultrafast laser systems have substantially expedited the pace of both experimental and theoretical research aiming to understand the fundamental processes involving light interaction with atoms and molecules.

Since their discovery in 1895 by Wilhelm Conrad Röntgen [1], X-rays have become an indispensable tool for studying the electronic structure and chemical composition of matter. The field of X-ray science has been advanced enormously with the developing of accelerator-based synchrotron light sources in 1960s. The synchrotron sources offer photon beams with much higher flux and intensity than previous X-ray sources such as X-ray tubes [2]. They are becoming increasingly more important thanks to their unique properties such as continuous spectrum with wavelength ranging from 10 nm to above 10 pm, (see Fig. 1.1) as well as high flux and brightness. Most importantly, the tunability of synchrotron light allows the probing of specific elements in molecules, thus allowing element specific photoionization studies. Along with the synchrotron sources, various different X-ray spectroscopic techniques have been developed, such as, soft X-ray absorption spectroscopy (XAS) [3], near-edge X-ray absorption fine structure (NEXAFS) spectroscopy [4], X-ray photoemission spectroscopy

(XPS) [5], Auger spectroscopy.

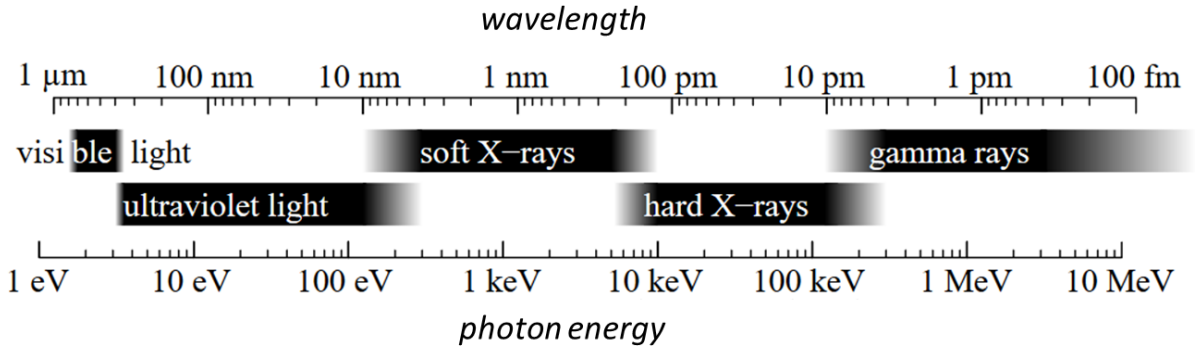

Figure 1.1: Electromagnetic wavelength and photon energy spectrum; Figure taken from https://en.wikipedia.org/wiki/X-ray

Equally important is the development of tabletop ultrafast laser systems. The invention of the continuous wave laser in 1960 [6], followed several years later by the first pulsed laser, opened up new avenues for scientific research. The widely used solid-state gain medium, titanium sapphire (Ti:Sapphire), enables the production of infrared laser pulses with pulse durations in femtosecond time scale [7]. Meanwhile, the chirped pulse amplification (CPA) technique [7] allows for the increase of maximum laser pulse intensity that can be used to ionize electrons from atoms and molecule. The development of such ultrashort, intense femtosecond laser pulses has created an entire new branch of ultrafast "*femtochemistry*" which has shed light on a number of fast molecular reactions [8–10]. The ultrafast lasers allowed scientists to study chemical reactions in femtoseconds (fs) (10^{-15} second) and attoseconds (as) (10^{-18} second) time scale. Pioneering research by Zewail *et al* used pump-probe experimental techniques in which a pump pulse initiates a dynamical process and a probe pulse is used to examine the evolution of the process. His research was awarded the Nobel prize in Chemistry in 1999 [11].

Apart from the light sources, the spectroscopic techniques played major role in the ultrafast molecular dynamic studies. In addition to the X-ray spectroscopic techniques mentioned above, beginning in the late 1980s, ion imaging methods emerged as a uniquely powerful tool. The birth of the ion imaging technique in application to the chemical dynamics problem is generally considered to be the work conducted by David Chandler and Paul Houston on

the photo-dissociation of methyl-iodide (CH_3I) [12]. Quite interestingly, in the same year, Joachim Ullrich and Horst Schmidt-Böcking reported the first measurements of a heavy ion collision with rare gas atoms with a recoil ion momentum spectrometer [13]. Before continuing, it is important to note that there were two different major avenues of imaging development in the late 1980s. One was the ion imaging community pioneered by David Chandler and Paul Houston. The community was interested in chemical dynamics research using mainly low repetition rate nanosecond lasers. The other constituency focused on event-by-event based coincidence measurements. Both eventually led to the ultrafast molecular dynamic research. At that era, the event-based coincidence measurements had taken advantage of the developments in the multi-wire position sensitive detection technique (which, in 1992, was awarded with the Nobel prize [14]). The multi-wire position sensitive detection technique was well suited for coincidence event-based studies using high repetition rate lasers and synchrotrons [15]. Since then, the imaging techniques on both avenues has been applied in variety of research in physics and chemistry communities [15]. In the early 1990s, Reinhard Dörner and his co-workers combined super cooled few Kelvin gas targets into recoil ion momentum spectroscopy, realizing the first generation cold target recoil ion momentum spectroscopy (COLTRIMS) [16, 17]. On the other avenue, in 1997, the velocity map imaging technique, which was reported by Eppink and Parker [18], had experienced an explosion of interest in chemical dynamics community. In the velocity map imaging method, electrostatic ion lenses are employed to focus ions and electrons. All particles with the same initial velocity vector are mapped onto the same point on a two dimensional detector, irrespective of their position of creation within the ionization volume. The high collection efficiency and the ability to detect ions and electrons with wide kinetic energy range with 4π emission angles, made VMI ideal candidate for studying angular distributions and kinetic energy release of gas-phase atomic and molecular targets. The COLTRIMS technique also developed vastly during the last two decade. The use of cold supersonic jet targets and well defined static electric fields combined with multi-hit time and position sensitive detectors for ion and electron detection has made it possible to conduct full three-dimensional kinematically complete measurements of atomic and molecular reactions in external field [19–27]. In recent

years, the gap between coincidence event based detection approaches and the conventional ion imaging techniques such as VMI has shrunk. The techniques once special only to one avenue of imaging community now started to complement both constituencies. This thesis work is an example of such hybrid combination of detection techniques.

In this thesis, X-ray synchrotron beams as well as ultrafast femtosecond laser pulses are used to study the photoionization and fragmentation of gas-phase molecular targets, in particular molecular isomers, which are described further in Section 1.1. In X-ray synchrotron studies, an upgraded VMI apparatus equipped with two multi-hit coincidence-capable detectors is used to conduct electron-ion-ion coincidence momentum imaging measurements after inner-shell photoionization of cold molecular isomer targets prepared by supersonic jet. The VMI experiments took place at the Advanced Light Source (ALS) X-ray synchrotron facility at the Lawrence Berkeley National Laboratory (LBNL). The strong-field ultrafast measurements took place at the J. R. Macdonald Laboratory of Kansas State University, utilizing a COLTRIMS apparatus.

1.1 What are Isomers?

The main goal of this thesis is to study the photoionization and Coulomb explosion dynamics of molecular isomers using X-ray synchrotron and ultrafast femtosecond laser pulses. One might ask, "what are the isomers?" and "why would anyone study their structure and dynamics through means of photoionization?".

Isomers are molecules with the same chemical formulas but different arrangements of the atoms or the bonds connecting them. Isomers are literally everywhere in our life, one basic example is human vision. The fact that human eyes are able to see is due to the *cis-trans* (geometric isomers, see Fig.1.2) isomerization. The retina in human eyes contains chromophore 11-cis-retinal isomer. (A chromophore is a molecule that can absorb light at a specific wavelength, and thus typically displays a characteristic color.) When visible light hits the chromophore, the chromophore undergoes an isomerization and changes its molecular arrangement to all-trans-retinal. Such light-induced change in geometry will result

in generation of electrical impulses that are transmitted to the brain and thus enabling the vision [28, 29]. Similar isomerization reactions are also investigated as prototypical molecular switches, e. g. in azobenzene or stilbene type molecules [30, 31]. Another example is the green fluorescent proteins, which are used to investigate protein trafficking inside living cells and which changes configuration from its well-ordered *cis*-isomer to a highly disordered *trans*-isomer upon absorption of light [32].

Depending on the differences in the arrangement of atoms and their positing, isomers can be further classified into different categories as shown in Fig. 1.2.

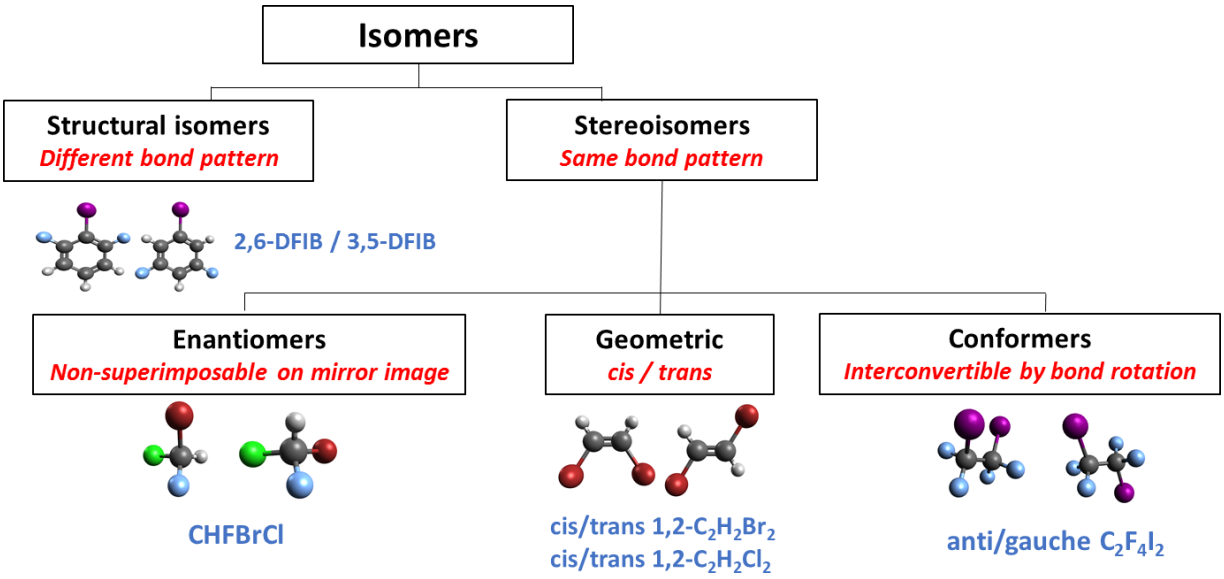

Figure 1.2: Diagram of isomer types

By the difference of bond patterns, the isomers can be classified into **structural isomers** and **stereoisomers**. Inner-shell I($4d$) photoionization and strong-field ionization of the structural isomers 2,6- and 3,5-difluoroiodobenzene (DFIB) are discussed in Chapter 5. The other group: stereoisomers can further grouped into **enantiomers**, **geometric isomers** and **conformers**. Enantiomers, also known as chiral molecules, are the isomers that are the mirror image of one another, but cannot interconvert from one form to the other without breaking the bonds to rearrange the atoms. Pitzer *et al* recently reported a study where Coulomb explosion imaging was used to separate a racemic mixture of CHIClF and CHBrClF by measuring five-fold coincidences after strong-field ionization [33, 34]. The study of transient

intermediates in the elimination reaction of 1,2-diiodoperfluoroethane conformers was conducted by Nobel laureate Zewail *et al* [11]. In Chapter 4 of this thesis, the Coulomb explosion of geometric isomers *cis*/*trans* 1,2-dibromoethene ($C_2H_2Br_2$), *cis*/*trans* 1,2-dichloroethene ($C_2H_2Cl_2$) after inner-shell photoionization with X-ray synchrotron beams and strong-field ionization with intense femtosecond pulses are reported.

1.2 Synopsis of Thesis

The main goal of this thesis work is to understand the fragmentation dynamics of molecular isomers after photoionization with X-rays and ultrafast strong laser pulses. For that reason, the Coulomb explosion imaging technique is employed. In particular, applying multi-fold ion-ion, ion-electron coincidence methods, photo-fragmentation of geometric *cis*/*trans* isomers and structural isomers are investigated.

The first question that the thesis would like to answer is: "Can one distinguish different isomers using the Coulomb explosion imaging method?". In order to answer this question, gas-phase molecular isomer targets are triply ionized and fragmented after the interaction with the light source. Three-dimensional momentum vectors of all fragment ions are reconstructed and correlations between chosen ion momentum vectors are used to determine the final molecular geometry after the photoionization. For photoionizing the isomers, two approaches were used. One is to inner-shell photoionize a selected atom's inner-shell, e.g. Br($3d$) and I($4d$), etc. with a tunable X-ray synchrotron beam and then reach the triply ionization state by emission of two Auger-electrons. The other approach is the strong-field ionization of the isomer targets with ultrafast femtosecond laser pulses. Those measurements were conducted on *cis*/*trans* 1,2-dibromoethene, 1,2-dichloroethene and 2,6-, 3,5-DFIB isomers.

In **Chapter2**, a brief overview of photoionization of atoms and molecules with X-rays and strong-field femtosecond laser pulses is given. Particularly, inner-shell photoionization of molecular targets with X-rays as well as strong-field ionization of molecules are briefly described. Moreover, a discussion of the Coulomb explosion imaging method and Coulomb explosion model simulation is presented.

In **Chapter3**, at first, brief details of X-ray synchrotron beams and ultrafast Ti-Sapphire laser system are given. Then, comprehensive details of the coincidence ion(-ion)-electron double-sided VMI as well as the ion momentum reconstruction procedures are given.

In **Chapter4**, the Coulomb explosion imaging of *cis*/*trans* geometric isomers after photoionization with X-ray synchrotron beam and strong laser pulses are studied. In both X-ray synchrotron and laser measurements, momentum correlation between two Br^+ fragments generated from photoionization of 1,2-$C_2H_2Br_2$ and two Cl^+ fragments from photoionization of 1,2-$C_2H_2Cl_2$ are used to distinguish *cis* and *trans* geometries of the isomers. In addition, channel-resolved coincidence electrons (e.g. photoelectrons- and Auger-electrons) are measured for two- and triple-ion coincidence channels. Finally, Coulomb explosion model simulations are conducted and compared with the experimental results. The major part of the chapter is published in the journal article: Ablikim *et al.*, Sci. Rep.**6**, 38202 (2016) [35].

In **Chapter5**, the Coulomb explosion imaging study reported in Chapter 4 is expanded to more complex structural isomers 2,6- and 3,5-DFIB. Coincidence momentum imaging of the isomers is studied with both X-ray synchrotron and ultrafast laser fields. For distinguishing the isomer structure with momentum correlation, F^+ and I^+ ion momenta were used. The results of the comparison between two isomers prove that the Coulomb explosion imaging method can also be used to distinguish larger and more complex molecules. In addition, using the three-dimensional momentum and kinetic energies of coincident ions, sequential fragmentation of DFIB isomers is studied. The major part of the chapter is published in the journal article: Ablikim *et al.*, Phys. Chem. Chem. Phys.**19**, 13419 (2017) [36].

Chapter6 summarizes the studies presented in this thesis work on the Coulomb explosion imaging of photoionized molecular isomers. Future perspectives for time-resolved *cis-trans* isomerization as well as time-resolved ring-opening studies are discussed.

Chapter 2

Photoionization and Coulomb Explosion Imaging of Molecular Isomers

The three-dimensional momentum imaging experiments described in this thesis are realized by photoionization and fragmentation of molecular isomers. The photoionization process in the synchrotron experiments is based on the absorption of a single photon and the ejection of an inner-shell electron. This process is then followed by an Auger relaxation processes that leads to the emission of additional electrons from the system. The strong-field ionization by femtosecond laser pulses is based on multi-photon absorption, which also leads to the removal of multiple electrons from the system. The aim of this chapter is to give a brief overview of these light-molecule interactions, thereby providing a theoretical and conceptual background for the experimental results presented in the following chapters.

2.1 Photoionization

The formation of an ion by the interaction of electromagnetic radiation with an atom or a molecule is referred to as photoionization. The photoionization can be caused by the

absorption of a single photon with sufficient energy to eject an electron from the system, or by absorption of many photons. As described in more detail below, the photoionization of atoms can lead to the ejection of one or several electrons from the system, leaving behind an ion with a charge that is equal to the number of electrons emitted. The photoionization of a molecule can result in the breakup of the molecule into several fragments, some of which may be ions and others which neutrals. The fragmentation process is often called photo-dissociation or photo-fragmentation. The fragments can carry information about the structure of the original parent molecules, as will be shown in Chapters 4 & 5, where the correlation of ion momentum vectors in a multi-fold coincidence channel is used to determine the molecular geometry.

When an atom or a molecule absorbs a photon with energy of $h\nu$, where ν is the frequency and h is the Planck constant, an electron can be emitted if the photon energy exceeds the minimum energy required to eject an electron from the system, which is defined as ionization potential E_{IP}. In that case, the kinetic energy, E_{kin}, of this so-called photoelectron is given by

$$E_{kin} = h\nu - E_{IP}. \tag{2.1}$$

Strictly speaking, this equation is only true under the assumption that the other electrons in the system remain unchanged. If more than one electron is emitted or excited, this can lead to so-called photoionization satellites or direct double ionization, which are discussed briefly in Section 2.1.1.1. If the photon energy is lower than the E_{IP} of a system, absorption of multiple photons can also ionize the atom or molecule, see Section 2.1.2. The specific photoionization processes described in this thesis are 1) inner-shell photoionization with an X-ray synchrotron beam and 2) strong-field laser ionization with femtosecond laser pulses. This chapter gives a brief overview of both processes and lays the theoretical background for the Coulomb explosion imaging method.

2.1.1 Single-Photon Ionization with X-rays

In general, when the photon energy approaches the energy required to ionize a specific inner-shell of an atom, the probability of the photon absorption (e.g. absorption cross section [37]) increases for the system. The shell-specific dependency of the photo-absorption cross section makes it easy to investigate inner-shell photoionization of atoms and molecules using tunable X-ray synchrotron beams. Generally, atomic photoionization can be described by the total photoionization cross section $\sigma(\omega)$, where ω is the frequency of the X-rays, the partial photoionization cross section $\sigma_i(\omega)$, and the angular anisotropy parameters $\beta_i(\omega)$, where i stands for the quantum numbers of the ionized electron in a certain sub-shell of the atom [37, 38]. The cross section is defined as the number of ionized atoms per unit time divided by the number of incident photons per unit time per unit area. At a given photon energy, the sum of the partial cross sections of all sub-shells is equal to the total photoionization cross section. The partial photoionization cross section is expressed via a photoionization amplitude, which is a matrix element of the operation describing the interaction of an electron with the electromagnetic field [37]:

$$\sigma_i(\omega) = \frac{4\pi^2}{\omega c}|\langle\phi_i|d|\phi_f\rangle|^2. \tag{2.2}$$

Here, d is the dipole moment, c is the speed of light, ω is the incoming light frequency, and ϕ_i and ϕ_f are the one-electron wave functions of the initial and final states, respectively. For a one-electron atom or ion, the total photoionization cross section σ can be derived (see reference [39]) as

$$\sigma = \frac{16\sqrt{2}\pi}{3}\alpha^8 Z^5 (\frac{m_e c^2}{\hbar\omega})^{7/2} a_0^2, \tag{2.3}$$

where α is the fine structure constant, $a_0 \approx 0.5\mathring{A}$ is the Bohr radius, Z is the atomic number of the element, and m_e is the mass of an electron. This equation can also be approximately applied to inner-shell photoionization in the X-ray regime. From this simple expression, it

can be seen that the photoabsorption rapidly decreases with higher photon energy. The term Z^5 implies that heavier elements have higher X-ray absorption than lighter elements. Fig. 2.1 shows a diagram for a simple single-photon absorption and photoionization of the $2s$ and $2p$ levels of neon. The right panel in the figure is the experimental data obtained by photoionization of neon gas with 100 eV synchrotron photons. Fig. 2.2 shows the partial cross sections of three electron levels of neon atom. The Ne($1s$) inner-shell can only be ionized once the photon energy exceeds 870.2 eV.

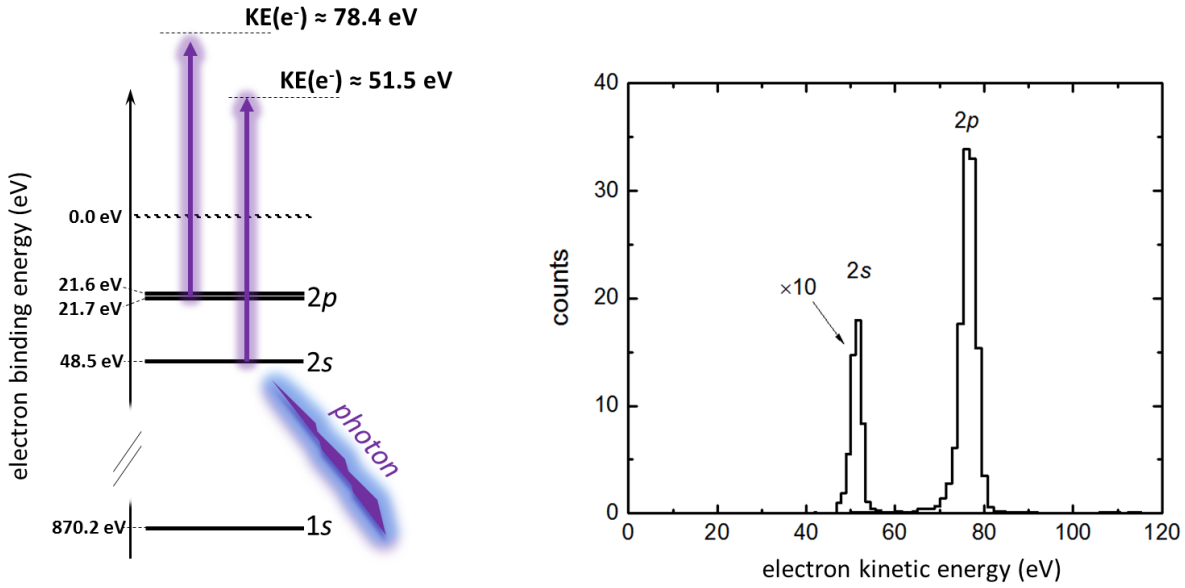

Figure 2.1: (Left) Single-photon ionization of a neon atom at 100 eV photon energy. The vertical axis represents the binding energies of different electron shells. The purple arrows show the possible ionization processes after absorption of a single photon. (Right) Kinetic energy distribution of $2s$ and $2p$ electrons after photoionization with 100 eV synchrotron photons.

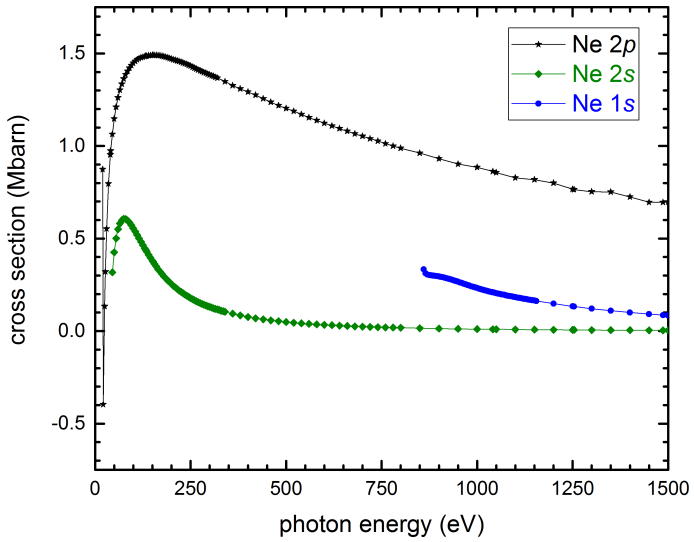

Figure 2.2: Partial absorption cross sections of neon atomic levels as a function of photon energy. The data are taken from reference [40]

Another important parameter in photoionization of atoms and molecules is the photoelectron angular distribution asymmetry parameter, β. The angular distribution of photoelectrons ejected from an atomic subshell by linearly polarized light is given by

$$\frac{d\sigma_i(h\nu,\theta)}{d\Omega} = \frac{\sigma_i(h\nu)}{4\pi}[1 + \beta_i(h\nu)P_2(cos\theta)], \tag{2.4}$$

where θ is the angle between the direction of polarization of light beam and the electron velocity vector, and $\mathrm{P_2}(\cos\theta)$ is the second-order Legendre polynomial. The term $\frac{d\sigma_i(h\nu,\theta)}{d\Omega}$ is referred to as differential cross section, where $\sigma_i(h\nu,\theta)$ is the partial cross section for ejection of photoelectrons into all angles and Ω is the solid angle in which the photoelectrons are ejected into. The β parameters of atoms are typically well known in literature, therefore they can be used to test and calibrate the spectrometer settings. In Chapter 3, the β parameter of the neon $2p$ photoelectron line is presented as an example.

2.1.1.1 Inner-shell Photoionization and Auger Decay

When an incoming photon has a higher photon energy than the binding energy of an inner-shell electron in a molecule, photoionization can take place and the inner-shell electron can

be ejected. During inner-shell photoionization, an inner-shell hole is created upon ejection of an electron from that shell, leaving the system in a highly excited state. The excited system usually has two pathways to liberate the excess energy: 1) through emission of florescence light after a valence electron fills the inner-shell hole; or 2) through a non-radiative Auger relaxation process where one or more secondary electrons are emitted from the system following the filling of the inner-shell hole by an electron from a higher lying energy level. Schematically, a simple two-step inner-shell photoionization of a system A can be expressed as [41]:

$$A + h\nu \rightarrow [A^+]^* + e^-_{photo} \ , \tag{2.5}$$

$$[A^+]^* \rightarrow A^{++} + e^-_{Auger} \ . \tag{2.6}$$

In this case, the system charge state changes twice, once after the ejection of the first electron and again after the subsequent Auger electron is emitted. The inner-shell photoionization process can be expressed with an energy level diagram as shown in Fig. 2.3. It shows some exemplary Auger-decay pathways following the $4d$ inner-shell ionization of a xenon atom. The kinetic energy of the Auger electrons emitted from the system depends on the decay pathway that the electron take. When an atomic or molecular system is inner-shell photoionized after absorption of a photon, the valence-shell electrons will be rearranged considerably in response to the reduced shielding of the nuclear attraction. In determining the Auger pathways involved in an inner-shell photoionization process, the newly rearranged valence energy levels need to be determined.

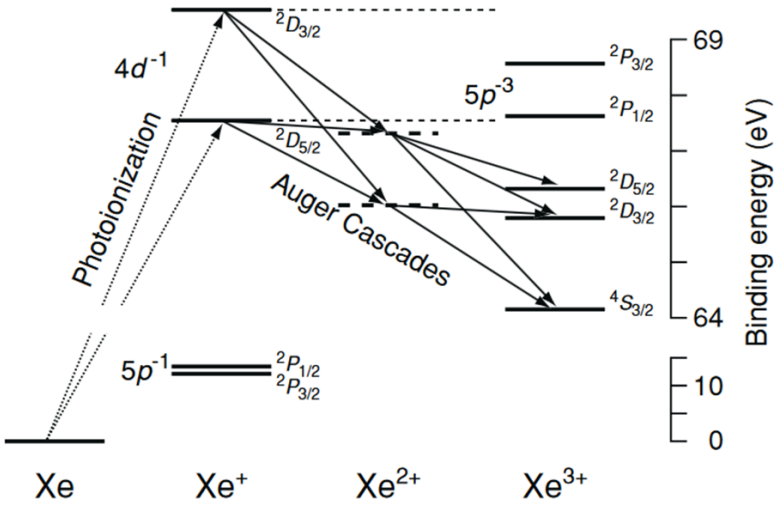

Figure 2.3: Energy level diagram for $4d$ inner-shell ionization of a xenon atom showing some of the Auger decay routes that can lead to a Xe^{+++} final state. Figure taken from [42]

The inner-shell photoionization studies reported in this thesis focused on multiple ionization of *cis*/*trans* geometrical isomers and structural isomers. For reaching the triple ionization channels of molecules, two Auger electrons are emitted from the system via Auger process. In a single Auger process shown in panel (2) of Fig. 2.4, one electron is emitted. In triple ionization processes involving two Auger electrons being emitted as shown in panel (3), the Auger electrons can be emitted from the system simultaneously or in two steps (e.g. one after another). If emitted simultaneously, the process is called double-Auger decay [43] or *shakeoff*, a process reported first by Carlson and Krause [44, 45]. If the electrons are emitted in stepwise manner, it is referred to as Auger-cascade [42].

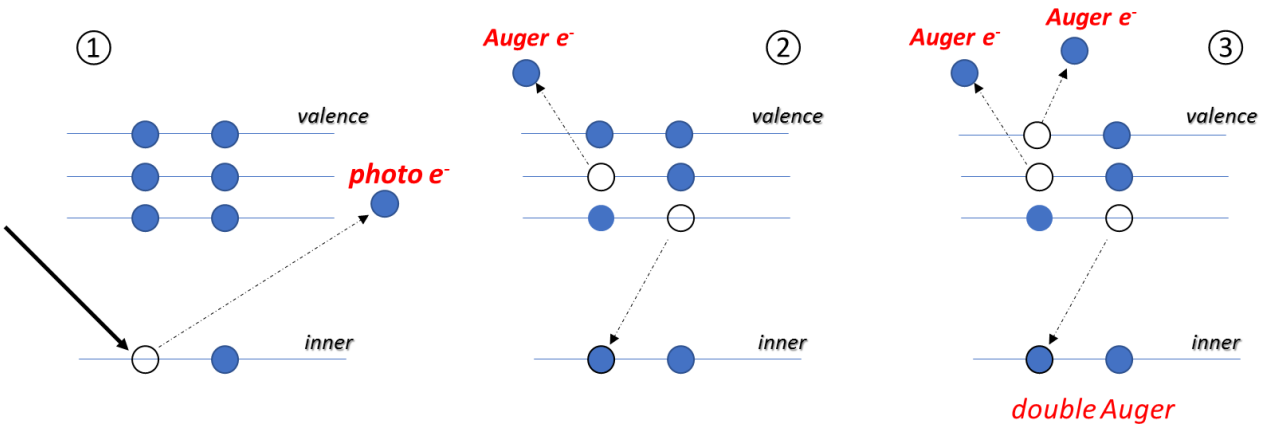

Figure 2.4: Schematic of Auger decay mechanism

In the double-Auger decay, the two Auger electrons share the liberated excess energy from the filling of inner-shell hole and the electron spectrum appear as continuum. In contrast to that, the two Auger electrons from an Auger cascade process have distinct well-defined kinetic energies [37]. However, if the electrons are not detected in coincidence, it is not easy to distinguish experimentally between double-Auger processes and stepwise cascade processes. Decay processes can involve many more types of relaxation processes such as shake-up, resonant Auger decay, etc. For brevity, only the main Auger processes are discussed here. Further details of the processes involved in the inner-shell photoionization and Auger relaxation processes can be found in [37, 38].

2.1.2 Strong-Field Ionization

If the photon energy is lower than the ionization energy of the system, however the light intensity is high enough, then the system can be ionized by absorbing multiple photons. Multi-photon ionization (or: "strong-field ionization") of atoms and molecules depends on the intensity and the wavelength of the incoming light. It can be classified with the *Keldysh* parameter [46] γ as expressed in

$$\gamma = \sqrt{\frac{E_{IP}}{2U_p}}, \tag{2.7}$$

$$U_p = \frac{I}{4\omega^2} \ \text{(in a.u)}. \tag{2.8}$$

Here, U_p is the pondermotive energy and I is the laser intensity. The pondermotive energy is the cycle-averaged kinetic energy of a free electron which quivers in the alternating field of the laser radiation. By comparing the strength of the electric field that an electron is exposed to inside an atom to the strength of the electric field of the incoming light, the ionization regime in a strong-field can be classified into **mutiphoton regime** and

tunneling regime. If the *Keldysh* parameter $\gamma >> 1$, the type of interaction is refereed to as $multi-photon\,ionization$ and if $\gamma << 1$, the interaction belongs to $tunneling\,ionization$. In the multi-photon ionization regime, the electric field strength is smaller than the atomic binding potential of the system, while in tunneling ionization regime, the electric field strength is comparable to or greater than the atomic binding potential of the system. Within the tunneling regime, if the intensity of the incoming light continues to increase to a level that the Coulomb barrier of the system is suppressed significantly, and the electrons start to spill into the continuum without tunneling out of the Coulomb barrier, the ionization process is often called $\mathbf{over-the-barrier\,ionization}$.

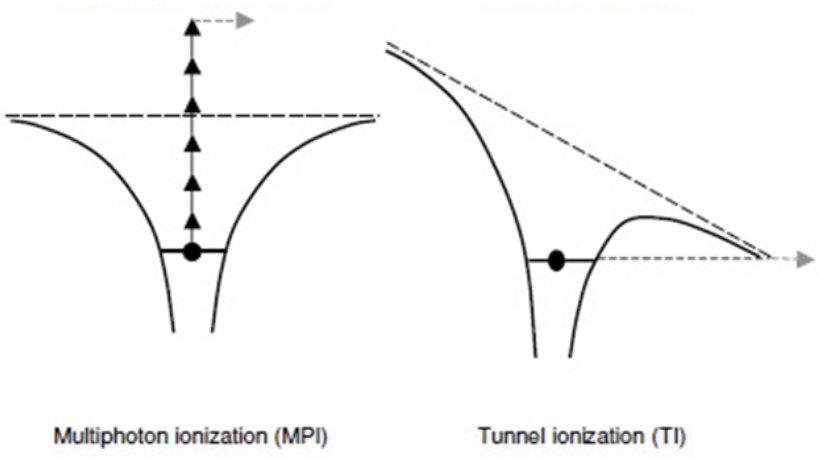

Figure 2.5: Strong-field ionization regimes: multi-photon ionization and tunneling ionization

An illustration of the multi-photon ionization and the tunnel ionization regimes is given in Fig. 2.5. Typically, strong-field ionization occurs when atoms or molecules interacts with a focused optical laser beam, e.g. from a Ti:sapphire lasers. At low laser intensities ($\leqslant 10^{13}$ W/cm^2 at $\lambda \approx 800$ nm), multi-photon ionization caused by the absorption of n photons can be described by the n-th order perturbation theory. Using a generalized cross section σ_n, the multi-photon ionization rate P can be derived as

$$P^n_{i\to f} = \sigma_n I^n, \tag{2.9}$$

where I is the intensity of the laser pulse, i and f represents the initial and final states, and

n is the number of photons that are absorbed. In the multi-photon regime, the system can absorb more photons than the minimum number of photons required for ionization. Such ionization is usually referred to as $above-threashold\,ionization$ or ATI for short.

In the experiments described in this thesis, triple ionization, e.g. the removal of three electrons from the system is required. For such processes, the molecule is typically exposed to high laser intensity on the order of 10^{14}W/cm^2. Expressing the pondermotive energy in units of electron volts and as a function of the laser wavelength and intensity, equation 2.8 can be rewritten as

$$U_p[eV] = 9.34 \times 10^{-20} \times (\lambda[nm])^2 I[W/cm^2]. \tag{2.10}$$

Using this equation, the pondermotive energy and the $Keldysh$ parameter for the molecules that are studied in this thesis can be calculated. At a typical laser intensity of 5×10^{14}W/cm^2, the pondermotive energy is 29.89 eV. The calculated $Keldysh$ parameters for this intensity and the ionization potentials of the isomers studied in this thesis are shown in the table below.

Molecules	E_{IP} [eV]	γ
cis 1,2-$C_2H_2Cl_2$	9.63	0.401
trans 1,2-$C_2H_2Cl_2$	9.66	0.402
cis 1,2-$C_2H_2Br_2$	9.63[a]	0.401
trans 1,2-$C_2H_2Br_2$	9.47[b]	0.398
2,6-DFIB	8.98	0.388
3,5-DFIB	9.03	0.389

The experiments performed in this thesis are thus in the tunneling ionization regime. However, since not all molecules are exposed to the maximum intensity because of focal averaging over different intensity regions along the beam direction and in the focal plane [49]. Most experimental strong-field ionization data therefore also contains a contributions from multi-photon ionization stemming from lower-intensity regions.

[0]a: Schander *et al* [47]; b: Wittel *et al* [48]

2.2 Coulomb Explosion Imaging

One of the methods developed in the study of molecular structure and dynamics is to ionize and stripe electrons away from the molecular system so that the resulting multiply charged molecule can fragment (*explode*) into smaller charged constituents that can contain geometric and dynamic information about the original system. The explosion of the charged fragments happens due to the Coulombic repulsion between like charges. Thus came the name **Coulomb explosion imaging**. However, if the equilibrium structure of the molecule shall be studied, the process of Coulomb explosion needs to happen fast before the molecule has undergone a significant structural change from its equilibrium position. If the ionization process takes place on a time scale that is much smaller than the time scale of nuclear motion, for example in a Coulomb explosion process initiated by inner-shell photoionization and fast Auger relaxation that takes place within a few femtoseconds, one can use the momenta of the fragment ions to extract geometrical information of the dissociating parent ion.

In this thesis, the Coulomb explosion imaging method is used to study the molecular structure of isomers. However, before discussing complex polyatomic molecules, Coulomb explosion imaging of diatomic molecules will be reviewed. The expression for the Coulomb explosion energy between two positive charge Q_1 and Q_2 is

$$U = \frac{1}{4\pi\epsilon_0}\frac{Q_1 Q_2}{R}, \tag{2.11}$$

where R is the distance between two charges and ϵ_0 is the electric constant. In the case of a diatomic molecule, R represents the distance between the two charges, one on each of the the two atoms. If a hypothetical diatomic molecule AB is photoionized and instantaneously lost two electrons, the initial population in its ground state is vertically transmitted to the Coulomb repulsion curve of AB^{++} as shown in Fig. 2.6.

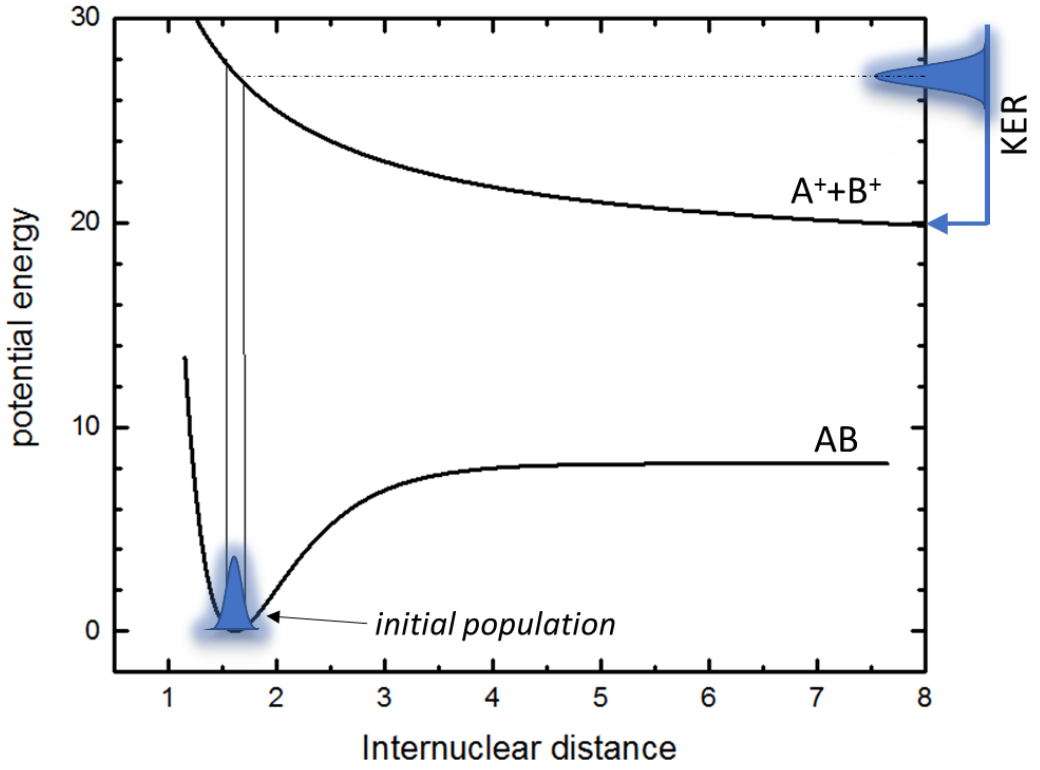

Figure 2.6: Schematic of Coulomb explosion process where the system's initial population is transferred instantaneously to the Coulomb repulsion curve by absorption of single photon.

The total kinetic energy release (KER) for the ionization of molecule AB into the A^++B^+ channel can thus be calculated by

$$U = \frac{1}{4\pi\epsilon_0}\frac{Q_1 Q_2}{R} = KE_{A^+} + KE_{B^+}. \tag{2.12}$$

The initial Coulomb potential energy is transferred to total kinetic energy release of the system. This example is under the assumption that the double ionization of AB molecule happened instantly and the nuclear motion is neglected during the transmission of the ground state population to the dicationic state. However, in multiple ionization of molecules with optical lasers and X-ray synchrotron beams, the process of fragmentation is rather complicated. The removal of the first electron from the system often brings the system to a cationic or an excited state where the molecular geometry can be distorted due to the nuclear motion, before the molecule absorbs more photons to remove the next electron to reach to a dicationic state. In such cases, the experimental result will include contributions from complex

intermediate dynamic processes that the molecule has undergone during the interaction with light. In strong-field laser ionization of the molecules with Ti:Sapphire lasers, the duration of the laser pulse determines the maximum time it can take to strip multiple electrons from the system. Using few-cycle laser pulses, the Coulomb explosion imaging of light molecules such as hydrogen and deuterium have been reported [50, 51]. Due to the relatively slower nuclear motion of heavier atomic constituents, laser pulses with longer pulse duration, e.g. 23 fs, can be used to perform Coulomb explosion imaging studies for molecules containing such heavier atoms. However, it is still important to keep in mind that the internuclear distances retrieved from this data may not correspond to the equilibrium values.

When the Coulomb explosion takes place among N number of ions, in another word, if the system breaks into N ions, the total kinetic energy release is expressed in units of electron volts as

$$E_{tot}[eV] = 14.4 \sum_{i \neq j}^{N} \frac{Q_i Q_j}{|R_i - R_j|},$$

where Q_i and Q_j are the charges of the ith and jth fragment and $|R_i - R_j|$ is the distance between the two charges prior to the fragmentation.

The Coulomb explosion model assumes that the ionization happens immediately and that there are no other effects disturbing the pure Coulombic potential. Such a model, when it matches well with the experimental fragmentation results in either inner-shell photoionization or ultrafast strong-field ionization, can be a powerful tool to image structure of a molecule. In time-resolved experiments aiming to study the temporal behavior of molecules after or during the excitation and fragmentation processes induced by external field, taking "snapshots" of each step and record the transition states of the molecule as a function of time with an imaging method is crucially important. Using Coulomb explosion imaging as a means to record the dynamics and structure of the molecule and ultimately reveal information about the initial or transitional state of the molecule and realizing the making of a "molecular movie" is the final goal in studying molecular dynamics.

2.2.1 Numerical Coulomb Explosion Simulations

In order to compare the experimentally determined fragment ion kinetic energies, momentum vectors, and correlations among momenta of different fragments to a pure Coulomb explosion model simulation based on classical mechanics, a simple numerical simulation is performed. The simulation only considers the ions and does not take into account any electrons. It assumes purely Coulombic repulsion between point charges with given masses, and the process starts from an equilibrium geometry of the molecule. This assumption is by no means to explain or give full theoretical support for the complex molecular dynamics that may take place under external light field, it is to simply compare the classical Coulomb model to the experimental data and provide an estimation for pure Coulomb explosion process.

The initial positions of the ions at the starting point, t=0 are the positions at the equilibrium geometry of the molecule. This is assuming that the charges are instantaneously created and the molecule stays at its equilibrium geometry during the localization of charges onto the relative fragments. The equilibrium geometries of the neutral molecule are determined by optimizing the molecular geometry using Gaussian 09 software package. The next step is to solve the numerical equation of motion for each ion involved in the Coulomb explosion. The motion of the individual ion is governed by Newton's law $\vec{F}$=m$\vec{a}$. For a diatomic molecule mentioned in Section 2.2, the force between the two ions at a given time t is

$$\vec{F}(t) = \frac{1}{4\pi\epsilon_0} Q_1 Q_2 \frac{\hat{\mathbf{r}}_1(t) - \hat{\mathbf{r}}_2(t)}{(\mathbf{r}_1(t) - \mathbf{r}_2(t))^2}, \tag{2.13}$$

where $\mathbf{r_1}$ and $\mathbf{r_2}$ are the position vectors of the fragments in three dimensional space. The velocities of a fragment along the Coulomb explosion direction is expressed as

$$\mathbf{v} = \frac{d}{dt}(\mathbf{r}_1(t) - \mathbf{r}_2(t)), \tag{2.14}$$

and the time dependent acceleration term is described with the following equation

$$\mathbf{a} = \frac{d\mathbf{v}}{dt} = \frac{1}{4\pi\epsilon_0}\frac{Q_1 Q_2}{m_1}\frac{\hat{\mathbf{r}}_1(t) - \hat{\mathbf{r}}_2(t)}{(\mathbf{r}_1(t) - \mathbf{r}_2(t))^2}. \tag{2.15}$$

The force on the particle is determined by the Coulomb force between two particles and, for a many-body Coulomb explosion model, the Coulombic forces from all the other charged particles in the system. As the force is only dependent on the distance between the particles at a given time t as shown in equation 2.13, the time becomes the independent variable in which the system is evolved. In numerically solving the time dependent velocities and acceleration terms for each new position $\mathbf{r}$(t), the velocities and acceleration of the previous point $\mathbf{r}$(t-dt) are used. This is a way to track the ion's position, velocity and acceleration as time evolves by step sizes of dt. For the whole time range, typically, 0 to 10 us is set and a commonly used 4th order RungeKutta algorithm is applied to calculate the momentum vectors and kinetic energies of all fragments for an ideal Coulomb explosion model. The 4th order Runge-Kutta algorithm is provided by the Matlab library as a robust method to calculate nonstiff ordinary differential equations. This library includes the use of an adaptive step size that changes automatically to keep the overall error of the iteration steps as small as possible. It also has options to provide exact step sizes, e.g. one can set the time step to be 5 fs instead of a system chosen automatic step size. However, if too small time step is chosen for the simulation, the total time for the calculation will be rather large and for simple two-body, three-body Coulomb explosion simulations, setting a fixed small time step proven to be almost identical to the option where the system automatically choose the time step by itself.

The Coulomb explosion simulation provides all kinematic information of point charges, such as position in space, velocity, momentum and kinetic energies. From the momentum vectors of those simulated fragments, the correlation angles can also be calculated between fragment momenta.

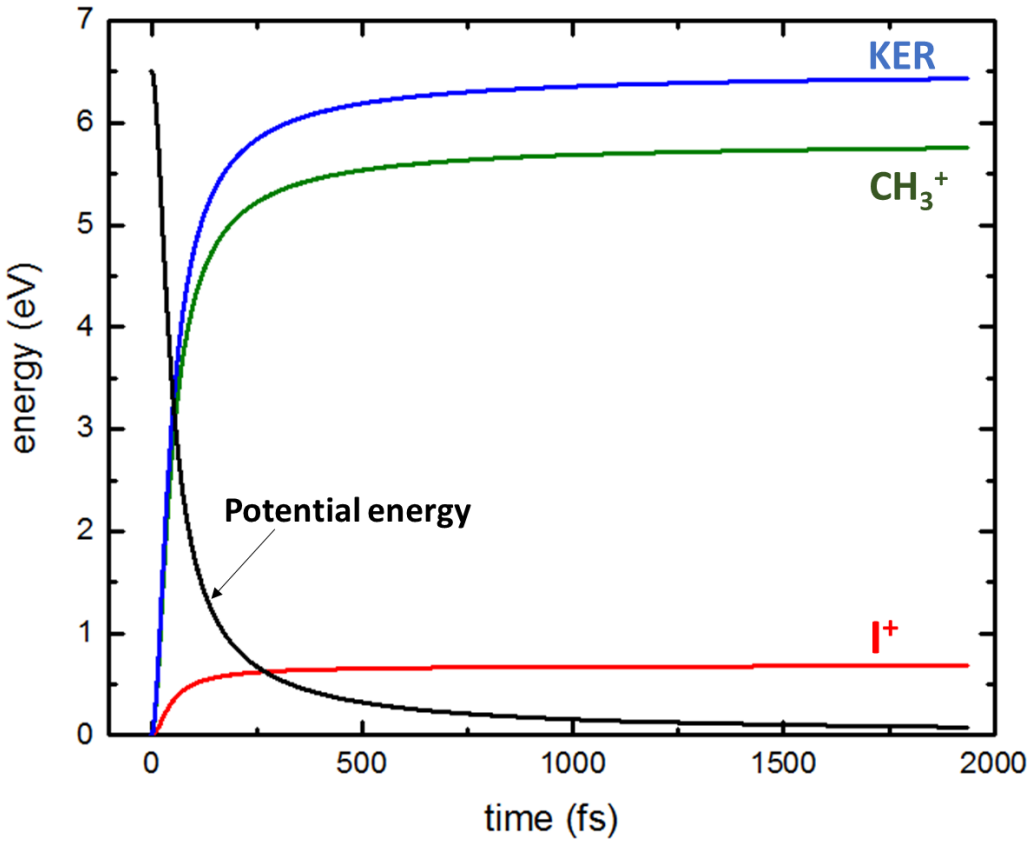

Figure 2.7: Coulomb explosion simulation of the kinetic and potential energy for a CH_3I molecule that fragments into CH_3^+ and I^+

An example of the two-body Coulomb explosion simulation of methyl iodide molecule (CH_3I) is given in Fig. 2.7. The total kinetic energy release (KER), individual kinetic energies as well as the potential energy between two fragmenting bodies are given as a function of propagation time. Only the first 2000 fs time scale is given as an example. In order to obtain final results at $t \rightarrow \infty$, the total time range is usually set to 10 us.

Chapter 3

Experimental Methods

The purpose of this thesis is to gain insight into the fragmentation dynamics of isomeric molecules after photoionization with soft X-ray synchrotron beams and ultrafast intense laser pulses. In order to study the fragmentation of individual molecules and obtain full three-dimensional kinematics of all fragmentation channels, ion-electron and ion-ion coincidence momentum imaging techniques are applied [52–54]. Position and time information of all ions and electrons resulting from the ionization of a molecule are measured in coincidence with time and position sensitive detectors [55, 56]. Such detection scheme enables the reconstruction of the final results of the interaction process by obtaining the momentum vectors of ionic particles. In order to achieve coincidence momentum imaging, two main experimental apparatuses, namely a double-sided coincidence VMI and a Cold target recoil ion momentum spectroscopy (COLTRIMS) system, are utilized in the experimental work described in this thesis. Both systems are equipped with a supersonic gas jet to prepare cold gas-phase molecular targets. The other important parts of the experiment are the soft X-ray synchrotron beam and the Ti-Sapphire infrared femtosecond laser pulses. The synchrotron beam is provided by the beamline 10.0.3 of the Advanced Light Source of Lawrence Berkeley National Laboratory and the laser facility is provided by the PULSAR laser system of J. R. Macdonald Laboratory at Kansas State University. In addition, a VUV synchrotron beam at beamline 9.0.2 of ALS is also employed and time of flight (TOF) mass spectroscopy

measurements are conducted in pursuit of finding the ionization potentials of the isomers described in the thesis.

This chapter gives comprehensive details about the experimental procedures and apparatuses utilized to conduct the measurements. The light sources applied in all experimental work are described first and the details of the experimental apparatuses, molecular jet, and detectors are given later.

3.1 X-ray Synchrotron Beams

The inner-shell photoionization experiments and the VUV photoionization yield scans reported in this thesis were conducted at the Advanced Light Source (ALS) of Lawrence Berkeley National Laboratory (LBNL). The ALS began operations in 1993 as one of the world's first 3rd generation synchrotron sources, providing VUV and X-ray beams for probing the electronic and magnetic structure of atoms, molecules, and solids, etc.

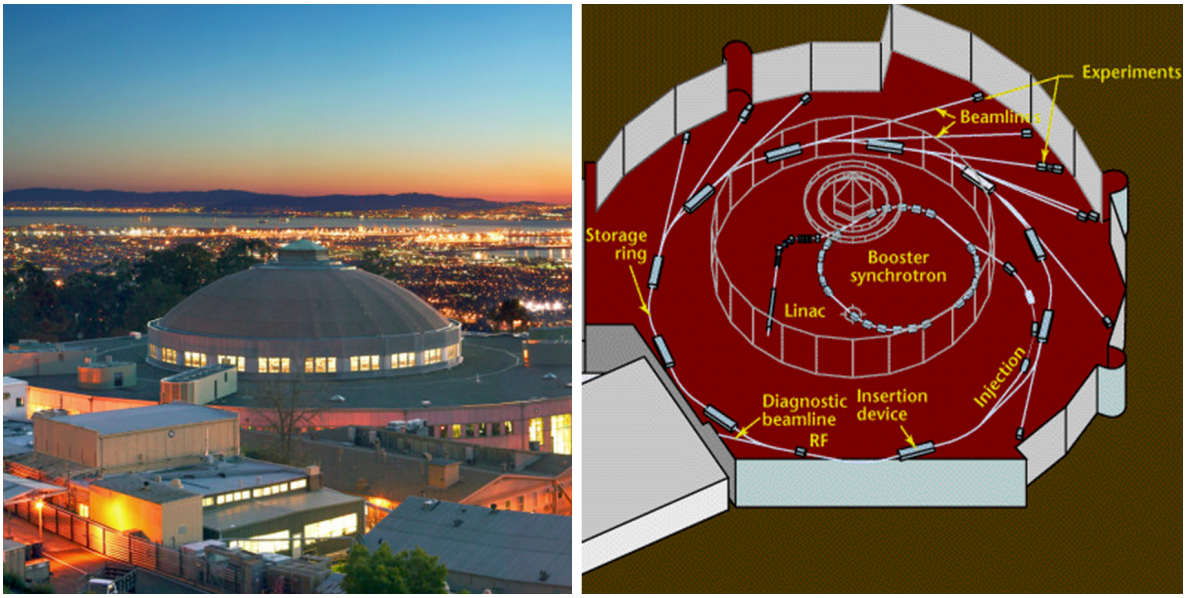

Figure 3.1: Picture of the ALS from outside (left) [57]; Floor diagram of inside the ALS (right) [58]

At the ALS, synchrotron radiation is produced from electron bunches that are generated from an electron gun and are accelerated to nearly the speed of light, reaching a final energy of

1.9 GeV. The trajectory of the electron bunches is forced onto a nearly circular path with 62 m diameter by the magnets inside the storage ring. Between the magnets, there are straight sections where there are dozens of magnets of alternating polarity contained in devices called **undulators**. When electrons pass through **undulators**, they emit beams of electromagnetic radiation from the infrared through the visible, ultraviolet, and X-ray regimes. The radiated light beam are collimated with beamline optics (e.g. monochrometer, slits, reflection mirrors) and directed to beamlines with experiment endstations. The synchrotron at the ALS runs at two different modes, multi−bunch mode and two−bunch mode. All the experiments reported here were performed in multi−bunch mode with linear light polarization. In this mode, the storage ring is filled with 270-320 electron bunches with 2 ns separation time [59]. In electron-ion coincidence studies using a double-sided VMI apparatus, fast electron timing signals can be used as timing−reference signal for the data acquisition system. This allows the coincidence experiments to run under multi−bunch mode and to not be restricted to run under two−bunch mode that comes with a "master−clock" signal.

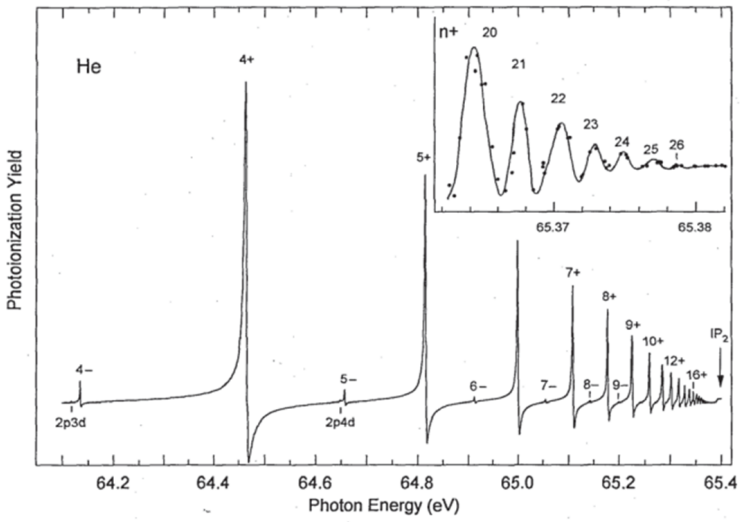

Figure 3.2: The photon energy resolution of Beamline 10.0.1 is demonstrated by a measurement of the three optically allowed Rydberg series in the double-excitation region of He below the N=2 ionization threshold of He. The inset shows the "+" Rydberg series from n=20 to n=26; Figure taken from G. Kaindl *et al* [60].

The synchrotron beam utilized to perform the ion-electron coincidence experiments reported in this thesis is provided by the beamline 10.0.1. The source of radiation for this

beamline is a 4.5 m-long, 8 cm-period undulator in a straight section of the ALS. Originally transferred from beamline 9.0.1, the beamline 10.0.1 has unprecedented spectral resolution. The measurements of the double-excitation resonances of He in a gas cell achieved a linewidth of 1.0 meV (FWHM), corresponding to a resolving power of 64,000 for the ($2p$, $3d$) double-excitation state of He at 64.12 eV [60]. Fig. 3.2 shows the original spectral resolution measurement on the double-excitation Rydberg series of He. Those Rydberg states are very long-lived, and are thus ideally suited for analyzing mono-chromator resolution. The beamline provides an intense source of linearly polarized light in the 17 eV to 350 eV photon energy range. Further details on the optical layout of the beamline can be found in reference [60, 61].

3.2 Ultrafast Femtosecond Lasers

This section gives a brief introduction to the femtosecond laser system that was used to conduct the strong−field ionization experiments in this thesis.

The laser system used in the experiments is a state of-the art Ti:sapphaire ultrafast laser system, named **PULSAR**: **P**rairie **U**ltrafast **L**ight **S**ource for **A**ttosecond **R**esearch. The laser system generates linearly p-polarized 2 mJ laser pulses at 10 kHz repetition rate with a pulse duration of 21 fs. The central wavelength of the laser pulses is around 800 nm. The stability of the carrier envelope phase (CEP) is below 300 mrad, thus enabling CEP dependence studies of molecular fragmentation. The high repetition rate of PULSAR allows experiments that would be impractical with lesser laser systems. The two main components of the **PULSAR** Ti:Sapphire ultrafast laser system, the "oscillator" and "amplifier", are briefly introduced below, further details of the laser system are described elsewhere in detail [62].

3.2.1 Oscillator

The laser pulses from the **PULSAR** laser system are generated by pumping a Ti:Sapphire crystal with a continuous (CW) 532 nm solid-state laser system. They are generated in a Kerr-lens mode-locked Ti:Sapphire oscillator with a repetition rate of 75.2 MHz. A typical mode-locked output from the oscillator has a full width at half maximum pulse duration of 14 fs; power of >300 mW, and a central wavelength of 780 nm with 80 nm bandwidth. The output of the oscillator beam is used to seed the amplifier.

3.2.2 Multipass Amplifier

The amplification in the **PULSAR** laser system is based on the chirped-pulse amplification (CPA) technique introduced by Strickland and Mourou [63]. A detailed description of a CPA femtosecond laser system can be found in [64]. In the CPA technique, the laser pulses provided by the oscillator are stretched in time from the femtosecond to the picosecond time scale to avoid damage to the amplifier crystal. The stretchers are used in the amplifier system of **PULSAR** are grating-based stretchers. The stretched pulses are selected by the Pockels cell, and only the reduced number of laser pulses are further amplified by the multipass amplification system. By doing so, the repetition rate of the laser pulses is reduced from 75.2 MHz to 10kHz. The laser amplification in **PULSAR** is done through two stages. In the first stage, the laser pulses with 10kHz repetition rate are generated with 1mJ pulse energy. In the second stage, the pulses are further amplified to 2mJ energy.

3.2.3 Spectrometers for Electron-Ion Coincidence Measurements

3.2.3.1 Double-sided Coincidence VMI

The velocity map imaging (VMI) technique is a powerful experimental tool that is capable of simultaneously determining the kinetic energies and angular distributions of ejected ions or electrons from gas-phase atomic or molecular targets [18]. In the experiments described in here, a modified double-sided VMI spectrometer is used to achieve electron-ion and ion-ion

coincidences at the same time. Similar spectrometer setups have been described by Rolles *et al* [65] and Strüder *et al* [66].

In the current version of the apparatus, both ions and electrons can be measured in coincidence after photoionization with soft X-ray synchrotron beams. Microchannel plates together with delay-line detectors are used to measure the TOF and the detector hit position of ions and electrons. A sketch of the double-sided VMI spectrometer is shown in Fig. 3.3.

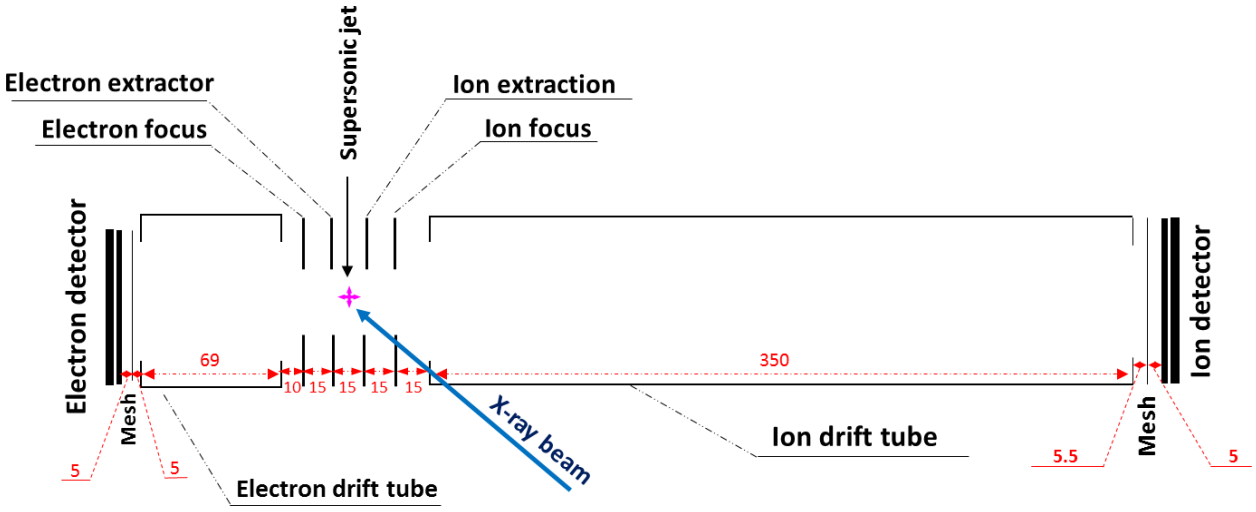

Figure 3.3: A schematic diagram of the VMI spectrometer. The dimensions given in the figure are in the units of millimeter (mm).

The voltages applied to the spectrometer, in particular to the electrostatic plates, labeled **electron focus**, **ion repeller**, **ion extraction** and **ion focus** and also the **ion** and **electron drift tubes**, are chosen such that particles with equal momentum vectors (i.e. equal kinetic energy and emission direction) hit the detector at the same position independent of their starting point. Both ions and electrons generated from the interaction needs to be focused onto their corresponding detectors. Due to the complex nature of choosing a perfect voltage that focuses both the electrons on the electron detector as well as the ions on the ion detector, the SIMION particle trajectory simulation software [67] is applied to simulate ion and electron flight trajectories to predict a good focusing condition. During the experiment, the voltage settings can be adjusted until ions with (almost) zero kinetic energy, such as molecular parent ions or nobel gas targets such as Ne^+, Ar^+, are focused to the smallest possible spot in the center of the ion detector, while the photoelectrons form sharp

circular structures. Fig. 3.4 demonstrates a screen shot of a typical ion and electron trajectory simulation with the SIMION software. The red curves are the electric field contours and the voltages applied to individual parts of the spectrometer are given on the top. A zoomed in box indicates the origin of particles that are initiated from three different points, vertically separated by 1 mm. It can be seen from the figure that both ions and electrons generated from three different points with same initial momentum are focused onto same points on their respective detectors.

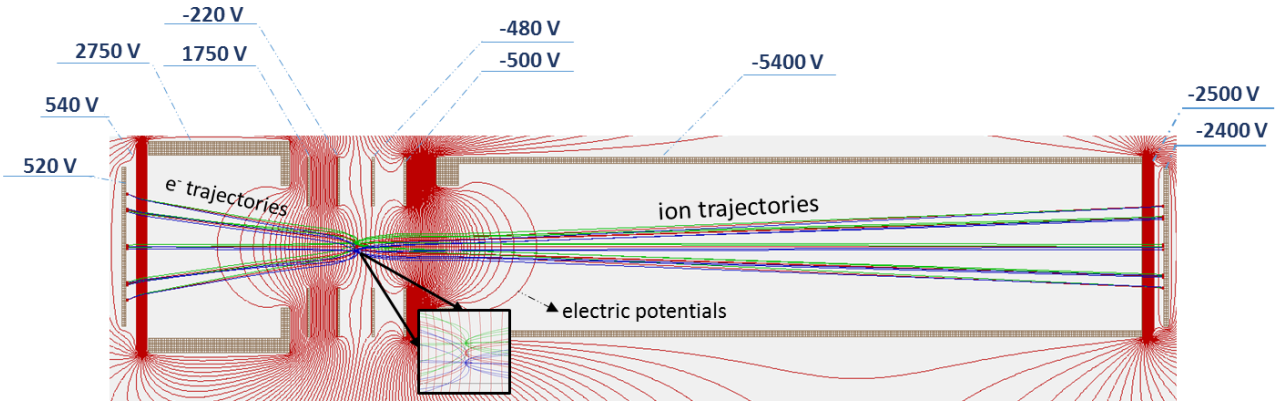

Figure 3.4: Ion and electron trajectories simulated in SIMION

The advantage of the spectrometer mentioned here is its capability to simultaneously detect electrons within wide kinetic energy range (0−250 eV) while performing high-resolution ion-ion coincidence detection of molecular fragmentation. The choice of voltages largely depends on the range of kinetic energies of the electrons that needs to be detected in the experiment with 4π angle. If the kinetic energies of electrons are expected to be high, for example, if 190−eV Auger−electrons that are ejected after inner-shell photoionization of Cl $2p$ needs to be focused, the voltages on the spectrometer should be set high enough so that the strong focusing electric field projects all electrons in 4π angle toward the detector. At the same time, in order to achieve high resolution ion momentum imaging on the opposite side, on the ion detector (in coincidence with the electrons), the provided electric field strength of the spectrometer can not be too high to worsen the temporal and spacial resolution of ion-ion coincidence imaging. The voltage settings for both the spectrometer parts and the detectors in the experiments described in current thesis are given in Appendix C.

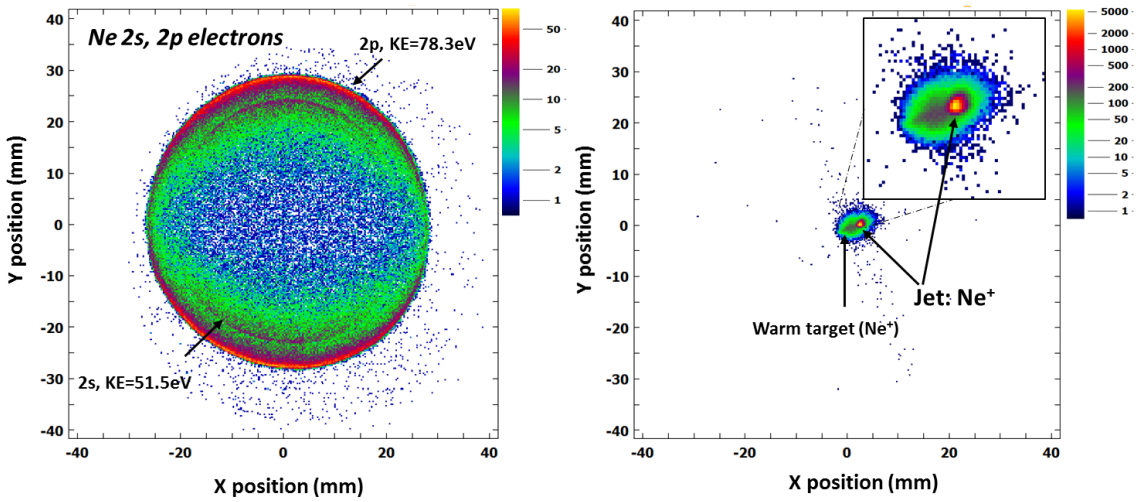

Figure 3.5: (a) Position spectrum of Neon $2s$ and $2p$ electrons after photoionization with 100 eV photons. (b) Ne^+ ion position at the detector center

During the operation of an electron–ion coincidence measurement, a valid coincidence event for the coincidence between one electron and one ion consists of a total of twelve signals: MCP timing signal on the electron side, a timing signal from the ion-side MCP, and ten position signals from which four of them are picked up from four ends of the two quad delay-line wires for electron position measurement and the other six position signals are generated from Hex delay-line wires, two from each wire for ion position measurement (further details on the delay-line detectors are given in Section 3.2.5). Examples of an electron and an ion position spectrum from a typical neon gas inner-shell photoionization experiment are shown in Fig. 3.5. Both $2s$ and $2p$ photo-electron lines after photoionization with 100−eV photons can be seen in electron spectrum on the left and the Ne^+ ion distribution is shown on the right. The well focused hot spot in the ion position distribution is from the cold molecular jet and the wider ion distribution is due to the warm neon gas target in the vacuum chamber.

3.2.3.2 COLTRIMS

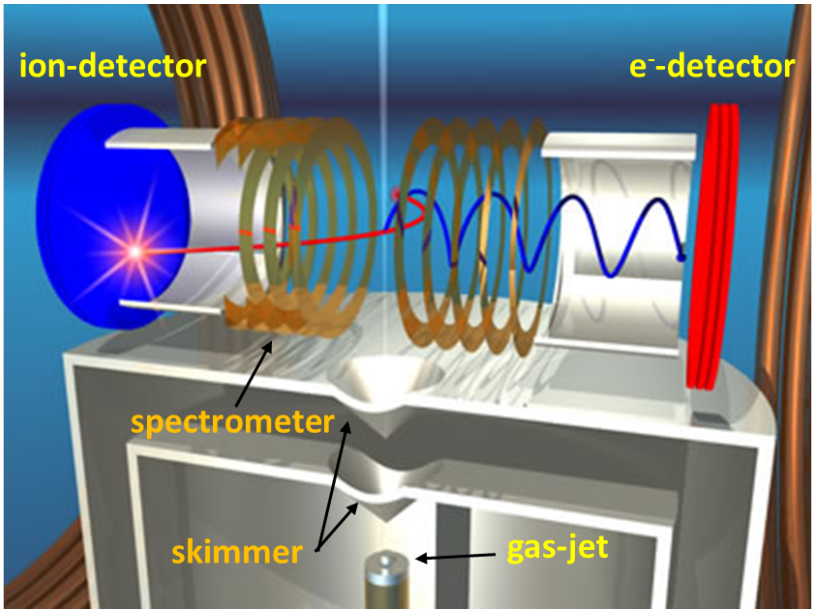

Figure 3.6: A schematic figure of a COLTRIMS apparatus. Figure taken from http://www.atom.uni-frankfurt.de/research/coltrims/

In the context of this thesis work, the experiments that involve ultrafast laser ionization and fragmentation of molecules are conducted using a COLTRIMS ion momentum imaging apparatus. COLTRIMS, also refereed to as reaction microscope, was originally designed for ion-atom collisions experiments [68]. Since then, COLTRIMS has become a versatile tool for kinematically complete studies of atomic and molecular processes [52]. Similar to the application of the double-sided VMI, where the goal is to image the final state momentum vectors of an ionization or fragmentation process, the COLTRIMS apparatus is employed to achieve coincidence ion-ion detection of gas-phase molecular targets after strong-field ionization by ultrafast femtosecond laser pulses.

For low-energy electron detection, usually, an additional magnetic field is needed to ensure 4π solid angle acceptance. However, in the experiments described here, the, electron spectra were not recorded, so the following description of the apparatus will focus only on the coincident detection of ions. Fig. 3.6 presents the schematics of a typical COLTRIMS apparatus. Similar to the COLTRIMS utilized in this thesis work, two skimmers are imposed

to generate the cold molecular beam target. The typical static electric field strength inside the spectrometer is around 10 V/cm during the Coulomb explosion measurments described in Chapters 4 & 5. This was achieved by applying 1400 volts across the spectrometer. For high-resolution measurments of atomic targets for calibration purposes, only 400 volts was applied across the spectrometer.

3.2.4 Microchannel Plates (MCP)

The micro-channel plate (MCP) detectors are micro fabricated arrays of channel tubes, each with a diameter of a few tens of microns and working as an independent electron multiplier. They are formed from a lead glass matrix and hexagonally packed to form a plate [69]. The main purpose of an MCP in the experiments of this thesis work is to measure time signal when the particle hits on the detector and to generate and amplify the secondary electrons inside the channel tubes to create electron shower that will enable delay-line detectors to generate position information of the particle. A schematic figure of a micro-channel detector is shown in Fig. 3.7. An ion generated from the light-matter interaction is accelerated to the MCP in the electric field provided by the spectrometer and hits the surface area or enters one of the micro channels. The surface area of the MCP is usually coated with Nichrome, a mixture between Nickle and Chrome elements. The channel tubes are made out of a specific reduced-hydrogen glass (a high temperature heating treatment of the channel tube glass material in order to increase electrical conductivity and secondary electron emission [70]), and the glass has an emissive property that helps emitting secondary electrons when ions, electrons or photons hit on the surface.

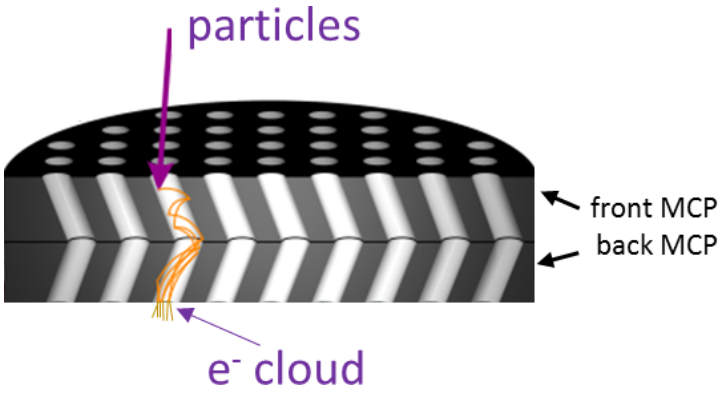

Figure 3.7: A schematic figure of a Chevron stack MCP and particle trajectories in the channel tube. Figure adopted from [71].

The surface open area ratio of the imaging quality commercial MCP for the experiments described in this thesis is 60%. This means when ions hit the surface of the MCP, there is 40% of the time that ions will hit the surface area between channel tubes and not enter the channel tubes. The MCP surface open area ratio ultimately affects the efficiency of the ion detection. The larger the open area ratio, the more efficient it is to detect particles. The ions that enter the channel tubes will hit the inner surface and create a free secondary electron which is accelerated by a large potential towards the back of the MCP. Each secondary electron frees further electrons upon hitting the channel′s inner surface. Such electron multiplication continues and eventually leads to an avalanche of electrons which carry a macroscopic current. Generally, coincidence momentum imaging setups use matched plates, where two MCP plates with similar resistance are stacked together in a v-like (Chevron) configuration as shown in Fig. 3.7. In a chevron MCP stack, the electrons that exit the front plate start the cascade in the back plate. The advantage of the chevron MCP over a straight channel MCP is significantly more gain at a given voltage due to the increased number of surface impact in chevron configuration. Typically, one particle that hits the front MCP is amplified and the number of electrons generated will reach to about 10^3 after the first plate and $\sim 10^6$ when all electrons departed from the back of the second MCP. The MCPs used in both the ion and electron sides of the double-sided VMI apparatus and the MCP used in the COLTRIMS apparatus are 80 mm in diameter.

3.2.5 Delay-line Detectors

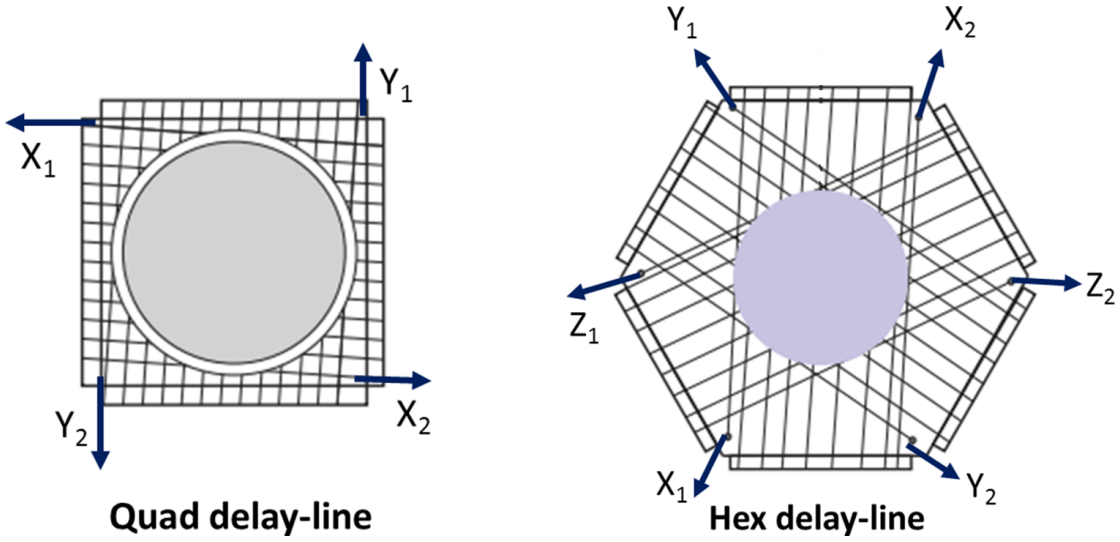

Figure 3.8: Quad and Hex delay-line detectors. Figure adopted from [72]

The position-sensitive detectors consist of two (Quad) or three (Hex) helical wire propagation (delay) lines, see Fig. 3.8. The detectors used in the experiments described within this dissertation are delay-line-detectors (DLD) purchased from RoentDek. The electron detector in the double-sided VMI and the ion detector in COLTRIMS are both Quad DLDs and the ion detector used in double-sided VMI is a Hex DLD. After the secondary electrons are multiplied and departed from the back of MCP, the cloud of electrons impinges onto the position detector wires of which one is used to determine the x position and the other one measures the y position. When the electron cloud hits the wires, it creates a pulse of current traveling in these wires toward the two ends. The details of the detector electronics and methods of how to pick up time and position signals from MCP and the ends of each wire are described in detail in Roendtek detector manual [55]. Using four time signals X_1, X_2 and Y_1, Y_2 picked up from position wires of a Quad DLD, the position information of a particle hit on the detector (x,y) is

$$x = (X_1 - X_2)v_{signal} + x_0, \tag{3.1}$$

$$y = (Y_1 - Y_2)v_{signal} + y_0, \tag{3.2}$$

where x_0, y_0 are arbitrary offsets.

The total time it takes for the pulses to travel to the end of the wires are proportional to the length of the wire. Since the length of each wire is a constant number, the sum of two time signals picked up from opposite ends of a wire should be a constant. The total time it takes for the position signals to propagate on the delay-line wires (T_{xsum}, T_{ysum} in the case of quad delay−lines) is refereed to as "time-sum" and is often used to eliminate useless random signals by setting gates on two sides of the sharp "time-sum" peaks. The equations describing the "time-sum" are given in 3.3. Note that due to the electronic settings, e.g. signal amplifiers, CFDs (constant fraction discriminator), the signal transmission wire lengths can be slightly different for each wire, so in the analysis of the signals, small offset factors can be tweaked to symmetrize the position distribution (e.g. Equation 3.1).

$$T_{xsum} = \frac{L_x}{v_{signal}} = X_1 + X_2 - 2T_0 \tag{3.3}$$

$$T_{ysum} = \frac{L_y}{v_{signal}} = Y_1 + Y_2 - 2T_0 \tag{3.4}$$

$$T_{zsum} = \frac{L_z}{v_{signal}} = Z_1 + Z_2 - 2T_0 \quad \text{(Hex DLD)} \tag{3.5}$$

L_x, L_y are the length of X and Y wires and v_{signal} is the speed of signal propagation, X_1, X_2 and Y_1,Y_2 are time signals picked up from two wire ends. T_0 is the time of impact on the surface of the MCP. The typical time−sum on ion and electron detectors in double-sided VMI apparatus is shown in Fig. 3.9.

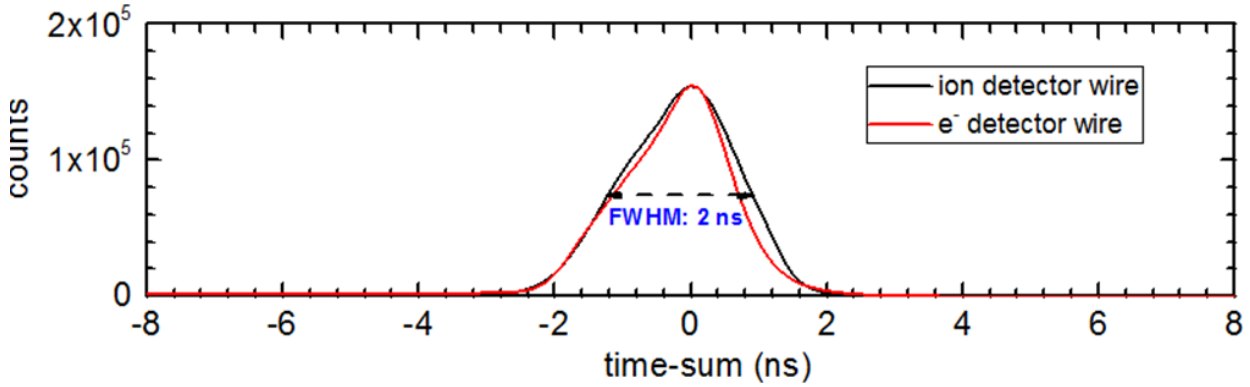

Figure 3.9: Time-sum distribution of two delay-line wires subtracted constants to center at zero. The signals for the two curves are separably taken from one of the Hex-anode delay-line wires from the ion detector and one of the electron Quad-anode delay-line wires in the VMI system.

For brevity, only the expression for the position signals for Quad DLD is given, the expression for position signals of Hex DLD can be found in the manual from Roendtek [55]. All time and position signals are amplified by a high-bandwidth fast amplifier and further processed by a Constant-Fraction-Discriminator (CFD), before the timing information is digitized by a multi-hit Time-Digital-Converter (TDC). The CFD is an electronic device which produces a standardized NIM signal output, if the voltage exceeds an adjustable threshold. The CFD plays an important role in providing timing output which is independent of the original pulse height of the incoming signal. The TDC card allows up to 16 hits per channel. In a typical multi-bunch operation of the ALS, the electron MCP signal provides the common start for the TDC, while it is triggered by a photodiode signal for the laser experiments. For each event, all TDC outputs are stored in a listmode (lmf) file, which allows analysis of the data event by event.

3.2.6 Coincidence Detection

In the inner-shell photoionization experiments using the double-sided VMI apparatus, fast electron time signals from electron's birth to the time of impact on the MCP (~5ns) are used as a trigger signals for the data acquisition system and all signals from MCP to position wires are recorded with respect to the time signal of electron generetated on the electron

MCP.

In the COLTRIMS measurement, a signal from a photodiode that is irradiated by a small fraction of the laser pulse is used to trigger the entire data acquisition system with 10 kHz repetition rate. The signals generated from the detector (TOF from the MCP and position signals from the delay-line anode) are measured with respect to the signal generated from this photodiode. The true time of each hit can be written as $\mathrm{TOF}_{ion} = \mathrm{T}_{total}$ - T_{PD}, where T_{PD} is the time difference between the time the laser pulse intersects the molecular target and the photodiode signal (including the associated time difference due to electronics). The photodiode signal is connected to the time to digital converter (TDC) as a start/reference signal. A wide temporal window that usually covers the TOF of heaviest (slowest) ion species from the interaction can be set starting from the reference signal T_{PD}. From the start time until all ions generated from the interaction reach the detector, the detected ions will be recorded as 1^{st}, 2^{nd}, 3^{rd}...hits in the order of their time of arrival. Their time and position information are recorded accordingly in an event file.

3.2.7 Coincidence Maps: PIPICO and PIPIPICO/TRIPICO

In order to find out the breakup channels after the interaction of a molecule and a light beam, a photoion-photoion coincidence map (**PIPICO**) is commonly used for identifying two-body coincidence channels, and a photoion-photoion-photoion coincidence map (**PIPIPICO** or also known as **TRIPICO**) for three-body channels. In the **PIPICO** spectrum, the yield of ionization channels is plotted as a function of the time of flight of the first hit, TOF_1, and the time of flight of the second hit, TOF_2. In the **TRIPICO** spectrum, the yield of channels is plotted with respect to the time of flight of one particle versus the sum of the time-of-flight of the other two particles. Fig. 3.10 shows a PIPICO (a) and a TRIPICO (b) spectra of the $C_2H_2Br_2$ molecule after photoionization with 140-eV photons, see Chapter 4.

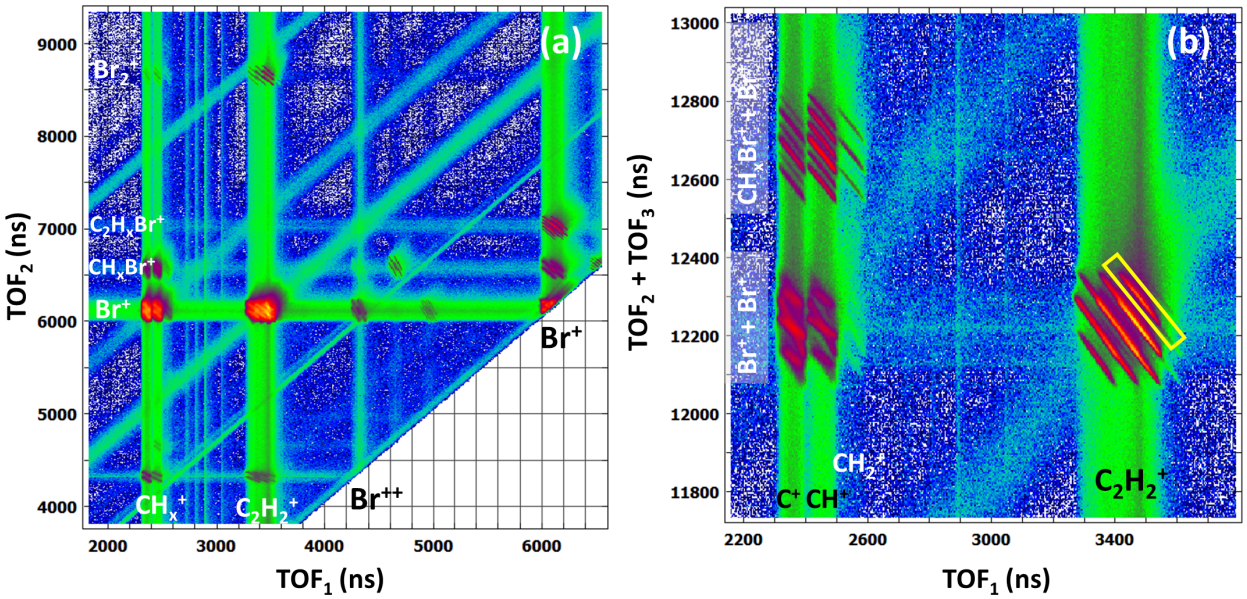

Figure 3.10: (a) PIPICO and (b) TRIPICO diagrams of $C_2H_2Br_2$ molecules after photoionization with 140 eV photons. The yellow box in (b) is shown as an example of time gate on a selected channel.

Due to the momentum conservation along the axis of the TOF direction, ions fragmented from a molecule end up in a diagonal coincidence stripes. If the molecule breaks up into two ions, the coincidence stripes can be observed in a PIPICO spectrum. For cases when the molecule breaks up into three ions, the coincidence stripes can be seen in a TRIPICO spectrum. The TRIPICO spectrum can be plotted in three forms: TOF_1 vs TOF_2+TOF_3, TOF_2 vs TOF_1+TOF_3 and TOF_3 vs TOF_1+TOF_2. The choice between those three TRIPICO spectra depends on whether the fragmentation channel of choice can be easily separated from other three-body channels that sometimes overlap on top of each other. The comprehensive details of PIPICO and TRIPICO coincidence spectra can be found in [59, 73]. After selection of a channel of interest, time gates as shown in Fig. 3.10 (b) can be applied on such coincidence spectra and only the events from within the chosen coincidence stripe area are isolated for further analysis.

3.2.8 Momentum Calibration: Double-sided VMI

The electric field in a VMI spectrometer is not homogeneous, as shown in Fig. 3.4, thus it is impossible to derive analytical formulas for the electric field that can be used to reconstruct the ion momenta from the measured time of flight and the hit positions of each ion. Instead, simulating the ion and electron trajectories with the SIMION software package allows one to construct empirical formulas connecting the hit position with the momentum vector components parallel to the detector and TOF of ions with momentum component that is perpendicular to the detector. In this section, this reconstruction of transverse (*parallel* to the detector) momentum components p_x and p_y and the longitudinal (along TOF axis) component p_z are introduced.

3.2.8.1 Transverse Momentum: p_x and p_y

The first step in the SIMION simulation is to "draw" the exact geometry of the spectrometer and detectors in the SIMION workbench. This includes the spacial positioning of all components inside the VMI spectrometer as well as the voltages applied in the specific experiment. When all parameters are set as close as possible to the real experiment, compiling (*refine*) the potential arrays in SIMION is needed before simulation.

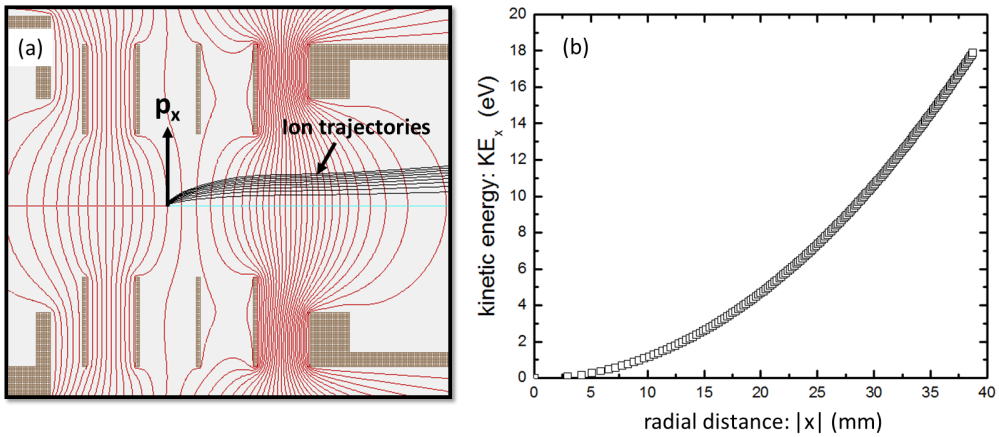

Figure 3.11: (a) Ion trajectory simulation with SIMION. (b) Simulated ion radial distribution on the detector vs. ion initial kinetic energy

Two important steps that were taken to reconstruct momentum components p_x and p_y are:

1) An array of ions whose initial energies are in an arithmetic sequence, e.g. E = n×ΔE -ΔE (eV), where n is the n^{th} ion to be simulated and ΔE is the step size of ion energy (constant arithmetic difference), are set to fly toward the detector driven by the simulated electric field of spectrometer. All ions started out from the center of the spectrometer (center of ion-extraction and ion-repeller, see Fig. 3.3). Fig. 3.11 (a) shows the ion simulation where all ions with a constant energy difference fly toward radial direction. In the simulations conducted within this thesis, ΔE is chosen to be 0.1 eV.

2) SIMION outputs the final position x and y on the detector. The initial energies of ions are plotted against the final position in Fig. 3.11 (b). The curve in the spectrum is fitted with a polynomial to extract an empirical formula connecting the hit position with the initial kinetic energy. A fifth order polynomial function 3.6 is used to get a higher level of proximity to the simulation results.

$$KE_x = C_1|x|^5 + C_2|x|^4 + C_3|x|^3 + C_4|x|^2 + C_5|x|; \tag{3.6}$$

$$KE_y = C_1|y|^5 + C_2|y|^4 + C_3|y|^3 + C_4|y|^2 + C_5|y|; \tag{3.7}$$

The x and y in the formula above stands for the coordinate of the particle on the detector. From a fit to the simulation shown in Fig. 3.11 (b), one finds the empirical formula that connects the initial kinetic energy and final position. Then, by inserting the experimentally measured (x, y) position information of ions to this formula, the kinetic energies that corresponds to the motion in x and y direction can be independently calculated. Due to cylindrical symmetry, the final positions x and y have a same dependence on the initial energy, thus the coefficients of the polynomial fits are identical for KE_x and KE_y. The momentum p_x, p_y

can be expressed as,

$$p_x = \frac{x}{|x|}\sqrt{\frac{KE_x}{2m_{ion}}} \tag{3.8}$$

$$p_y = \frac{y}{|y|}\sqrt{\frac{KE_y}{2m_{ion}}} \tag{3.9}$$

Note that the momentum components p_x, p_y are assigned with the $\pm$ signs of x and y.

3.2.8.2 Longitudinal Momentum: p_z

The momentum component along the TOF axis is calculated using the TOF information of ions and the empirical formula that connects the initial kinetic energy KE_z to the ion TOF. In order to find such formula, ions with initial kinetic energies are simulated to fly *toward* and *away* from the detector. In the real experiment, the ions that fragmented with zero momentum along TOF axis spend TOF_c time to reach to the MCP. In ion TOF spectrum, TOF_c is the center of the TOF distribution for a specific ion, see H^+ TOF peak and its TOF_c in Fig. 3.12 (a).

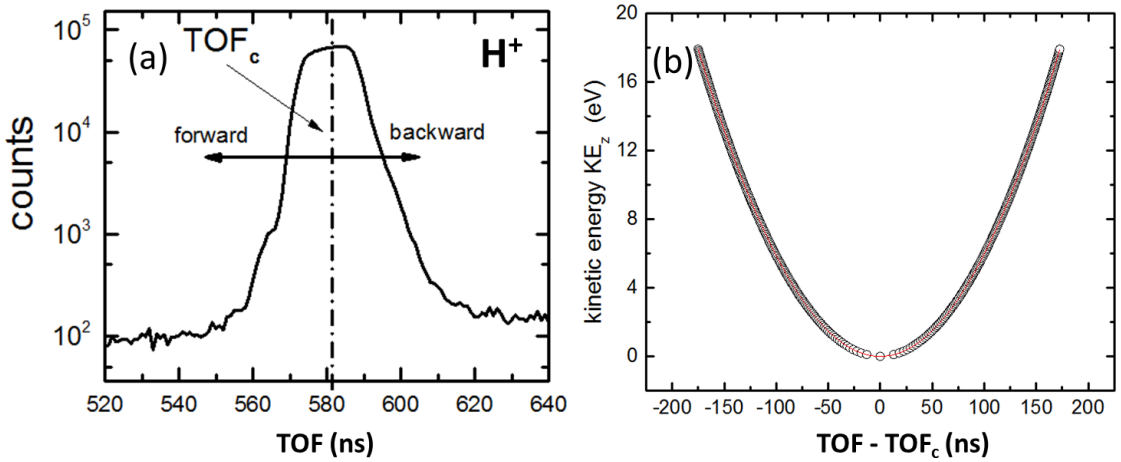

Figure 3.12: (a) Experimental TOF distribution of H^+ ions; (b) Final ion TOF spread vs. initial kinetic energy for ions simulated to fly toward and away from the detector surface.

The initial energies and the final TOF spread, TOF-TOF_c, of ions are plotted in Fig. 3.12 (b). When TOF-TOF_c is larger than zero, it means the ions are simulated to fly *away* (backward) from the detector and when the TOF spread is smaller than zero, the ions are

simulated to fly *toward* (forward) the detector. The simulated distribution in Fig. 3.12 (b) can be fitted with a polynomial,

$$KE_z = B_1\Delta\text{TOF}^5 + B_2\Delta\text{TOF}^4 + B_3\Delta\text{TOF}^3 + B_4\Delta\text{TOF}^2 + B_5\Delta\text{TOF}; \tag{3.10}$$

where ΔTOF = TOF - TOF$_c$. B_1 - B_5 are coefficients that depend on the ion mass and its charge. The momentum component p_z along the TOF axis can be expressed as,

$$p_z = \frac{\text{TOF} - \text{TOF}_c}{|\text{TOF} - \text{TOF}_c|}\sqrt{\frac{KE_z}{2m_{ion}}}. \tag{3.11}$$

Note that the direction of the momentum component p_z is decided by the signs of the TOF spread. In the reconstruction of the momentum components for a specific ion, TOF$_c$ is first assigned the value of the center of the TOF peak of the ion (chosen from TOF spectrum). During the symmetrization of ion momentum components, e.g. symmetrizing forward and backward p_z components, TOF$_c$ can be slightly tweaked to optimize the symmetrization.

3.2.9 Calibration of Ion-ion Coincidence Measurements

As compared to COLTRIMS measurements, the electric field strength applied inside the interaction region of the spectrometer is 3 to 4 times higher in the double-sided VMI apparatus. The reason behind stronger electric field in the VMI is the need to measure high energy electrons in coincidence with the fragmentation ion channels. The higher the energies of electrons that should be detected with full 4π angular detection efficiency, the stronger electric field is required, thus compromising the TOF and kinetic energy resolution of ion-ion coincidence measurement. In order to quantify the ion energy resolution in the VMI apparatus and to calibrate the kinetic energy spectrum, inner-shell photoionization and fragmentation of N_2 molecule to $N^+ + N^+$ channel is studied and the kinetic energy release spectrum of the channel is compared with the benchmark COLTRIMS measurement from Weber *et al* [74].

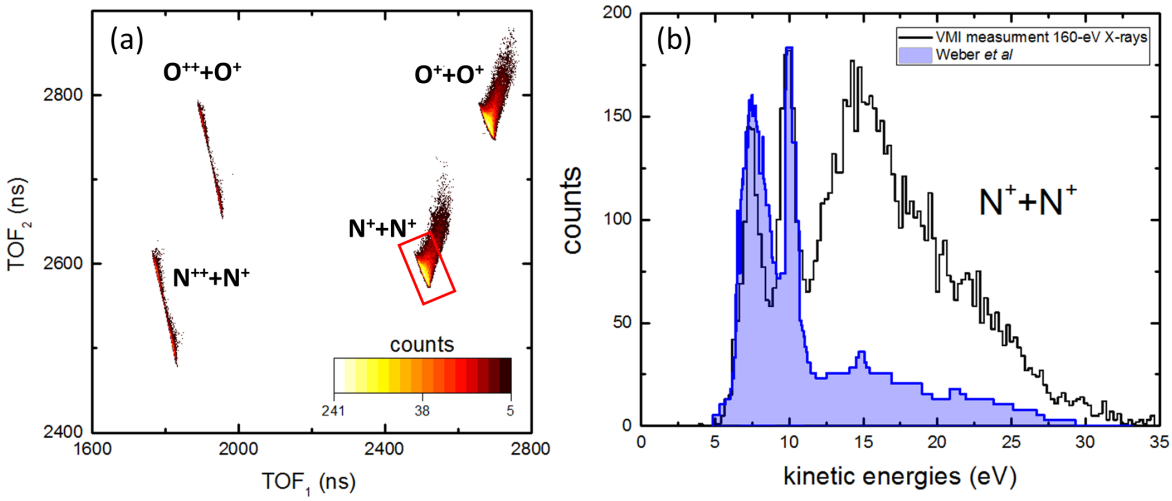

Figure 3.13: (a) PIPICO map of N_2 and O_2 from air after photoionization with 160 eV photons. (b)Kinetic energy release of N^++N^+ channel (black) from the VMI soft X-ray measurements, (blue shaded area) compared to the kinetic energy release of N^++N^+ channel adopted from Weber *et al* [74]

Fig. 3.13 (a) shows the PIPICO spectrum when **air** is fed to the supersonic gas jet with 1 atm backing pressure. Photoionization and fragmentation channels of N_2 and O_2 molecules in the air with 160-eV photons can be seen in the PIPICO spectrum. Fig. (b) shows the kinetic energy release spectrum of the current calibration measurement overlapped with the previously reported KER spectrum (Fig.2 (b) in [74]). The two KER spectra overlaps closely. The significant difference of the yield at high kinetic energies is due to different branching ratios between the dicationic final states at different photon energies. In Weber *et al* [74], 419.3 eV photons were used to probe the K-shell in N_2 while 160-eV photons were used in the VMI experiment. The sharp central peak corresponding to the $D^1\Sigma_u^+ \rightarrow N^+(^3P)+N^+(^1D)$ fragmentation pathway has similar peak width as compared to the COLTRIMS measurement. (Weber *et al* [74] FWHM: 0.96 eV; double-sided VMI: 0.98 eV). The peak assignment was originally reported in a high resolution Doppler-free kinetic energy release spectrum of N_2^{++} in reference [75] as shown in Fig. 3.14. In this spectrum, the peak width of the dominant peak at 10.316 eV was around 50 meV. In comparison, the broadening of the peak at around 10 eV in both COLTRIMS and the VMI measurements can possibly be attributed to 1) the difference in cross sections of ionization, especially inner-shell photoionization processes in COLTRIMS and the VMI measurements and electron impact ionization measurement in [75],

2) instrumental resolution.

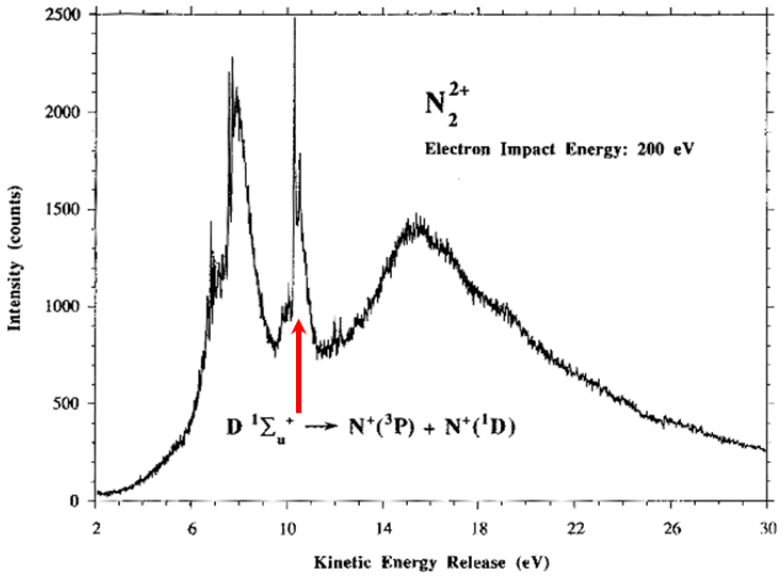

Figure 3.14: Doppler-free kinetic energy release distribution of N^++N^+ channel. Figure adopted from Lundqvist *et al* [75]

3.2.10 Coincidence Electron Spectra

In the double-sided VMI spectrometer, electrons can be measured in coincidence with ionic fragmentation channels. Electrons belonging to specific final states and fragmentation channels can be isolated by setting time gates for ions or ion-ion coincidence channels. In this section, a brief introduction is given on channel-resolved electron spectroscopy.

3.2.10.1 Electron Detector Calibration with Neon 2s, 2p Lines

The principle of the VMI is that after photoionization, the charged particles are projected onto the detectors by applying voltages to the spectrometer. In order to detect the position distribution of the projected particles, phosphor plates or delay-line position detectors can be used together with MCPs. The position distribution is the two-dimensional projections of a three-dimensional momentum sphere of the charged particles. All particles with the same velocity are mapped to the same radius, R. The radius is proportional to the velocity of the outgoing particles.

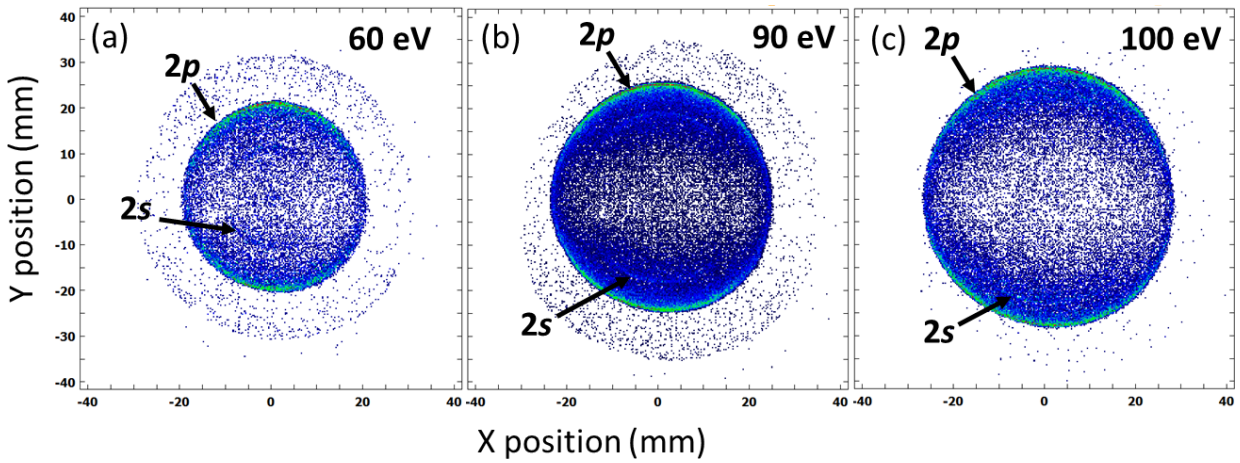

Figure 3.15: Position distribution of Neon $2s$, $2p$ electrons after the system absorbs (a) 60 eV, (b) 90 eV, (c) 100 eV photons.

In the VMI experiments in this thesis, in order to calibrate the electron position detector and find empirical formula that connects the electron radius (R) to its kinetic energies KE = hν - $E_{binding}$, neon $2s$ and $2p$ electrons generated after photoionization of neon gas at various photon energies are collected on the electron detector. Both the energies and the photoelectron angular distribution with respect to the light polarization direction, e.g. β parameter, of neon gas are well studied before [37]. The binding energies of $2s$ and $2p$ levels are $E(2p)_{binding}$ = 21.6 eV and $E(2s)_{binding}$ = 48.5 eV.

Fig. 3.15 shows three electron position spectra of neon $2s$ and $2p$ photoelectrons at three different photon energies, 60 eV, 90 eV and 100 eV. The radius of the electron distribution increases as photon energies increases. This is because both $2s$ and $2p$ electrons ejected with higher kinetic energies when the system absorbs more energetic photons. In order to convert the position information to kinetic energies of the electrons, an Onion Peeling [76, 77] electron inversion code is applied.

One thing to pay attention before proceeding with the electron inversion is that, the position spectra of the electrons do not always appear circular and electrons with a same initial energy appear at different radius at different angles. There are a few reasons for such imperfect electron spectra: 1) the earth magnetic field distorting the high energy electron trajectories; 2) the interaction region of the gas target shifted from the center of the

spectrometer by small amount; or 3) non-cylindrically symmetric distortions of the electric extraction field, e.g. due to the spectrometer mounts or the gas jet, which is in close proximity of the spectrometer. As a result, the energy resolution of electrons will be affected significantly. For that matter, a VMI image circularization method that can remove the angular dependence of the radial distribution needs to be applied. Gascooke *et al* discussed the "circularization" correction method in reference [78]. Such image correction is applied to to the distorted electron spectra included in this thesis.

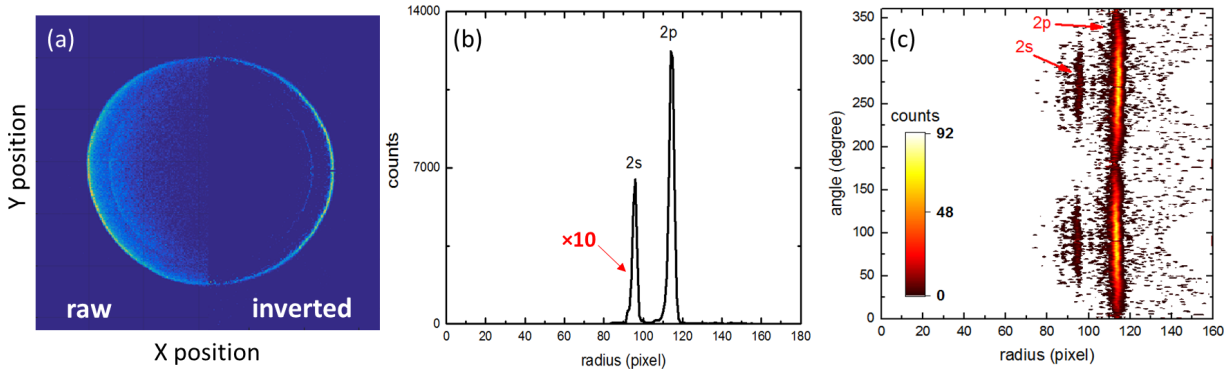

Figure 3.16: (a) Raw/Inverted position distribution of $2s$, $2p$ electrons; (b) Inverted 1D distribution; (c) Inverted radius vs. angle distribution of $2s$, $2p$ electrons after circularization.

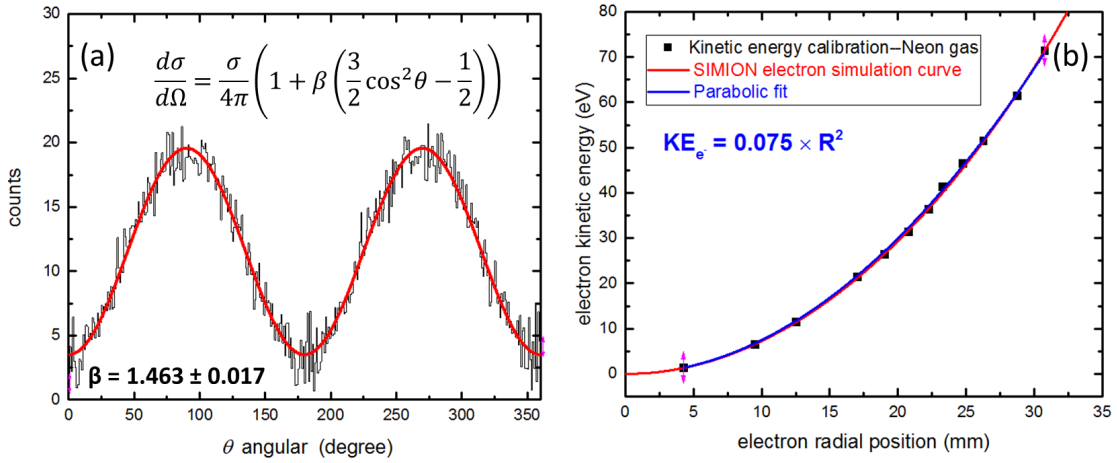

Figure 3.17: (a) $2p$ electron angular distribution and β parameter extraction fit (b) Electron radial distribution vs. electron energy.

After the electron inversion, the one-dimensional photoelectron spectrum is shown in Fig. 3.16 (b). The β parameter (see Section 2.1.1) can be determined from the radial vs.

angular distribution in Fig. 3.16 (c). The extracted β parameter of neon $2p$ electrons is shown Fig. 3.17, the result matches well with the previously reported value of 1.46 [79]. In the experiment, multiple electron spectra at photon energies ranging from 50 eV to 100 eV are measured and the correlation between the $2s$ and $2p$ electron energy peaks and their radial position are incorporated in Fig. 3.17 (b). The SIMION electron energy simulation curve is shown in red. A parabolic function is fitted to the the experimental kinetic energy distribution in order to extract an empirical formula that connects the electron position to kinetic energies.

The absolute error of this energy calibration, which is defined by the uncertainty of the absolute photon energy calibration of the beamline monochromator and the precision with which the radius in the experimental Ne photoelectron images can be determined, is estimated to be less than 200 meV for an electron energy around 50 eV.

3.2.11 Momentum Calibration: COLTRIMS

As illustrated in Section 3.2.7, in order to obtain three-dimensional momentum vectors of coincidence events, a two-body or three-body fragmentation channel of interest first needs to be isolated from PIPICO or TRIPICO spectrum. Unlike the momentum calibration procedure of the coincidence VMI technique described in Section 3.2.8, which requires simulation of ion flight trajectories with SIMION software, in the COLTRIMS data analysis, the momentum components of each ion in three dimensions can be calculated analytically using the time and position of hits as well as spectrometer parameters such as spectrometer geometry and electric field strength.

The ion flight distance l on the TOF axis can be expressed as

$$l = \frac{1}{2}\frac{qE}{m}\mathrm{TOF}_{ion}{}^2 + \frac{p_z}{m}\mathrm{TOF}_{ion} + z_0, \tag{3.12}$$

where p_z is the longitudinal momentum of ion after fragmentation; E is the electric field strength; q is ion charge, m is the mass of an ion and z_0 is the birth position of ions along

TOF axis. Thus, from equation 3.12, the p_z momentum component of ions can be expressed as

$$p_z = m\frac{(l - z_0)}{\mathrm{TOF}_{ion}} - \frac{1}{2}\frac{qU}{l}\mathrm{TOF}_{ion}. \tag{3.13}$$

The ion flight distance l, also denoted as spectrometer length, is 23.705 cm. U is the voltage applied to the spectrometer. By using the hit position on the detector, (x, y), and the initial birth position of ions (x_0, y_0), the transverse momentum components can be described as

$$p_x = m\frac{(x - x_0)}{\mathrm{TOF}_{ion}}, \tag{3.14}$$

$$p_y = m\frac{(y - y_0)}{\mathrm{TOF}_{ion}}. \tag{3.15}$$

3.3 Supersonic Molecular Jet and Vacuum System

In coincidence momentum imaging measurements with either the VMI or COLTRIMS apparatus, having a cold atomic or molecular gas target is crucial to obtain high momentum resolution. Typically, in COLTRIMS ion imaging experiments with ultrafast 800 nm laser pulses, the recoil momentum transferred from ejected photo-electrons to the ions are on the order of 1 a.u. In inner-shell photoionization studies in the coincidence VMI, energies of electrons ejected from the system are much higher, thus the recoil momentum transferred to ion counterparts are 1 to 4 times higher than the COLTRIMS measurement. However, the typical mean quadratic momentum from Maxwell-Boltzmann distribution at a room temperature is in the order of tens of atomic units. Thus, a cooled down gas target immensely increases the ability to image ion and electron momenta with high precision.

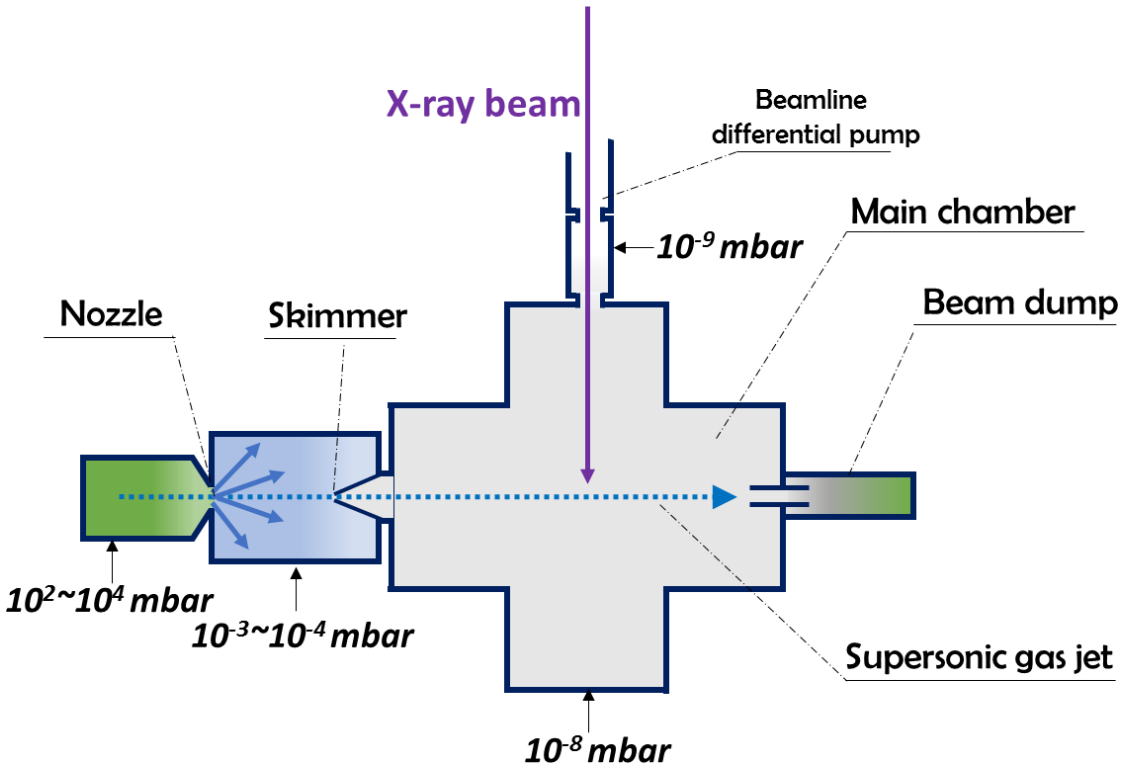

Figure 3.18: A schematic diagram of the vacuum system of the VMI instrument. Typical pressures during the experiment are indicated.

A schematic of the gas jet and pressure status of each parts of the double-sided VMI system is shown in Fig. 3.18. The target gas at room temperature is obtained from a gas bottle or a "bubbler" that contains liquid chemical sample that evaporates and expand into the vacuum chamber at a stagnation pressure of 10^2 to 10^4 torr. The gas will expand through a nozzle with 30μm diameter into the supersonic jet chamber that has pressure ranges from 10^{-3} to 10^{-4} torr. The supersonic gas jet chamber pressure is maintained by two large turbo pumps with 800 l/s pumping speed each. In order to achieve a clean supersonic gas beam, a skimmer with 500 μm diameter is placed at the end of the gas jet chamber and the entrance port of the main chamber that maintains a high pressure differential between the two chambers. As shown in Fig. 3.18, one skimmer is used in the double-sided VMI apparatus to generate supersonic beam that has temperature of few tens of Kelvin. In supersonic gas jet applied in COLTRIMS system, two skimmers are used in order to obtain cold gas-phase atomic and molecular beams, see Section 3.2.3.2.

3.4 VUV Synchrotron Measurement of Ionization Potentials

At the beamline 9.0.2 of the ALS, the undulator and beamline optical elements are suitable for vacuum ultraviolet (VUV) radiation with photon energy spanning from 7.2 eV to 24 eV with 0.05 eV energy resolution [80]. The beamline is mainly used for physical chemistry research where valence ionization and fragmentation of large bio-molecules, cluster beams and nanoparticle beams are studied [81–84].

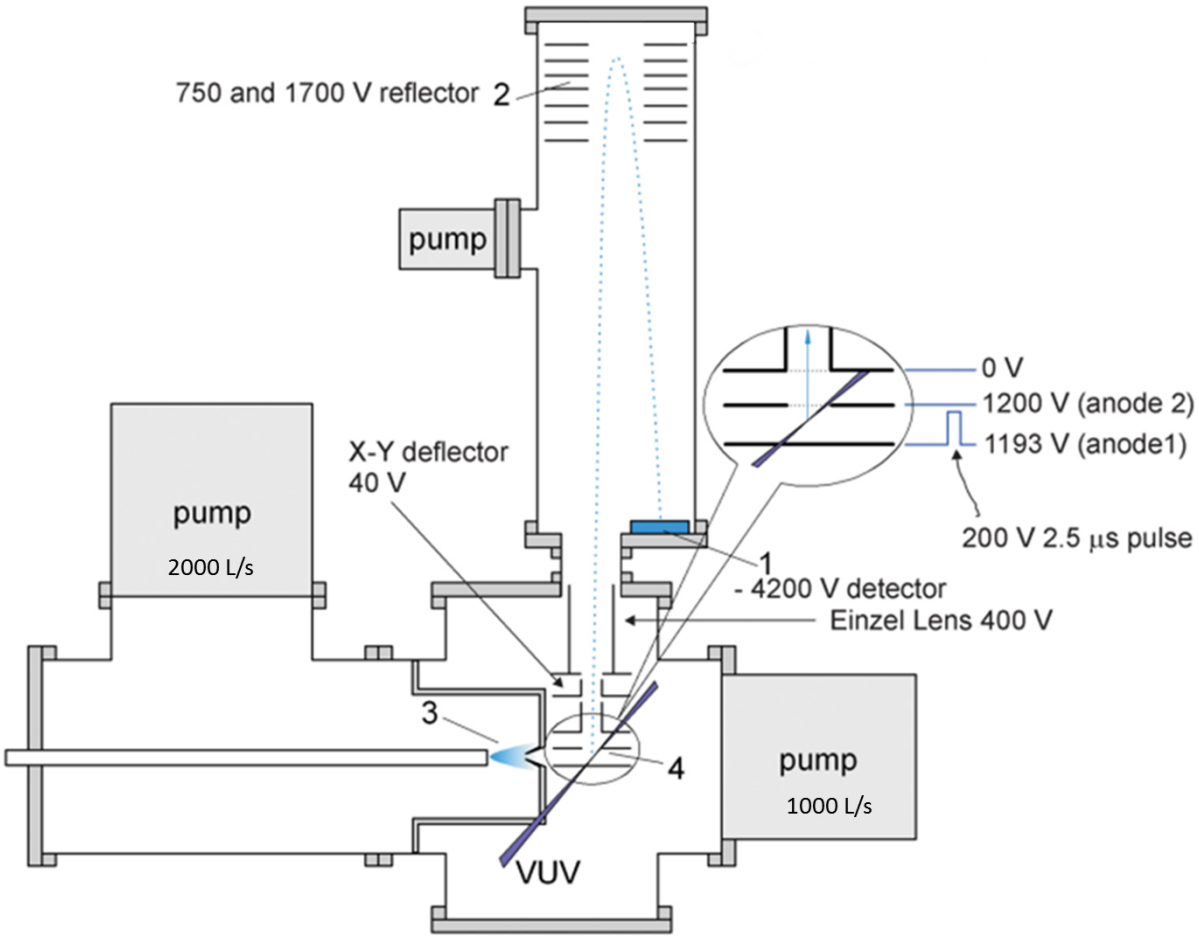

Figure 3.19: Schematic of the experimental apparatus at beamline 9.0.2 of the ALS with voltages shown. (1) Microchannel plate detector, (2) Reflector mirror, (3) Molecular Beam region, (4) Ion optics for extraction; Figure taken from reference [85].

For this thesis work, the photoionization potential of *cis*- and *trans*-$C_2H_2Cl_2$ isomers, 2,6- and 3,5-difluroiodobenzene molecules as well as 2(5*H*)-Thiophenone molecules were measured by using a molecular beam machine equipped with a reflectron (a type of TOF mass spectrometer) together with a VUV synchrotron beam. The photoionization yield of the molecules in VUV synchrotron beam can be extracted from the TOF mass spectrum measured by the system shown in Fig. 3.19. The details of system geometries and operational procedures are discussed in [85, 86].

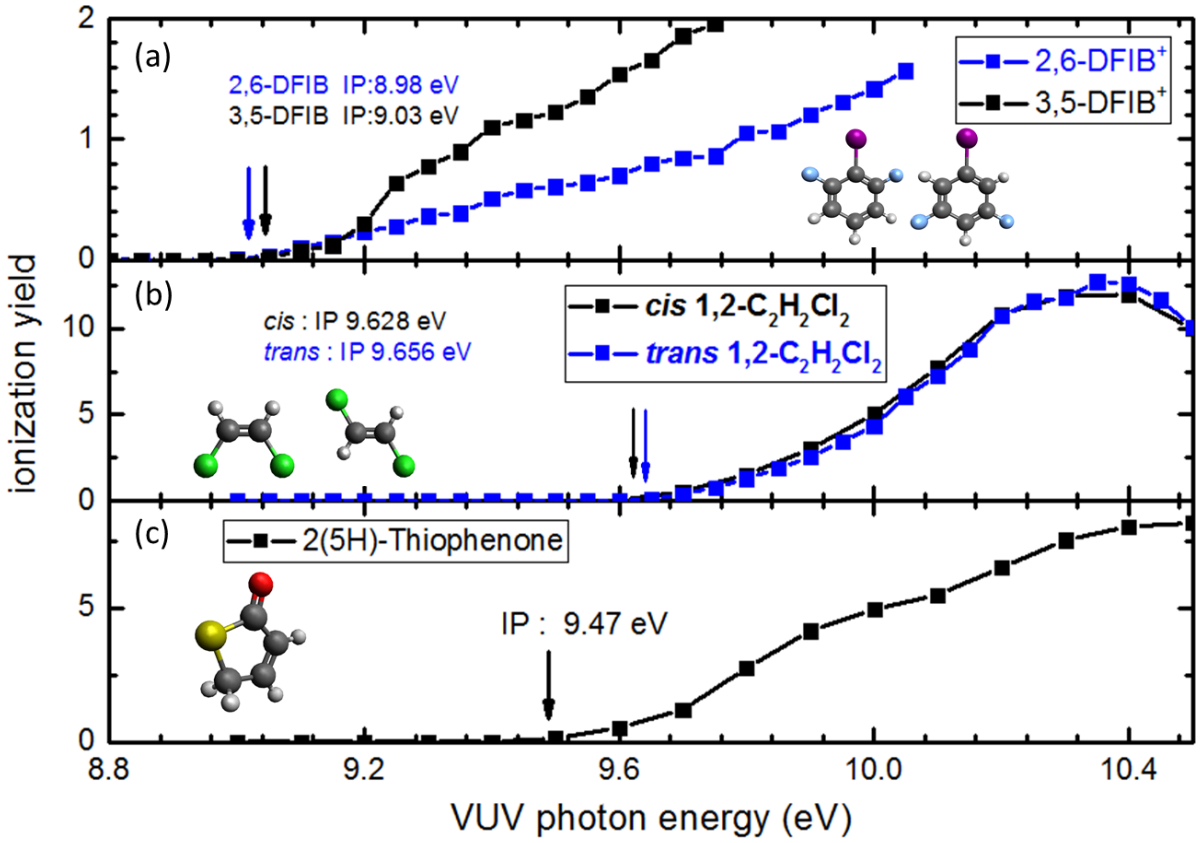

Figure 3.20: Photoionization yield of 2,6-, 3,5-DFIB cations; *cis*/*trans* 1,2-$C_2H_2Cl_2^+$ and 2(5*H*)-Thiophenone cation.

By setting time gates on parent molecular ions such as 2,6- and 3,5-DFIB$^+$; *cis*/*trans* 1,2-$C_2H_2Cl_2^+$ and $C_4H_4OS^+$ (2(5*H*)-Thiophenone), the ionization energy can be determined from the photoionization efficiency (PIE) curve. The photoionization energies of the molecules are inserted in Fig. 3.20 (a,b,c) shown below. The resolution for the photon energy is 0.05 eV. The ionization energies are determined from the PIE curves by fitting a linear function to

the increasing yield and then determining the crossing point between the fitted line and the baseline. Details of methods on how to find the ionization potentials from photoionization yield can be found in reference [86].

Isomers can have different ionization potentials due to their different electronic structure and valence orbitals. In many cases, since the mass of isomers are identical, the photoionization efficiency yield scanned with VUV synchrotron beams is a signature for determining the geometry of the isomer [87, 88]. Previously, *cis* 1,2-$C_2H_2Cl_2^+$ isomer ionization potential have been reported to be 9.631 eV [89] and the *trans* isomer was reported to be 9.658 eV [90]. The current measurements on 1,2-$C_2H_2Cl_2$ ionization energies differ from the previous work by less than 1%. For 2(5*H*)-Thiophenone molecule, the ionization energy of the molecule was previously reported by Thorstad *et al* in 1975 [91] to be 9.78 eV which differs from the current measurment by 0.31 eV. The ionization potentials of 2,6- and 3,5-DFIB molecules were not reported previously.

Chapter 4

Identification of *cis*-*trans* Isomers via Coulomb Explosion Imaging

4.1 Introduction

Isomers, i.e. molecules with the same chemical formula but different geometric structures, play an important role in many biological processes [92–97]. For example, our vision requires a protein called rhodopsin, which inter-converts between different geometric structures (i.e. isomers) during the absorption of light [29]. Another example is the green fluorescent protein, which is used to investigate protein trafficking inside living cells and which changes configuration from its well-ordered *cis* isomer to a highly disordered *trans* isomer [32] upon absorption of light in the blue to ultraviolet range. Despite containing the same atomic constituents, isomers can have very different physical, chemical, and biological properties. Therefore, it is of particular interest to experimentally distinguish isomers in order to investigate isomer-specific reactions and, specifically, to study the interconversion between different isomers in time-resolved experiments [98]. A prototypical example is the isomerization between acetylene (HCCH) and vinylidene (H_2CC) via hydrogen migration, which has been studied, e.g. using synchrotron radiation [99] and by femtosecond time-resolved experiments with intense, ultrashort optical [100, 101] and XUV or X-ray pulses [102–104]. All

of these experiments have employed the Coulomb explosion coincidence momentum imaging technique [23, 105–107], in which all charged fragments that are created when the multiply charged parent ion breaks up (*explodes*) are measured in coincidence and their momentum vectors are used to extract information about the dynamical change in the geometry of the parent molecule. Recently, this technique was also used to separate two enantiomers in a racemic mixture of the chiral molecules CHIClF and CHBrClF by measuring five-fold coincidences after strong-field laser ionization [33, 34], and the related beam-foil Coulomb explosion method was used to study the absolute configuration of trans-2,3-dideuterooxirane ($C_2H_2D_2O$) [108].

In this chapter, Coulomb explosion imaging of molecular structures of geometric isomers, namely 1,2-dibromoethene and 1,2-dichloroethene, after photoionization with soft X-rays synchrotron beams as well as ionization with ultrafast femtosecond laser pulses are discussed. Earlier work on the Coulomb explosion of geometric isomers using intense laser pulses found strikingly different angular distributions of ions in isomers, but since those experiments were not performed using coincidence momentum imaging, the experimental data alone could not be used to identify the geometric and positional isomers of the molecule [109]. Utilizing ion-ion and ion-electron coincidence imaging techniques, this study shows an experimental route to efficiently identify geometric isomers, namely *cis* and *trans* isomers of 1,2-dibromoethene ($C_2H_2Br_2$) and 1,2-dichloroethene ($C_2H_2Cl_2$) by inner-shell photoionization of Br($3d$) and Cl $2p$ with X-ray synchrotron beam. Furthermore, similar Coulomb explosion measurement using ultrafast 800 nm intense laser pulses are conducted to study the feasibility of the technique in strong-field ionization. The methodology is directly applicable to time-resolved pump-probe experiments studying the *cis-trans* isomerization using either strong-field or inner-shell ionization as a probe since it allows performing an in-situ measurement of the isomer ratio of an isomerically mixed sample.

The results of the study show, both X-rays and ultrafast strong laser pulses can be utilized to conduct Coulomb explosion imaging measurements in order to identify geometric isomer structures. Albeit different physical processes are involved in photoionization with different light sources, e.g. inner-shell photoionization with X-rays and valence ionization

with infrared laser pulses, the study shows that the Coulomb explosion imaging method can be used irrespective of light sources. Major part of the work described in this chapter was published in the reference [35].

4.2 Coulomb Explosion Imaging of *cis* and *trans* 1,2-dibromoethene

4.2.1 X-ray Synchrotron Studies: 1,2-$C_2H_2Br_2$

The experiments were performed at beamline 10.0.1.3 of the Advanced Light Source (ALS) at Lawrence Berkeley National Laboratory during the standard ALS multi-bunch top-off mode of operation. As described in experimental Chapter 3, a double-sided coincidence VMI apparatus was utilized for the synchrotron measurements. The data acquisition system, which consisted of two multi-hit time-to-digital (TDC) converters, was triggered by the detection of an electron, which arrived at the detector after a flight time of approximately 5 nanoseconds. The time of flight of the ions was then measured with respect to the arrival time of the prompt electrons. The position and time-of-flight information of the ions are used to reconstruct their full three-dimensional momentum vectors. The experimental apparatus is illustrated in Fig. 4.1 (a). The chemical sample used in the experiment was commercially purchased (Sigma Aldrich, 98.3% purity) and contained a mixture of *cis* and *trans* isomers at a mixing ratio of 32.1% (*cis*) to 66.2% (*trans*), according to a gas chromatography analysis by the vendor. In the *cis* isomer, the two bromine atoms, each attached to one of the two carbon atoms, are pointing in the same hemisphere with respect to the C=C double bond, while they are across from each other in the *trans* isomer (see Fig. 4.1 (b)). The double bond between the carbon atoms restricts the inter-conversion from one isomer to the other such that the two isomers are stable at room temperature. For initiating the photoionization and fragmentation of the molecule, we chose a photon energy of 140 eV (bandwidth $\pm$ 20 meV), which is 63 eV above the binding energy of the bromine $3d$ inner-shell electrons in

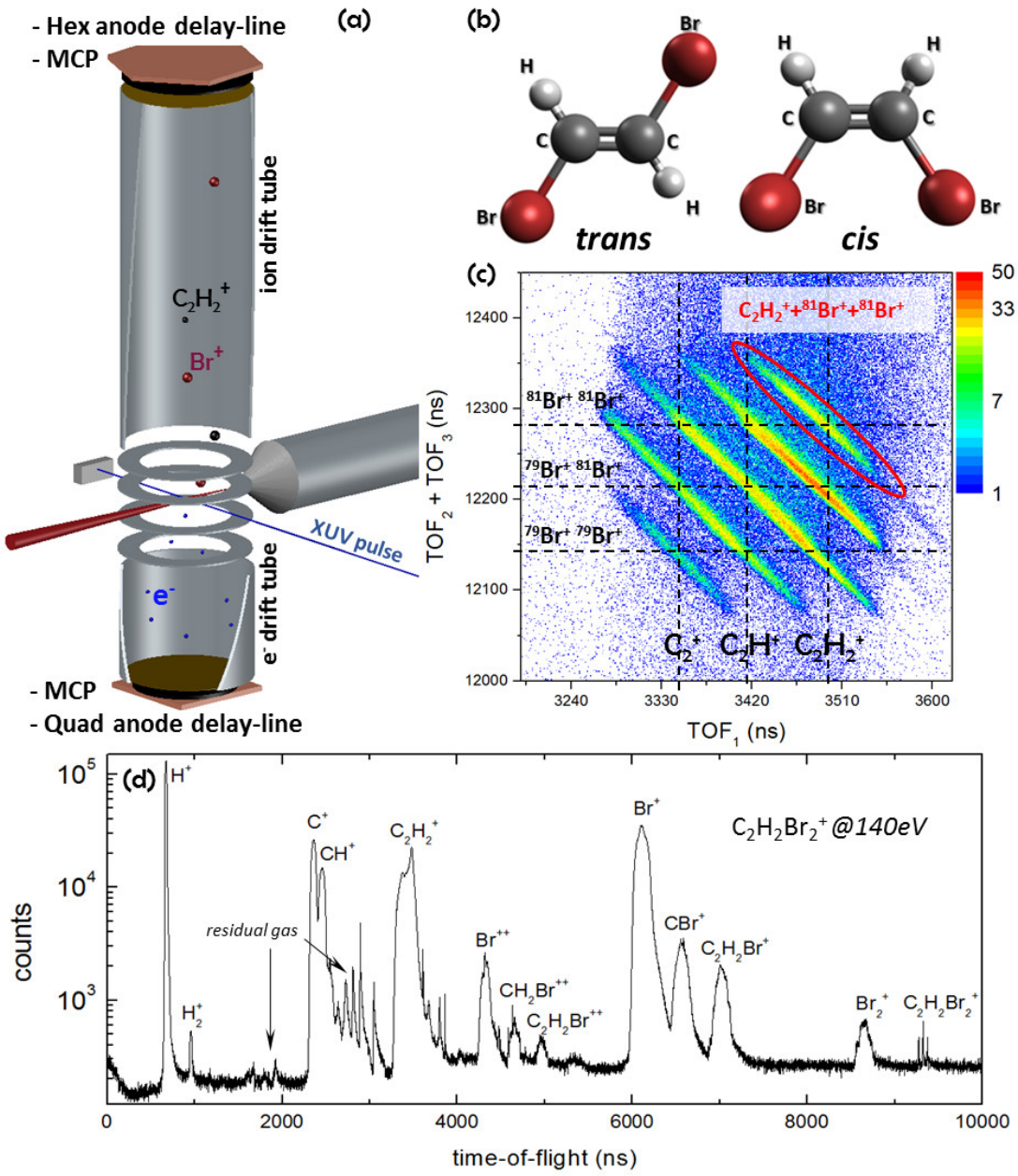

Figure 4.1: (a) Schematic of the experimental setup including a supersonic molecular beam and a double-sided VMI spectrometer with time- and position-sensitive delay line detectors. The spacing between the spectrometer electrodes is 15 mm, and the total distance between the interaction region and the detector is 398 mm for the ions and 112 mm for the electrons. (b) Molecular structure of *cis* and *trans* 1,2-dibromoethene. (c) Yield of the $C_2H_n^+$ + Br^+ + Br^+ ($n = 0, 1, 2$) coincidence channel shown in a photoion-photoion-photoion coincidence (PIPIPICO) plot as a function of the time of flight (TOF) of the first hit versus the sum of the TOFs for the second and third hits. (d) Ion time-of-flight mass spectrum of all ions generated in the X-ray induced ionization and fragmentation of 1,2-dibromoethene at 140 eV photon energy.

1,2-dibromoethene [110]. Absorption of a 140-eV photon thus leads predominantly to $3d$ inner-shell ionization followed by Auger decay that typically ejects one or two additional electrons. Depending on the specific relaxation pathway, the resulting doubly or triply charged molecular cation typically breaks up into several charged and/or neutral fragments (see Fig. 4.1 (d)). Here, we concentrate on the three-body fragmentation channel $C_2H_2^+$ + Br^+ + Br^+, for which we measure the time of flight and hit positions of all three fragments in coincidence. Due to the similarities of Br $3d$ photoionization to the case of Kr, we assume that most of the triply charged final states are reached via sequential emission of two Auger electrons in an Auger cascade [42]. The Auger-electron spectrum measured in coincidence with the $C_2H_2^+$+Br^++Br^+ channel shown in Fig. 4.10 supports this assumption. In Kr, the Auger lifetimes are 8 fs for the first step and 20 fs for the second step [111], and we expect the lifetimes to be of the same order in $C_2H_2Br_2$. In the zoomed-in triple-ion coincidence plot in Fig. 4.1 (c), the three-body fragmentation channel $C_2H_2^+$ + Br^+ + Br^+ appears as sharp diagonal lines due to momentum conservation during the breakup process. In this case, a total of nine diagonal lines are present corresponding to the $C_2H_2^+$ + Br^+ + Br^+, C_2H^+ + Br^+ + Br^+, and C_2^+ + Br^+ + Br^+ channels with different combinations of the two stable bromine isotopes, ^{79}Br and ^{81}Br, which have approximately equal natural abundance (^{79}Br: 50.69%; ^{81}Br: 49.31%). Since several of these lines are overlapping, we selected only the region containing the $C_2H_2^+$ + $^{81}Br^+$ + $^{81}Br^+$ channel for further analysis since this channel is clearly separated. In order to reconstruct the ion momenta from the measured time of flight and hit positions of each ion, we used the SIMION software package [67] to construct empirical formulas connecting the hit position with the momentum vector components parallel to the detector, P_x and P_y, and the time-of-flight spread of each ion with the momentum component along spectrometer axis, P_z. Using this procedure, which is described in more detail in Chapter 3 (Section 3.2.8), the momentum sum of all fragments in this triple coincidence channel was found to peak at zero, as expected due to momentum conservation, with a full width at half maximum of ± 9 au. In the following, we selected this main peak around zero in order to select only *true* coincidence events, where all fragments stem from the same parent molecule. The three-dimensional momentum vectors of all three fragments were then used

to calculate the emission angle of the fragments, their kinetic energies, and the total kinetic energy release. Figure 4.2 shows the angle θ between the momentum vectors of the two Br^+

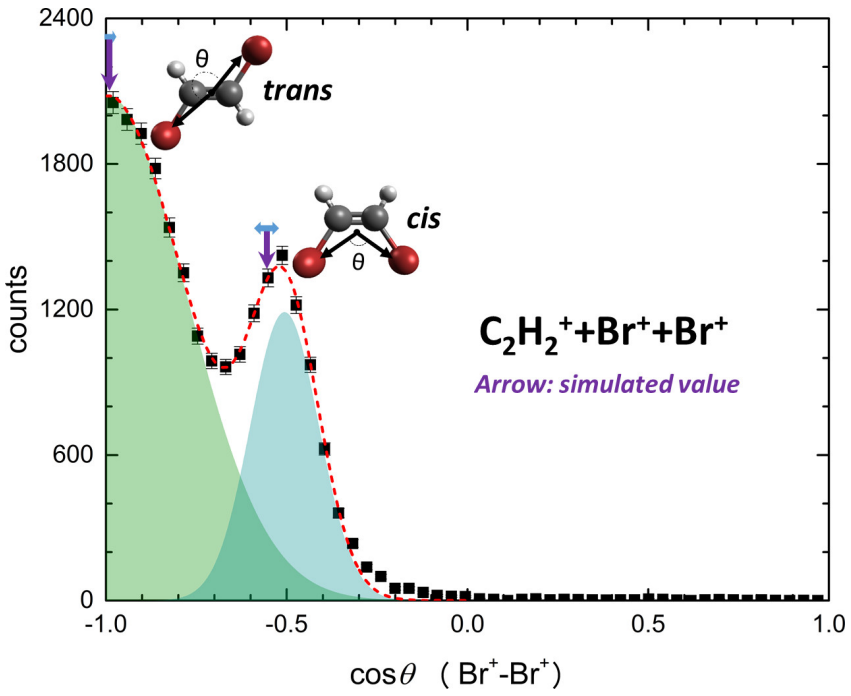

Figure 4.2: Angle between the Br^+ ion momenta in the triple-coincidence channel $C_2H_2^+ + Br^+ + Br^+$. A fit of two Gaussians (shaded areas) to the experimental data (black circles) is shown as a red dashed line. The angles expected from a classical Coulomb explosion model are indicated by arrows, with the horizontal bars indicating the broadening due to the experimental momentum resolution.

fragments detected in coincidence with a $C_2H_2^+$ fragment. This angular distribution displays two peaks which we attribute to bromine ions emitted from the *trans* ($\cos\theta = -1$) and *cis* ($\cos\theta = -0.58$) isomers. We corroborate this assignment by a numerical Coulomb explosion simulation, assuming purely Coulombic repulsion between point charges located at the center of mass of each fragment and instantaneous creation of the charges followed by explosion from the equilibrium geometry of the neutral molecule. By numerically solving the classical equations of motions for all the fragment ion in the Coulomb field using a 4th order Runge-Kutta method as described in Chapter 2 (Section 2.2.1), the momentum vectors and kinetic energies of all fragments can thus be obtained for an ideal Coulomb explosion model. The simulated Br^+-Br^+ angles for Coulomb explosion of *cis* and *trans* isomers are shown as purple arrows in Fig. 4.2 and are in excellent agreement with the two maxima in the experimentally

determined distribution. By fitting two Gaussians to the experimental data, we determine a ratio between the *trans* and *cis* isomers of 2.04 ± 0.07, which agrees with the isomeric composition of the sample determined by gas chromatography. By selecting only those

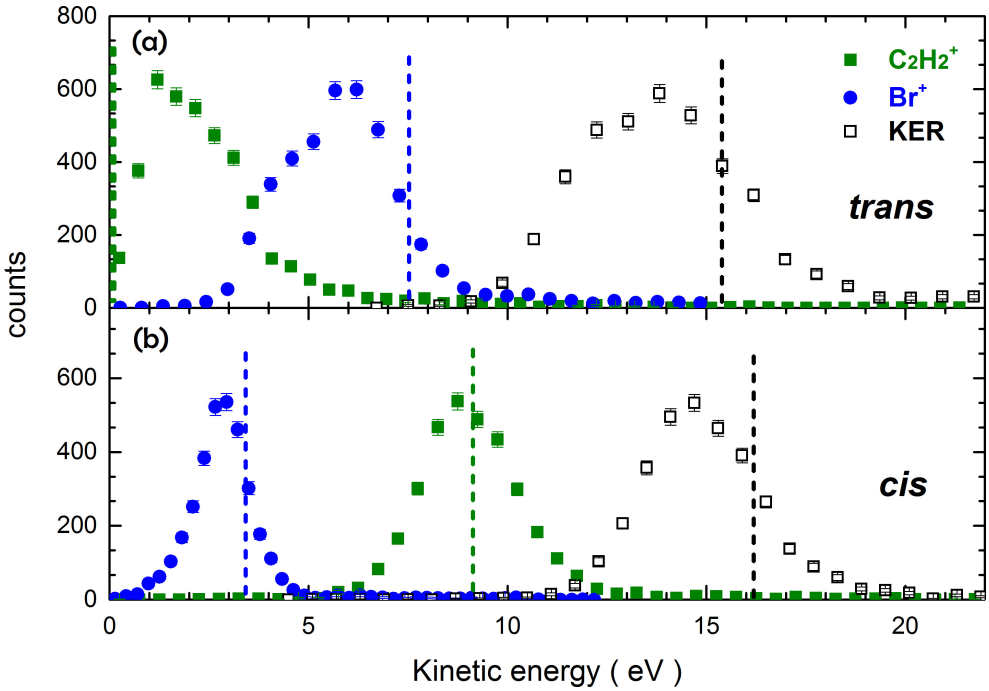

Figure 4.3: Kinetic energy distributions of the Br^+ and $C_2H_2^+$ fragments as well as total kinetic energy release in the $C_2H_2^+ + Br^+ + Br^+$ triple-coincidence channel for (a) *trans* and (b) *cis* isomers, as selected by the Br^+- Br^+ angle θ. The results of the Coulomb explosion model are shown as dashed lines.

coincidence events for which the Br^+-Br^+ angles lie within the intervals of $\cos\theta$=[-0.45, -0.55] and [-0.9, -1.0], respectively, we can experimentally distinguish the *cis* and *trans* isomers and extract the isomer-selected fragmentation kinematics. The isomer-selected kinetic energies of the individual ions and the total kinetic energy release are shown in Fig. 4.3. For the *trans* isomer, the kinetic energy distribution of the $C_2H_2^+$-fragment has a maximum around 1 eV and that of the Br^+-fragments peaks around 6 eV, while for the *cis* isomer, the Br^+-fragments are emitted with lower and the $C_2H_2^+$-fragment with considerably higher kinetic energy. This can be explained by an obstructed instantaneous explosion [112, 113] in the case of the *trans* isomer, where the $C_2H_2^+$-fragment is trapped between the two Br^+-fragments, while it obtains a much higher kinetic energy in the fragmentation of the *cis* isomer, where

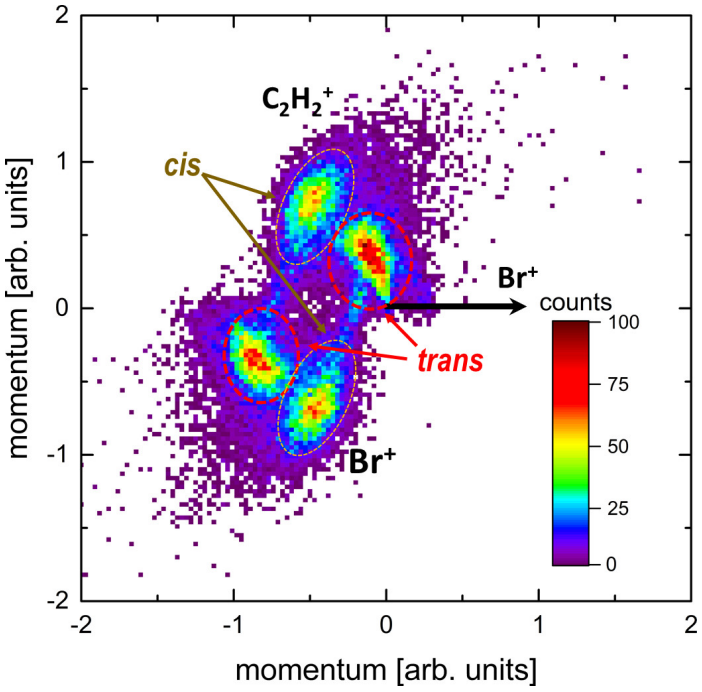

Figure 4.4: Newton plot of the $C_2H_2^+ + Br^+ + Br^+$ triple-coincidence channel. The momenta of $C_2H_2^+$ fragments (upper half) and one of the Br^+ fragments (lower half) are shown in the frame of the momentum of the second Br^+ fragment, which is shown as a black horizontal arrow. The momentum vectors of the $C_2H_2^+$ fragment and the first Br^+ fragment are normalized to the length of momentum vector of the second Br^+. The contributions corresponding to the *cis* and *trans* isomers are indicated.

it is repelled by the two Br^+-fragments that are located in the same hemisphere. This simple picture is also corroborated by the results of the Coulomb explosion model calculations shown in Fig. 4.3, which predict values that lie very close to the maxima of the experimental kinetic energy distribution and also reproduce the difference between the KERs of the two isomers. It can also be visualized directly in a Newton plot [113] for this particular triple-coincidence channel shown in Fig. 4.4, where the momenta of two fragments ($C_2H_2^+$ and Br^+) are shown in the frame of the momentum of the third fragment (Br^+). For the *trans* isomer, the Newton plot shows that the two Br^+ fragments are emitted close to back to back, while the $C_2H_2^+$ fragment remains almost at rest, as one would expect from an instantaneous fragmentation in the undistorted equilibrium geometry, where the center of mass of the C_2H_2 moiety is exactly in the middle between the two Br atoms. The *cis* isomer, however, has a distinctly different fragmentation pattern with $C_2H_2^+$ and Br^+ fragments being emitted at an angle of close to

125 degree with respect to each other and carrying momenta of similar magnitude. From

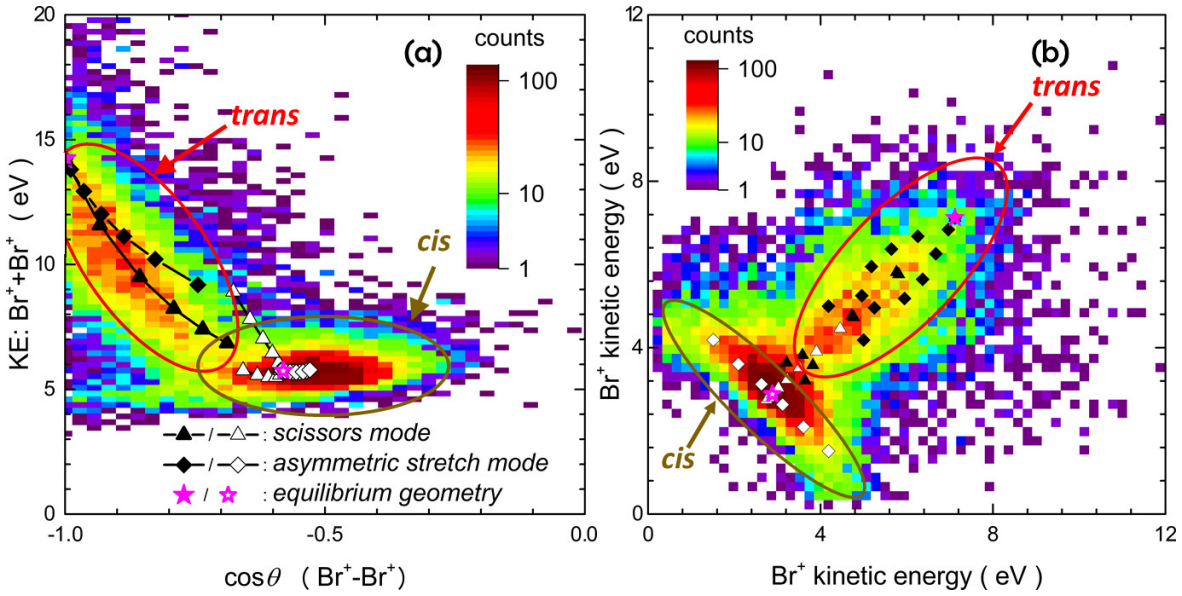

Figure 4.5: (a) Sum of the kinetic energies of the two Br^+ fragments as a function of the angle θ between them, and (b) correlation between the kinetic energies of two Br^+ fragments, both for the $C_2H_2^+ + Br^+ + Br^+$ triple-coincidence channel. The results of the Coulomb explosion simulations for various stretching and bending modes are shown as symbols, with the stars representing the results for the equilibrium geometries. The plots depict the isomerically mixed sample, but selecting one isomer via selection of the Br^+ - Br^+ angle as done for Fig. 4.3 would select only the contributions shown in the regions marked *cis* and *trans*.

the shape of the momentum distributions seen in the Newton plots as well as from the good agreement between the experimental data and the simulation, we conclude that the break-up of the molecule into this three-body channel happens mainly via concerted fragmentation in a molecular geometry that still resembles the equilibrium geometry. However, we attribute the widths of the angular distributions and the kinetic energy distributions beyond the experimental momentum resolution to small deviations from this equilibrium geometry due to stretching and bending motions of the molecule in either the neutral molecule (e.g. vibrations due to the temperature of the molecular beam) or in the cationic state(s) that are reached after the ionization. These geometry changes can be included empirically in the Coulomb explosion model by varying the bond lengths and angles is a systematic fashion (see Fig. 4.6 for a sketch of the stretching and bending modes considered here). The results are plotted and compared to the experimental data in Fig. 4.5. Since the calculations slightly overestimate

the kinetic energies, as seen in Fig. 4.3, the calculated Br^+ energies are shifted by -0.65 eV for better comparison to the experimental data. In Fig. 4.5 (a), the sum of the kinetic energies of the two Br^+ fragments is shown as a function of the angle θ between the Br^+ fragments, while Fig. 4.5 (b) shows the correlation between the kinetic energies of the two Br^+ fragments. In the Coulomb explosion calculations, the C-Br bond distance is varied between 100% and 40% of the equilibrium bond length (in steps of 10%) for the asymmetric stretch mode, and the bond angle by ± 25 degrees (in steps of 5 degrees) around the equilibrium angle for bending in the scissor mode. A combination of both modes reproduces the shape of the Br^+ - Br^+ kinetic energy correlation for the *trans* isomer, which is centered around the line of equal energy sharing between the two Br^+ ions. According to the model calculations, the spread in the angle between the two Br^+ ions for the *trans* isomer is mainly due to bending in the scissor mode, while the the broadening of the Br^+ kinetic energy sum and the deviations from equal energy sharing are likely due to asymmetric stretching. For the *cis* isomer, asymmetric stretching of the C-Br bonds reproduces well the almost constant sum of the Br^+ kinetic energies, but it cannot fully explain the spread in the angle that reaches values up to $\cos\theta = -0.2$ in the experimental data. This may be an indication that some channels that lead to the fragmentation of the *cis* isomer possibly involve a delayed charging of one of the Br atoms, thus resulting in deviations from the concerted fragmentation model. Further information on the pathways and intermediate ionic states that give rise to these events could be obtained, e.g., from coincident high-resolution Auger electron spectra. Some of the events that are not accounted for in the Coulomb explosion simulation might also stem from a two-step fragmentation mechanism involving intermediate states that are long-lived as compared to the rotational period of the molecule. Such a "delayed fragmentation" usually leads to a ring-like structure in the Newton plots [73, 114], which seems to also be present in Fig. 4.4. Further information about differences in the fragmentation dynamics between the two isomers or possible isomerization dynamics in the cationic state may be obtained from future time-resolved pump-probe experiments.

In the Coulomb explosion simulation that is used to compare with experimental data in this chapter, the equilibrium geometry of the neutral *trans* and *cis* dibromoethelene

($C_2H_2Br_2$) and the dichloroethene ($C_2H_2Cl_2$) molecule are determined by the Gaussian software package. It is well known that the molecule may undergo geometry changes, e.g. due to vibrations in the neutral or cationic states or due to a geometric rearrangement, such as the beginning of an isomerization, that may occur during the photoionization process *prior* to the Coulomb break-up. In order to model the effect of these deviations from the equilibrium geometry in Coulomb explosion simulations, the large number of vibrational modes and other possible geometry changes have broken down into a few basic stretching and bending motions, as shown in Fig. 4.6. In this study, two stretching and two bending modes involving the C-Br bonds that are considered to be the most likely and most relevant are selected. Within such classical calculations, one cannot distinguish if the geometric changes occur in the neutral or cationic state, but this information may be derived from more detailed calculations of the electronic structure and dynamics or from future time-resolved experiments.

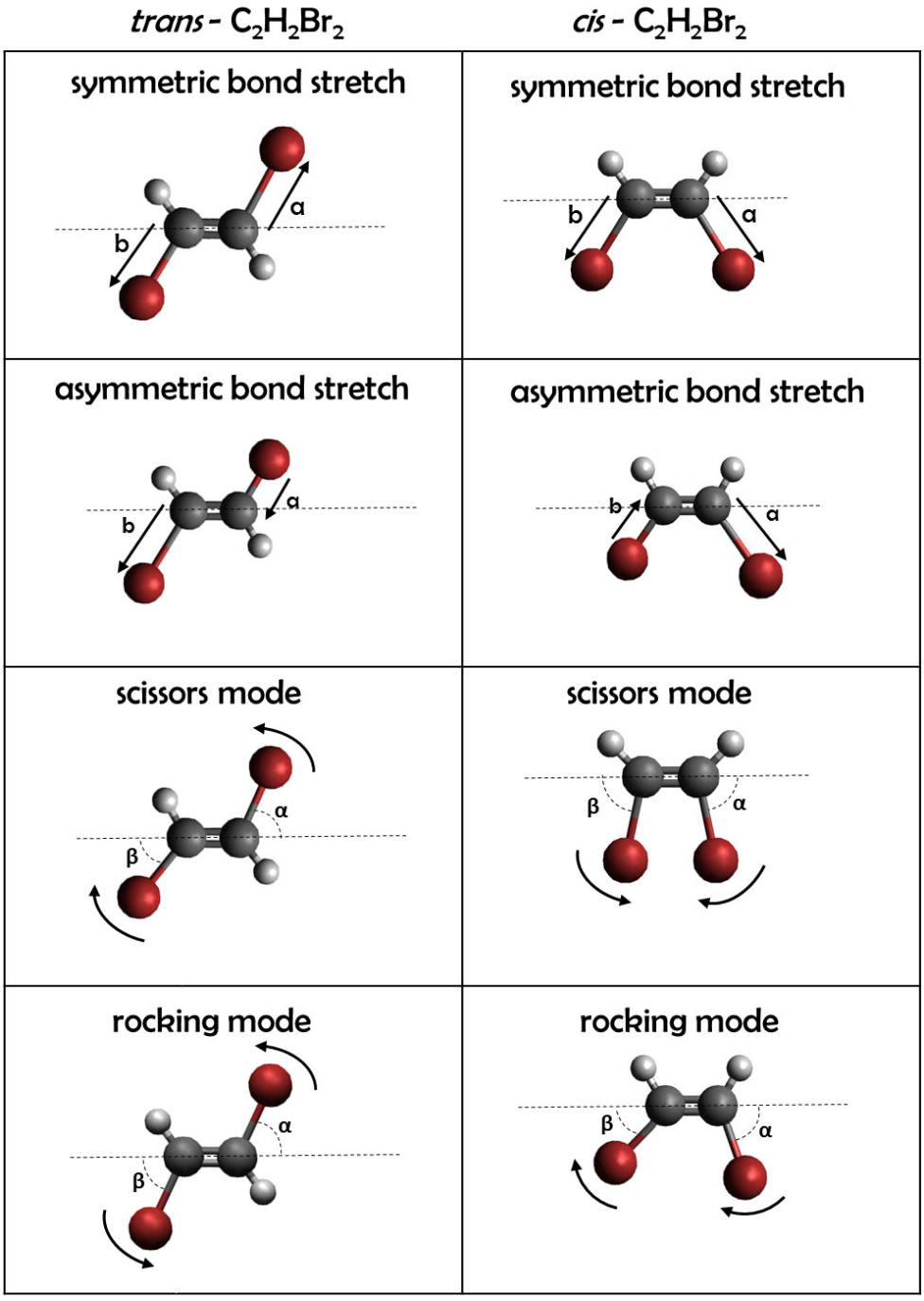

Figure 4.6: Overview of stretching and bending modes in *trans* and *cis* $C_2H_2Br_2$ considered in the Coulomb explosion simulations. The effect of bending in the rocking mode (i.e. both Br atoms rotating in the same direction) is not shown in Fig. 5 since it barely influences the outcome of the model calculations, while symmetric stretching of the C-Br bonds simply broaden the kinetic energy distribution at a fixed value of $\cos\theta$.

4.2.2 Photo- and Auger-electron spectra of 1,2-$C_2H_2Br_2$

X-ray photoelectron spectroscopy of gas-phase molecules has long been a popular subject. The technique probes the energy and angular distribution of electrons ejected from molecular systems via irradiation by X-rays. The ejected electrons contain information regarding the electronic structure and atomic composition of the system. In recent years, ion-electron coincidence measurements have also been conducted widely. Such coincidence measurements can provide element specific information and can help resolve many overlapping electronic states that often form broad bands in molecular electron spectra. The advantage of the electron-ion coincidence technique that is utilized in this experimental work is that it allows resolving such complicated overlapping photo- and Auger-electrons to specific final charge states and fragmentation channels. For example, it can distinguish the electrons that are in coincidence with $C_2H_2Br^+$+Br^+ and $C_2H_2^+$+Br^++Br^+ channels. For $C_2H_2Br_2$, absorption of a 140-eV photon leads predominantly to Br $3d$ inner-shell ionization followed by Auger decay processes that typically ejects one or two additional electrons. This is due to the large cross section for photoionization of Br $3d$ at this photon energy.

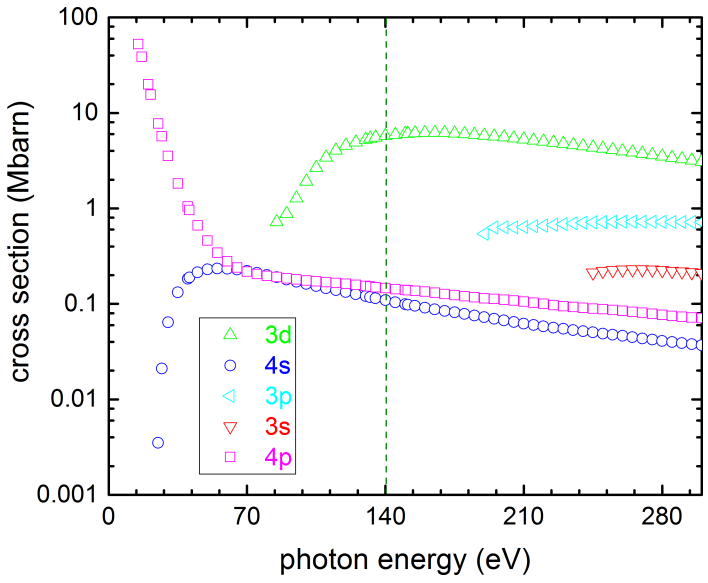

Figure 4.7: X-ray photoionization cross sections for different energy levels of Bromine atom. Figure taken from reference [40].

At the energy of 140 eV, the photon can probe the $3d$ inner-shell which has a binding energy of 69 eV for $3d_{3/2}$ and 70 eV for $3d_{3/2}$ levels [115]. The photoionization cross section for $3d$ is 5.97 Mbarn, see Fig. 4.7. The deeper electronic levels, e.g. $3p$, $3s$ and $2p$, $2s$ are not reachable with the photon energy due to higher binding energies. Valence electrons can be ejected after absorption of a 140-eV photons, however the photoionization cross sections for valence levels are about factor of 2.5 lower than the $3d$ shell. Fig. 4.8 shows a raw position, recorded by the delay-line detector, spectrum containing the majority of the electrons produced from the photoionization.

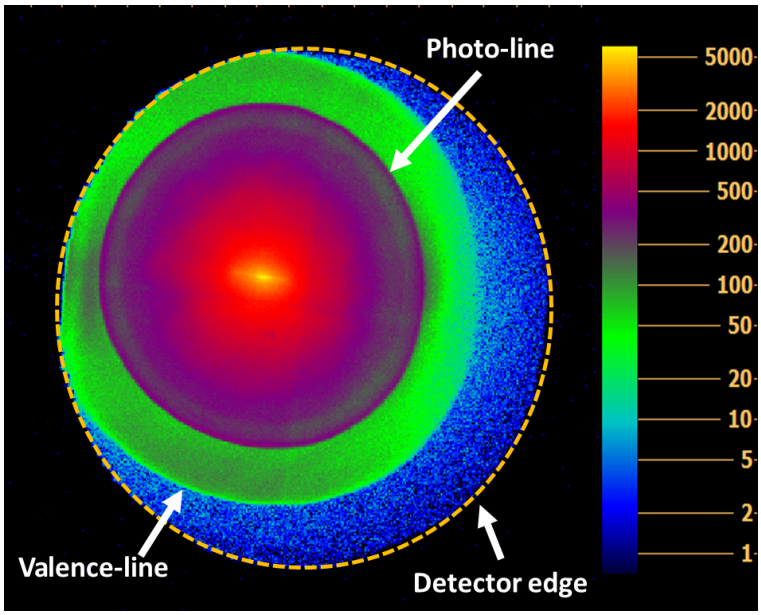

Figure 4.8: Raw position distribution of all electrons generated from the interaction of 1,2-$C_2H_2Br_2$ molecules with a 140-eV synchrotron photon.

Parts of the high kinetic energy valence electrons are lost at the left edge of the detector. The major reason of the electron loss in this particular case is the offset of the electron position distribution with respect to the center of the detector, which is possibly due to the imperfect alignment of the spectrometer and experimental chamber and/or due to magnetic fields. Such an offset does not affect the electron measurement other than causing parts of the high energy electrons to escape from the detector. Using the cylindrically symmetric nature of the electron-detection with the VMI, one can first shift the whole position image to the center of the coordinate system (0,0) and then choose half or quarter of the position

image and replicate such "complete" part of the spectrum to the rest so that a symmetric image can be further used for electron inversion. The Onion-Peeling image inversion method [77] is employed to invert the electron position spectrum in order to extract kinetic energy distribution.

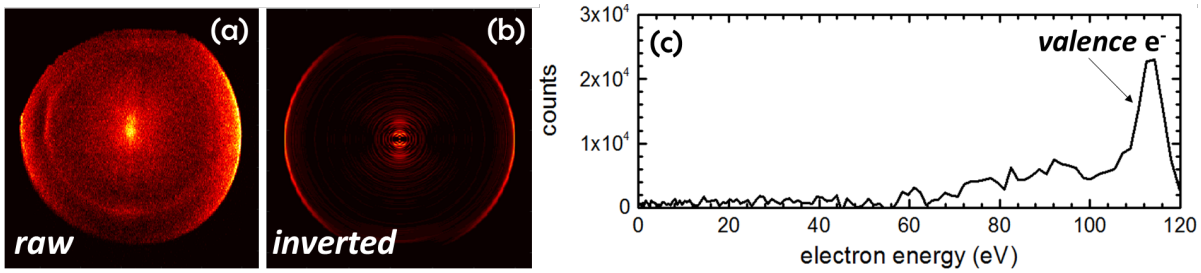

Figure 4.9: (a) Position spectrum of valence electrons after gating on $C_2H_2Br_2^+$ ion TOF; (b) Inverted position spectrum of (a); (c) Extracted kinetic energy distribution of valence electrons after photoionization of the $C_2H_2Br_2$ molecule with a 140-eV photon.

By selecting individual ions in the TOF spectrum in Fig. 4.1 (c) and applying time gates, one can assign coincidence electrons to specific final states. For two- and three-body ion coincidence channels, time gates are applied in PIPICO and PIPIPICO spectra in order to extract the coincidence electrons. Fig. 4.10 demonstrates the position and energy distribution of electrons that are in coincidence with, Br^+, CBr^+ and $C_2H_2Br^+$ as well as two- and three-body ion coincidence channels: $C_2H_2Br^+$+Br^+ and $C_2H_2^+$+Br^++Br^+. In panels (k)-(o) of Fig. 4.10, the peak at 61 eV represents the photo-electrons ejected from the Br $3d$ shell. This means the binding energy of Br $3d$ electrons in 1,2-$C_2H_2Br_2$ molecule is E_{x-ray} - $KE_{Br(3d)}$ $\approx$ 79 eV.

An electron spectrum generated by gating on an individual ion TOF contains all electrons that are emitted during the photoionization and the generation of such ion. For example, if the electrons in coincidence with Br^+ ions are extracted, it includes electrons emitted during any fragmentation channel that produce Br^+ ion. Such electron spectra is still complicated due to the contribution from many overlapping final states. If an ion coincidence channel is selected, only two or three kinds of electrons remain that are ejected during the production of this particular fragmentation channel.

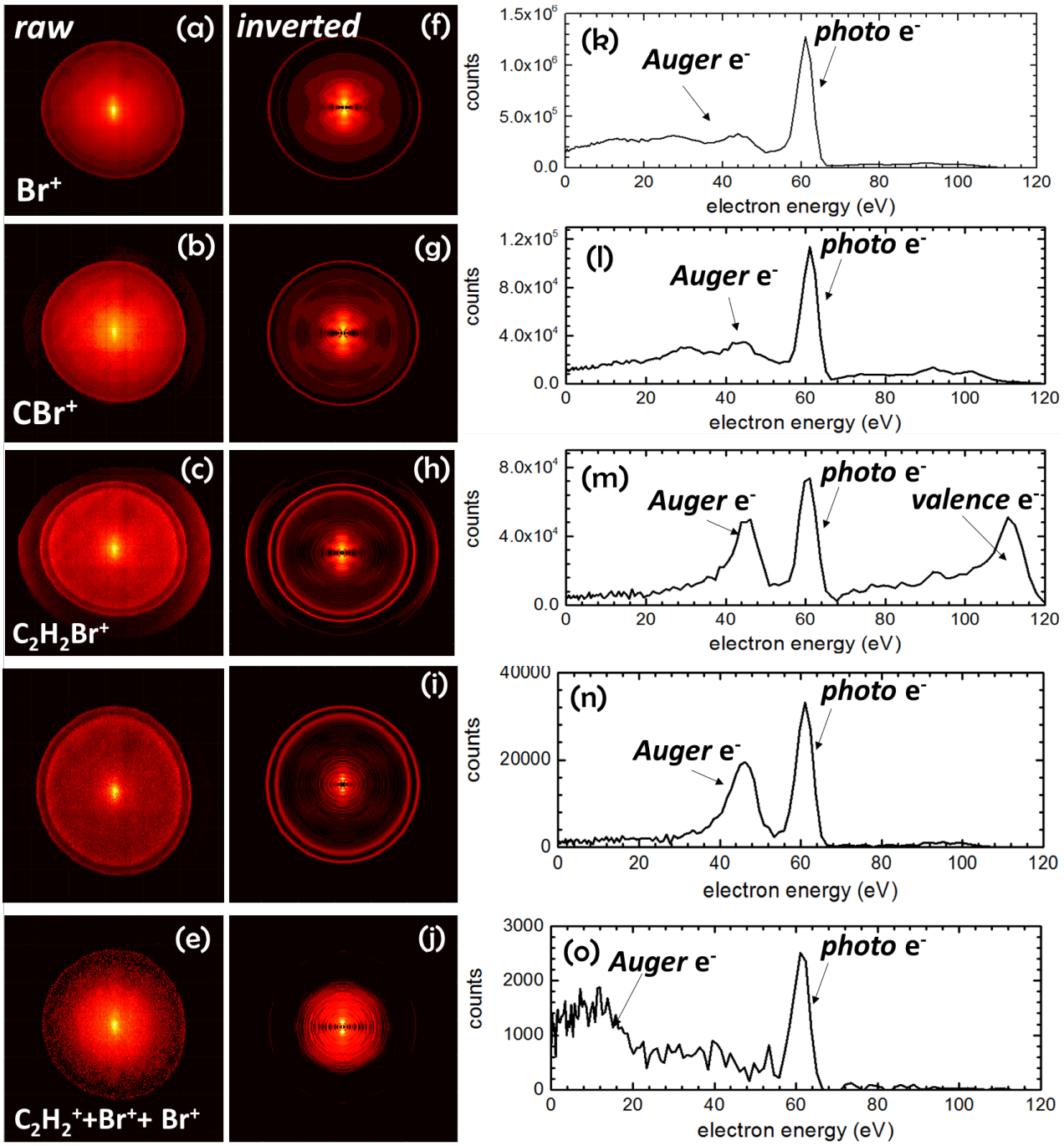

Figure 4.10: Position spectrum of coincidence electrons after gating on (a) Br^+; (b) CBr^+; (c) $C_2H_2Br^+$; (d) $C_2H_2Br^+$+Br^+ channel (e) $C_2H_2^+$+Br^++Br^+ channel; (f-j) Inverted position spectrum for (a-e) by using Onion Peeling inversion algorithm; (k-o) Extracted kinetic energy distribution of coincidence electrons shown in (a-e) after photoionization of the $C_2H_2Br_2$ molecule with a 140-eV photon.

There are three important conclusions one can draw from this set of electron spectra:

- In inner-shell photoionization and fragmentation of the molecule into $C_2H_2Br^+$+Br^+ channel, a photo-electron is ejected with 61 eV kinetic energy, which is then followed by an emission of a 46-eV Auger electron.

- In single ionization of the molecule by the synchrotron beam, a valence electron is ejected and the parent ion $C_2H_2Br_2^+$ can fragment into $C_2H_2Br^+$+Br channel.

- After inner-shell photoionization and fragmentation of the molecule to triple coincidence channel $C_2H_2^+$+Br^++Br^+, Auger-electrons with lower kinetic energy (e.g. <20 eV) are emitted from the system.

4.2.3 Strong-Field Laser Studies: 1,2-$C_2H_2Br_2$

The Coulomb explosion imaging study conducted on 1,2-$C_2H_2Br_2$ after inner-shell photoionization with soft X-rays demonstrates that the imaging technique can be used to identify and separate *cis* and *trans* geometrical isomers from a mixed sample. The physical process in inner-shell photoionization is to first remove an electron from inner-shell after absorbing an X-ray photon, then due to Auger relaxation processes, one or multiple Auger electrons can be emitted from the system. Another approach to efficiently ionize the molecule is to use high intensity laser pulses to strip valence electrons from the system. The availability of ultrafast femtosecond Ti-Shaphire laser facility as well as ion-ion coincidence measurement apparatus: COLTRIMS at J. R. Macdonald Laboratory of Kansas State University made it possible to conduct strong-field measurements of gas-phase molecular samples. This section introduces the Coulomb explosion imaging measurement of 1,2-$C_2H_2Br_2$ *cis* and *trans* mixture after strong-field ionization with ultrafast laser pulses. The gas-phase dibromoethene isomers are delivered to the interaction region of the COLTRIMS spectromter via supersonic jet in the form of cold and continuous molecular beam. The Fourier-transform limited laser pulses with 25 fs pulse duration and 4×10^{14}W/cm^2 intensity crossed with the molecular beam at the center of the spectrometer. Ions generated from the laser-molecule interaction are detected on the microchannel plate and the ion time of flights are shown in Fig. 4.11. It

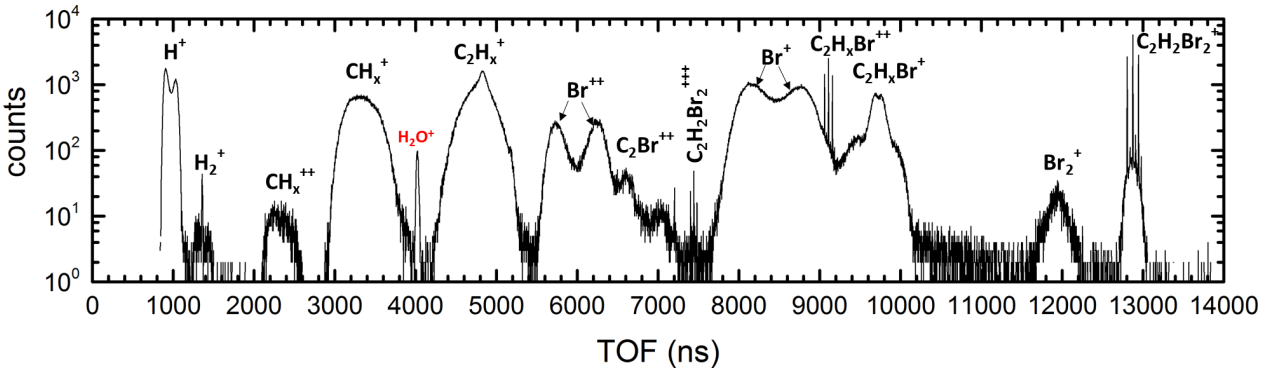

Figure 4.11: Time-of-flight mass spectrum for *cis* and *trans* mixture 1,2-$C_2H_2Br_2$ isomers after ionization with 25 fs laser pulses at 800 nm with 4×10^{14}W/cm^2 laser intensity.

is evident from the spectrum that the laser intensity is strong enough to doubly and triply ionize the parent molecule. There are long lived $C_2H_2Br_2^{++}$ and $C_2H_2Br_2^{+++}$ ions that are detected before further fragmenting into multiple ionic species.A new bond between two Br atoms can be formed by isomerization process and, as a result Br_2^+ ions are generated. It is an interesting task to compare the Br_2^+ formation and study the fragmentation dynamics of such "isomerization" channel after inner-shell photoionization with X-rays and strong-field ionization with laser pulses. However, in this thesis, Br-Br bond formation will not be discussed in further detail. Fig. 4.12 shows the coincidence PIPICO spectrum taken at the same conditions as in Fig. 4.11. The observed two-body coincidence channels are labeled in white and the fragmentation channel from residual gas CH_3I in the background is labeled in red. All two-body coincidence channels, meaning the molecule breaks into two ionic species with both ions containing one or two charges, appear as sharp diagonal lines due to momentum conservation. Fragmentation channels of three or more ions and the channels containing neutral fragments appear as "blobs" in PIPICO spectrum. The triple-ion channel, e.g. $C_2H_2^+$+Br^++Br^+ that is used in the study for determining isomer structures is selected from the TRIPICO map shown in Fig. 4.13. It is interesting to note that in strong-field ionization of 1,2-$C_2H_2Br_2$, the only observed triple-coincidence channel is $C_2H_2^+$+Br^++Br^+, while in a synchrotron measurement, the inner-shell photoionization lead to the deprotonation of the molecule and $C_2H_2^+$ fragment and C_2^+, C_2H^+ fragments were also detected in coincidence with two Br^+ ions. The isotope of bromine with mass 79 amu and 81 amu

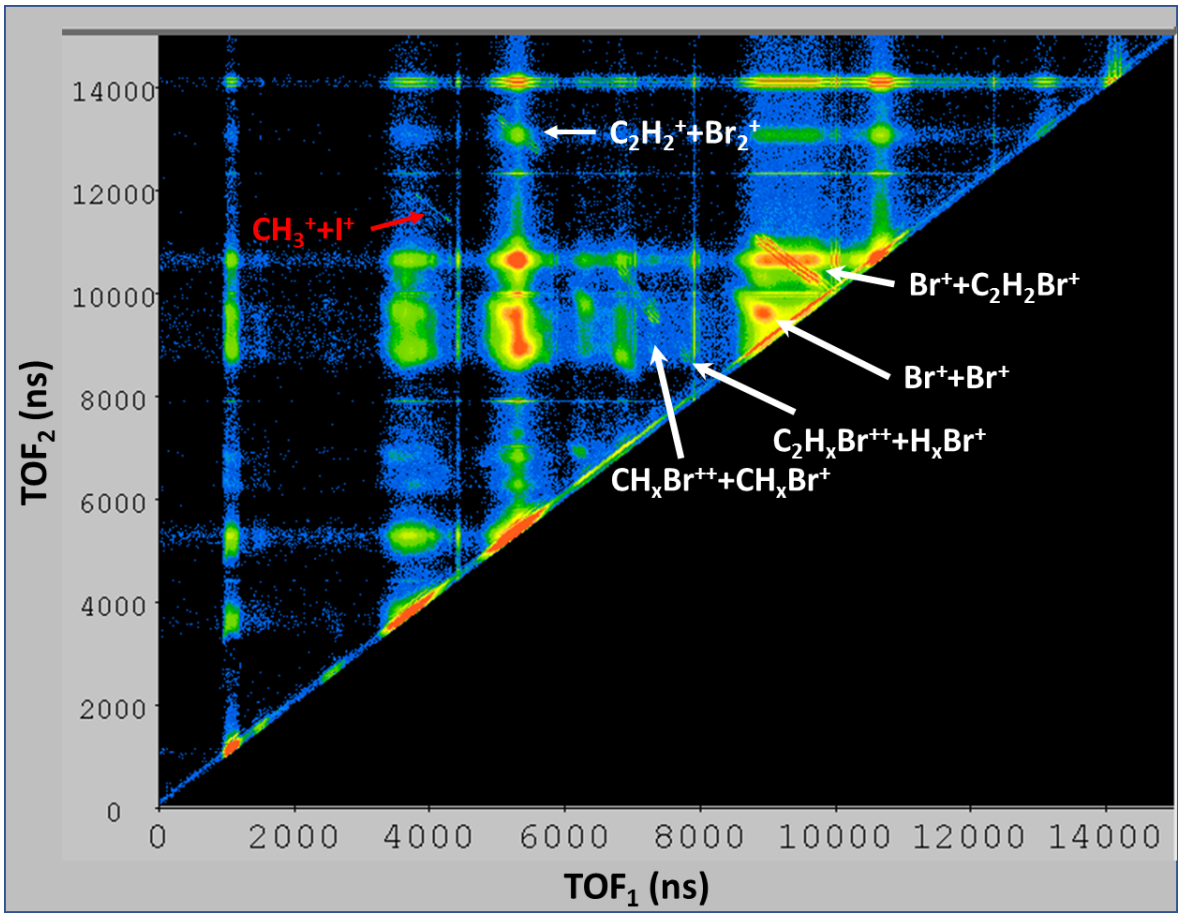

Figure 4.12: Ion-ion coincidence map (PIPICO) for *cis* and *trans* mixture 1,2-$C_2H_2Br_2$ isomers after ionization with 25 fs laser pulses at 800 nm with 4×10^{14}W/cm^2 laser intensity.

produce three triple-coincidence combinations: $C_2H_2^+ + {}^{79}Br^+ + {}^{79}Br^+$, $C_2H_2^+ + {}^{79}Br^+ + {}^{81}Br^+$, $C_2H_2^+ + {}^{81}Br^+ + {}^{81}Br^+$.

In the next step, the ion momenta are calculated using the measured time of flight and hit positions of each ion. The momentum sum of all fragments in this triple coincidence channel peaks at zero due to momentum conservation, see Fig. 4.14. The molecules have initial momentum before the fragmentation due to the finite temperature and the recoil momentum from the electrons, thus, total momentum conservation is not fulfilled exactly and the momentum sums in all three directions appear as sharp peaks with certain width. The momentum sum of p_z component of three ion momentum vectors have the smallest FWHM of only 2.3 au. The widest momentum sum peak appears in p_y component, which is in the direction of the molecular jet. Momentum sum gates are applied and only the events

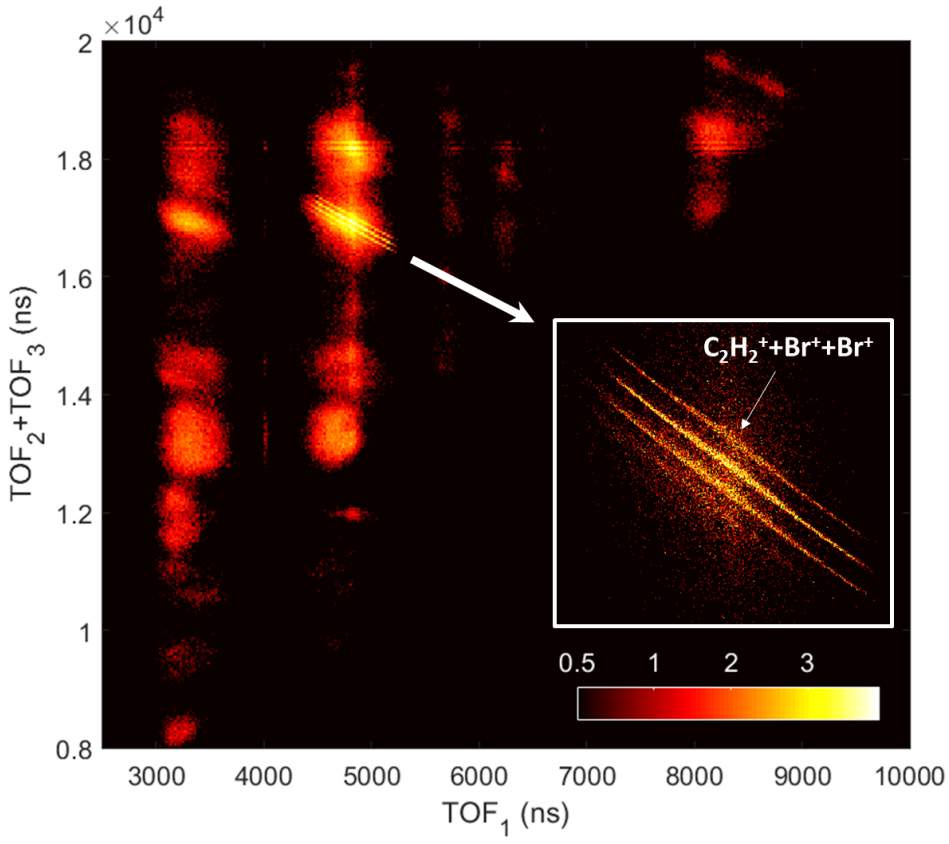

Figure 4.13: Ion-ion-ion coincidence map (PIPIPICO) for *cis* and *trans* mixture 1,2-$C_2H_2Br_2$ isomers after ionization with 25 fs laser pulses at 800 nm with 4×10^{14}W/cm^2 laser intensity.

fall under the sharp peaks in p_x, p_y and p_z momentum sums are chosen in order to study the *true* triple coincidence events.

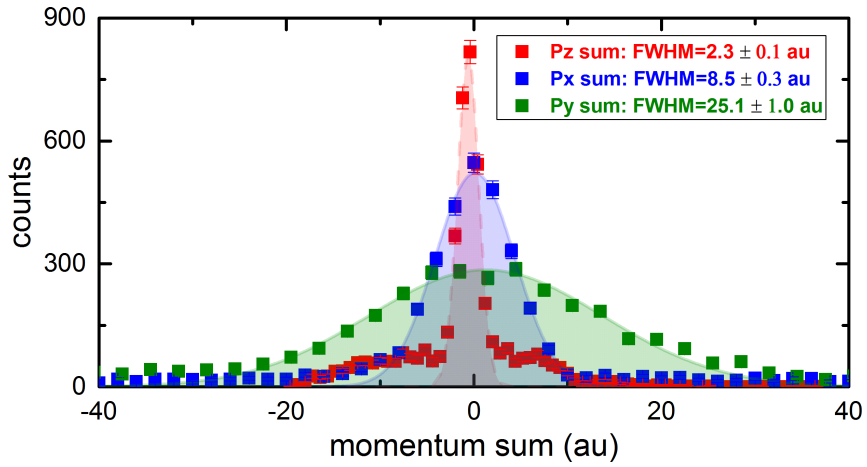

Figure 4.14: Momentum sum of p_x, p_y and p_z components in $C_2H_2^+ + {}^{81}Br^+ + {}^{81}Br^+$ channel. The experimental data (squares) are fitted with Gaussian (shaded area).

Correlation between two Br^+ momentum vectors is shown in Fig. 4.15. The two angular peaks correspond to *cis* and *trans* geometries of 1,2-$C_2H_2Br_2$. The values of angular peaks correspond to *trans* and *cis* geometry are $\cos\theta$=-1 and $\cos\theta$=-0.58. The Coulomb explosion simulation values are shown as arrows. It is apparent that the experimental angular peaks matches closely with the numerical Coulomb explosion simulation. The area ratio of gaussian fits for *trans* and *cis* isomer peaks are estimated to be 3±0.8 in Fig. 4.15. This result is different from the *trans*/*cis* isomer ratio estimated from the synchrotron measurement:2.04 ± 0.07. The reason behind the differences in *trans*/*cis* ratios can be directed to the difference in strong-field ionization cross sections of isomers that is recently discussed the work of Zigo et al [116]. In order to study the isomer resolved kinetic energies of ions, angular gates on $\cos\theta$ spectrum are applied. The kinetic energy distribution of $C_2H_2^+$ and Br^+ and total kinetic energy release in both isomeric cases are generated from the events that fall under $\cos\theta$ gates of *trans*: -1< $\cos\theta$ <-0.9; *cis*: -0.65< $\cos\theta$ <-0.55.

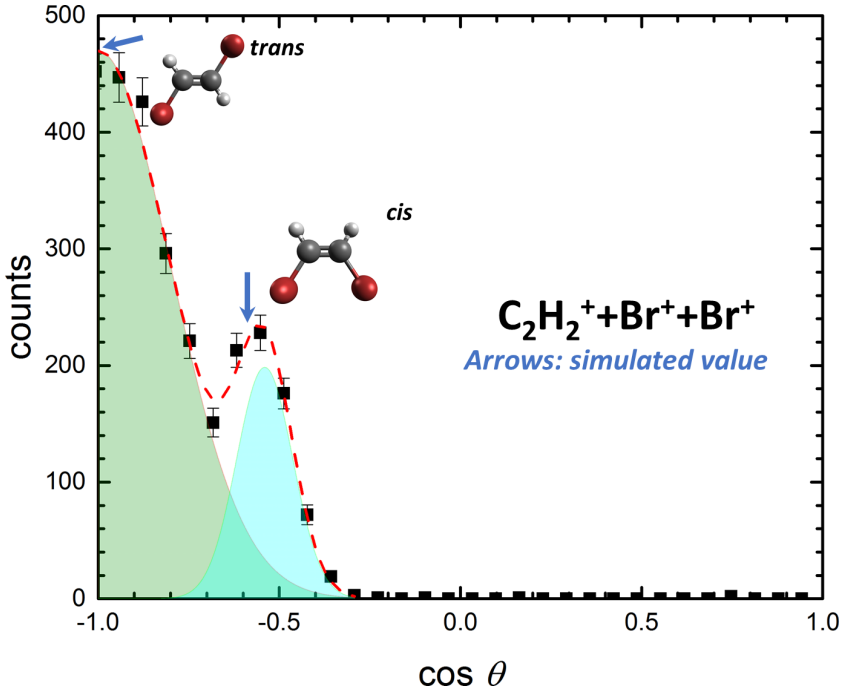

Figure 4.15: Angle between the Br^+ ion momenta in the triple-coincidence channel $C_2H_2^+$ + Br^+ + Br^+. A fit of two Gaussians (shaded areas) to the experimental data (black boxes) is shown as a red dashed line. The angles expected from a classical Coulomb explosion model are indicated by arrows.

As it can be seen from Fig. 4.16 (a,b) that the Coulomb explosion simulation values overestimates the total kinetic energy distributions. A possible explanation could be that in the strong-field ionization with 25 fs laser pulses, the presence of the electric field is long enough for the bonds between atoms to stretch before fragmentation [117, 118]. This process can possibly happen in the neutral, cationic or di-cationic electronic states. At first, the system can absorb some photons to reach to a certain state where the C−Br bonds can stretch to a larger bond length R(C−Br), then the molecule absorbs more photons in the presence of the laser pulse and reaches the final Coulombic potential curve of $C_2H_2Br_2^{+++}$. Finally, the molecule explodes due to the Coulombic repulsion among three ions starting from a longer bond length than original equilibrium molecular geometry. As a result, the total kinetic energy released from the system is smaller than the Coulomb explosion model projection. The schematics of such process is shown in Fig. 4.16 (c).

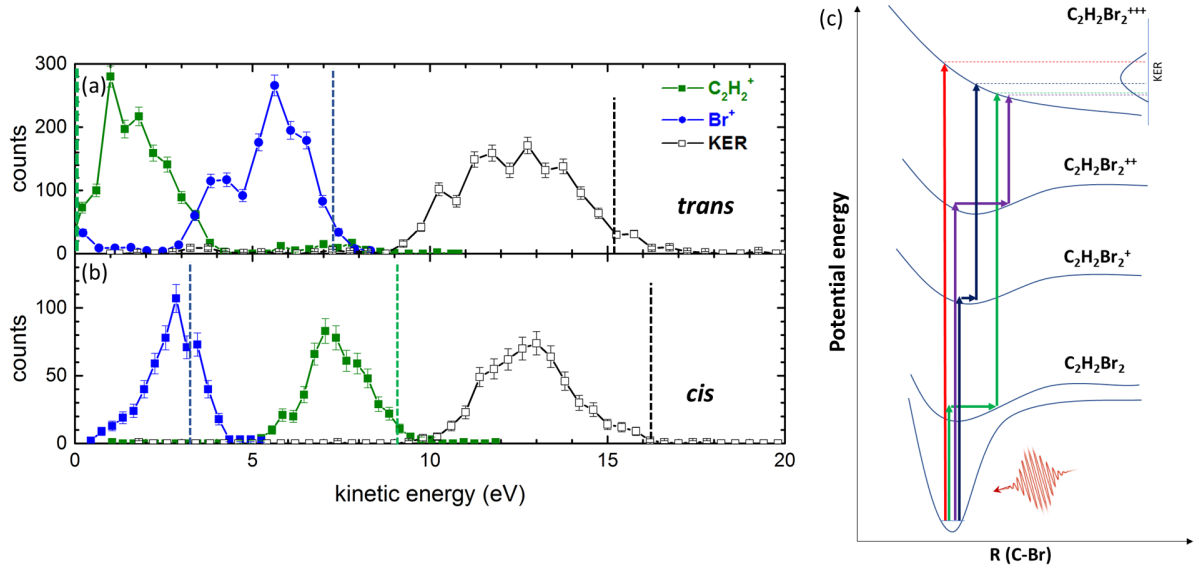

Figure 4.16: Kinetic energy distributions of the Br^+ and $C_2H_2^+$ fragments as well as total kinetic energy release in the $C_2H_2^+$ + Br^+ + Br^+ triple-coincidence channel for (a) *trans* and (b) *cis* isomers, as selected by the Br^+- Br^+ angle θ. The results of the Coulomb explosion model are shown as dashed lines. (c) Schematics of C-Br bond stretching at different electronic states of $C_2H_2Br_2$ molecule.

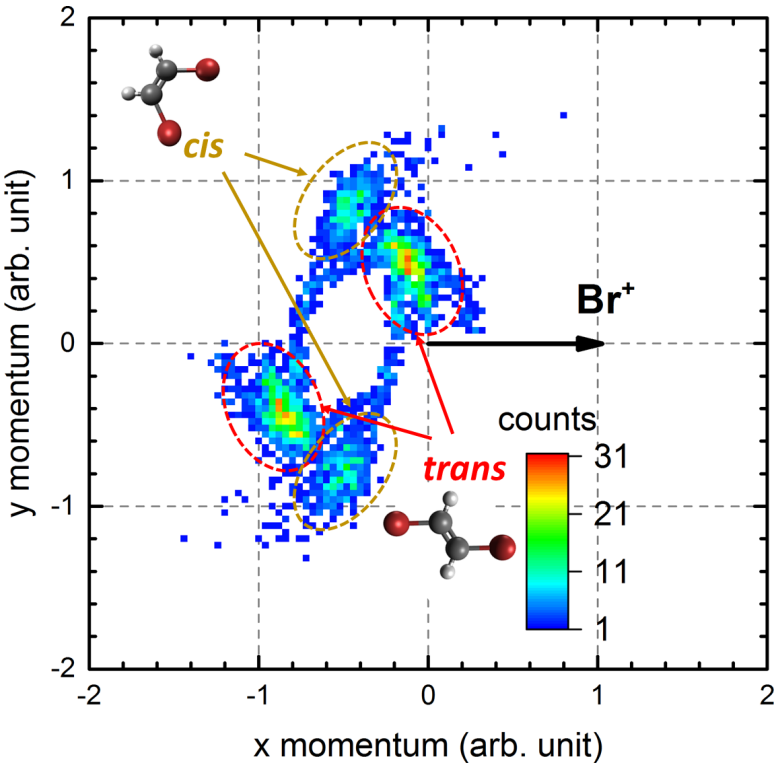

Figure 4.17: Newton diagram of $C_2H_2^+$+Br^++Br^+ channel after ionization of 1,2-$C_2H_2Br_2$ with 25 fs laser pulses at 4×10^{14}W/cm^2.

This is different from the case of inner-shell photoionization discussed in Section 4.2.1, where the Auger decay processes seem to occur so fast that the molecule can emits all three electrons and Coulomb explosion process happens before significant distortion of the molecular geometry occurs. The Newton diagram for $C_2H_2^+$+Br^++Br^+ channel is shown in Fig. 4.17. The momentum distribution is strikingly similar to the result from X-ray photoionization measurement in Section 4.2.1. The clearly separated momentum structures of fragments originated from *cis* and *trans* isomers are the further proof that the application of the Coulomb explosion imaging together with strong-field ionization can be used to identify and separate geometrical isomers.

4.3 Coulomb Explosion Imaging of *cis* and *trans* 1,2-dichloroethene

4.3.1 X-ray Synchrotron Studies: 1,2-$C_2H_2Cl_2$

In previous sections, the Coulomb explosion imaging study was conducted on the mixed *cis* and *trans* samples of 1,2-$C_2H_2Br_2$ after inner-shell photoionization with X-rays as well as ionization with strong 800 nm laser pulses. In this section, as an extension of the study to distinguish geometric isomers as well as to study a pure individual *cis* or *trans* sample, 1,2-dichloroethene (1,2-$C_2H_2Cl_2$) isomers are chosen as targets of study. Contrary to 1,2-dibromoethene, which could not be purchased as isomerically pure sample, pure *cis* and *trans* samples of 1,2-dichloroethene are commercially available from Sigma Aldrich. In this experiment, a photon energy of 240 eV was chosen in order to photoionize the Cl ($2p$) inner-shell in the 1,2-$C_2H_2Cl_2$ molecule. The binding energies of the $2s$, $2p_{1/2}$ and $2p_{3/2}$ levels are 270, 202, 200 eV respectively [115] (Note that the references for the inner-shell electron binding energies were determined for Cl_2 molecule). Previous experiments on 1,2-$C_2H_2Cl_2$ molecule reported the valence ionization energies of the two isomers are *cis*: 9.631 eV [89]; *trans*: 9.658 eV [119]. Using the valence ionization energies and the $2p$ electron binding energy, one can roughly estimate the highest Auger electron kinetic energies to be around $E_{binding}$-E_{IP}-$E_{IP\,of\,ion} \approx 180$ eV [120], where $E_{binding}$ is the binding energy of $2p$ core hole and E_{IP} is the approximate energy of the level from which a valence electron falls down to fill the core hole. The $E_{IP\,of\,ion}$ is the binding energy of the valence electron that is ejected from the ionic system as Auger electron. The photoelectron kinetic energies are estimated to be E_{photon}-$E_{binding} \approx 40$ eV. Since the extraction voltages that need to be applied on the spectrometer depend on the kinetic energies of electrons that needs to be focused, this estimation is of great importance to the experiment in setting and optimizing the spectrometer voltages. In order to capture 180-eV Auger electrons with the coincidence VMI apparatus, voltages up to 3.3 kV are applied to spectromter plates in order to create

a strong focusing field to image all electrons in 4π angle. The details of voltage values and other experimental parameters used in this measurement are shown in Appendix C. The resulting photo- and Auger-electron spectra for both cis and trans isomers are discussed in Section 4.3.2 .

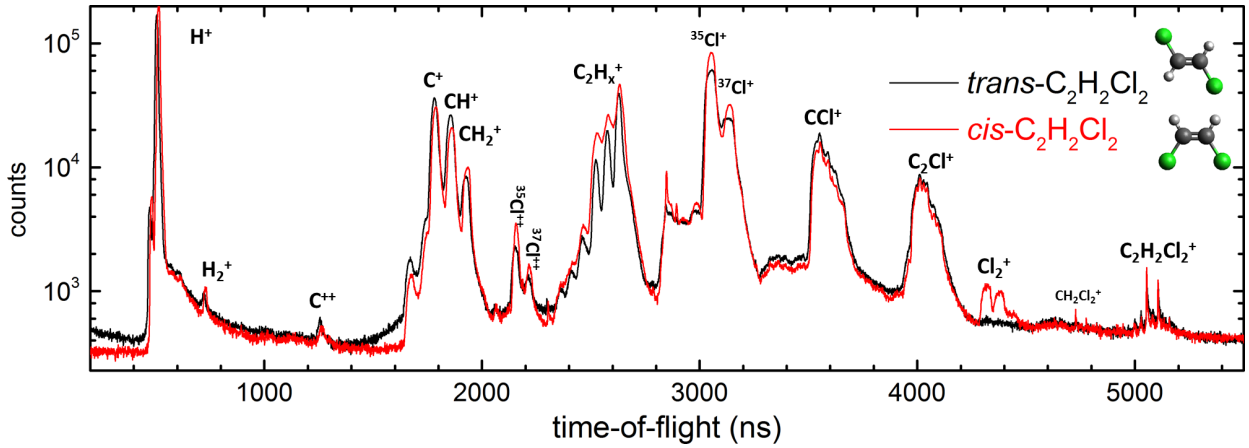

Figure 4.18: Time-of-flight mass spectrum for *cis* and *trans* 1,2-$C_2H_2Cl_2$ isomers after photoionization with 240 eV X-ray synchrotron beam.

Fig.4.18 shows the ion TOF spectrum for all ions generated after inner-shell photoionization of Cl($2p$) electrons of 1,2-$C_2H_2Cl_2$ isomers. TOF spectra of *cis* and *trans* measurements are overlapped on top of each other for comparison. The natural abundance of the two stable chlorine isotopes are ^{35}Cl: 75.6% and ^{35}Cl: 24.1%. Multiple sharp peaks corresponding to the parent ion, namely $C_2H_x{}^{35}Cl_2$ and $C_2H_x{}^{37}Cl_2$ (x is the number of hydrogen) can be seen around 5100 ns. It is evident from the TOF spectrum that a bond-recombination takes place in *cis* isomer where a new bond forms between two Cl fragments and the Cl_2^+ ions are generated. The fact that in 1,2-$C_2H_2Cl_2$, only in *cis*, after inner-shell photoionization, one can see the formation of Cl_2^+ species is, by itself, a separate methodology to identify a *cis* geometry from *trans* in 1,2-$C_2H_2Cl_2$. In this section, the main focus is using the similar momentum imaging technique described in previous sections to identify geometric structure of 1,2-$C_2H_2Cl_2$.

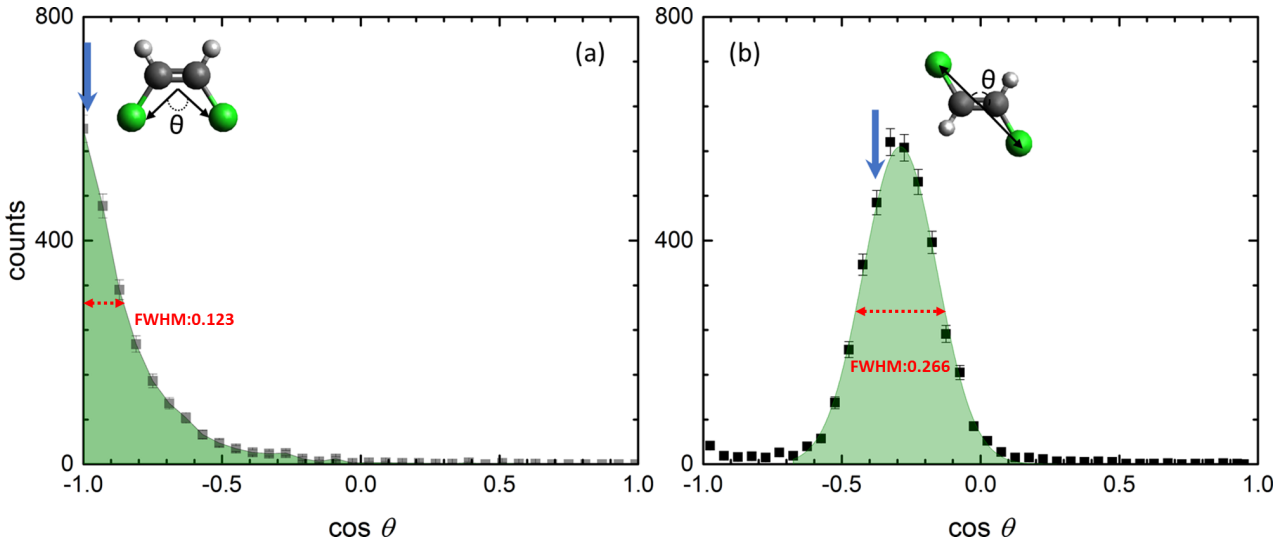

Figure 4.19: Angle between the Cl^+ ion momenta in the triple-coincidence channel $C_2H_2^+$ + Cl^+ + Cl^+ in (a) *trans* 1,2-$C_2H_2Cl_2$ and (b) *cis* 1,2-$C_2H_2Cl_2$. The angles expected from a classical Coulomb explosion model are indicated by arrows.

Fig. 4.19 (a,b) shows the momentum correlations between two Cl^+ ions. The arrows in the figure point to $\cos\theta$ values that are expected from Coulomb explosion simulation. In both *cis* and *trans* measurements of 1,2-$C_2H_2Cl_2$ isomers, the Coulomb explosion simulation closely match the experimental distribution. The Newton diagrams of two measurements are shown in Fig. 4.20. In *trans* measurement, two chlorine ions fly toward opposite directions, thus the distribution of the second Cl^+ is close to the horizontal axis and separated far from the unit vector that represents the first Cl^+. The relative momentum of $C_2H_2^+$ is distributed around 0 due to the fact that the ion is trapped between two Cl^+ and gained least momentum from the breakup. In *cis* scenario, all three ions fly toward three separate directions with large angles between them. The kinetic energy distribution of both isomer measurements are plotted in Fig. 4.21. The coincidence events included in the energy spectra are selected from a narrow cosine gates (*trans*: -1<$\cos\theta$ <-0.9; *cis*: -0.45<$\cos\theta$ <-0.35;) set in Fig. 4.19. The kinetic energy distributions and the matching Coulomb energy simulation values in dashed lines further prove that the imaging technique can identify geometrical isomers.

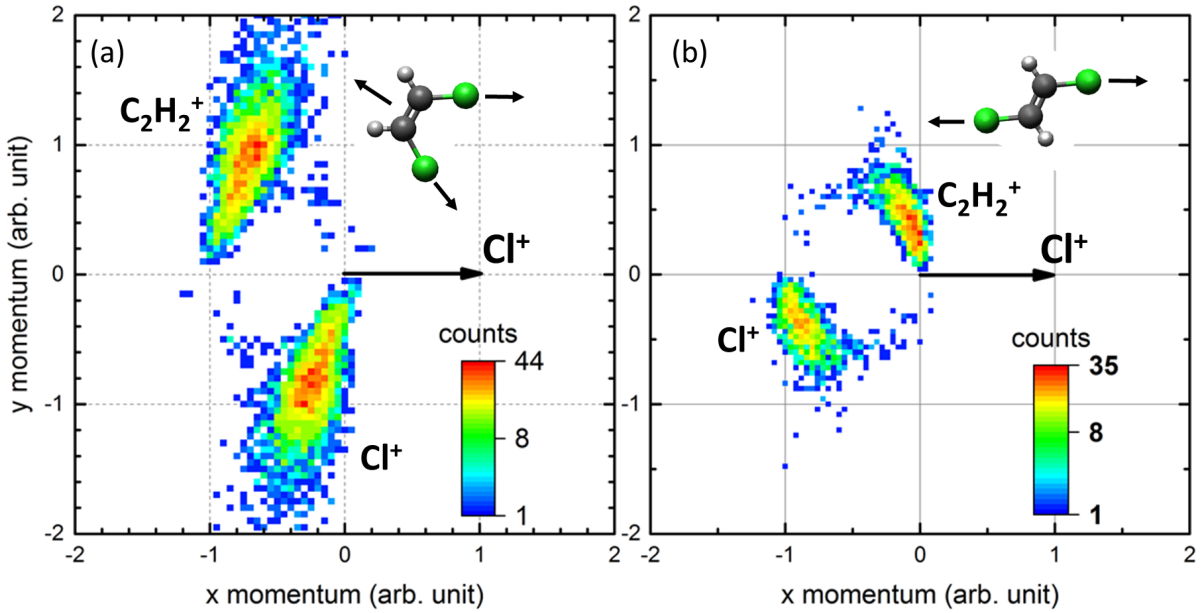

Figure 4.20: Newton plots of the $C_2H_2^+ + Cl^+ + Cl^+$ channel for (a) *cis* and (b) *trans* isomers. The momenta of $C_2H_2^+$ fragments (upper half) and of one of the Cl^+ fragments (lower half) are shown in the frame of the momentum of the second Cl^+ fragment, which is shown as a black horizontal arrow. The momentum vectors of the $C_2H_2^+$ fragment and the first Cl^+ fragment are normalized to the length of momentum vector of the second Cl^+.

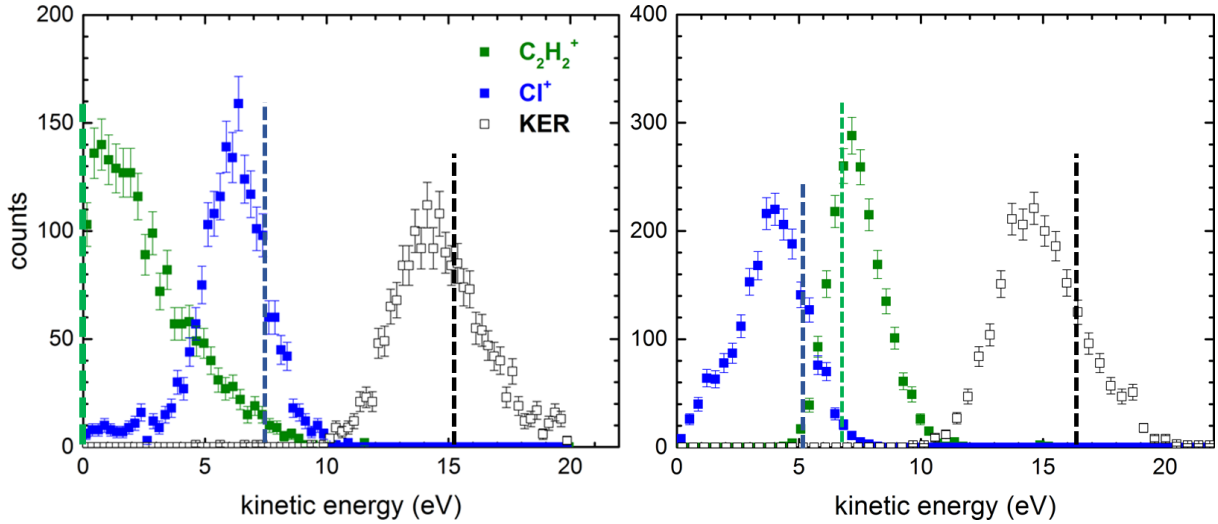

Figure 4.21: Kinetic energy distributions of the Cl^+ and $C_2H_2^+$ fragments as well as total kinetic energy release in the $C_2H_2^+ + Cl^+ + Cl^+$ triple-coincidence channel for (a) *trans* and (b) *cis* isomers. The results of the Coulomb explosion model are shown as dashed lines.

4.3.2 Photo- and Auger-electron spectra of 1,2-$C_2H_2Cl_2$

As discussed in Section 4.2.2, the advantage of double-sided coincidence VMI in terms of electron measurement is that one can not only resolve photo- and Auger-electrons that are in coincidence with corresponding ions, but also resolve electrons that are in coincidence with a specific ion-ion coincidence channels, for example, the detection of electrons in coincidence with $C_2H_2Cl^+$+Cl^+ channel. In this section, the electrons that are in coincidence with selected ion species as well as two- and three-body ion-ion(-ion) coincidence channels are demonstrated.

Fig. 4.22 contains rich information about the electrons emitted from the *cis* isomer of 1,2-$C_2H_2Cl_2$ after inner-shell photoionization of Cl 2p electrons. The raw electron position spectra (a-e) are first generated by setting time gates on the ion TOF spectrum shown in Fig. 4.18. Then the spectra are symmetrized along horizontal and vertical axis and inverted using the Onion-Peeling electron inversion technique [77]. The kinetic energy distribution of electrons that are extracted from the position spectra are shown in (k-o) panels. It is clear that both Cl^+ and CCl^+ ions are in coincidence with a 40-eV photo-electron and an Auger-electron with a 180−190 eV kinetic energy. In panel (m), one can see that the $C_2H_xCl^+$ ions coincide with not only photo- and Auger-electrons but also with valence-electrons with high kinetic energy of around 230−240 eV.

However, when the 1,2-$C_2H_2Cl_2$ molecule breaks into $C_2H_2Cl^+$+Cl^+ channel, there is no high energy valence electron appear in coincidence electron spectrum, see Fig. 4.22 (n). Thus, by combining electron spectra in (m),(k) and (n) panels, one can conclude that in order for the molecule to break into $C_2H_xCl^+$+Cl^+ channel, a 2p inner-shell electron together with an Auger-electron are emitted from the system. However, for the molecule to fragment into $C_2H_xCl^+$+Cl channel, only a valence ion is ejected after absorbtion of an X-ray photon. The electrons coincide with the triple-ionization channel: $C_2H_2^+$+Cl^++Cl^+ are shown in the last panel of Fig.4.22. The three electrons emitted from the system during the fragmentation are (1) the photo-electron ejected from 2p inner-shell, (2) a high energy Auger-electron (∼180 eV) and (3) a low energy Auger-electron (10 eV). The coincidence electron spectra

of *trans* isomers are given in Fig. 4.23. Overall, there is no significant difference between coincidence electron energy distributions of *cis* and *trans* isomers.

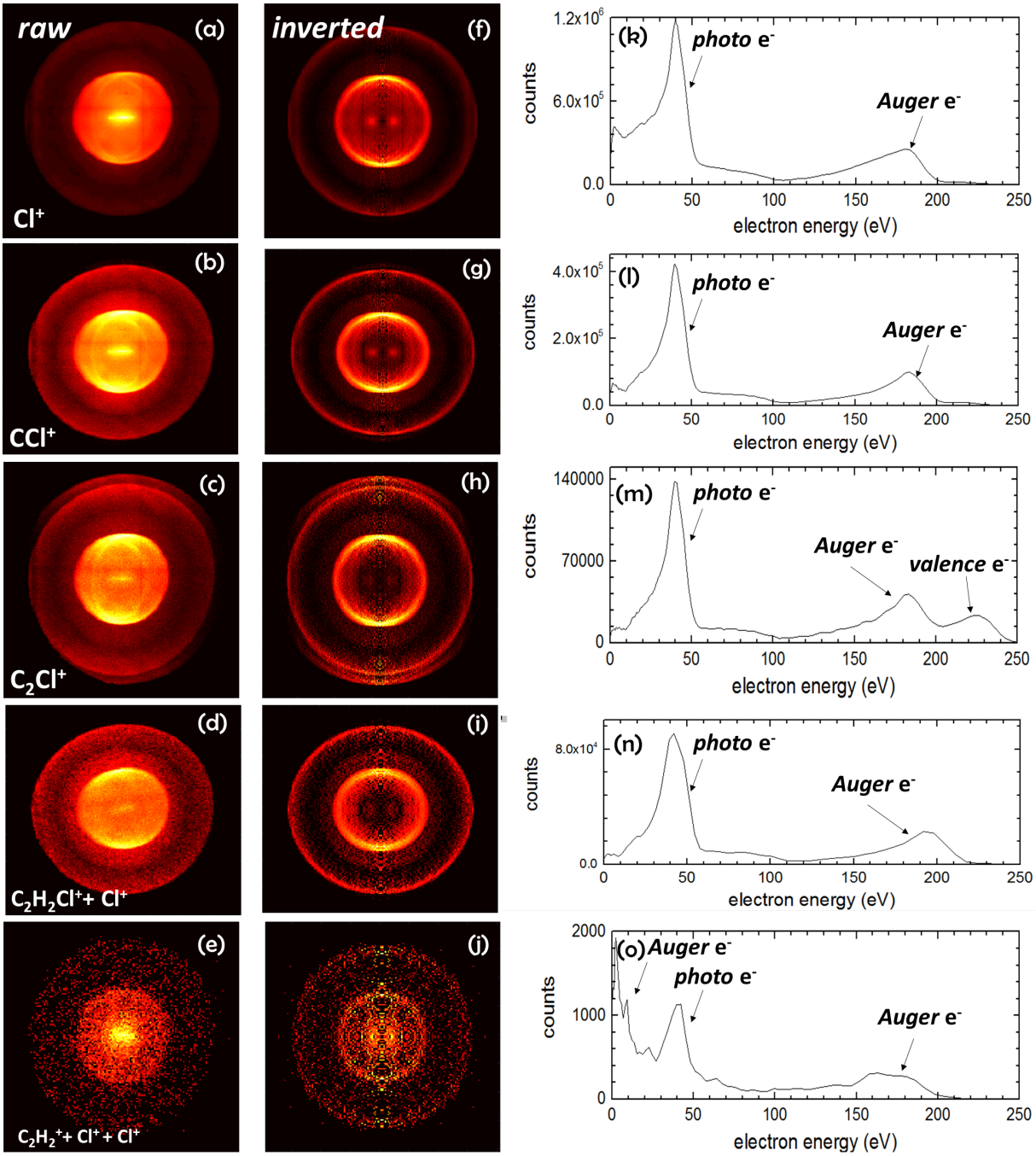

Figure 4.22: Position spectrum of coincidence electrons after gating on (a) Cl^+; (b) CCl^+; (c) $C_2H_2Cl^+$; (d) $C_2H_2Cl^+$+Cl^+ channel (e) $C_2H_2^+$+Cl^++Cl^+ channel; (f-j) Inverted position spectrum for (a-e) by using Onion Peeling inversion algorithm; (k-o) Extracted kinetic energy distribution of coincidence electrons shown in (a-e) after photoionization of the *cis* $C_2H_2Cl_2$ molecule with a 240-eV X-ray photon.

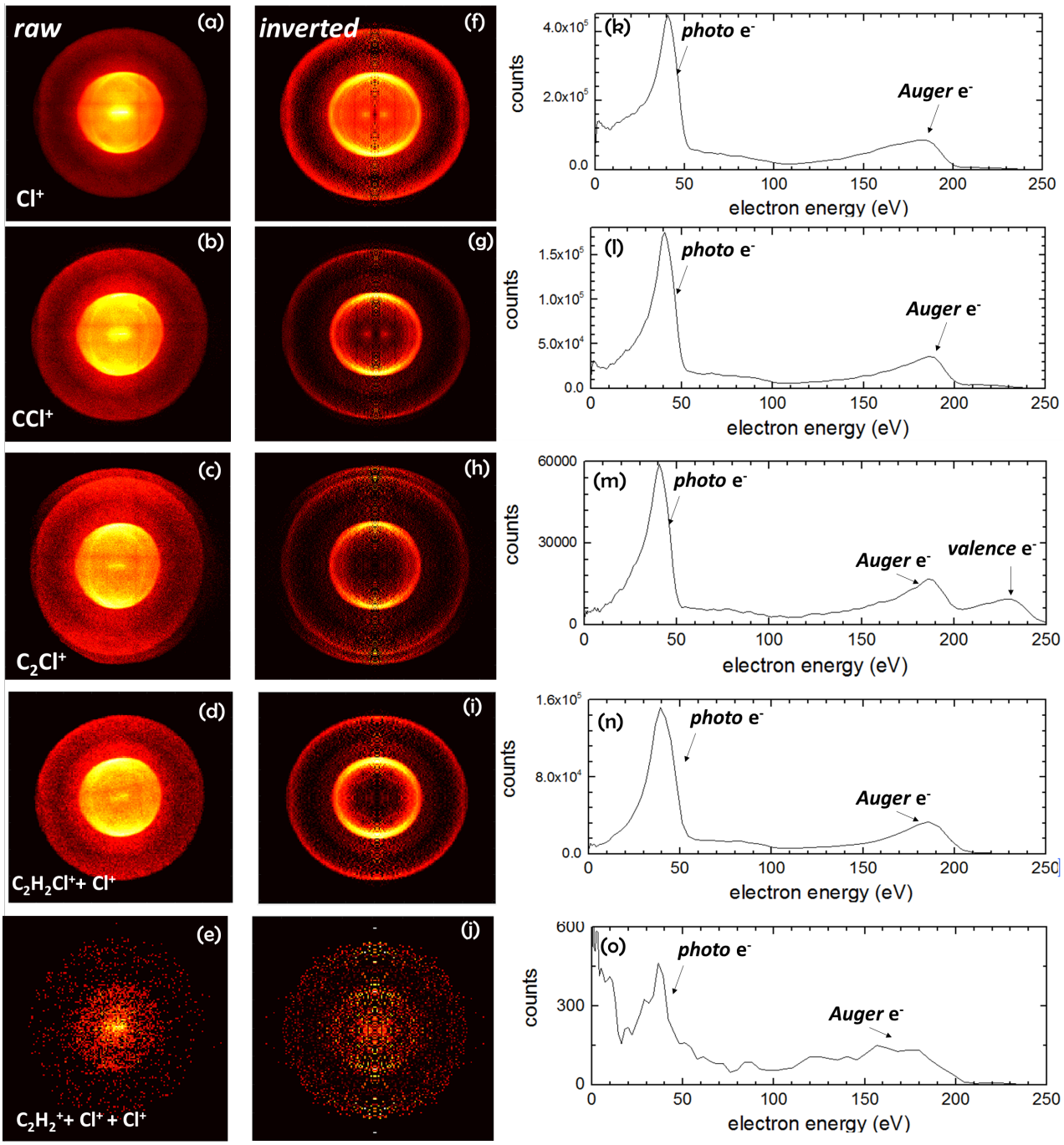

Figure 4.23: Position spectrum of coincidence electrons after gating on (a) Cl^+; (b) CCl^+; (c) $C_2H_2Cl^+$; (d) $C_2H_2Cl^+$+Cl^+ channel (e) $C_2H_2^+$+Cl^++Cl^+ channel; (f-j) Inverted position spectrum for (a-e) by using Onion Peeling inversion algorithm; (k-o) Extracted kinetic energy distribution of coincidence electrons shown in (a-e) after photoionization of the *trans* $C_2H_2Cl_2$ molecule with a 240-eV X-ray photon.

4.3.3 Strong-Field Laser Studies: 1,2-$C_2H_2Cl_2$

Similar to the goals of strong-field Coulomb explosion imaging studies of 1,2-dibromoethene, *cis* and *trans* mixed samples described in Section 4.2.3, the focus in the current section is to investigate the strong-field laser ionization of *cis* and *trans* 1,2-dichloroethene, specifically, to test the feasibility of Coulomb explosion imaging method to identify *cis* and *trans* samples after valence ionization with strong femtosecond laser pulses. This experiment was also conducted using COLTRIMS apparatus. In previous measurements, Yatsuhashi *et al* [109] reported the strikingly different Coulomb explosion behavior for *cis* and *trans* 1,2-dichloroethene using 40 fs laser pulses with 800 nm wavelength. The authors used time-of-flight mass spectrometer to measure individual ion yields at different laser polarization angle and found out a drastic difference between angular distributions of H^+, Cl^+, C^+ in *cis* and *trans* samples. Another detailed study [121] of the dissociative photoionization of cis/trans 1,2-$C_2H_2Cl_2$ and 1,1-$C_2H_2Cl_2$ using VUV synchrotron radiation measured the ion yield dependence on incident VUV photon energy. The ion yield scan of the dichlorothene isomers combined with ab initio calculations provides rich information for the valence ionization dynamics of the molecule.

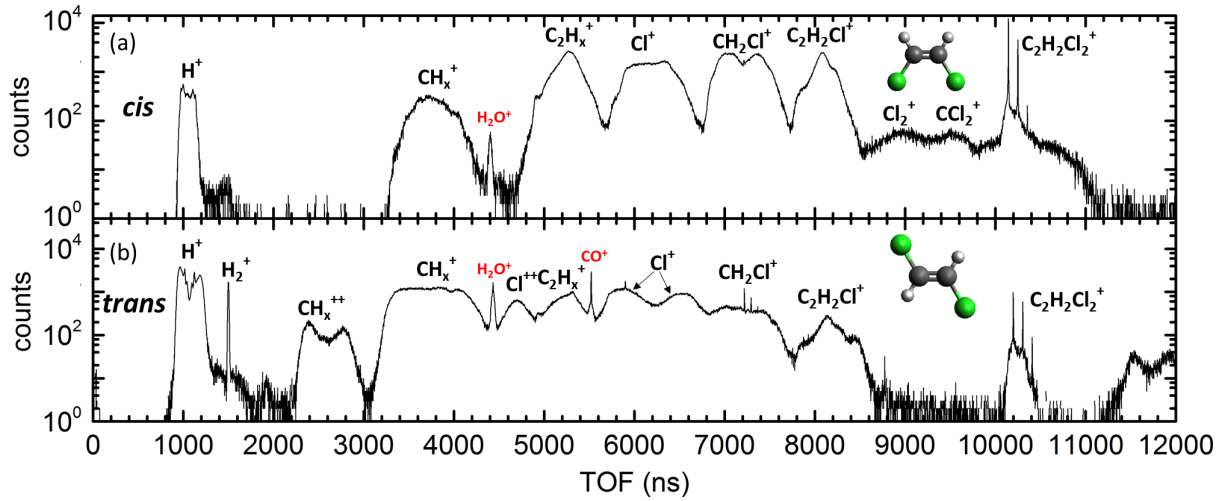

Figure 4.24: Time-of-flight mass spectrum for *cis* and *trans* 1,2-$C_2H_2Cl_2$ isomers after ionization with 25 fs laser pulses at 800 nm with laser intensities at $\sim 1\times10^{14}$W/cm^2 for measurement in (a) and $\sim 5\times10^{14}$W/cm^2 for measurement in (b).

In this work, ion momentum imaging technique is applied to study the strong-field fragmentation dynamics of 1,2-dichlorothene isomers, specifically to identify isomer structures with Coulomb explosion imaging. Fig. 4.24 (a,b) show the ion time-of-flight mass spectra of *cis* and *trans* 1,2-$C_2H_2Cl_2$ isomers after ionization with 25 fs transform limited laser pulses with 10kHz repetition rate. The laser intensities are *cis*: (a) $\sim 1\times10^{14}$W/cm^2; *trans*: (b) $\sim 5\times10^{14}$W/cm^2. The reason for the choice of different intensities for two isomers is merely due to the selection of available data sets with the highest statistics for analysis. From the TOF spectrum, one can see that the Cl_2^+ and CCl_2^+ ions that are generated through a bond-recombination reaction in which a new Cl-Cl bond forms after the laser molecule interaction is only present in *cis* isomers. Similar to the previous sections, correlation angle θ between momentum vectors of two Cl^+ ions are given in (a,b) of Fig. 4.25. It is evident from the figure that the angular peaks for both *cis* and *trans* isomers are similar to the results from X-ray synchrotron measurements described in Section 4.3.1. However the width of the angular distribution is narrower when compared to the synchrotron measurement shown in 4.19. This can be caused by two reasons, the first one is the possibility of the bond-stretching and bending modes of the molecule are different in two processes and strong-field ionization of the molecule result in less spread in angular distribution. The second reason is the poorer ion momentum resolution of the $C_2H_2Cl_2$ synchrotron data as compared to the strong-field measurement as well as synchrotron measurements of $C_2H_2Br_2$. The relatively poor resolution is due to the need to focus high energy Auger-electrons produced by photoionization of Cl($2p$) and thus applying high focusing electric field for electrons and ions. The arrows representing the Coulomb explosion model simulation closely match the experimental values. It is worthwhile to note that in Fig. 4.25 (a) there is a small peak at $\cos\theta = -1$. There can be two possible reasons for a peak at $\cos\theta = -1$, one could be due to the impurity of the *cis* chemical sample (Sigma Adrich *cis* 1,2-$C_2H_2Cl_2$: 96%) and contamination of small amount of *trans* isomers in the chemical sample and the second reason can be *cis* to *trans* isomerization process that lead to the geometric change in molecular structure. In order to see the relative momentum distribution among ions, Newton diagrams for both isomers are presented in Fig. 4.26. The cartoons that represent geometries of *cis* and *trans* isomers

are embedded in Newton diagrams to help visualize the fragmentation pattern. The kinetic energy distribution for both *cis* and *trans* isomers are plotted in Fig. 4.27 and the Coulomb explosion simulation values are plotted in dash lines.

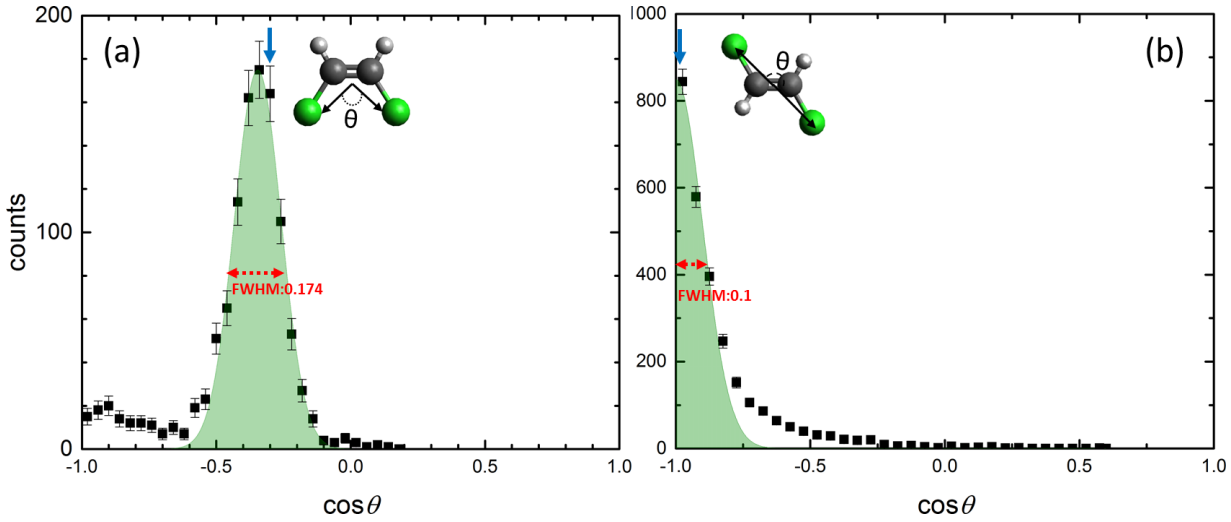

Figure 4.25: Angle between the Cl^+ ion momenta in the triple-coincidence channel $C_2H_2^+ + Cl^+ + Cl^+$ in (a) *cis* 1,2-$C_2H_2Cl_2$ and (b) *trans* 1,2-$C_2H_2Cl_2$. Fit of Gaussian (shaded areas) to the experimental data (black boxes) are given for both isomers. The angles expected from a classical Coulomb explosion model are indicated by arrows.

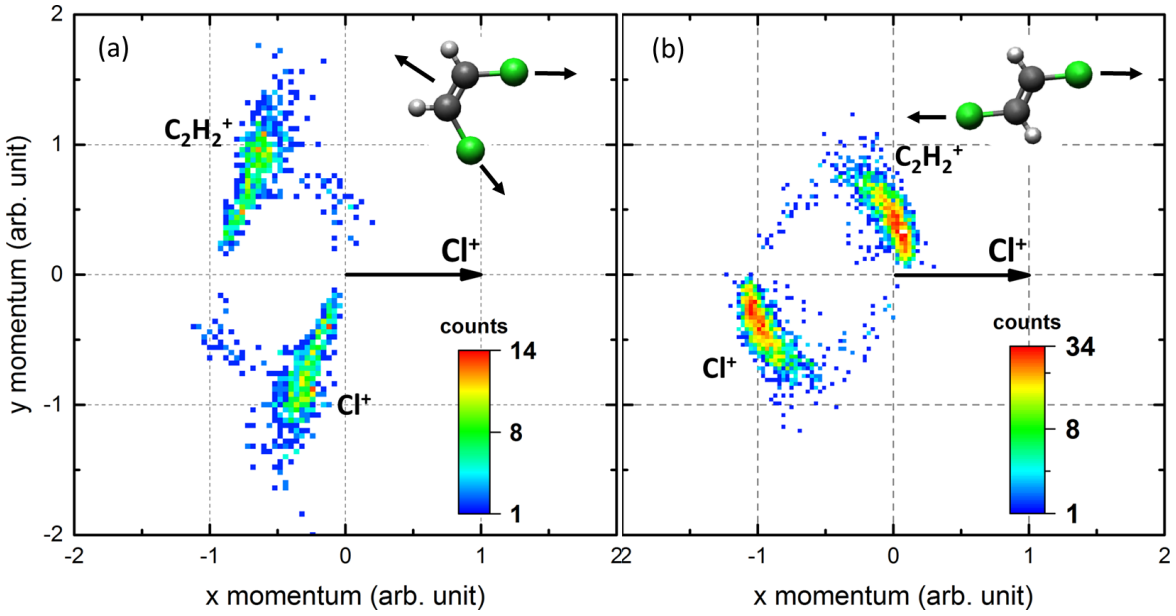

Figure 4.26: Newton plot of the $C_2H_2^+ + Cl^+ + Cl^+$ triple-coincidence channel after inner-shell photoionization of Cl $2p$ in 1,2-$C_2H_2Cl_2$ isomers. The momenta of $C_2H_2^+$ fragments (upper half) and one of the Cl^+ fragments (lower half) are shown in the frame of the momentum of the second Cl^+ fragment, which is shown as a black horizontal arrow. The momentum vectors of the $C_2H_2^+$ fragment and the first Cl^+ fragment are normalized to the length of momentum vector of the second Cl^+. The contributions corresponding to the *cis* and *trans* isomers are indicated.

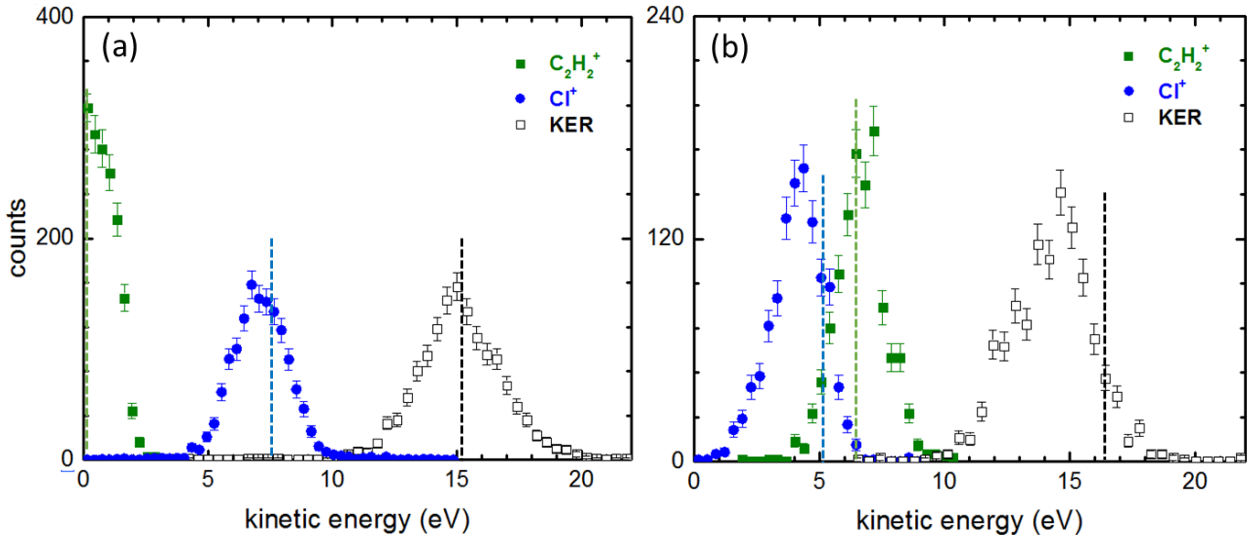

Figure 4.27: Kinetic energy distributions of the Cl^+ and $C_2H_2^+$ fragments as well as total kinetic energy release in the $C_2H_2^+ + Cl^+ + Cl^+$ triple-coincidence channel for (a) *trans* and (b) *cis* isomers. The results of the Coulomb explosion model are shown as dashed lines.

4.3.4 Conclusion

Driven by the availability of intense, short-pulse XUV- and soft X-ray sources such as free-electron lasers and high-order harmonic sources, there is a high current interest in developing schemes to directly image molecular structure during ultrafast photochemical reactions. The coincidence Coulomb explosion imaging technique is a promising candidate in this respect, and was used already in a number of time-resolved experiments studying, e.g., the isomerization between acetylene and vinylidene [100–104].

In this study, it is shown that both (single-photon) soft X-ray inner-shell photoionization and strong-field laser induced ionization can be used to distinguish geometric isomers and determine their isomer ratio. In particular, the experimental results demonstrate that the Coulomb explosion of 1,2-dibromoethene into $C_2H_2^+ + Br^+ + Br^+$ and the Coulomb explosion of 1,2-dichloroethene into $C_2H_2^+ + Cl^+ + Cl^+$ can be used as a probe for the initial geometric structure of the molecule, enabling us to experimentally distinguish the *cis* and *trans* isomers and to measure the isomer-specific ionization and fragmentation dynamics. While some isomers can be easily separated due to their different physical properties, others cannot be easily prepared as pure samples, e.g. in cases where they can interconvert between different structures at room temperature. The coincidence Coulomb explosion imaging method allows studying isomer-specific properties also in the latter case.

Furthermore, in the X-ray inner-shell photoionization studies, position spectra of overlapping photo- and Auger-electrons as well as valence-electrons emitted from the system are disentangled by selecting coincidence ions in TOF spectrum and ionic channels in PIPICO and TRIPICO spectra. Electron spectra of $C_2H_2Br_2$ isomers show that the binding energy of Br $3d$ electrons in the molecule is 79 eV, and during the inner-shell photoionization, a group of different Auger electrons of which the energy is centered around 41-eV are emitted from the system. In triple ionization channel $C_2H^+ + Br^+ + Br^+$, additional Auger-electron with < 20 eV kinetic energy is emitted. In inner-shell photoionization of $C_2H_2Cl_2$ *cis*, *trans* isomers, no significant difference in photoelectron spectra were found. The system emits 230-eV Auger-electrons after photoionization of a Cl $2p$ shell electrons. In triple ionization

of the molecule, an Auger cascade process result in the emission of one 230-eV and another low energy (10eV) Auger electrons.

Chapter 5

X-ray and Laser-Induced Fragmentation of 2,6- and 3,5-Difluoroiodobenze

5.1 Introduction

The fragmentation or *Coulomb explosion* of polyatomic molecules after VUV or X-ray photoionization [22, 23, 34, 102, 104, 122], strong-field ionization in intense laser fields [33, 100, 101, 123–125], or electron and ion impact ionization [73, 126–130] has been investigated extensively in order to understand the dynamics of the ionization and fragmentation processes as well as to study the link between the fragmentation pattern and the geometric structure of the molecules. Early experiments were mostly performed using ion time-of-flight mass spectrometry techniques such as ion-ion coincidence spectroscopy [112, 131–133]. Later, the development of ion imaging techniques [12, 18, 134] and, in particular, coincident ion momentum imaging [52–54] has significantly increased the amount of information that can be extracted from such fragmentation studies. Recently, several studies have focused on the identification of molecular isomers, i.e. molecules with the same chemical formula but different geometric structures, from the fragmentation patterns. For example, it was

demonstrated that it is possible to separate two enantiomers in a racemic mixture of small chiral molecules by measuring five-fold ion coincidences after strong-field ionization [33, 34] or beam-foil induced Coulomb explosion [108], while three-fold ion coincidences after inner-shell photoionization were used to identify the *cis* and *trans* geometric isomers of dibromoethene [35], as also discussed in Chapter 4.

In this chapter, an experimental study of the fragmentation dynamics of structural isomers, 2,6- and 3,5-difluoroiodobenzene ($C_6H_3F_2I$; DFIB;) after I ($4d$) inner-shell photoionization with X-ray synchrotron beams using coincident electron and ion momentum imaging in a double-sided VMI system is reported. As part of the study, ultrafast strong-field laser ionization of both isomers is studied using a COLTRIMS setup. The study aims at extending the coincidence momentum imaging investigations to larger and more complex molecules and, in particular, at determining if, for such complex molecules, (i) if it is still possible to distinguish the geometric structures of different isomers via coincident momentum imaging, and (ii) if the fragmentation can still be described by a simple, classical Coulomb explosion model. The choice of the particular molecules was motivated by previous work on laser alignment of difluoroiodobenzene molecules [135–139], where both strong-field and X-ray photon induced Coulomb explosion were used to diagnose the degree of one- and three-dimensional molecular alignment. Since those measurements showed very distinct angular distributions of the F^+ fragments, it is interesting to investigate if a coincident momentum imaging experiment that can determine the angle between the I^+ and F^+ fragment ion momenta would be able to separate the different isomers in a similar way as our previous study on dibromoethene reported in Chapter 4.

The two isomers indeed show characteristically different ion momentum correlations and fragmentation patterns that can be linked to the geometric structure of the molecules and that can still be described adequately in terms of a classical Coulomb explosion. However, the comparison of the experimental data with the Coulomb explosion simulations also reveals some distinct differences that may be the result of ultrafast charge separation across the benzene ring as well as of a sequential breakup of the triply charged cation on a time scale of several hundred femtoseconds, which seems to occur only in the 2,6-DFIB isomer. Other

many-body fragmentation channels show clear evidence of sequential fragmentation on a time scale larger than the rotation period of the fragments.

5.2 Soft X-ray induced fragmentation of 2,6- and 3,5-DFIB

As described in Chapter 1, the emission of an inner-shell photoelectron is often followed by the emission of one or multiple Auger electrons and the subsequent breaking of chemical bonds, which causes the molecule to fragment. The positively charged molecule fragments into ionic and/or neutral species. The process of fragmentation after photoionization can be simultaneous (concerted), where the molecule breaks simultaneously into multiple fragments, or sequential, where for example, one chemical bond of the molecule breaks first, generating two fragments, and after some delay, the second step fragmentation happens where another chemical bond breaks, causing the molecule to break into even smaller ions or neutrals [73, 140].

Previously, X-ray photoelectron spectroscopic studies of gas-phase iodine containing molecules are widely investigated. Lindle *et al* [141] and Holland *et al* [142] measured the photoemission of the $4d$ and $4p$ subshells in methyliodine and Cutler *et al* [143] measured I ($4d$) photoelectron spectra for iodine containing molecules. Recently, Mertens *et al* [144] studied the fragmentation patterns of CH_2I_2 and CH_3I molecules following a multiphoton excitation in the vicinity of $4d$ giant resonance regime. In this study, $4d$ inner-shell electrons of iodine atom in DFIB molecule is targeted with 107 eV photons provided by the ALS synchrotron beam in order to photoionize and fragment the molecule. Photoionization will result in breaking the DFIB molecule into two, three or multiple ionic and neutral fragments. In this experimental work, only the ionic fragments are detected with the double-sided VMI spectrometer that is described in Chapter 3.

Fig. 5.1 (a) shows the ion TOF mass spectra of 2,6- and 3,5-DFIB, and the normalized difference of TOF spectra recorded at 107 eV photon energy is shown in (b). In order to

see the spread in position of each ion on the detector, the horizontal position of ion hits on the detector is plotted as a function of TOF, Fig. 5.2. Both $C_6H_3F_2I^+$ and $C_6H_3F_2I^{++}$ ions appear as small hot spots at the center of the detector due to the negligible recoil momentum gained by ejection of one and two electrons.

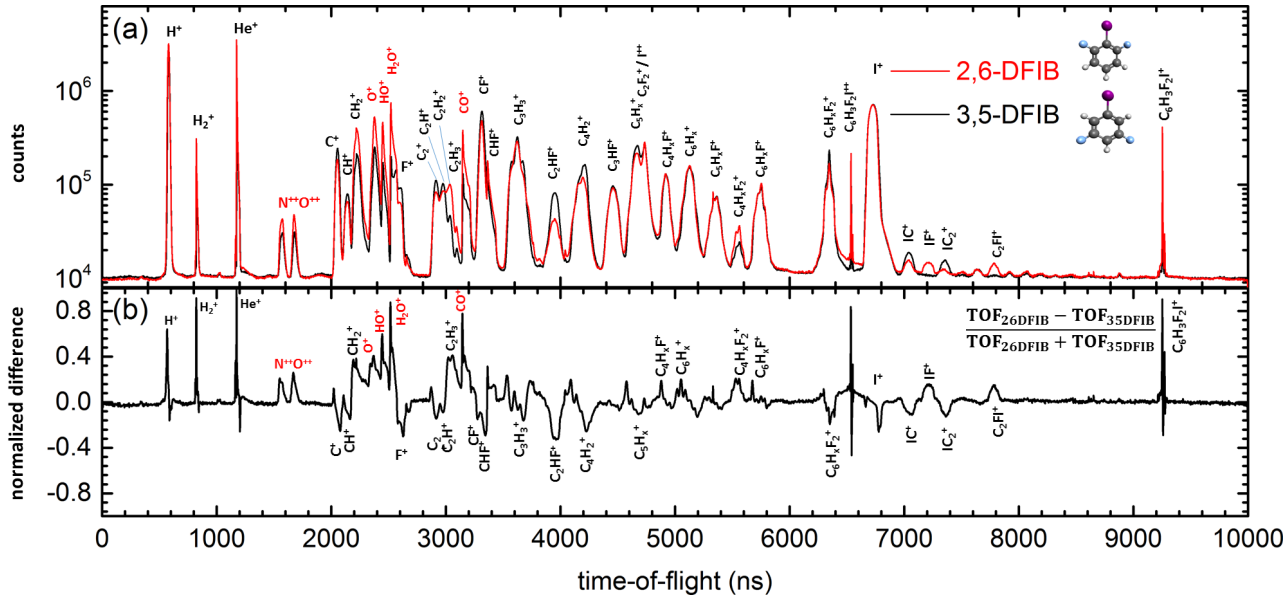

Figure 5.1: (a) Ion time-of-flight mass spectra generated by photoionization of 2,6- and 3,5-DFIB at 107 eV photon energy. Peaks from residual gas are labeled in red. (b) Normalized difference between the two ion mass spectra.

With 107 eV photon energy, which is approximately 50 eV above the I ($4d$) ionization threshold but below the iodine $4p$ ionization threshold in DFIB, a single photon can ionize any of the molecular valence and inner-valence shells as well as the iodine $4d$ shell. While valence ionization predominantly leads to singly charged final states that either remain bound or fragment into one ionic and one or several neutral fragments, emission of an I ($4d$) inner-shell photoelectron is typically followed by rapid Auger decay processes that will put the molecule into doubly or triply charged cationic states. As a reference, the typical Auger lifetimes of a $4d$-ionized Xe atom, which is electronically similar to iodine, are 6 fs for the first Auger decay and 23 fs for the second Auger step [145]. It is reasonable to expect these values to be a good order of magnitude estimate of the lifetimes of the dominant atomic-like Auger channels in DFIB molecule.

After Auger decay processes, the di-cationic and tri-cationic states in DFIB generally

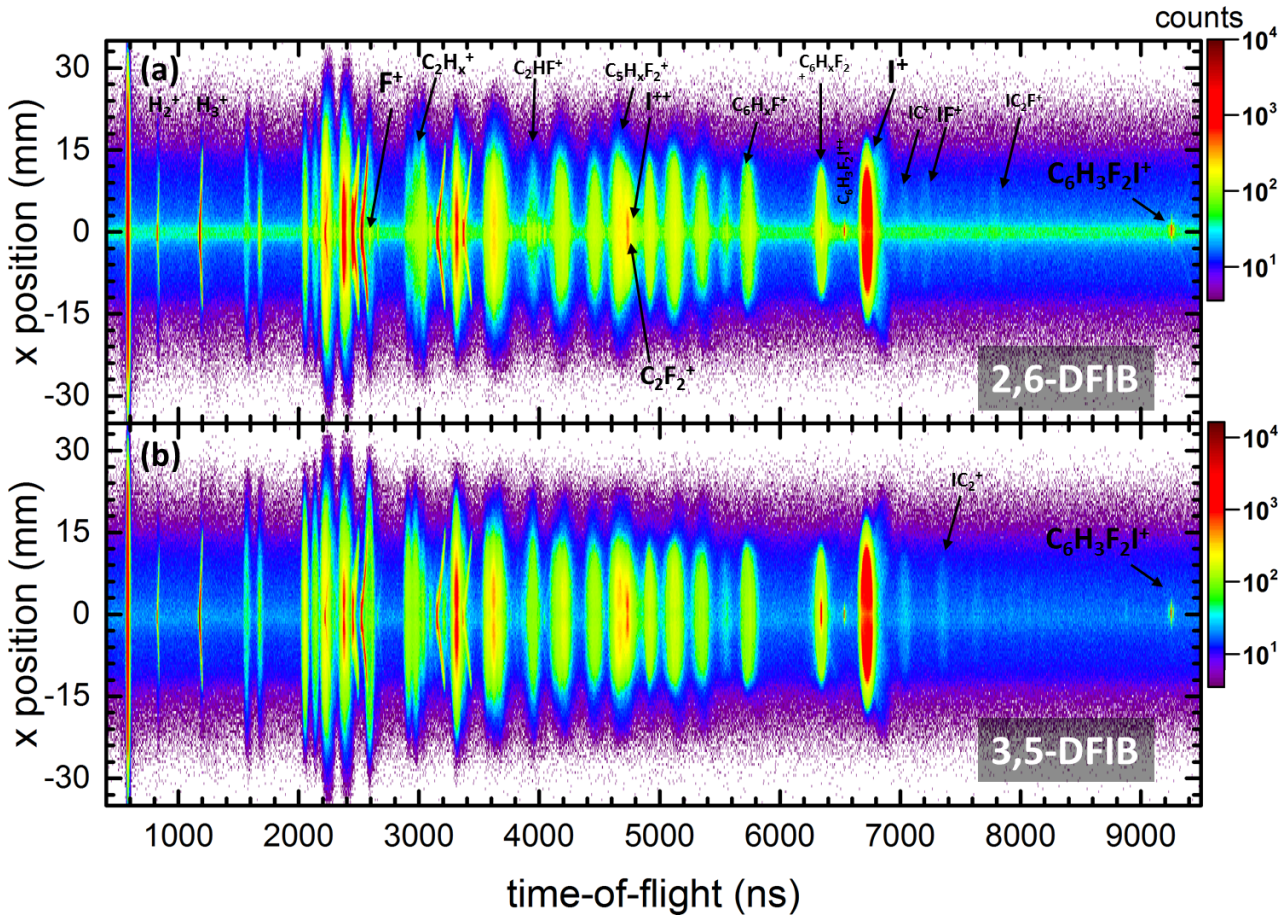

Figure 5.2: Time-of-flight vs. the position distribution of all ions after photoionization of (a) 2,6- and (b) 3,5-DFIB at 107 eV photon energy.

fragment into two or three charged fragments that are emitted with relatively high kinetic energies due to the Coulomb repulsion of the positive charges (hence, this process is referred to as a *Coulomb explosion*). Additionally, further neutral fragments may be produced, which are not detected in this experiment. The coincidence fragmentation channels can be represented in a PIPICO map, as shown in Fig. 5.3, where the ion-ion coincidence channel yields are shown as a function of the time of flight of the first and second detected ions. The PIPICO maps for both isomers show that the molecule can break up in a large number of different channels, producing almost every charged fragment that is stoichiometrically possible. In particular, narrow diagonal peaks in the PIPICO map correspond to two-body fragmentation channel or channels where the remaining fragment(s) carry negligible momentum, while broader features correspond to breakup into three or more heavy and

energetic fragments. If the molecules breaks up into three ionic fragments, one can construct a PIPIPICO map, as shown in Fig. 5.4, where the ion yield is plotted as a function of the time of flight of one of the fragments and the *sum* of the time of flight of the other two fragments that were detected in coincidence. Again, narrow peaks correspond to events, where the momenta of the three ionic fragments add to zero, while broader features represent the molecule break up into more than three species or one of the constituent in the breakup channel is neutral.

While the ion TOF mass spectra and PIPICO/PIPIPICO maps of 2,6- and 3,5-DFIB look rather similar at first sight, some differences, especially in the yield of F^+, $C_2H_2^+$ and fluorine containing fragments such as C_2HF^+, as well as of heavy fluorine and iodine containing fragments, such as IF^+ and C_2FI^+ are visible upon closer inspection. This can also be seen in Fig. 5.1 (b), where the normalized difference between the ion time-of-flight mass spectra of 2,6- and 3,5-DFIB is shown. The generation of F^+ ions from both 2,6 and 3,5-DFIB is very rare due to the large electronegativity of fluorine, as can be seen from Fig. 5.1 (a), but it is higher in 3,5-DFIB than in 2,6-DFIB. Many of the other differences in the fragment ion yield can be explained when considering the geometry of the molecule, which favors certain fragments in one isomer as compared to the other. This is particularly evident for the C_2FI^+ fragment, which is only formed from 2,6-DFIB, since a C_2FI group does not exist in the 3,5-DFIB molecule. In this context, it is interesting to point out the IF^+ fragment, which is only produced from 2,6-DFIB. Formation of this fragment requires the breaking of two bonds, C−F and C−I, and the formation of a new bond between the iodine and fluorine atoms. As one may intuitively expect, this bond formation only occurs in 2,6-DFIB, where iodine and fluorine are bound to neighboring carbons. The following will focus on the discussion of the kinetic energies and momentum correlations observed in particular coincidence channels, and on the conclusions about the fragmentation dynamics that can be drawn from this information.

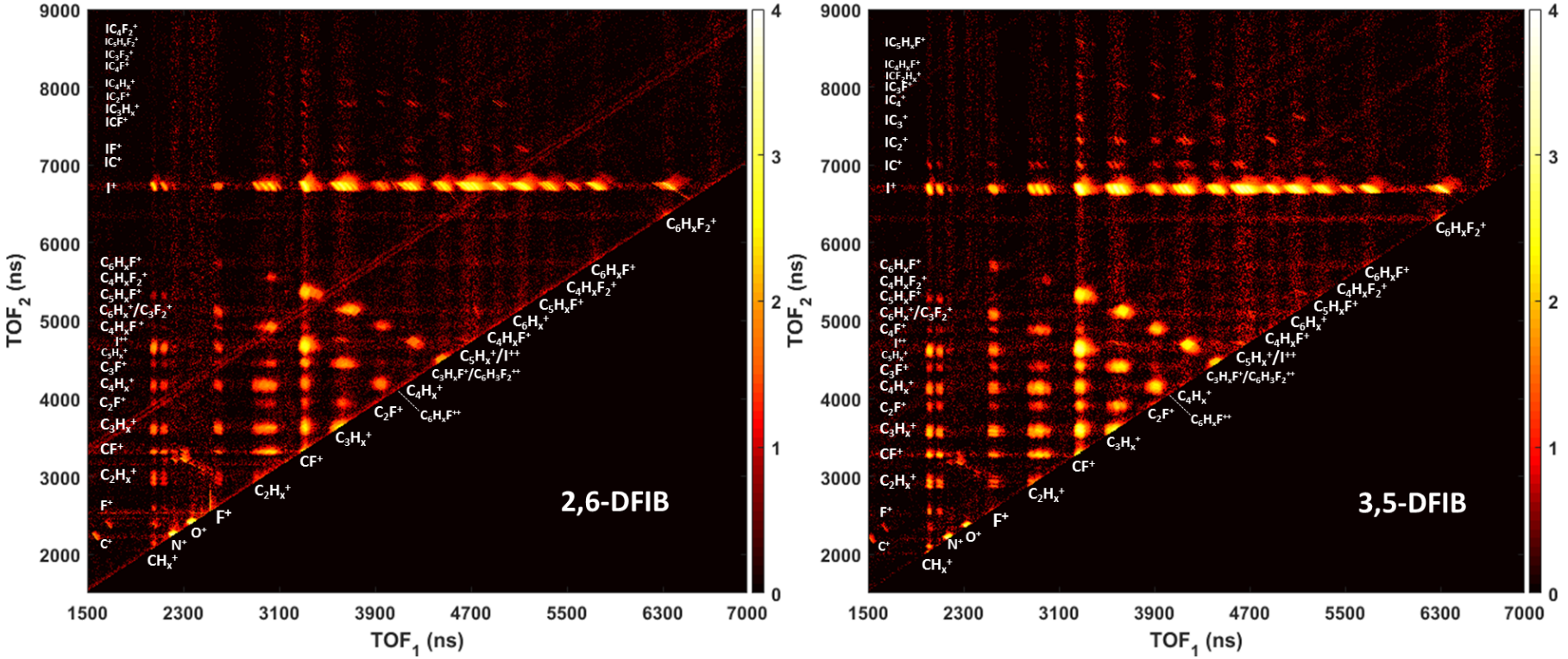

Figure 5.3: PIPICO maps for 2,6- and 3,5-DFIB at 107eV photon energy.

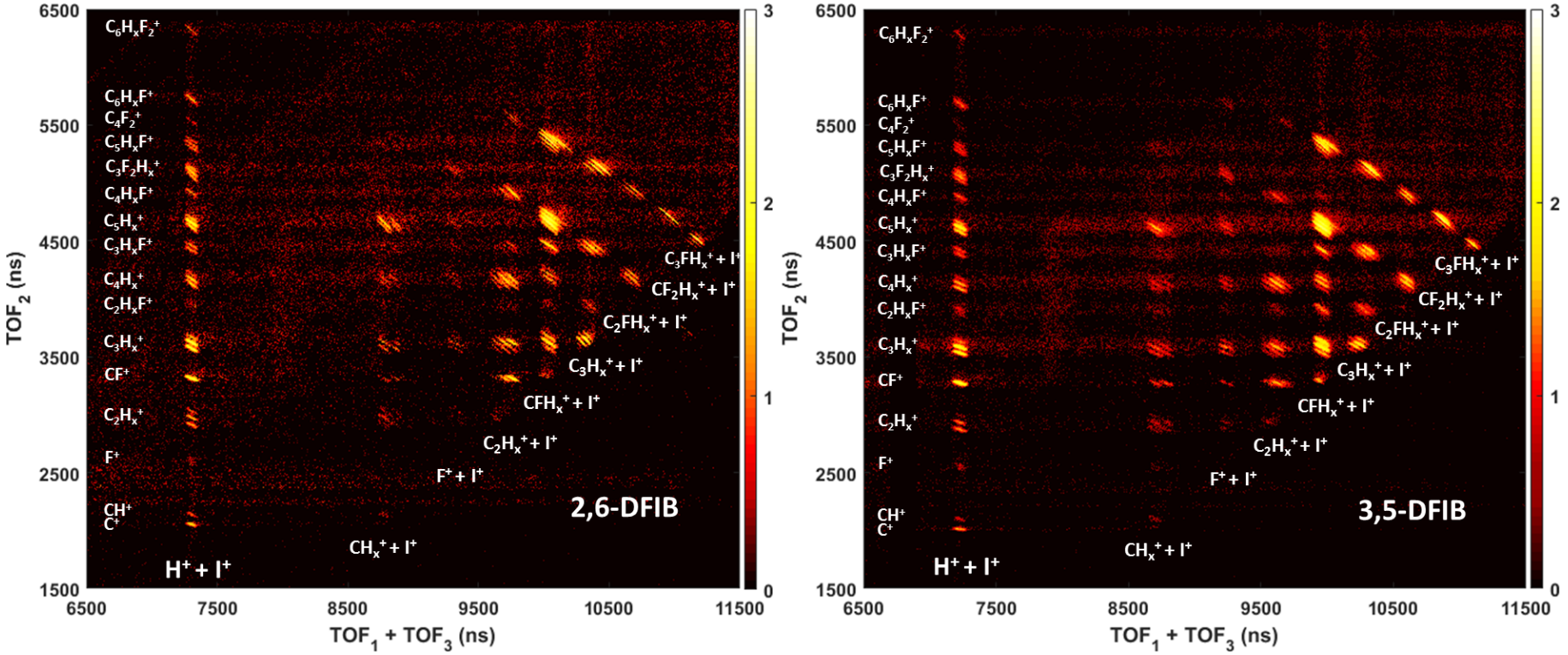

Figure 5.4: Photoion-photoion-photoion coincidence (PIPIPICO) plot for 2,6- and 3,5-DFIB at 107eV photon energy.

5.2.1 $C_6H_3F_2^+ + I^+$ and $C_6H_3F_2^{++} + I^+$ two-body fragmentation channels

As briefly mentioned in Section 5.2, the conceptually easiest fragmentation channels are "complete" two-body fragmentation, where the molecule breaks into two charged fragments, which, when combined, contain all atoms that were in the original molecule. In these cases, the two fragments are emitted strictly back-to-back due to momentum conservation, and they share all of the available Coulomb energy. The strongest two-body fragmentation channel of this type is the $C_6H_3F_2^+ + I^+$ channel, which is predominantly produced by I ($4d$) inner-shell ionization followed by ultrafast Auger decay, as proven by the electron spectrum measured in coincidence with this fragmentation channel, which is shown in Fig. 5.5 (c). The I ($4d$) photoelectrons have a kinetic energy of 50 eV, while a distinct Auger peak appears at 29 eV, which is similar to the energy of the most energetic Auger lines observed after I ($4d$) ionization of CH_3I [141, 142]. Note that there is also a smaller peak between 70 and 80 eV kinetic energy that is attributed to valence double ionization process, which also produces a doubly charged final state that can fragment into $C_6H_3F_2^+ + I^+$.

The electron spectrum for the triply charged $C_6H_3F_2^{++}+I^+$ final state shown in Fig. 5.5 (d) also contains the I ($4d$) photoelectron peak, but instead of the Auger peak at 29 eV, the spectrum contains a broader Auger feature with a maximum slightly above 10 eV, which is reminiscent of the lower-energetic Auger group observed in CH_3I [141]. Although the electron spectra are only shown for one photon energy, we have recorded the spectra at other photon energies to confirm that the photoelectrons indeed change their kinetic energy, while the Auger electrons remain at a fixed kinetic energy, as expected.

The kinetic energy distributions of the $C_6H_3F_2^+$ and the I^+ fragments in the $C_6H_3F_2^+ + I^+$ coincidence channel as well as the total kinetic energy release (KER) for 2,6-DFIB and 3,5-DFIB are shown in Fig. 5.6 (a,b), respectively. In both isomers, the KER is peaked at $\approx$ 3.1 eV, with each fragment carrying about half of the energy since they have almost the same mass (the peaks of the experimental kinetic energy distributions are at 1.65 eV for $C_6H_3F_2^+$ and 1.45 eV for I^+). Assuming that the two charged fragments can be approximated as

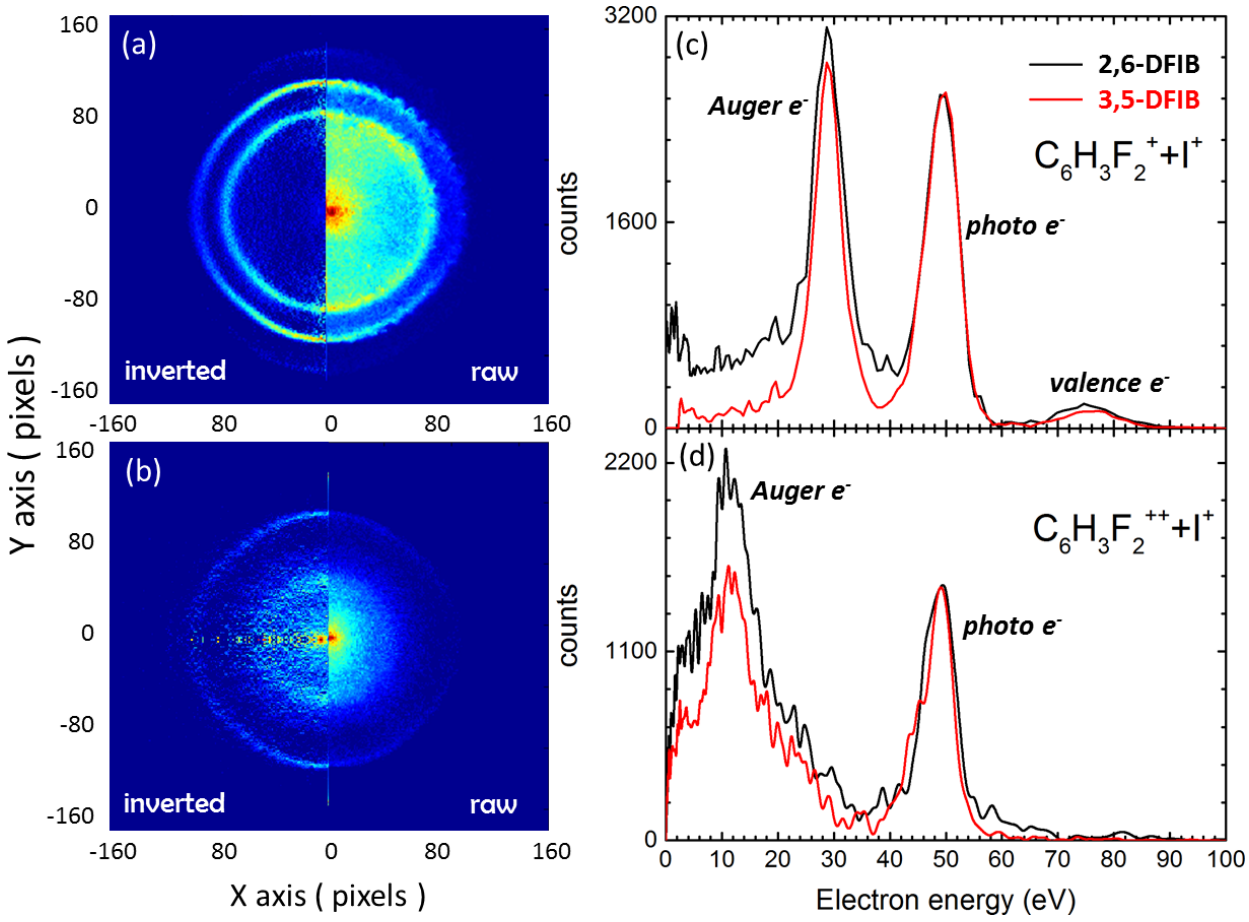

Figure 5.5: Electron image and kinetic energy spectrum measured in coincidence with the $C_6H_3F_2^+$+I^+ (a,c) and $C_6H_3F_2^{++}$+I^+ (b,d) channels in 2,6-DFIB; (a,b): Raw (right) and inverted (left) electron image. (c,d) Electron kinetic energy spectrum.

point charges and that the molecule breaks up on a purely Coulombic potential energy curve after both charges are created, Coulomb explosion energies can be calculated for different locations of the two charges, as described in Cahpter 3. The dashed lines in Fig. 5.6 show the value of this Coulomb energy if one of the two charges is localized on the iodine fragment, while the other one is located at three different positions on the phenyl ring: (A) on the carbon atom furthest away to the iodine (corresponding to a distance between the charges of 4.91 Å), (B) at the center of the ring (corresponding to a distance of 3.52 Å), and (C) on the carbon atom closest to the iodine (corresponding to a distance of 2.12 Å). Case (A) agrees almost perfectly with the maximum of the measured KER distribution, case (B) lies in the high energy "shoulder" of the KER distribution, while case (C) clearly overestimates

the energy significantly. From this, we conclude that either (i) the fragmentation does not occur along a Coulombic potential curve and a significant fraction of the Coulomb energy is transformed into internal energy, e.g. in electronic, vibrational or rotational excitations; (ii) the C−I bond has stretched significantly before the second charge was created; or (iii) the second charge has localized at the far end of the phenyl ring before the Coulomb explosion occured.

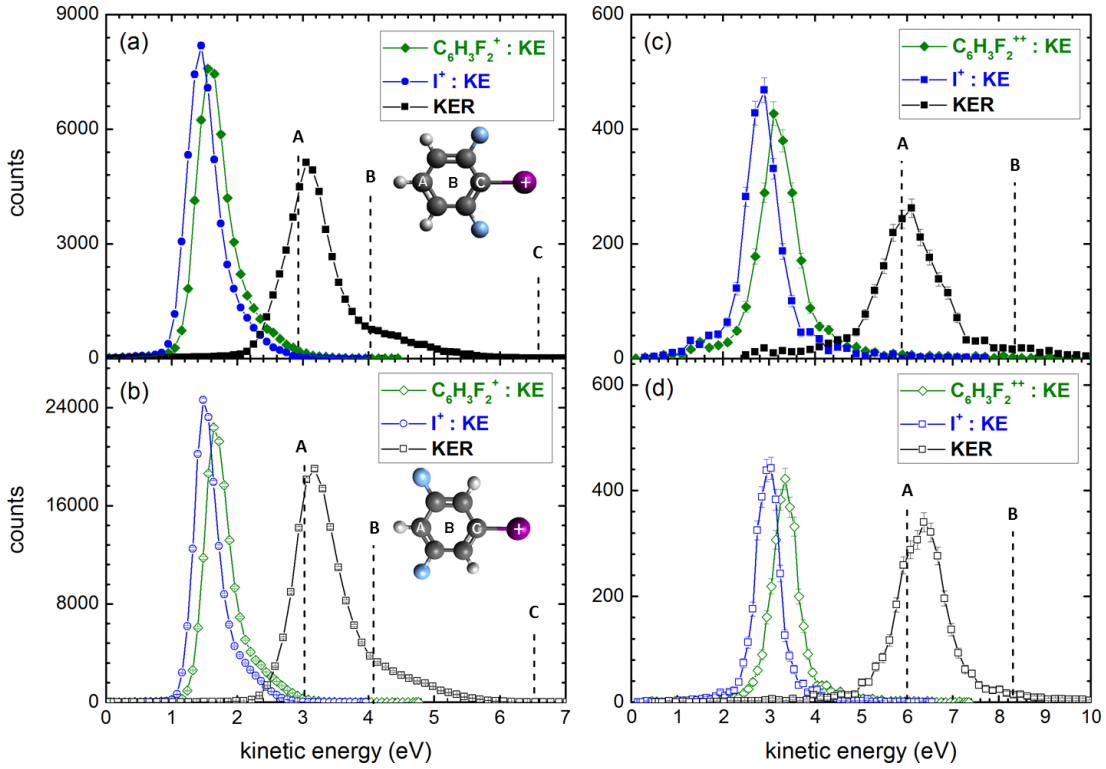

Figure 5.6: Kinetic energy release (black squares) of the $C_6H_3F_2^+$+I^+ two-body fragmentation channel for 2,6-DFIB (top) and 3,5-DFIB (bottom) along with the kinetic energies of the $C_6H_3F_2^+$ (red) and I^+ (blue) fragments. The simulated fragment ion kinetic energies in case A are 1.38 eV for I^+ and 1.54 eV for $C_6H_3F_2^+$.

Since one cannot distinguish between these possibilities without detailed quantum chemistry calculations, another two-body fragmentation channel can be used to provide further information. Fig. 5.6 (c,d) show the measured fragment ion kinetic energy distributions and KER for the $C_6H_3F_2^{++}$ + I^+ channel in both 2,6- and 3,5-DFIB, compared to the calculated Coulomb energies for two of the three scenarios described above (the dashed line for scenario c is outside of the range of the plot and is therefore not shown). Again, the situation where

both charges on the $C_6H_3F_2{}^{++}$ fragment are located at the far end of the phenyl ring gives almost perfect agreement with the experimental data. Since it is unlikely that the amount of internal energy in the molecular fragment, which would have to be 6 eV to explain the difference, would have increased so drastically in this case as compared to the doubly charged fragmentation channel, so it can be concluded that ultrafast charge localization is the most likely scenario: After photoionization removes an I ($4d$) electron, the inner-shell vacancy in the iodine atom is filled by a valence or inner-valence electron via an Auger process that ejects a second and sometimes a third valence electron. This leaves the system with two or three holes in the valence shell. Charge migration along the phenyl ring, driven by the Coulomb repulsion between the holes, could lead to a situation where the holes localize at opposite ends of the molecule before the molecule fragments. Similar ultrafast charge migration after inner-shell ionization of a benzene compound was recently suggest in a theoretical study of nitrosobenzene molecules [146]. In that study, the authors investigated charge migration in the valence shell that is driven solely by electron correlation and electron relaxation. The phenomenon is termed charge migration to underline the difference from standard electron and hole transfer, which is driven by nuclear motion [147, 148] and is consequently much slower, in general. The calculations show that in core-ionized nitrosobenzene, charge migration occurs within slightly less than 1 femtosecond and, in particular, even faster than the Auger decay. In the present experimental data, there is no direct evidence for such a charge migration effect in DFIB nor can one draw any conclusions about the quantum mechanical origin of the possible charge migration or about its time scale, but it has to be noted that such effect could explain the experimentally observed fragment energies.

The differences in the yield of F^+ ions and fluorine-containing fragments seen in Fig. 5.1 (a) and the ratio between F^+ and I^+ fragments presented in Fig. 5.7 may further support this hypothesis: If charge migration leads to a positive charge at the end of the ring opposite to the iodine, i.e. close to the fluorine atoms in 3,5-DFIB, a lack of electrons in the vicinity of the fluorine might make it more likely to produce F^+ ions and fluorine containing fragments than in the case of 2,6-DFIB, where the positive charge on the benzene ring is further away from the fluorine atoms.

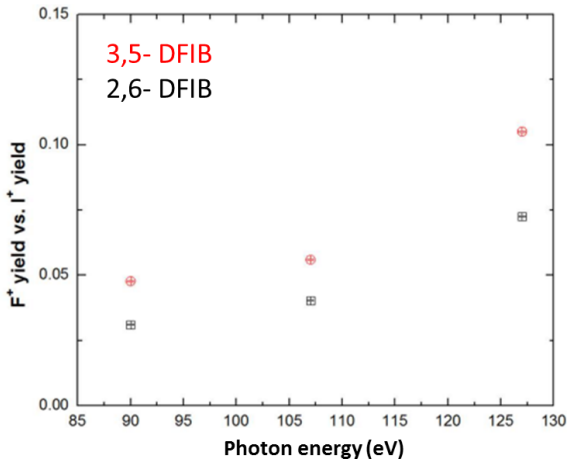

Figure 5.7: Ratio of yields for F^+ and I^+ in 3,5-DFIB (red), 2,6-DFIB(black).

5.2.2 Sequential breaking of C-I and C-C bonds

While the majority of DFIB molecules are in a doubly ionized final state after I ($4d$) inner-shell ionization and subsequent Auger decay, a significant fraction of the molecules end up in a triply charged final state, as demonstrated by Fig. 5.4. This can happen via direct double ionization, most likely via a *shake-off* process [142], in the first ionization step followed by a single Auger process, or via emission of a single photoelectron followed by emission of two Auger electrons, either simultaneously (*double-Auger*) or sequentially (*Auger cascade*) [42, 149]. For the triply charged $C_6H_3F_2{}^{++}$+I^+ final state, the electron spectrum in Fig. 5.5 (d) clearly shows that this state is reached via single photoelectron emission in the first step, since direct double photoionization would not yield a well-defined photoline at 50 eV kinetic energy. This first step is followed, most likely, by a sequential Auger cascade, since "double-Auger" emission would also produce a more continuous electron kinetic energy distribution than what is observed here [42]. The triply charged DFIB parent ion is not stable, thus it decays after the Auger processes into two or three charged fragments and, possibly, further neutral fragments. As the triple-ion coincidence maps in Fig. 5.3 show, the strongest contributions among the channels with three ionic fragments are those fragmentation channels where an I^+ ion and two fragments from the benzene ring are produced. Here, three triple ion coincidence channels, namely CF^++$C_5H_3F^+$+I^+, C_2HF^++C_4HF^++I^+, C_3HF^++$C_3H_2F^+$+I^+ are discussed.

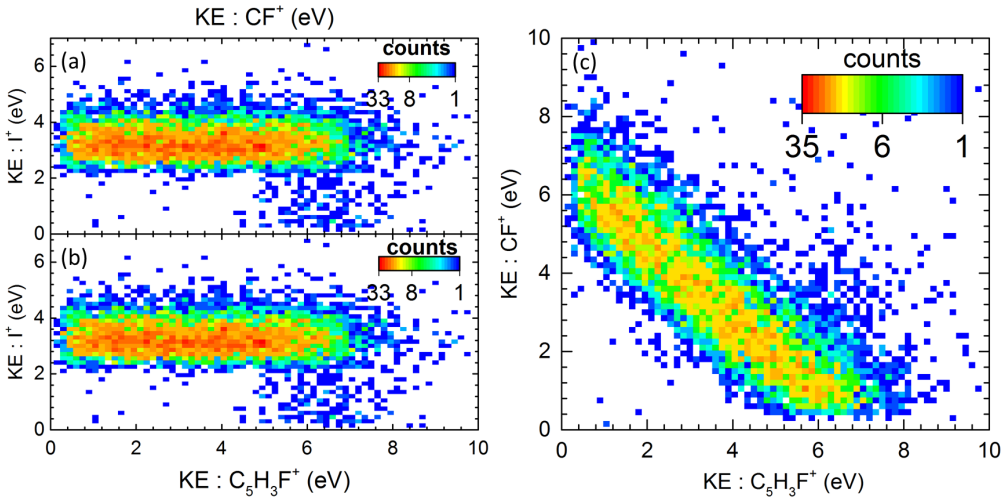

Figure 5.8: (a,b) Kinetic energy distribution of CF^+ and $C_5H_3F^+$ ions in CF^++$C_5H_3F^+$+I^+ channel with respect to I^+ kinetic energy. (c) Kinetic energy distribution of CF^+ vs. $C_5H_3F^+$ ions in 2,6-DFIB measurement.

After obtaining the three dimensional momenta of all ionic fragments in these coincidence channels, individual ion kinetic energies can be calculated. The distribution of an ion's kinetic energy with respect to the other ions in the CF^++$C_5H_3F^+$+I^+ channel from 2,6-DFIB measurement is shown in Fig. 5.8. The similar energy spectra for the other two coincidence channels are not shown due to the similarity of such energy distribution in all three channels. The kinetic energies of I^+ vs. CF^+ and $C_5H_3F^+$ as well as CF^+ vs $C_5H_3F^+$ fragments in Fig. 5.8 (a,b,c) as well as individual kinetic energies in Fig. 5.9 show that *i*) I^+ kinetic energy distribution is very narrow (FWHM: 1.25eV) and *ii*) its value stays as constant with respect to the broad kinetic energy distributions of both CF^+ and $C_5H_3F^+$. *iii*) In Fig. 5.8 (c), the diagonal distribution of two ion energies indicate that the sum of those kinetic energies, namely CF^+ and $C_5H_3F^+$ appears to be constant. For all three fragmentation channels, the kinetic energy distributions are similar in both isomers, 2,6- and 3,5-DFIB, see Fig. 5.9. Furthermore, it is interesting to note that the narrow kinetic energy distributions of the iodine ions are almost identical to those in $C_6H_3F_2{}^{++}$+I^+ two-body Coulomb explosion channel.

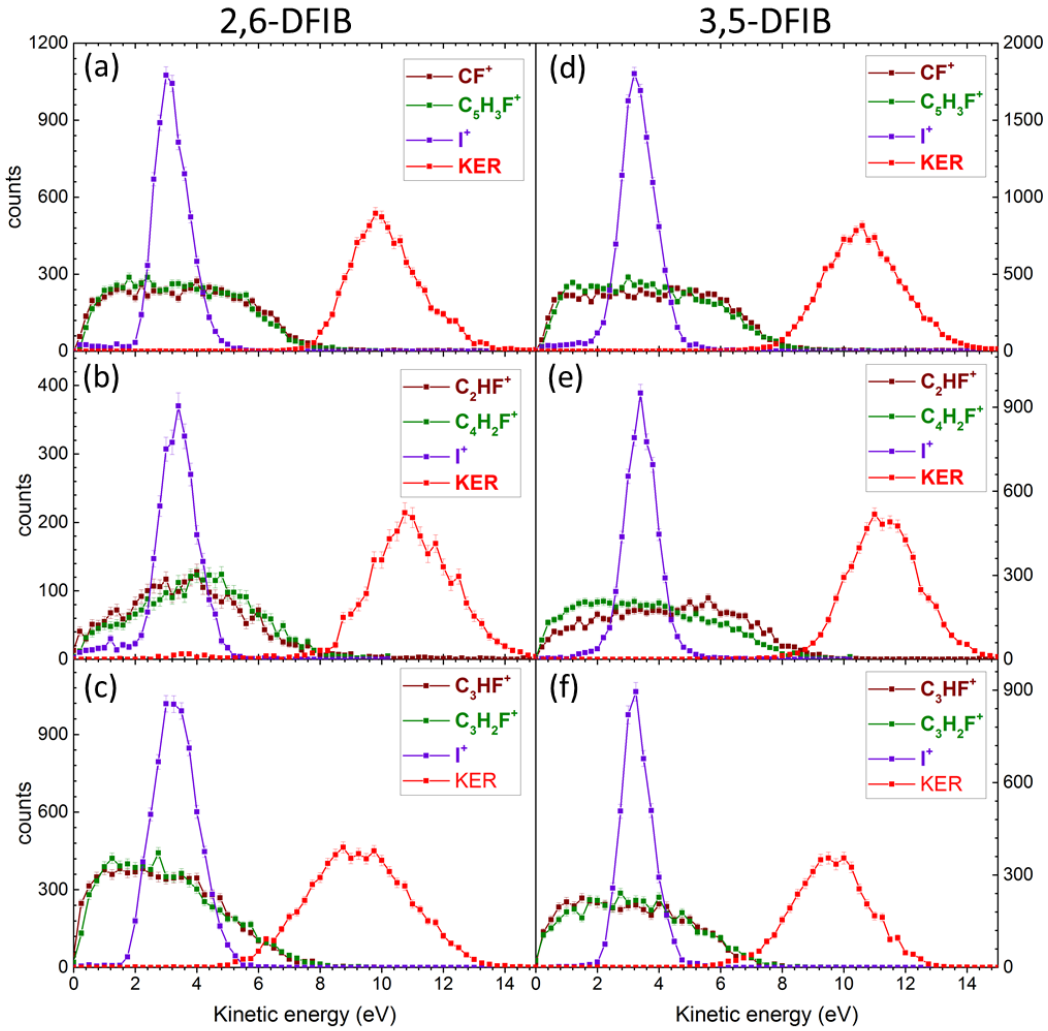

Figure 5.9: Kinetic energies of individual ionic fragments and total kinetic energy release from channels, respectively, $CF^+ + C_5H_3F^+ + I^+$, $C_2HF^+ + C_4HF^+ + I^+$, $C_3HF^+ + C_3H_2F^+ + I^+$; a,b,c) 2,6-DFIB; d,e,f) 3,5-DFIB;

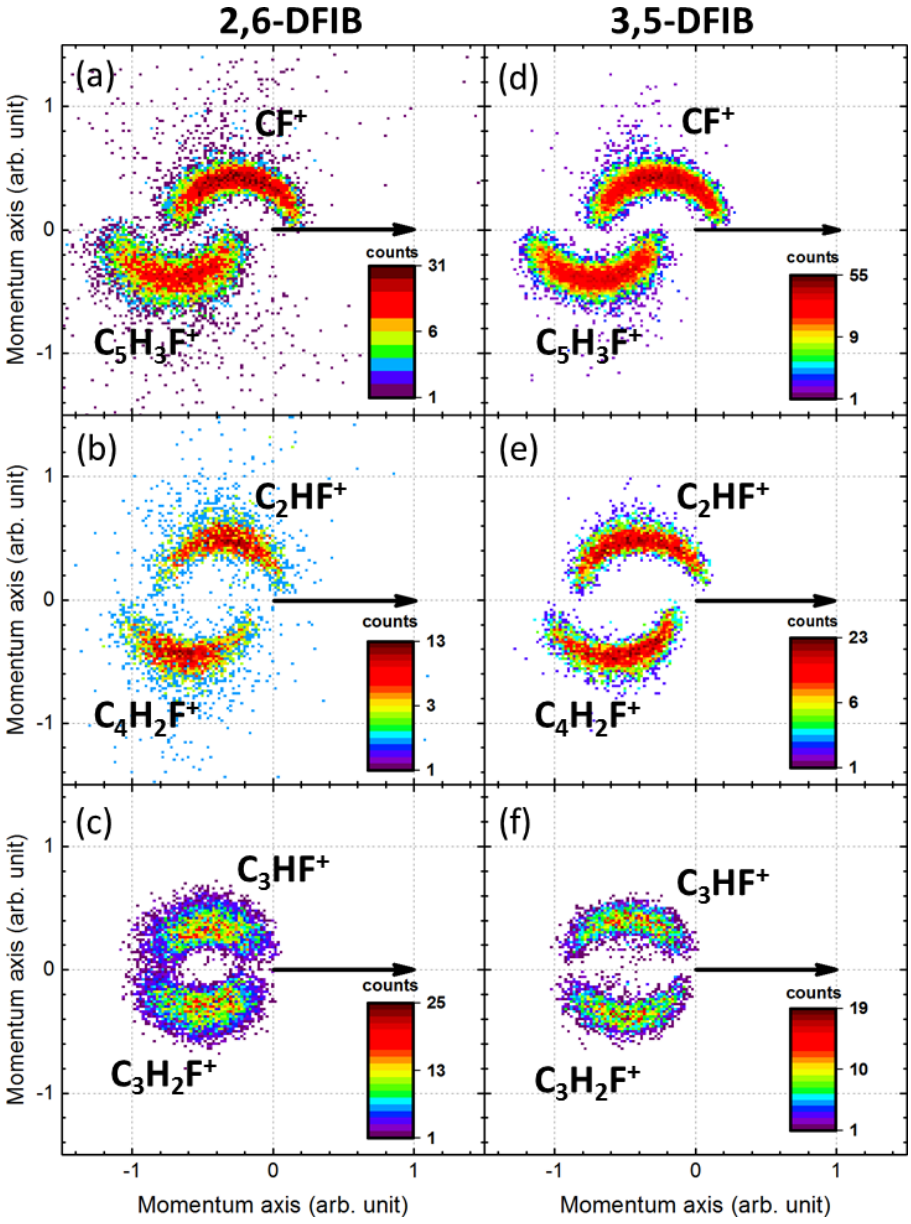

Figure 5.10: Newton diagrams of three coincidence channels where I^+ is a unit vector (black arrow) and two other ionic fragment momenta are plotted respectively on upper and lower panels;, respectively for channels, CF^++$C_5H_3F^+$+I^+, C_2HF^++C_4HF^++I^+, C_3HF^++$C_3H_2F^+$+I^+; a,b,c) 2,6-DFIB; d,e,f) 3,5-DFIB.

In order to gain further insight into the fragmentation mechanism leading to these three-body channels, Newton plots are shown in Fig. 5.10, where the momenta of the two carbon-containing fragments are plotted with respect to the momentum of the iodine ion, which is represented by a black arrow. The curved, semi-circular structures that appear in these Newton plots are a strong indication for a sequential fragmentation [73, 114, 128, 130, 150–

153], with a delay between the breaking of the C−I bond and the subsequent breaking of the C−C bonds longer than the rotational period of the $C_6H_3F_2{}^{++}$ fragment, which is on the order of 100 *ps* in the rotational ground state. Thus, a hypothesize about the process leading to these three-body channels proceeds as follows: Inner-shell photoionization followed by emission of two Auger electrons leave the molecule in a triply charged state, which undergoes Coulomb explosion into $C_6H_3F_2{}^{++}+I^+$, leading to a singly charged iodine ion with about 3 eV final kinetic energy and a metastable $C_6H_3F_2{}^{++}$ di-cation with about 3.5 eV kinetic energy, both repelled in opposite directions. The sequential fragmentation mechanism can also be revealed in Dalitz plots [73]. Fig. 5.11 demonstrates the Dalitz plot, the energy sharing, of three ions in $CF^+ + C_5H_3F^+ + I^+$ channel. The diagonal distribution inside the circle of the Dalitz plot represents the sequential nature of the fragmentation. The other two sequential triple fragmentation channels have similar Dalitz plot distribution.

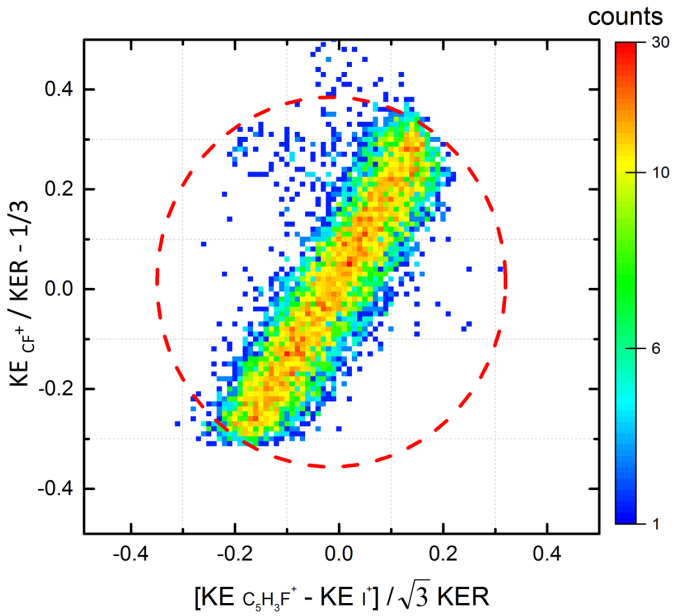

Figure 5.11: Dalitz plot for $CF^+ + C_5H_3F^+ + I^+$ channel in 3,5-DFIB measurement.

As illustrated in the cartoon shown in Fig. 5.12, after a delay longer than its rotational period, the metastable $C_6H_3F_2{}^{++}$ di-cation breaks up into two singly charged fragments, each containing a fluorine atom and different numbers of carbon atoms. The rotation of the $C_6H_3F_2{}^{++}$ di-cation around its center of mass *before* the second fragmentation step results in an isotropically distributed angle between the iodine ion momentum and the momenta of

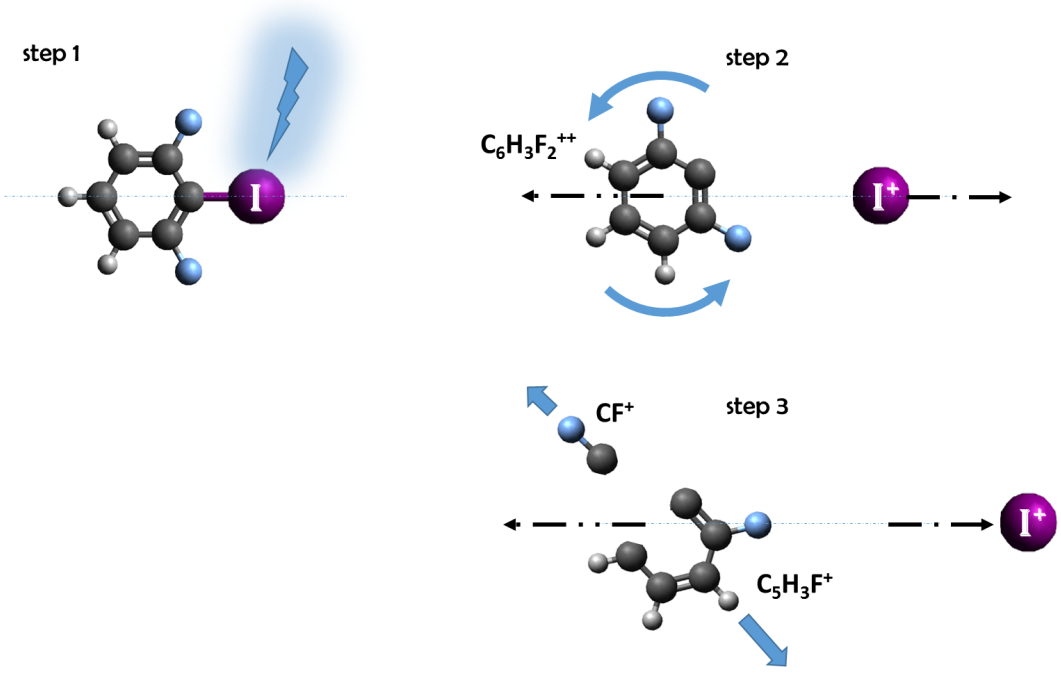

Figure 5.12: Schematics of sequential fragmentation for 2,6-DFIB

the other two fragments, which leads to the distinct semi-circular structures in the Newton plots. Moreover, from the narrow I^+ kinetic energy distribution that is independent of the kinetic energies of ions generated in the second fragmentation step, it can be concluded that the distance between the $C_6H_3F_2{}^{++}$ di-cation and the iodine ion at the time of the second fragmentation is large enough that the Coulomb force between the two is negligible. Under this assumption, one can retrieve the kinetics of the second-step fragmentation by subtracting the center-of-mass velocity of the $C_6H_3F_2{}^{++}$ di-cation, which can be calculated from the measured I^+ momentum because of momentum conservation, from each of the other fragment velocities, thus retrieving the kinetic energy spectrum of the second Coulomb explosion step, which is shown in Fig. 5.13. The momenta used in the second step fragmentation is in the center of mass frame of the metastable di-cation $C_6H_3F_2{}^{++}$ and the momentum of CF^+ and $C_5H_3F^+$ in this frame can be shown as:

$$\vec{P}'_{CF^+} = \vec{P}_{CF^+} - \frac{M_{CF^+}}{M_{CF^+} + M_{C_5H_3F^+}}\vec{P}_{I^+} \tag{5.1}$$

$$\vec{P}'_{C_5H_3F^+} = \vec{P}_{C_5H_3F^+} - \frac{M_{C_5H_3F^+}}{M_{CF^+} + M_{C_5H_3F^+}}\vec{P}_{I^+}. \tag{5.2}$$

where, $\vec{P}_{CF^+}$ and $\vec{P}_{C_5H_3F^+}$ are the momentum of respective fragments in total center of mass frame, e.g. laboratory frame.

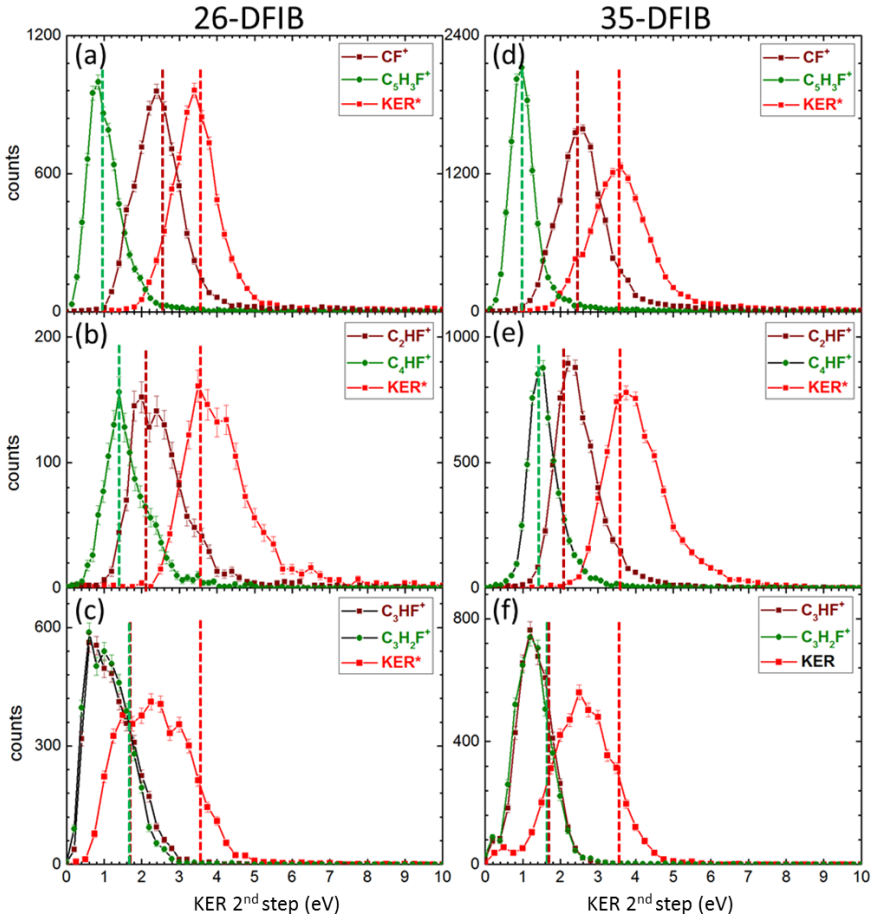

Figure 5.13: Kinetic energies of individual fragments and total kinetic energy release for the second step Coulomb explosion

The classical model simulation, shown as dashed lines in Fig. 5.13, are in good agreement with the experimental data, suggesting that the second-step decay also occurs along Coulombic potential curves. To obtain the best match with the experimental kinetic energies, in Coulomb explosion simulation of the second step, two charges are placed on the two edge of the remaining system, one on the fluorine atom and the other one on the carbon atom that is furthest away from the fluorine atom. This yields very good agreement in the two asymmetric fragmentation channels but overestimates the kinetic energies in the symmetric C_3HF^++$C_3H_2F^+$+I^+ fragmentation, suggesting an intermediate geometry where the two charges are even further apart in that case, possibly due to a deformed geometry of the

metastable di-cation.

5.2.3 Identification of molecular isomers via fragment-ion momentum correlations in three-body fragmentation channels

In Chapter 4, it is shown that the momentum correlations in certain three-body fragmentation channels can be used to identify geometric isomers by determining the angle between the momentum vectors of the two Br^+ ions that are emitted in coincidence with a $C_2H_2^+$ fragment. For DFIB molecule, one might expect that the angle between I^+ and F^+ fragments could be used to distinguish between 2,6- and 3,5-DFIB, if the fragmentation occurs fast enough to preserve the angular correlation between these two fragments. First, the section will concentrate on the $F^+ + C_6HF^+ + I^+$ fragmentation channel, in which all the heavy atoms are accounted for in the ionic fragments, and only two hydrogen atoms are missing. The missing hydrogens were most likely emitted as neutrals since the momentum sum of the three ionic fragments is very narrow around zero (FWHM=$\pm$7.5 a.u). Fig. 5.14 shows the Newton plots for this fragmentation channel in both 2,6- and 3,5-DFIB. The first observation from these Newton plots, where the momenta of two fragments (F^+ and C_6HF^+) are plotted in the frame of the momentum of the third fragment (I^+), is the appearance of well-defined peaks rather than smeared out circular structures, suggesting that both bond breaks between the charged fragments occur on a time scale faster than a molecular rotation. Furthermore, there is a clear difference in the fragmentation patterns of the two isomers, with smaller relative momenta of the F^+ and C_6HF^+ fragments in the case of 3,5-DFIB and a larger angle between I^+ and F^+ fragments as compared to 2,6-DFIB. The difference in the fragmentation patterns for the two isomers is also very apparent in Fig. 5.15, where the KER and the fragment ion kinetic energies for this channel are shown for both isomers, along with the angle θ between the momentum vectors of the F^+, I^+, and C_6HF^+ fragments detected in coincidence. The KER and F^+ kinetic energies are rather similar in 2,6- and 3,5-DFIB, with the main difference being a lower I^+ and higher C_6HF^+ kinetic energy in 2,6-DFIB in comparison to 3,5-DFIB, where both fragments have almost identical kinetic energies. The

angles show large differences between the two isomers, with the angle between F^+ and I^+ fragments peaking at $\approx 84\,^\circ$ ($cos\ \theta = 0.1$) for 2,6-DFIB in contrast to $120\,^\circ$ ($cos\ \theta = -0.6$) for 3,5-DFIB.

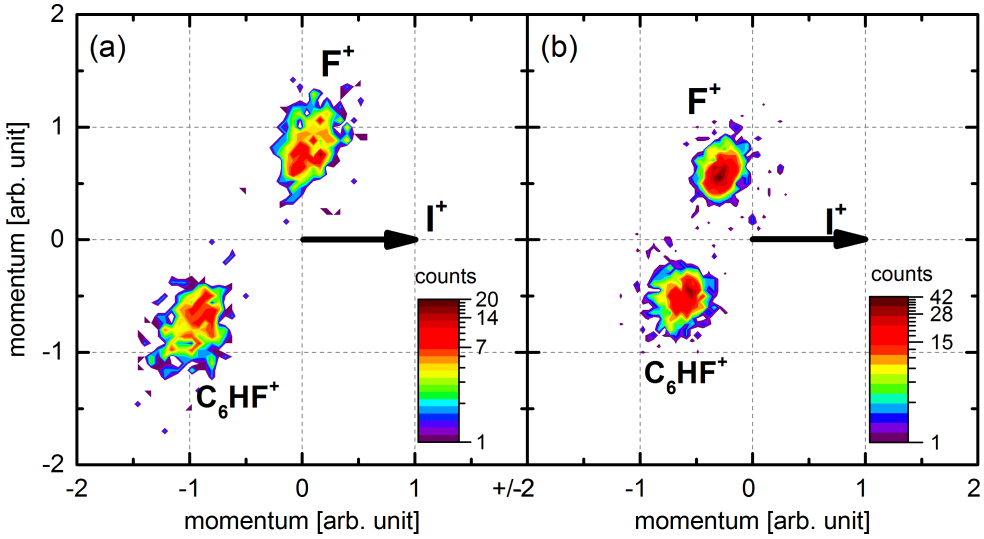

Figure 5.14: Newton plots of the $F^+ + C_6HF^+ + I^+$ fragmentation channel for (a) 2,6-DFIB and (b) 3,5-DFIB. The momentum vectors of F^+ and C_6HF^+ are normalized to the size of the momentum vector of I^+.

While these plots show that the momentum correlation between the F^+ and I^+ fragments can indeed be used to separate and identify the two isomers, the experimentally observed angles are surprising for 2,6-DFIB, where one may have naively expected a smaller angle between F^+ and I^+ since the angle between the F and I atoms in the equilibrium geometry of the neutral 2,6-DFIB molecule is $61\,^\circ$. The Coulomb explosion simulation for the three-body fragmentation shows that this naive expectation is not justified, since the charged fragments repel each other in a way that the angles between the detected ion momenta are not necessarily equal or even close to the bond angles in the molecule. While the Coulomb explosion simulations, shown as dashed lines in Fig. 5.15, are in good agreement with the experimentally observed kinetic energies and angles in 3,5-DFIB, they do not reproduce the observed angles for 2,6-DFIB. In this simulation, one charge is placed at the position of the iodine atom, the second at the position of the fluorine atom, and the third one in the center of the ring. Both the C−I and the C−F bond are assumed to break simultaneously, a scenario commonly referred to as *concerted fragmentation*. For 2,6-DFIB, concerted fragmentation

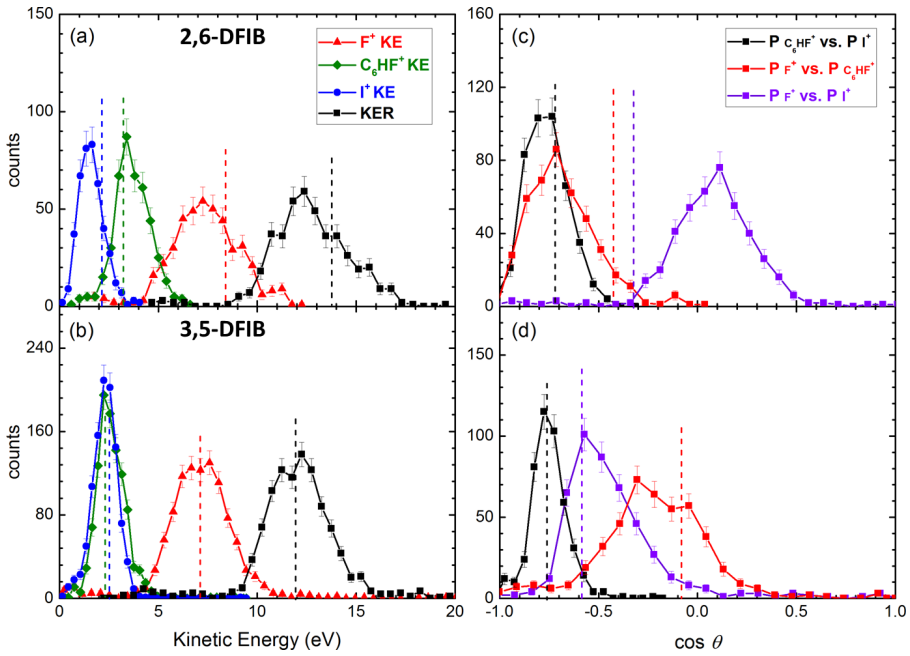

Figure 5.15: Total kinetic energy release, kinetic energies of the individual ionic fragments, and angle θ between the momentum vectors of the F^+, I^+, and C_6HF^+ fragments for the $F^+ + C_6HF^+ + I^+$ fragmentation channel in 2,6-DFIB (top) and 3,5-DFIB (bottom). The kinetic energies and angles obtained from a classical Coulomb explosion simulation are shown as dashed lines.

for any charge configuration yields angles between the fragments that do not match the experimentally determined angles. Various other possible positions of the charge on the C_6HF^+ were also simulated but none of them could reproduce the experimentally observed energies and/or angles. In particular, they all yield too large of an angle between the F^+ and I^+ fragments. Interestingly, for some charge configurations, concerted fragmentation of 2,6-DFIB can even lead to F^+-I^+ angles that are very similar to those observed in 3,5-DFIB, suggesting that the seemingly "obvious" link between the molecular geometry and the fragment angle correlations should be considered with caution and on a case-by-case basis, rather than as a general rule.

A mechanism that could lead to a smaller angle between F^+ and I^+ fragments would be a step-wise ionization and/or fragmentation, where the I−C bond is broken first, e.g. after the first Auger decay, and the remaining $C_6H_xF_2{}^+$ remains in an excited state that decays, via a second Auger decay, after a few hundred femtoseconds, when the distance to the iodine has

already increased considerably due to the first Coulomb explosion step. A further indication for such a delay of the second-step Auger decay is the kinetic energy of the I^+ fragment, which is significantly lower than any concerted fragmentation scenario would allow. One scenario that would lead to a smaller angle between F^+ and I^+ fragments would be a step-wise ionization and/or fragmentation, where the I-C bond is broken first, e.g. after the first Auger decay, and the the remaining $C_6H_xF_2{}^+$ remains in an excited state that decays, via a second Auger decay, after a few hundred femtoseconds, when the distance to the iodine has already increased considerably due to the first Coulomb explosion step. A further indication for such as delay of the second-step Auger decay is the kinetic energy of the I^+ fragment, which is significantly lower than any concerted fragmentation scenario would allow. As described in Section 2.1, one can model a delayed ionization and fragmentation by introducing a time τ, after which the charge of a specific fragment is increased and/or a specific bond is broken. Fig. 5.16 shows the result of these calculations for step-wise fragmentation of 2,6-DFIB for the case that the two charges, in the first step, are located at the position of the iodine atom and the carbon atom that is furthest away from it, and for two different locations of the charges in the second step, as a function of the delay τ between the two steps. When assuming that the charge on the $C_6HF_2{}^+$ fragment in the second step is located in the vicinity of (but not too close to) the F^+ fragment, the simulation can reproduce all of the experimentally observed kinetic energies and angles, within reasonable accuracy, at a delay τ around 400 fs, as shown in Fig. 5.16 (e,f).

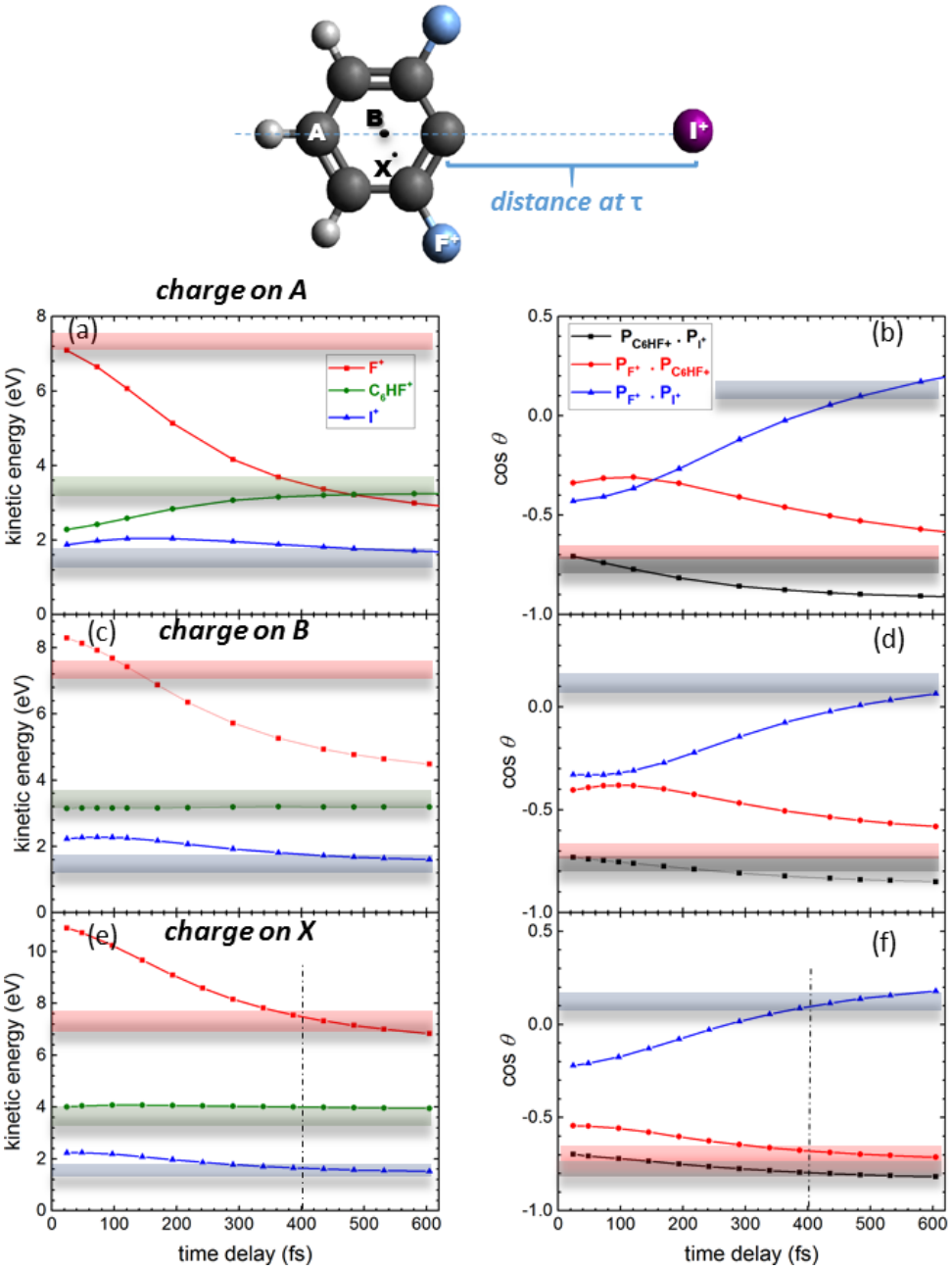

Figure 5.16: Fragment ion kinetic energies and angles between the momentum vectors obtained from the Coulomb explosion simulation of a two-step fragmentation of 2,6-DFIB with a variable time delay τ between the two fragmentation steps (see text) and for different locations of the charge on the C_6HF^+ fragment. Top row: one of the charges in the second-step Coulomb explosion is placed on the carbon furthest away from the iodine (labeled A); Middle row: placed in the center of the benzene ring (labeled B), and in the bottom row, it is placed close to the fluorine atom at the position labeled X.

Any other scenario (including many more that have been tried but that are not shown

here) yields significant deviations in at least one observable. Without having a direct proof for this hypothesis beyond the agreement between the Coulomb explosion simulation and the experimental data, the observation can be tentatively explained as follows: After the initial Auger decay following the creation of a I($4d$) vacancy, there is a certain probability that molecule fragments into an I^+ and an electronically excited $C_6H_xF_2{}^{+*}$ fragment. If the electronic energy in the $C_6H_xF_2{}^{+*}$ is sufficient, e.g. if it has an inner-valence hole, this fragment can decay further into a multitude of tri-cationic channels that can be seen in Fig. 5.4. Most of these secondary Auger decays will occur much faster than the ≈400 fs lifetime that is derived from the Coulomb simulation, leading, e.g., to the three-body fragmentation channels discussed in Section 3.2. However, since the fragmentation into F^+ + C_6HF^+ + I^+ is a rather weak channel, it is conceivable that it only occurs after an initial Auger decay into a rather long-lived state with an inner-valence vacancy with a lifetime on the order of ≈ 400 fs. Furthermore, since fluorine has a very high electronegativity, it is very unlikely to dissociate into a F^+ fragment, unless the inner-valence vacancy in the $C_6H_xF_2{}^+$ is located in an orbital that has significant overlap with one of the near-atomic fluorine orbitals. Even without further calculations, it is therefore conceivable that the different geometry of 2,6- and 3,5-DFIB and, in particular, the different location of the fluorine atoms with respect to the iodine atom, may lead to significantly different lifetimes of the intermediate states that lead to this particular fragmentation channel.

Of course, the classical Coulomb explosion model is unable to test or predict any of these detailed electronic dynamics, but it seems to be clear that a step-wise fragmentation model needs to be considered in order to obtain satisfying agreement with the experimental data for 2,6-DFIB. It has to be noted that there is, of course, not only an ambiguity in the exact positioning of the charge in our model, but also in the geometry of the intermediate state. This leads to an uncertainty of the exact delay, for which a satisfactory agreement of the simulated kinetic energies and angles with the experimental data can be achieved. A multi-parameter least-square fitting procedure is not performed to obtain a more accurate number for the delay τ, since the classical Coulomb explosion model is not suitable to draw such precise and quantitative conclusions. Nevertheless, it yields, at least, an estimate for

the lifetime of the second-step Auger process, if the assumption of a two-step Auger process is correct.

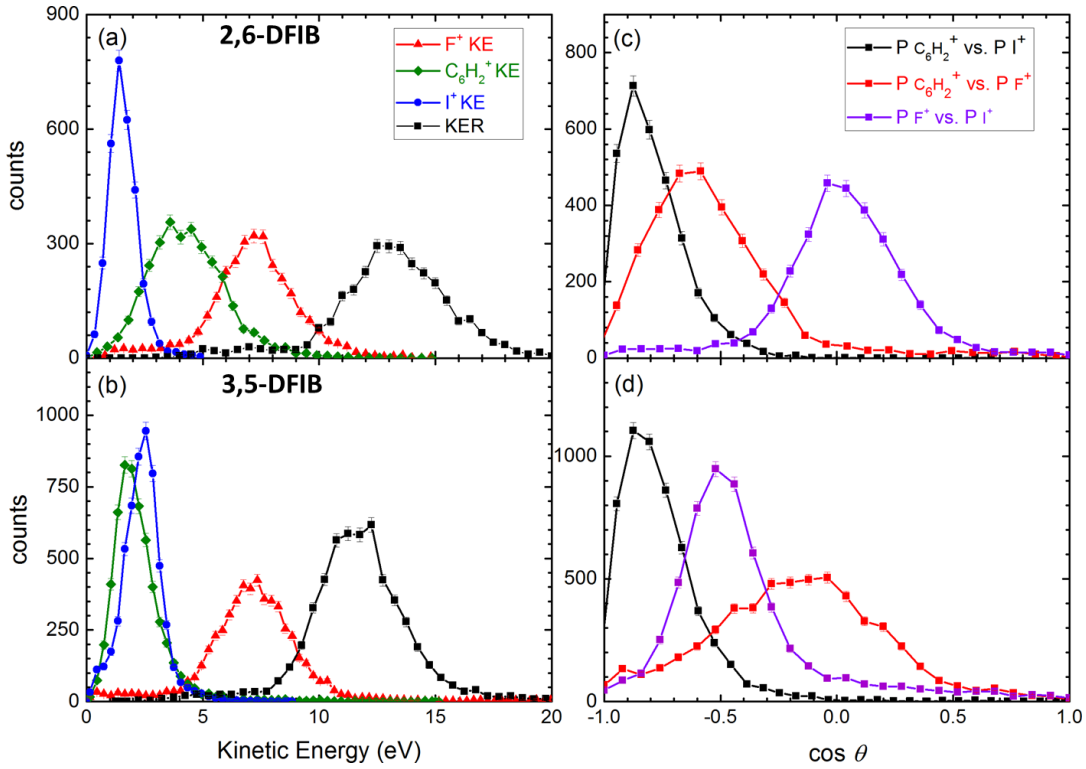

Figure 5.17: Total kinetic energy release, kinetic energies of the individual ionic fragments, and angle between the momentum vectors of the F^+, I^+, and $C_6H_2^+$ fragments for the F^+ + $C_6H_2^+$ + I^+ fragmentation channel.

Finally, it is important to investigate how general the above findings are for other channels involving F^+ production. Fig. 5.17 shows the kinetic energy and momentum angle distributions for the strongest three-body fragmentation channel containing F^+, namely F^+ + $C_6H_2^+$ + I^+, where the missing fluorine and hydrogen atoms are emitted as one or two neutral fragment(s). For 3,5-DFIB, the distributions are very similar to the F^+ + C_6HF^+ + I^+ fragmentation channel, with the angular distributions for F^+ + $C_6H_2^+$ + I^+ being slightly broader. For 2,6-DFIB, both kinetic energy and angular distributions are significantly broadened, while the peak positions are still close the the former case. Furthermore, Fig. 5.18 shows the I^+-F^+ angle for all events where F^+ is detected as the first fragment and I^+ as the last fragment, thus integrating over all possible partner fragments. Again, the I^+-F^+ angles are very similar to the F^+ + C_6HF^+ + I^+ fragmentation channel discussed above,

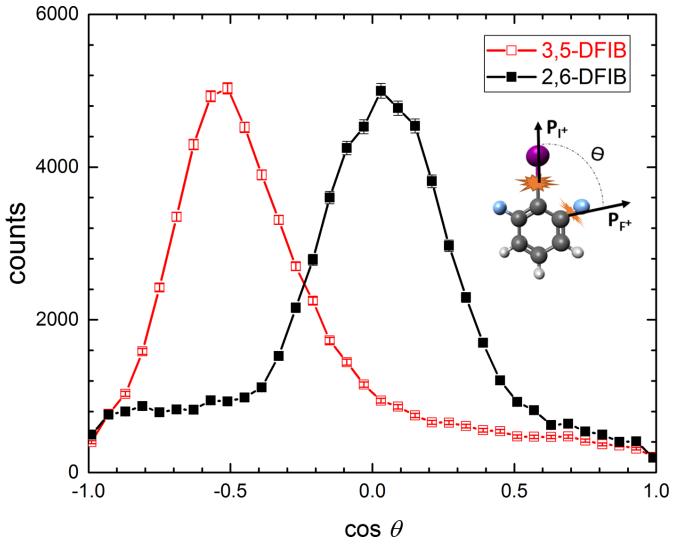

Figure 5.18: Momentum vector correlation between F^+ and I^+ fragments in 2,6-DFIB (black solid symbols) and 3,5-DFIB (red open symbols) for fragmentation channels where F^+ is the first and I^+ is the third detected fragment.

suggesting that the ultrafast sequential breakup is common to all triply charged final states that involve F^+ production in 2,6-DFIB, while a concerted fragmentation is well suited to describe the breakup in 3,5-DFIB.

5.3 Ultrafast femtosecond laser induced fragmentation of 2,6- and 3,5-DFIB

The process of ionizing a molecule through X-ray inner-shell photoionization and strong-field laser induced ionization are fundamentally different. In strong-field ionization with infrared laser beams, multiple photons are absorbed by the molecule and one or more valence electrons are stripped away from the molecule. Previously reported strong-field measurements on DFIB isomers were mainly focused on laser-induced alignment [135–137]. Although some discussions were included on the fragmentation dynamics of the complex benzene compound [136], a more detailed measurement of the kinematics is helpful for the understanding of the breakup mechanism of the isomers in an ultrafast strong laser field. In this study, the fragmentation of DFIB isomers by femtosecond laser pulses ($\lambda_c \approx 800$ nm, $\Delta t \approx 27$ fs,

I≈5×10^{14} W/cm^2) were investigated using the COLTRIMS ion-ion coincidence momentum imaging technique at J. R. Macdonald laboratory of Kansas State University. All of the laser measurement described in this section use the same laser parameters mentioned above.

In the context of the present work, the strength of the laser intensity applied to the DFIB molecule is considered to be strong enough to induce significant modifications of its energy landscape. For the ionization process the strong-field regime starts if pondermotive energy U_p is bigger than E_{IP} of the DFIB molecules. Using the mass spectroscopic technique described in Chapter 3, a separate molecular beam experiment is conducted with VUV synchrotron beams at the 9.0.2 beamline of the ALS in order to know the ionization potential of both 2,6- and 3,5-DFIB molecules. The results show that the ionization potential of the 2,6- and 3,5-DFIB molecules are 8.98 eV and 9.03 eV. If the ionization potentials of the isomers are compared to the pondermotive energy $U_p = 9.34 \times 10^{-20} \times (800\,nm)^2 \times 5\times10^{14}$ W/cm^2 = 29.9 eV, see Chapter 2, it is clear that the ionization is taken place in a strong-field regime.

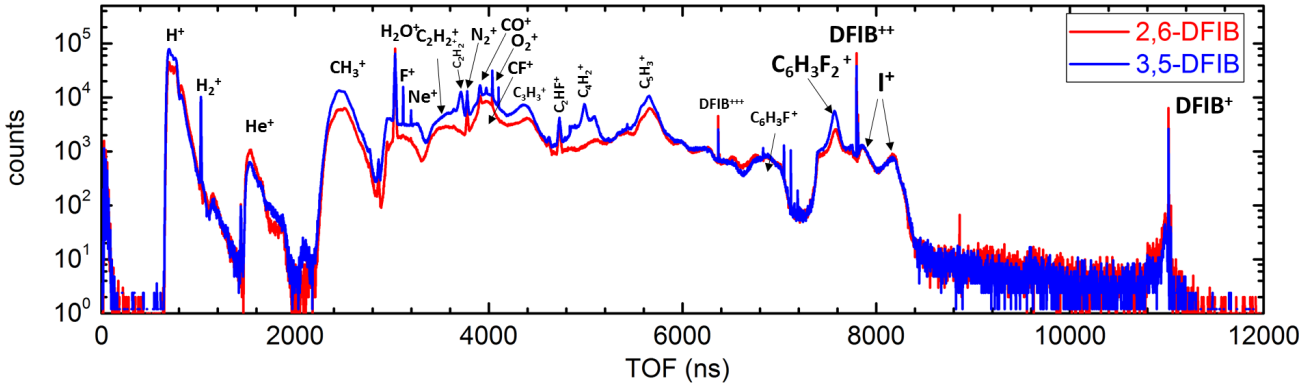

Figure 5.19: Ion time-of-flight mass spectra generated by ionization of 2,6-difluroiodobenzene with 27 fs laser pulses with 800 nm central wavelength at ~5×10^{14}W/cm^2 laser intensity. The two spectra are normalized with I^+ peak height.

Fig. 5.19 presents the TOF spectra for both isomers after ionization with a same laser pulse. The two spectra are normalized using the peak height of I^+ in order to compare the yields of different fragment ions generated from the isomers. It is clear from the figure that the generation of F^+ and $C_4F_2^+$ are more efficient in 3,5-DFIB than in 2,6-DFIB. The other differences in the yield of fragment ions are not further discussed here. The ion particles' spread in position are showed in Fig. 5.20. From such plot, one can distinguish doubly or

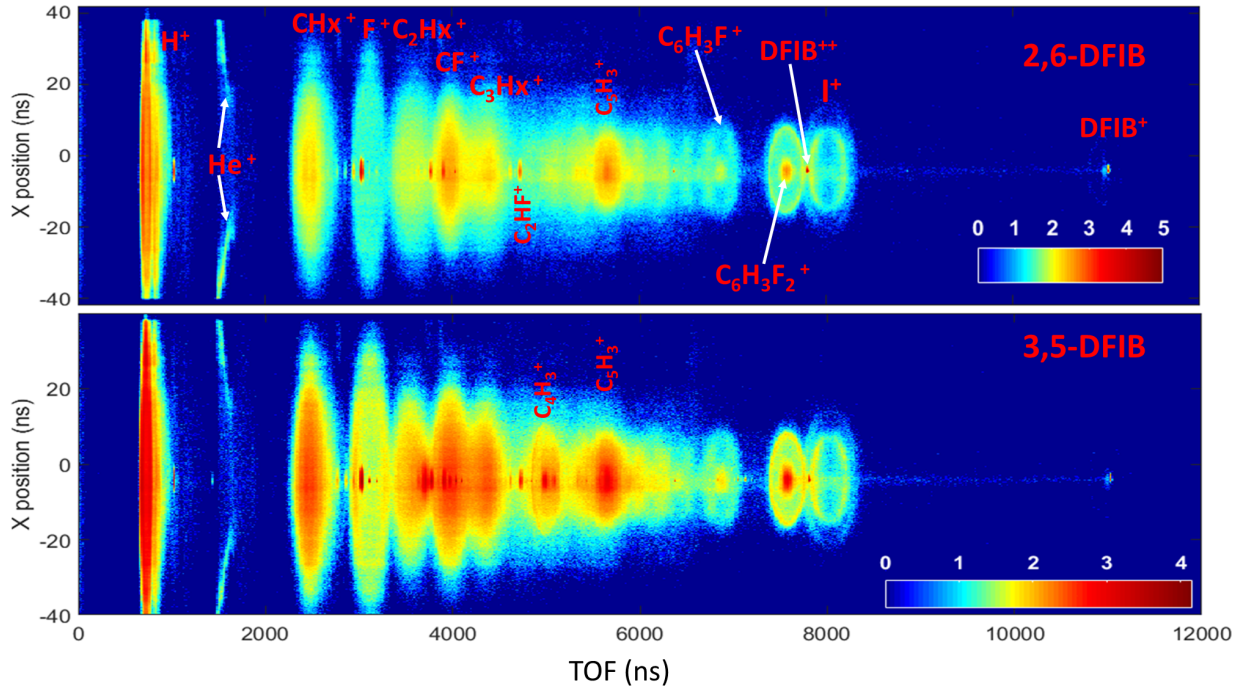

Figure 5.20: Ion time-of-flight mass spectra vs. X direction position distribution of both 2,6- and 3,5-DFIB after ionization with 27 fs laser pulses with 800 nm central wavelength at $\sim 5 \times 10^{14} \mathrm{W/cm^2}$ laser intensity.

triply charged parent molecule as well as background residual gas contributions, e.g. H_2O, N_2, O_2...etc, because those ions appear as hot spots at the center of the detectors. The majority of the fragment ion position distribution involves larger spread and does not appear as hot spots in the center of X position axis. Using position and time information of the ions, three dimensional momenta of all coincidence ion channels are obtained and kinetic energies for individual ion fragments are calculated. Fig. 5.21 shows the PIPICO maps of 2,6- and 3,5-DFIB molecules after exposure to a strong laser pulse. As mentioned in previous chapters, the sharp diagonal lines in a PIPICO map correspond to the coincidence two-body channels where the parent molecule is ionized and fragments to two ionic species. In a large complex molecule like DFIB, the outcome that is shown in the PIPICO map includes many different coincidence channels. In the following section, the two-body coincidence ionic channels are discussed, namely $C_6H_3F_2^+ + I^+$ and $C_6H_3F_2^{++} + I^+$, in order to compare the fragmentation dynamics to the inner-shell photoionization results described in Section 5.2.1.

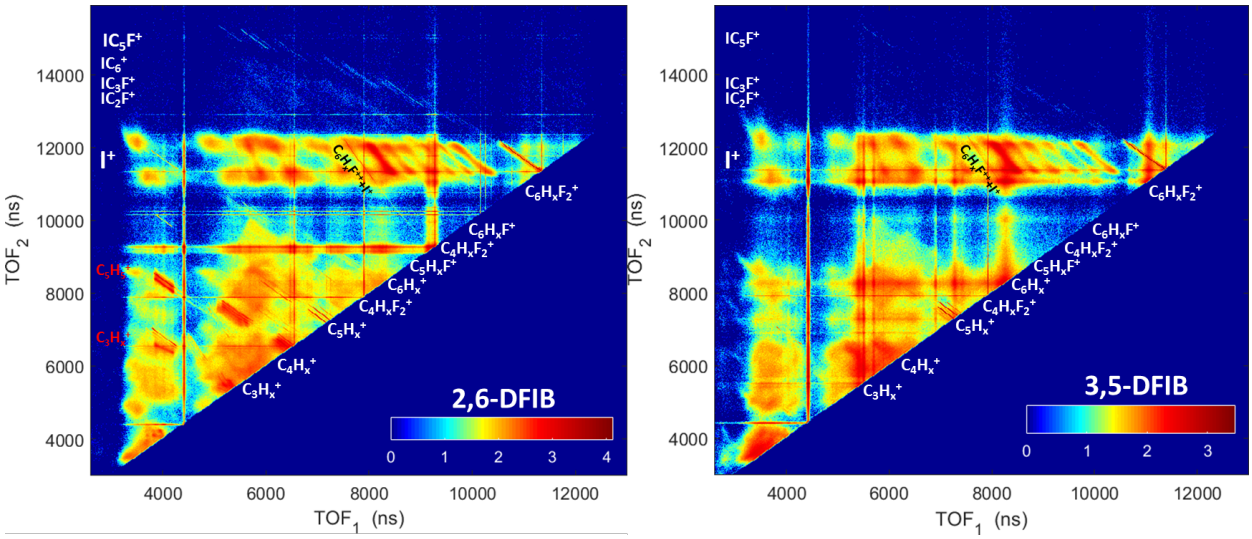

Figure 5.21: PIPICO maps of 2,6- and 3,5-DFIB with 25 fs laser pulses with 800 nm central wavelength at $\sim 5\times10^{14}$W/cm^2 laser intensity.

5.3.1 $C_6H_3F_2^+ + I^+$ and $C_6H_3F_2^{++} + I^+$ two-body fragmentation channels

Nevo *et al* [136] studied the alignment of the DFIB molecules using a Nd: YAG laser beam for aligning in combination with a strong 800 nm laser pulses for ionizing the molecule. The two iodine energy peaks they observed were reported to be from $C_6H_3F_2^+ + I^+$ and $C_6H_3F_2^{++} + I^+$ final states. In our study, ion-ion coincidence momentum imaging technique allow us to obtain three dimensional momenta of all coincidence ionic channels, which will open the door to investigate fragmentation dynamics at specific final states. Fig. 5.22 shows the kinetic energies of individual ion fragments as well as total kinetic energies for both $C_6H_3F_2^+ + I^+$ and $C_6H_3F_2^{++} + I^+$ channels. The dashed lines are simulated values from a Coulomb explosion model. Similar to the the description in Section 5.2, the simulation results for two scenarios are given when the charge on the benzene ring: $C_6H_3F_2$ is located on a) the furthest carbon from Iodine atom (labeled as A) and b) at the center of the benzene ring (labeled as B).

It is clear from Fig. 5.22 that the experimental kinetic energies match closely with the Coulomb explosion simulation results when the charge on the ring is located on the furthest

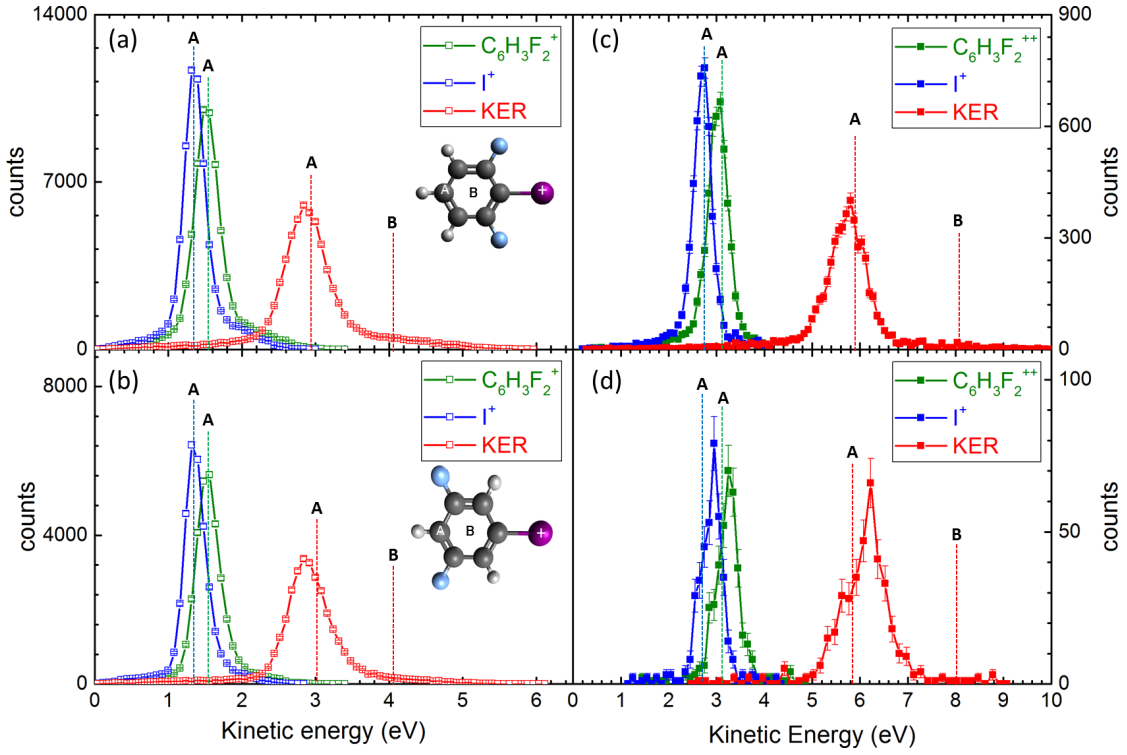

Figure 5.22: Kinetic energies of individual fragments and total kinetic energy release of coincidence two-body channels: $C_6H_3F_2^+ + I^+$ and $C_6H_3F_2^{++} + I^+$ for 2,6-DFIB (a,c) and 3,5-DFIB (b,d).

carbon atom. This comparison between experimental and simulated results indicates that both 2,6- and 3,5-DFIB isomers, after absorbing multiple photons in a strong femtosecond laser field, will undergo a Coulomb explosion process. However, there can be two possible scenarios have taken place prior to the fragmentation. 1) three electrons are directly stripped away from the system by the strong laser field and the two charges localized to two ends of the molecule by Coulomb repulsion. 2) the C-I bonds stretch within the laser field before the fragmentation and the Coulomb explosion starts from a much larger C-I distance than the equilibrium C-I bond length. In the triple ionization channel $C_6H_3F_2^{++} + I^+$, similar to the results in the inner-shell photoionization measurement, the situation where both charges on the $C_6H_3F_2$ fragment are located at the far end of the phenyl ring gives almost perfect agreement with the experimental data. Hence, it can be concluded that regardless of ionizing the molecule through strong-field multiphoton valence ionization or single photon inner-shell photoionization followed by the Auger decay processes, both 2,6- and 3,5-DFIB isomers

isomers will undergo a Coulomb explosion process where the molecule fragments into two ions after double or triple ionization.

5.3.2 Sequential fragmentation in strong laser field

The sequential C-I and C-C bond-breaking of DFIB isomers after inner-shell photoionization is discussed in Section 5.1. In current section, laser induced sequential fragmentation dynamics of DFIB molecules are reported. Recent studies on molecular imaging of sequential fragmentation dynamics focused on triatomic molecules such as CO_2 [73, 114] and OCS [154]. It has been reported that the first bond, e.g. C-O in CO_2 and C-S in OCS molecules will break leaving the metastable dication $CO_2^{+\,+}$ and CS^{++} rotationally excited while being repelled from the first ion (O^+ from $CO_2^{+\,++}$ and S^+ from OCS^{+++}). After the distance between the two charged particles are far enough until the Coulomb repulsion can be ignored, then the second step fragmentation happens where CO^{++} breaks into C^+ and O^+, CS^{++} breaks into C^+ and S^+. In present work, multi-coincidence channels, especially three-body channels are studied, in order to *i*) explore the existence of such sequential dynamics in more complex molecules such as DFIB and *ii*) to see if the sequential fragmentation phenomena observed in the three-body channels after inner-shell photoionization of DFIB molecules (described in Section 5.2.2) can be reproduced in strong-field ionization. Fig. 5.23 shows that there are three sets of triple-coincidence channels observed for both 2,6- and 3,5-DFIB measurements, namely CH_xF^++$C_5H_xF^+$+I^+, $C_3H_3^+$+$C_3F_2^+$+I^+, $C_4H_2^+$+$C_2F_2^+$+I^+.

The obvious difference between triple coincidence channels in X-ray inner-shell photoionization measurement and laser ionization is that only three sets of channels are observed in strong-field ionization. In the laser fragmentation channel $C_4H_2^+$+$C_2F_2^+$+I^+, two fluorine atoms appeared to be on the same fragment $C_2F_2^+$. Since in the original structure of the DFIB molecule, two fluorine atoms are not connected to the neighboring carbons, this channel indicates that one fluorine atom possibly migrated from original site and connected to the neighboring carbon atom that is closer to the other fluorine atom during the laser interaction.

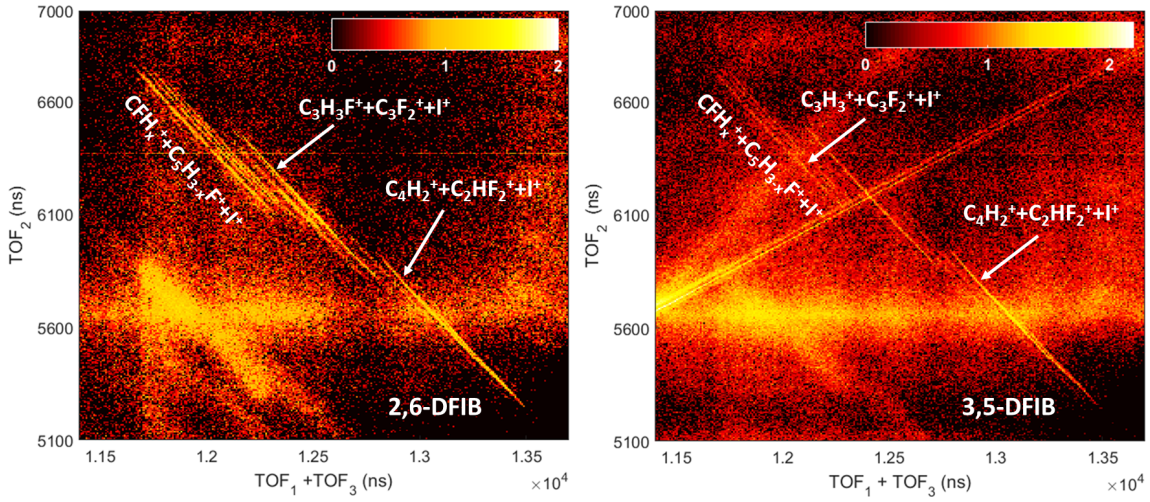

Figure 5.23: PIPIPICO maps of a) 2,6-DFIB, b) 3,5-DFIB after strong-field ionization with 27 fs, $\sim 5\times10^{14}$W/cm^2 laser pulses

In order to understand the dynamics of triple-coincidence channels after strong-field laser ionization, three dimensional momentum and kinetic energies for all ions and total kinetic energy release of the three channels are obtained and shown in Fig. 5.24. The kinetic energy distribution in strong-field ionization appears similar to the results in inner-shell photoionization measurement. In all three coincidence channels for both 2,6 and 3,5-DFIB molecules, the iodine ion has a sharp kinetic energy distribution peaked at around 3 eV. Both the peak energy value and its FWHM are similar to the iodine energy distribution in the two-body fragmentation channel $C_6H_3F_2^{++}$+I^+ shown in Fig. 5.6 (c,d). This indicates the possibility that the molecule breaks into I^+ and $C_6H_3F_2^{++}$ channel during the first step fragmentation. The first and second ions in all three channels appear to have similar broad energy distribution as shown in the sequential fragmentation channels after inner-shell photoionization Fig. 5.9. The total kinetic energy release is similar in two isomeric cases of all triple-coincidence channels. In order to further confirm the sequential nature of these coincidence channels, Newton diagrams shown in Fig. 5.25 are generated using three dimensional momentum vectors of all ionic fragments. Similar to the description of sequential ionization with the inner-shell photoionization in Section 5.2.2. The curved, semi-circular structures appear in these Newton plots are a strong indication of a sequential fragmentation dynamics [73].

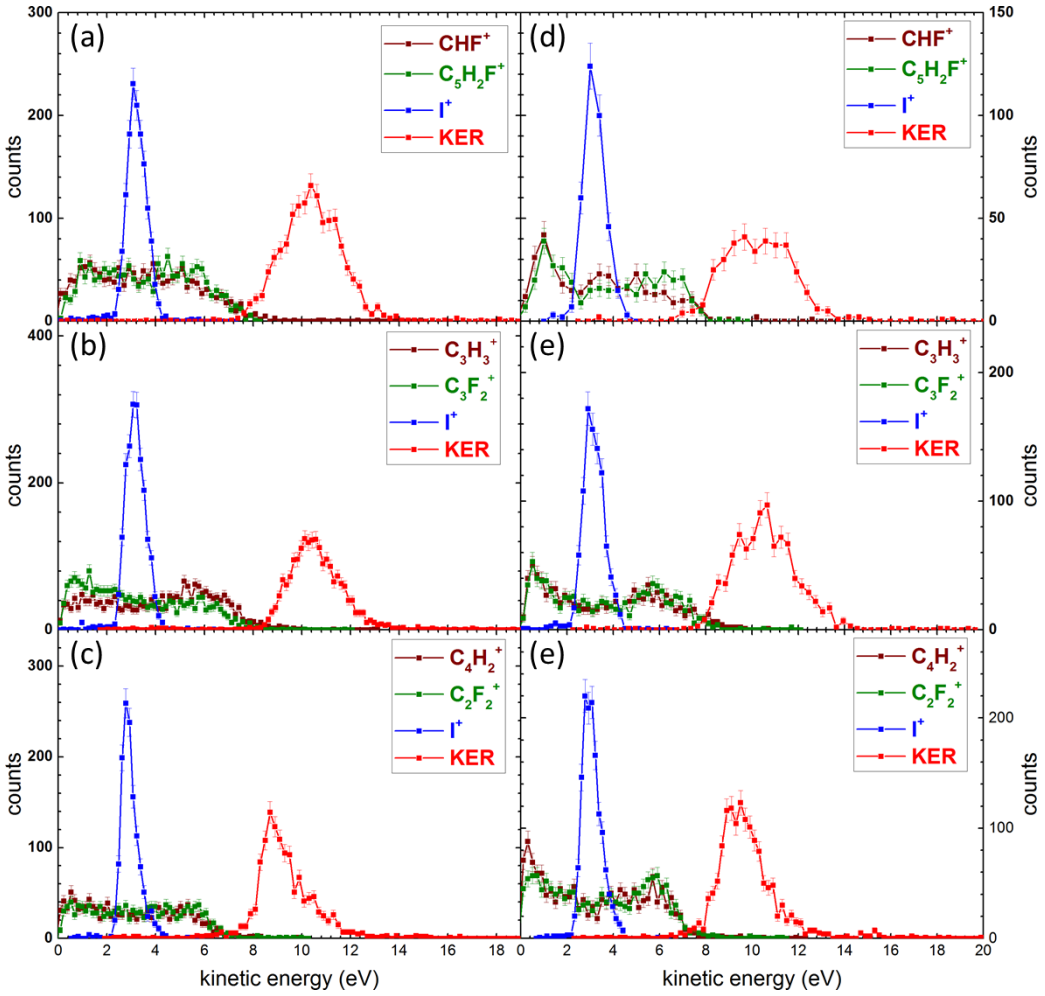

Figure 5.24: Kinetic energies of individual ionic fragments and total kinetic energy release from channels: $CFH_x^+ + C_5FH_{(3-x)}^+ + I^+$, $C_3H_3^+ + C_3F_2^+ + I^+$ and $C_4H_2^+ + C_2HF_2^+ + I^+$; a,b,c) 26-DFIB; d,e,f) 3,5-DFIB;

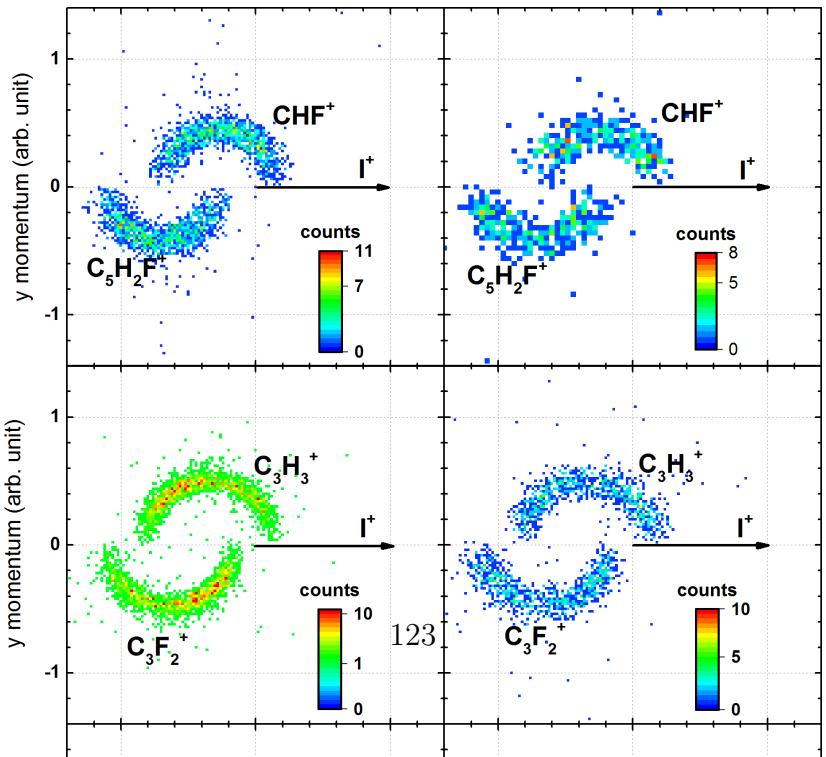

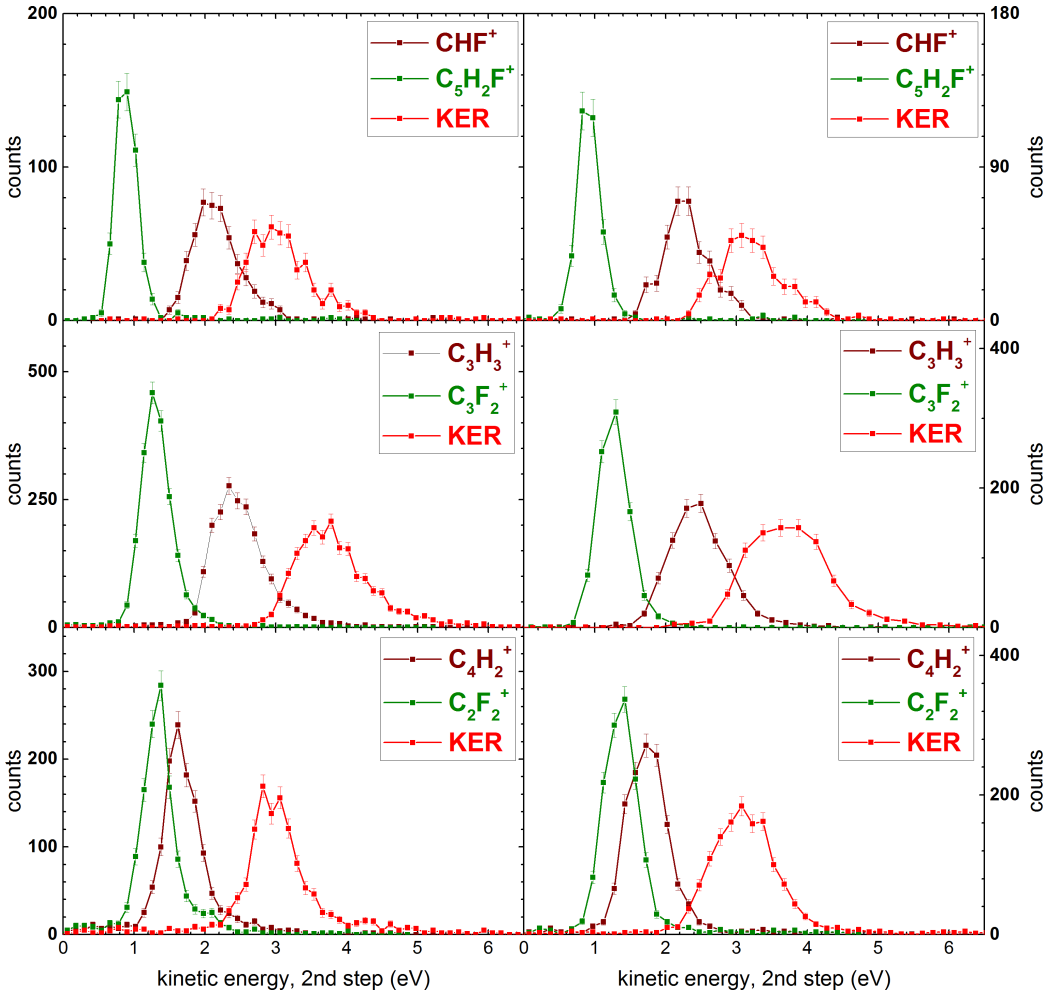

Figure 5.26: Kinetic energies for second step fragmentation process of sequential breakup channels, respectively, CHF^++$C_5H_2F^+$+I^+, $C_3H_3^+$+$C_3F_2^+$+I^+, $C_4H_2^+$+$C_2F_2^+$+I^+; a,b,c) 2,6-DFIB; d,e,f) 3,5-DFIB;

Unlike X-ray photoionization, in strong laser pulses, the molecule gains enough photon energy to be able to eject three valence electrons from itself, reaching a triply charged state. Then the iodine ion breaks apart from the rest of the metastable dication: $C_6H_3F_2^{++}$, carrying 3 eV kinetic energy. When the distance between two ions are far apart and Columbic force can be ignored, the dication fragments into two ionic species. Furthermore, due to possible excitation of bending and vibrational states of the system throughout the ionization process, the dication initially gains angular momentum during Coulomb interaction with Iodine ion, thus rotating while being repelled by I^+ ion. The rotation of the $C_6H_3F_2{}^{++}$ di-cation around its center of mass *before* the second fragmentation step results in an isotropic momentum

distribution on a semi-circle in Newton plots. The kinetics of the second-step fragmentation can be retrieved by subtracting the energy component gained from the initial repulsion of I^+ as described in Section 5.2.2.

Chapter 6

Summary and Future Perspectives

The goal of the experimental work described in this thesis was to use Coulomb explosion imaging with both X-ray synchrotron beams and ultrafast femtosecond laser pulses to unravel the photoionization and photo-fragmentation dynamics of molecular isomers and to explore how this method can be used to probe ultrafast photo-induced molecular reaction dynamics. The synchrotron experiments, conducted at the ALS of LBNL in California, focused on inner-shell photoionization of gas-phase isomeric molecules and on imaging the Coulomb explosion processes with a coincidence VMI technique. In order to complement the inner-shell photoionization studies, strong-field ultrafast measurements on the same isomeric gas-phase targets were conducted using an ion-ion coincidence momentum imaging apparatus, COLTRIMS, together with laser pulses of $\sim$23 fs pulse duration at the J.R. Macdonald Laboratory at Kansas State University.

The most important question that started the experimental work described in the thesis is: "Can we use the Coulomb explosion imaging method to distinguish different isomers of a molecule?". In order to answer this question, two types of isomers, namely geometric and structural isomers were studies. The geometric isomers, which are commonly known as *cis/trans* isomers, have two distinct geometrical structures albeit having the same chemical formula, e.g. *cis/trans* 1,2-$C_2H_2Br_2$. The photoionization process that leads to the breaking of two C-Br bonds can produce three ionic species, namely two Br^+ and a $C_2H_2^+$ (e.g. in

the triple-ionization channel) and those ions can fly apart instantaneously due to Coulomb explosion. The idea was to image the 3D momentum components of all three ions from the photo-fragmentation to retrieve original geometrical structures of the isomers using ion momentum correlation. Since *cis* and *trans* 1,2-$C_2H_2Br_2$ isomers have two distinct positions for the bromine atoms, after the Coulomb explosion, two Br^+ ions fly toward angles that are largely different in two isomeric cases. This angular difference is observed in the correlation between the Br^+ momentum vectors. The experimental data was then supported by the classical Coulomb explosion model simulation.

Apart from distinguishing the two isomer components from a mixed original sample, isomer specific momentum and kinetic energies were extracted by selecting the coincidence events from the angular correlation spectrum. Furthermore, in the synchrotron measurement, the branching ratios between *cis* and *trans* fragmentation events evaluated from the photoionization data matches closely with the sample component analysis provided by the chemical vendor. This may open a new route to evaluate and quantify the amount of isomer components in a *cis*/*trans* mixed isomer sample.

The successful use of the Coulomb explosion imaging technique is confirmed by the measurements of dichloroethene. The pure *cis* and *trans* isomers of 1,2-$C_2H_2Cl_2$ were studied via inner-shell photoionization and strong-field ionization processes. The results show that via both photoionization mechanisms, Coulomb explosion imaging can be used to identify the final correlation angle which is the marker for distinguishing the isomer structure. Coulomb explosion model simulation matches with experimental results of both *cis* and *trans* 1,2-$C_2H_2Cl_2$ isomers.

The two examples of Coulomb explosion imaging studies on *cis*/*trans* geometrical isomers will be followed by time-resolved isomerization studies in the future. The next important question, then, will automatically be: "Can we observe *cis*/*trans* isomerization using time-resolved Coulomb explosion imaging?". Such study involves a pump-probe technique, where the pump pulse is used to initiate the isomerization process via excitation of an initial *cis* or *trans* isomer. During this excitation process, the bond between the two carbons rotates, then the probe pulse can be used to Coulomb explode the molecule. By changing the delay

between the two pulses, one can take snapshots at different moments to record the structural change of the molecule over time. Fig. 6.1 shows a potential energy diagram of different final states for 1,2-$C_2H_2Br_2$ isomers [155]. According to the diagram, a UV photon with 10.6 eV can excite the *trans* isomer from its ground state to the transition state TS1. The molecule can then evolve into *cis* geometry or role back to keep its *trans* geometry in a cationic state. After a delay of Δt, a probe pulse can Coulomb explode the molecule and ionic fragment momentum information can be obtained to determine the molecular structure before the Coulomb explosion process.

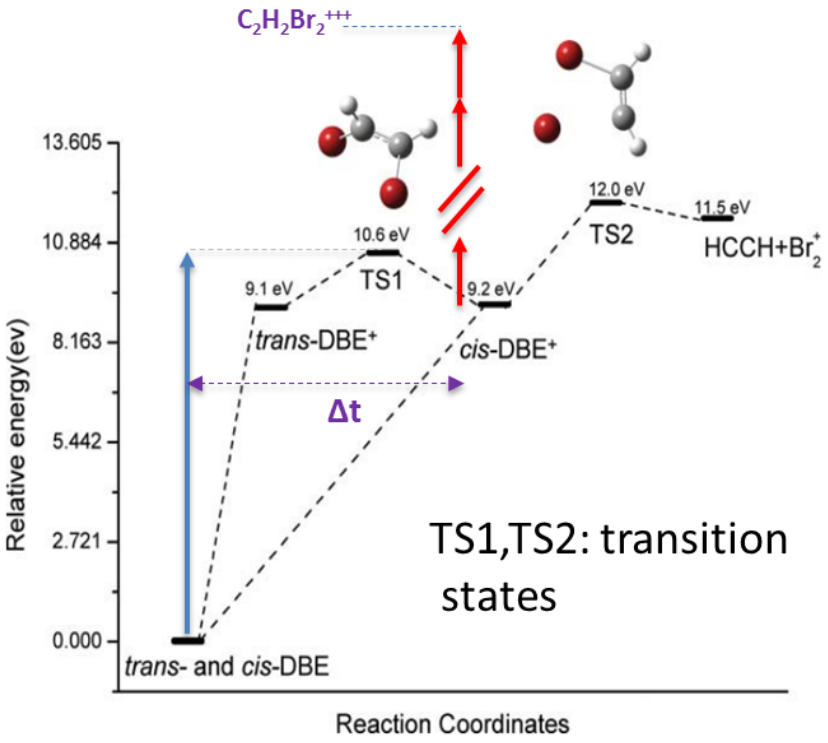

Figure 6.1: Energy diagram of ground, cationic and transition states of 1,2-$C_2H_2Br_2$ isomers. Adapted from reference [155].

In Chapter 5, the Coulomb explosion studies were extended to larger benzene-type molecules in order to determine if one can still distinguish between the geometric structures of isomers via coincident momentum imaging, and if the fragmentation can still be described by a simple classical Coulomb explosion model. For this purpose, the photoionization of the structural isomers of difluoroiodobenzen were investigated. The study used

two "marker ions": F^+ and I^+ produced from the interaction, to distinguish the 2,6 (e.g. F atoms are closer to I) and 3,5 (e.g. F atoms are far from I) isomers of difluoroiodobenzene. In inner-shell photoionization measurements, the momentum correlation between F^+ and I^+ from two isomers appear to be explicitly different and thus can be used to identify geometric structures of 2,6- and 3,5-DFIB isomers. In addition, triple coincidence fragmentation channels present sequential breakup dynamics where I^+ departs from the system in the first step and the rotating benzene ring dication further fragments into two more species in a later time. The sequential dynamics is observed in both inner-shell photoionization with synchrotron beams as well as in strong-field ionization results involving ultrafast laser pulses.

The Coulomb explosion imaging method which was successfully implemented to retrieve structural information of large organic molecules with chemical relevance opens new pathways for investigation of molecular dynamics in femtosecond time scale. For example, photoinduced ring opening reactions, which is a promising candidate for building molecular switches and can serve as benchmark system for fundamental, light-driven biochemical reactions, can be investigated utilizing a time-resolved Coulomb explosion imaging method. In particular, a pump-probe technique can be implemented to first break open the ring with a pump pulse and then taking snapshots by Coulomb exploding the evolving molecule with a strong probe pulse to record a "molecular movie" of a ring opening process.

In order to visualize such "movie-taking" process in a thiophenone molecule, which was previously observed in the condensed phase using ultrafast transient absorption spectroscopy [156], a schematic of a future pump-probe experiment utilizing the Coulomb explosion imaging method is given in Fig. 6.2 (b), together with the calculated ground state potential energy diagram of the molecule in (a).

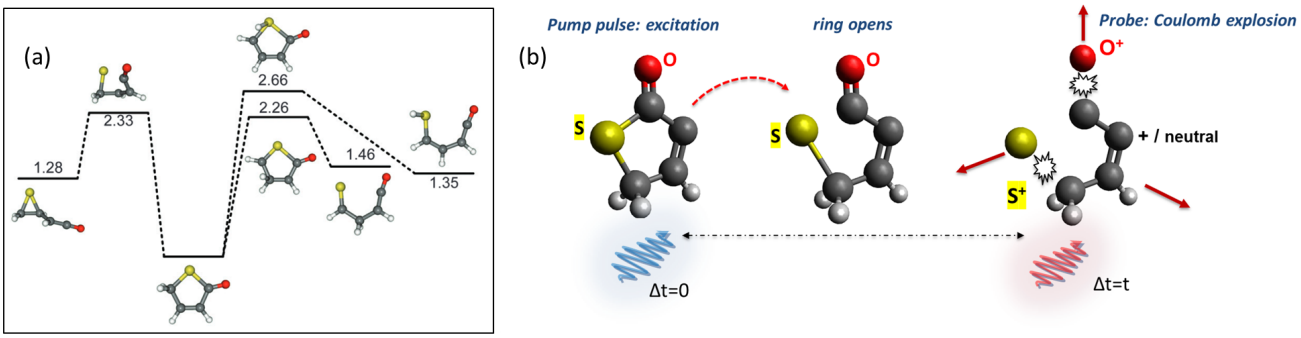

Figure 6.2: (a) Ground state potential energy scheme for three proposed photoinduced ring-opening pathways calculated at the MP2/6-311+G(d,p) level of theory. The figure is taken from reference [156]. The units for the energies are given in electron volts. (b) Schematics of a pump-probe experiment utilizing the Coulomb explosion imaging method to record ring-opening reaction in thiophenone (C_4H_4SO).

Both the study of *cis*/*trans* isomerization and ring opening reactions can provide crucial knowledge of chemical and biological relevance. Successful application of the Coulomb explosion imaging method to distinguish molecular structures of the isomers in static single pulses measurements paves the way for future time-resolved Coulomb explosion studies that can record the molecular dynamic process as "molecular movies".

Bibliography

[1] W. C. Röntgen, Ann. Phys. **300**, 12 (1898).

[2] J. Als-Nielsen and D. McMorrow, *Elements of Modern X-ray Physics*, 2nd ed. (Wiley, 2011).

[3] C. Bressler and M. Chergui, Annu. Rev. Phys. Chem. **61**, 263 (2010).

[4] J. Stöhr and R. Jaeger, Phys. Rev. B **26**, 4111 (1982).

[5] K. Siegbahn and K. Edvarson, Nuclear Physics **1**, 137 (1956).

[6] T. Maiman, Nature **540**, 199 (1960).

[7] D. E. Spence, P. N. Kean, and W. Sibbett, Opt. Lett. **16**, 42 (1991).

[8] S. A. Rice, Nature **403**, 496 (2000).

[9] A. Assion, T. Baumert, M. Bergt, T. Brixner, B. Kiefer, V. Seyfried, M. Strehle, and G. Gerber, Science **282**, 919 (1998).

[10] P. Brumer and M. Shapiro, Chem Phys. Lett. **126**, 541 (1986).

[11] A. H. Zewail, J. Phys. Chem. A **104**, 5660 (2000).

[12] D. W. Chandler and P. L. Houston, J. Chem. Phys. **87**, 1445 (1987).

[13] J. Ullrich and H. Schmidt-Böcking, Phys. Lett. A **125**, 193 (1987).

[14] Georges Charpak, *The Nobel Prize in Physics 1992*.

[15] A. G. Suits and R. E. Continetti, eds., *Imaging in Chemical Dynamics*, Vol. 770 (American Chemical Society, 2000).

[16] J. Ullrich, R. Doerner, V. Mergel, O. Jagutzki, L. Spielberger, and H. Schmidt-Boecking, *Cold-target recoil-ion momentum-spectroscopy: First results and future perspectives of a novel high resolution technique for the investigation of collision induced many-particle reactions* (1994), gSI–94-63(PREPR),.Germany.

[17] *History of COLTRIMS*, https://www.atom.uni-frankfurt.de/research/coltrims/history/.

[18] A. T. J. B. Eppink and D. H. Parker, Rev. Sci. Instrum. **68**, 3477 (1997).

[19] S. Svensson, J. Phys. B: At. Mol. Opt. Phys. **38**, S821 (2005).

[20] G. Prümper and K. Ueda, Nucl. Instrum. Methods Phys. Res., Sect. A **574**, 350 (2007).

[21] M. Lavollée and V. Brems, J. Chem. Phys. **110**, 918 (1999).

[22] K. Ueda and J. H. D. Eland, J. Phys. B: At., Mol. Opt. Phys. **38**, S839 (2005).

[23] Y. Muramatsu, K. Ueda, N. Saito, H. Chiba, M. Lavollée, A. Czasch, T. Weber, O. Jagutzki, H. Schmidt-Böcking, R. Moshammer, U. Becker, K. Kubozuka, and I. Koyano, Phys. Rev. Lett. **88** (2002).

[24] A. De Fanis, N. Saito, A. A. Pavlychev, D. Y. Ladonin, M. Machida, K. Kubozuka, I. Koyano, K. Okada, K. Ikejiri, A. Cassimi, A. Czasch, R. Dörner, H. Chiba, Y. Sato, and K. Ueda, Phys. Rev. Lett. **89**, 023006 (2002).

[25] A. Landers, T. Weber, I. Ali, A. Cassimi, M. Hattass, O. Jagutzki, A. Nauert, T. Osipov, A. Staudte, M. Prior, H. Schmidt-Böcking, C. Cocke, and R. Dörner, Phys. Rev. Lett. **87**, 013002 (2001).

[26] A. Lafosse, M. Lebech, J. C. Brenot, P. M. Guyon, O. Jagutzki, L. Spielberger, M. Vervloet, J. C. Houver, and D. Dowek, Phys. Rev. Lett. **84**, 5987 (2000).

[27] F. Heiser, O. Gessner, J. Viefhaus, K. Wieliczek, R. Hentges, and U. Becker, Phys. Rev. Lett. **79**, 2435 (1997).

[28] R. Casiday and R. Frey, "I Have Seen the Light!" Vision and Light-Induced Molecular Changes Http://www.chemistry.wustl.edu/ edudev/labtutorials/vision/vision.html.

[29] R. W. Schoenlein, L. A. Peteanu, R. A. Mathies, and C. V. Shank, Science **254**, 412 (1991).

[30] J. M. Mativetsky, G. Pace, M. Elbing, M. A. Rampi, M. Mayor, and P. Samorì, J. Am. Chem. Soc. **130**, 9192 (2008).

[31] F. Leyssner, S. Hagen, L. Óvári, J. Dokić, P. Saalfrank, M. V. Peters, S. Hecht, T. Klamroth, and P. Tegeder, J. Phys. Chem. C **114**, 1231 (2010).

[32] J. N. Henderson, Ai Hui-Wang, R. E. Campbell, and S. J. Remington, Proc. Natl. Acad. Sci. U. S. A. **104**, 6672 (2007).

[33] M. Pitzer, M. Kunitski, A. S. Johnson, T. Jahnke, H. Sann, F. Sturm, L. P. H. Schmidt, H. Schmidt-Böcking, R. Dörner, J. Stohner, J. Kiedrowski, M. Reggelin, S. Marquardt, A. Schießer, R. Berger, and M. S. Schöffler, Science **341**, 1096 (2013).

[34] M. Pitzer, G. Kastirke, M. Kunitski, T. Jahnke, T. Bauer, C. Goihl, F. Trinter, C. Schober, K. Henrichs, J. Becht, S. Zeller, H. Gassert, M. Waitz, A. Kuhlins, H. Sann, F. Sturm, F. Wiegandt, R. Wallauer, L. P. H. Schmidt, A. S. Johnson, M. Mazenauer, B. Spenger, S. Marquardt, S. Marquardt, H. Schmidt-Böcking, J. Stohner, R. Dörner, M. Schöffler, and R. Berger, ChemPhysChem **17**, 2465 (2016).

[35] U. Ablikim, C. Bomme, H. Xiong, E. Savelyev, R. Obaid, B. Kaderiya, S. Augustin, K. Schnorr, I. Dumitriu, T. Osipov, R. Bilodeau, D. Kilcoyne, V. Kumarappan, A. Rudenko, N. Berrah, and D. Rolles, Sci. Rep. **6**, 38202 (2016).

[36] U. Ablikim, C. Bomme, E. Savelyev, H. Xiong, R. Kushawaha, R. Boll, K. Amini, T. Osipov, D. Kilcoyne, A. Rudenko, N. Berrah, and D. Rolles, Phys. Chem. Chem. Phys. **19**, 13419 (2017).

[37] U. Becker and D. Shirley, A, *Vuv and Soft X-Ray Photoionization* (Springer, 1996).

[38] B. M. D. Erk, *Fragmentation Dynamics of Small Molecules upon Multiple Ionization by X-Ray Free-Electron Laser Pulses*, Ph.D. thesis, Heidelberg University (2013).

[39] B. H. Bransden and C. J. Joachain, *Physics of atoms and molecules*, 2nd ed. (Pearson, 2003).

[40] J. -J. Yeh, *Atomic Calculation of Photoionization Cross-sections and Asymmetry Parameters* (Gordon & Breach Science Publishers, 1993).

[41] D. Rolles, "Scattering and Coherence Phenomena in the Photoionization of Small Molecules," (Diplom-Physiker, Berlin, 2005).

[42] J. Viefhaus, M. Braune, S. Korica, A. Reinköster, D. Rolles, and U. Becker, J. Phys. B: At., Mol. Opt. Phys. **38**, 3885 (2005).

[43] J. Viefhaus, A. Grum-Grzhimailo, N. Kabachnik, and U. Becker, J. Electron. Spectrosc. Relat. Phenom. **141**, 121 (2004).

[44] T. A. Carlson and M. O. Krause, Phys. Rev. Lett. **14**, 390 (1965).

[45] T. A. Carlson and M. O. Krause, Phys. Rev. Lett. **17**, 1079 (1966).

[46] L. V. Keldysh, Sov. Phys. JETP **20**, 1307 (1965).

[47] J. Schander and B. R. Russell, J. Am. Chem. Soc. **98**, 6900 (1976).

[48] K. Wittel, W. S. Felps, L. Klasinc, and S. P. McGlynn, J. Chem. Phys. **65**, 3698 (1976).

[49] R. Boll, *Imaging Molecular Structure with Photoelectron Diffraction*, Ph.D. thesis, Heidelberg University (2014).

[50] Th. Ergler, A. Rudenko, B. Feuerstein, K. Zrost, C. D. Schröter, R. Moshammer, and J. Ullrich, Phys. Rev. Lett. **97**, 193001 (2006).

[51] A. Rudenko, T. Ergler, B. Feuerstein, K. Zrost, C. D. Schröter, R. Moshammer, and J. Ullrich, Chem. Phys. **329**, 193 (2006).

[52] J. Ullrich, R. Moshammer, R. Dörner, O. Jagutzki, V. Mergel, H. Schmidt-Böcking, and L. Spielberger, J. Phys. B: At., Mol. Opt. Phys. **30**, 2917 (1997).

[53] R. Dörner, V. Mergel, O. Jagutzki, L. Spielberger, J. Ullrich, R. Moshammer, and H. Schmidt-Böcking, Phys. Rep. **330**, 95 (2000).

[54] J. Ullrich, R. Moshammer, A. Dorn, R. Dörner, L. P. H. Schmidt, and H. Schmidt-Böcking, Rep. Prog. Phys. **66**, 1463 (2003).

[55] RoentDek Handels GmbH, http://www.roentdek.com.

[56] O. Jagutzki, A. Cerezo, A. Czasch, R. Dorner, M. Hattas, M. Huang, V. Mergel, U. Spillmann, K. Ullmann-Pfleger, T. Weber, H. Schmidt-Bocking, and G. D. W. Smith, IEEE Trans. Nucl. Sci. **49**, 2477 (2002).

[57] *ALS building night view*, http://today.lbl.gov/wp-content/uploads/sites/3/2014/09/lbnlnight.jpeg.

[58] *ALS floor diagram*, http://www2.lbl.gov/MicroWorlds/ALSTool/.

[59] T. Osipov, *Experimental Study of Photo-Electron Diffraction from Two-Center Molecules by Means of the COLTRIMS Technique*, Ph.D. thesis, Kansas State University (2013).

[60] G. Kaindl, K. Schulz, P. Heimann, J. Bozek, and A. Schlachter, Synchrotron Radiation News **8**, 29 (1995).

[61] T. Warwick, P. Heimann, D. Mossessian, W. McKinney, and H. Padmore, Rev. Sci. Instrum. **66**, 2037 (1995).

[62] M. Zohrabi, *Quantum control of molecular fragmentation in strong laser field*, Ph.D. thesis, Kansas State University (2014).

[63] D. Strickland and G. Mourou, Opt. Commun. **55**, 447 (1985).

[64] J.-C. Diels and W. Rudolph, *Ultrashort Laser Pulse Phenomena, Chapter 7, Femtosecond Pulse Amplification*, 2nd ed. (Academic Press, 2006).

[65] D. Rolles, R. Boll, M. Adolph, A. Aquila, C. Bostedt, J. D. Bozek, H. N. Chapman, R. Coffee, N. Coppola, P. Decleva, T. Delmas, S. W. Epp, B. Erk, F. Filsinger, L. Foucar, L. Gumprecht, A. Hömke, T. Gorkhover, L. Holmegaard, P. Johnsson, C. Kaiser, F. Krasniqi, K.-U. Kühnel, J. Maurer, M. Messerschmidt, R. Moshammer, W. Quevedo, I. Rajkovic, A. Rouzée, B. Rudek, I. Schlichting, C. Schmidt, S. Schorb, C. D. Schröter, J. Schulz, H. Stapelfeldt, M. Stener, S. Stern, S. Techert, J. Thøgersen, M. J. J. Vrakking, A. Rudenko, J. Küpper, and J. Ullrich, J. Phys. B: At., Mol. Opt. Phys. **47**, 124035 (2014).

[66] L. Strüder, S. Epp, D. Rolles, R. Hartmann, P. Holl, G. Lutz, H. Soltau, R. Eckart, C. Reich, K. Heinzinger, C. Thamm, A. Rudenko, F. Krasniqi, K.-U. Kühnel, C. Bauer, C.-D. Schröter, R. Moshammer, S. Techert, D. Miessner, M. Porro, O. Hölker, N. Meidinger, N. Kimmel, R. Andritschke, F. Schopper, G. Weidenspointner, A. Ziegler, D. Pietschner, S. Herrmann, U. Pietsch, A. Walenta, W. Leitenberger, C. Bostedt, T. Möller, D. Rupp, M. Adolph, H. Graafsma, H. Hirsemann, K. Gärtner, R. Richter, L. Foucar, R. L. Shoeman, I. Schlichting, and J. Ullrich, Nucl. Instrum. Methods Phys. Res., Sect. A **614**, 483 (2010).

[67] SIMION® 8, *The field and particle trajectory simulator, Scientific Instrument Services, Inc*, (Date of access:29/04/2015).

[68] R. Moshammer, M. Unverzagt, W. Schmitt, J. Ullrich, and H. Schmidt-Böcking, Nucl. Instr. Meth. Phys. Res. B **108**, 425 (1996).

[69] J. L. WIZA, Nucl. Instr. Meth. Phys. Res. **162**, 587 (1979).

[70] T. Gys, Nucl. Instrum. Methods Phys. Res., Sect. A **787**, 254 (2015).

[71] P. Cörlin, *Tracing ultra-fast molecular dynamics in O_2^+ and N_2^+ with XUV-IR pump-probe experiments*, Ph.D. thesis, Heidelberg University (2015).

[72] N. Neumann, *Fragmentationsdynamik von CO_2*, Ph.D. thesis, Goethe University Frankfurt (2010).

[73] N. Neumann, D. Hant, L. P. H. Schmidt, J. Titze, T. Jahnke, A. Czasch, M. S. Schöffler, K. Kreidi, O. Jagutzki, H. Schmidt-Böcking, and R. Dörner, Phys. Rev. Lett. **104** (2010).

[74] T. Weber, O. Jagutzki, M. Hattass, A. Staudte, A. Nauert, L. Schmidt, M. H. Prior, A. L. Landers, A. Bräuning-Demian, and H. Bräuning, J. Phys. B: At., Mol. Opt. Phys. **34**, 3669 (2001).

[75] M. Lundqvist, D. Edvardsson, P. Baltzer, and B. Wannberg, J. Phys. B: At., Mol. Opt. Phys. **29**, 1489 (1996).

[76] S. Manzhos and Loock Hans-Peter, Comput. Phys. Commun. **154**, 76 (2003).

[77] C. E. Rallis, T. G. Burwitz, P. R. Andrews, M. Zohrabi, R. Averin, S. De, B. Bergues, B. Jochim, A. V. Voznyuk, N. Gregerson, B. Gaire, I. Znakovskaya, J. McKenna, K. D. Carnes, M. F. Kling, I. Ben-Itzhak, and E. Wells, Rev. Sci. Instrum. **85**, 113105 (2014).

[78] J. R. Gascooke, S. T. Gibson, and W. D. Lawrance, J. Chem. Phys. **147**, 013924 (2017).

[79] A. Derevianko, W. R. Johnson, and K. T. Cheng, At. Data Nucl. Data Tables **77**, 97 (2001).

[80] P. A. Heimann, M. Koike, C. W. Hsu, D. Blank, X. M. Yang, A. G. Suits, Y. T. Lee, M. Evans, C. Y. Ng, C. Flaim, and H. A. Padmore, Rev. Sci. Instrum. **68**, 1945 (1997).

[81] T. Yang, T. P. Troy, B. Xu, O. Kostko, M. Ahmed, A. M. Mebel, and R. I. Kaiser, Angew. Chem. Int. Ed. **55**, 14983 (2016).

[82] A. Golan, K. B. Bravaya, R. Kudirka, O. Kostko, S. R. Leone, A. I. Krylov, and M. Ahmed, Nat. Chem. **4**, 323 (2012).

[83] O. Kostko, L. Belau, K. R. Wilson, and M. Ahmed, J. Phys. Chem. A **112**, 9555 (2008).

[84] B. Xu, M. I. Jacobs, O. Kostko, and M. Ahmed, ChemPhysChem (2017).

[85] A. Golan and M. Ahmed, J. Vis. Exp. (2012).

[86] C. Nicolas, J. Shu, D. S. Peterka, M. Hochlaf, L. Poisson, S. R. Leone, and M. Ahmed, J. Am. Chem. Soc. **128**, 220 (2006).

[87] T. A. Cool, J. Wang, K. Nakajima, C. A. Taatjes, and A. Mcllroy, Int. J. Mass spectrom. **247**, 18 (2005).

[88] F. Qi, R. Yang, B. Yang, C. Huang, L. Wei, J. Wang, L. Sheng, and Y. Zhang, Rev. Sci. Instrum. **77**, 084101 (2006).

[89] H. K. Woo, P. Wang, K. C. Lau, X. Xing, and C. Y. Ng, J. Phys. Chem. A **108**, 9637 (2004).

[90] Y. J. Bae, M. Lee, and M. S. Kim, J. Phys. Chem. A **110**, 8535 (2006).

[91] O. Thorstad, Acta. Chem. Scand. B. **29**, 647 (1975).

[92] U. K. Genick, S. M. Soltis, P. Kuhn, I. L. Canestrelli, and E. D. Getzoff, Nature **392**, 206 (1998).

[93] C. Ko, B. Levine, A. Toniolo, L. Manohar, S. Olsen, H.-J. Werner, and T. J. Martinez, J. Am. Chem. Soc. **125**, 12710 (2003).

[94] N. Abshiru, O. Caron-Lizotte, R. E. Rajan, A. Jamai, C. Pomies, A. Verreault, and P. Thibault, Nat. Commun **6**, 8648 (2015).

[95] R. Hubbard and G. Wald, Science **115**, 60 (1952).

[96] D. W. Ball, J. W. Hill, and R. J. Scott, *The Basics of General Organic and Biological Chemistry* (Saylor Foundation, 2011).

[97] C. Desfrançois, H. Abdoul-Carime, C. P. Schulz, and J. P. Schermann, Science **269**, 1707 (1995).

[98] K. Pande, C. D. M. Hutchison, G. Groenhof, A. Aquila, J. S. Robinson, J. Tenboer, S. Basu, S. Boutet, D. P. DePonte, M. Liang, T. A. White, N. A. Zatsepin, O. Yefanov, D. Morozov, D. Oberthuer, C. Gati, G. Subramanian, D. James, Y. Zhao, J. Koralek, J. Brayshaw, C. Kupitz, C. Conrad, S. Roy-Chowdhury, J. D. Coe, M. Metz, P. L. Xavier, T. D. Grant, J. E. Koglin, G. Ketawala, R. Fromme, V. Šrajer, R. Henning, J. C. H. Spence, A. Ourmazd, P. Schwander, U. Weierstall, M. Frank, P. Fromme, A. Barty, H. N. Chapman, K. Moffat, J. J. van Thor, and M. Schmidt, Science **352**, 725 (2016).

[99] T. Osipov, C. L. Cocke, M. H. Prior, A. Landers, T. Weber, O. Jagutzki, L. Schmidt, H. Schmidt-Böcking, and R. Dörner, Phys. Rev. Lett. **90**, 233002 (2003).

[100] A. Matsuda, M. Fushitani, E. J. Takahashi, and A. Hishikawa, Phys. Chem. Chem. Phys. **13**, 8697 (2011).

[101] H. Ibrahim, B. Wales, S. Beaulieu, B. E. Schmidt, N. Thiré, E. P. Fowe, É. Bisson, C. T. Hebeisen, V. Wanie, M. Giguére, J.-C. Kieffer, M. Spanner, A. D. Bandrauk, J. Sanderson, M. S. Schuurman, and F. Légaré, Nat. Commun **5**, 4422 (2014).

[102] Y. H. Jiang, A. Rudenko, O. Herrwerth, L. Foucar, M. Kurka, K. U. Kühnel, M. Lezius, M. F. Kling, J. van Tilborg, A. Belkacem, K. Ueda, S. Düsterer, R. Treusch, C. D. Schröter, R. Moshammer, and J. Ullrich, Phys. Rev. Lett. **105** (2010).

[103] Y. H. Jiang, A. Senftleben, M. Kurka, A. Rudenko, L. Foucar, O. Herrwerth, M. F. Kling, M. Lezius, J. V. Tilborg, A Belkacem, K. Ueda, D. Rolles, R. Treusch, Y. Z. Zhang, Y. F. Liu, C. D. Schröter, J. Ullrich, and R. Moshammer, J. Phys. B: At. Mol. Opt. Phys. **46**, 164027 (2013).

[104] C. E. Liekhus-Schmaltz, I. Tenney, T. Osipov, A. Sanchez-Gonzalez, N. Berrah, R. Boll, C. Bomme, C. Bostedt, J. D. Bozek, S. Carron, R. Coffee, J. Devin, B. Erk, K. R.

Ferguson, R. W. Field, L. Foucar, L. J. Frasinski, J. M. Glownia, M. Gühr, A. Kamalov, J. Krzywinski, H. Li, J. P. Marangos, T. J. Martinez, B. K. McFarland, S. Miyabe, B. Murphy, A. Natan, D. Rolles, A. Rudenko, M. Siano, E. R. Simpson, L. Spector, M. Swiggers, D. Walke, S. Wang, T. Weber, P. H. Bucksbaum, and V. S. Petrovic, Nat. Commun **6**, 8199 (2015).

[105] Z. Vager, R. Naaman, and E. P. Kanter, Science **244**, 426 (1989).

[106] Z. Vager, D. Zajfman, T. Graber, and E. P. Kanter, Phys. Rev. Lett. **71**, 4319 (1993).

[107] K. Ueda, A. D. Fanis, N. Saito, M. Machida, K. Kubozuka, H. Chiba, Y. Muramatu, Y. Sato, A. Czasch, O. Jaguzki, R. Dörner, A. Cassimi, M. Kitajima, T. Furuta, H. Tanaka, S. L. Sorensen, K. Okada, S. Tanimoto, K. Ikejiri, Y. Tamenori, H. Ohashi, and I. Koyano, Chem. Phys. **289**, 135 (2003).

[108] P. Herwig, K. Zawatzky, M. Grieser, O. Heber, B. Jordon-Thaden, C. Krantz, O. Novotny, R. Repnow, V. Schurig, D. Schwalm, Z. Vager, A. Wolf, O. Trapp, and H. Kreckel, Science **342**, 1084 (2013).

[109] T. Yatsuhashi, N. Nakashima, and J. Azuma, J. Phys. Chem. A **117**, 1393 (2013).

[110] B. Wannberg, S. Svensson, M. P. Keane, L. Karlsson, and P. Baltzer, Chem. Phys. **133**, 281 (1989).

[111] T. Uphues, M. Schultze, M. F. Kling, M. Uiberacker, S. Hendel, U. Heinzmann, N. M. Kabachnik, and M. Drescher, New J. Phys. **10**, 025009 (2008).

[112] J. Eland, Mol. Phys. **61**, 725 (1987).

[113] S. Hsieh and J. H. D. Eland, J. Phys. B: At., Mol. Opt. Phys. **30**, 4515 (1997).

[114] C. Wu, C. Wu, D. Song, H. Su, Y. Yang, Z. Wu, X. Liu, H. Liu, M. Li, Y. Deng, Y. Liu, L.-Y. Peng, H. Jiang, and Q. Gong, Phys. Rev. Lett. **110** (2013).

[115] A. Thompson, *X-Ray Data Booklet*, 3rd ed. (Lawrence Berkeley National Laboratory, 2009).

[116] S. Zigo, A.-T. Le, P. Timilsina, and C. A. Trallero-Herrero, Sci. Rep. **7**, 42149 (2017).

[117] J. H. Posthumus, L. J. Frasinski, A. J. Giles, and K. Codling, J. Phys. B: At. Mol. Opt. Phys. **28**, L349 (1995).

[118] J. H. Posthumus, A. J. Giles, M. R. Thompson, and K. Codling, J. Phys. B: At., Mol. Opt. Phys. **29**, 5811 (1996).

[119] K.-C. Lau and C.-Y. Ng, Acc. Chem. Res. **39**, 823 (2006).

[120] M. Thompson, P. A. Hewitt, and D. S. Wooliscroft, Anal. Chem. **50**, 690 (1978).

[121] A. Bodi, W. R. Stevens, and T. Baer, J. Phys. Chem. A **115**, 726 (2011).

[122] B. Erk, D. Rolles, L. Foucar, B. Rudek, S. W. Epp, M. Cryle, C. Bostedt, S. Schorb, J. Bozek, A. Rouzee, A. Hundertmark, T. Marchenko, M. Simon, F. Filsinger, L. Christensen, S. De, S. Trippel, J. Küpper, H. Stapelfeldt, S. Wada, K. Ueda, M. Swiggers, M. Messerschmidt, C. D. Schröter, R. Moshammer, I. Schlichting, J. Ullrich, and A. Rudenko, Phys. Rev. Lett. **110**, 053003 (2013).

[123] A. Hishikawa, A. Iwamae, K. Hoshina, M. Kono, and K. Yamanouchi, Chem. Phys. Lett. **282**, 283 (1998).

[124] J. H. Sanderson, A. El-Zein, W. A. Bryan, W. R. Newell, A. J. Langley, and P. F. Taday, Phys. Rev. A **59**, R2567 (1999).

[125] F. Légaré, K. Lee, I. Litvinyuk, P. Dooley, S. Wesolowski, P. Bunker, P. Dombi, F. Krausz, A. Bandrauk, D. Villeneuve, and P. Corkum, Phys. Rev. A **71** (2005).

[126] D. Mathur, Phys. Rep. **225**, 193 (1993).

[127] P. Moretto-Capelle, D. Bordenave-Montesquieu, and A. Bordenave-Montesquieu, J. Phys. B: At., Mol. Opt. Phys. **33**, L539 (2000).

[128] L. Adoui, M. Tarisien, J. Rangama, P. Sobocinsky, A. Cassimi, J. Y. Chesnel, F. Frémont, B. Gervais, A. Dubois, M. Krishnamurthy, and others, Phys. Scripta **2001**, 89 (2001).

[129] T. Kitamura, T. Nishide, H. Shiromaru, Y. Achiba, and N. Kobayashi, J. Chem. Phys. **115**, 5 (2001).

[130] M. R. Jana, P. N. Ghosh, B. Bapat, R. K. Kushawaha, K. Saha, I. A. Prajapati, and C. P. Safvan, Phys. Rev. A **84** (2011).

[131] L. J. Frasinski, M. Stankiewicz, K. J. Randall, P. A. Hatherly, and K. Codling, J. Phys. B: At., Mol. Opt. Phys. **19**, L819 (1986).

[132] J. H. D. Eland, Chem. Phys. Lett. **203**, 353 (1993).

[133] K. Codling and L. J. Frasinski, Contemp. Phys. **35**, 243 (1994).

[134] S. Hsieh and J. H. D. Eland, J. Phys. B: At., Mol. Opt. Phys. **29**, 5795 (1996).

[135] S. Viftrup, V. Kumarappan, S. Trippel, H. Stapelfeldt, E. Hamilton, and T. Seideman, Phys. Rev. Lett. **99** (2007).

[136] I. Nevo, L. Holmegaard, J. H. Nielsen, J. L. Hansen, H. Stapelfeldt, F. Filsinger, G. Meijer, and J. Küpper, Phys. Chem. Chem. Phys. **11**, 9912 (2009).

[137] X. Ren, V. Makhija, and V. Kumarappan, Phys. Rev. Lett. **112** (2014).

[138] E. Savelyev, R. Boll, C. Bomme, N. Schirmel, H. Redlin, B. Erk, S. Düsterer, E. Müller, H. Höppner, S. Toleikis, J. Müller, M. Kristin Czwalinna, R. Treusch, T. Kierspel, T. Mullins, S. Trippel, J. Wiese, J. Küpper, F. Brauβe, F. Krecinic, A. Rouzée, P. Rudawski, P. Johnsson, K. Amini, A. Lauer, M. Burt, M. Brouard, L. Christensen, J. Thøgersen, H. Stapelfeldt, N. Berrah, M. Müller, A. Ulmer, S. Techert, A. Rudenko, and D. Rolles, New J. Phys **19**, 043009 (2017).

[139] K. Amini, R. Boll, A. Lauer, M. Burt, J. W. L. Lee, L. Christensen, F. Brauβe, T. Mullins, E. Savelyev, U. Ablikim, N. Berrah, C. Bomme, S. Düsterer, B. Erk, H. Höppner, P. Johnsson, T. Kierspel, F. Krecinic, J. Küpper, M. Müller, E. Müller, H. Redlin, A. Rouzée, N. Schirmel, J. Thøgersen, S. Techert, S. Toleikis, R. Treusch, S. Trippel, A. Ulmer, J. Wiese, C. Vallance, A. Rudenko, H. Stapelfeldt, M. Brouard, and D. Rolles, The Journal of Chemical Physics **147**, 013933 (2017).

[140] S. Hsieh and J. H. D. Eland, J. Chem. Phys. **103**, 1006 (1995).

[141] D. W. Lindle, P. H. Kobrin, C. M. Truesdale, T. A. Ferrett, P. A. Heimann, H. G. Kerkhoff, U. Becker, and D. A. Shirley, Phys. Rev. A **30**, 239 (1984).

[142] D. Holland, I. Powis, G. Öhrwall, L. Karlsson, and W. von Niessen, Chem. Phys. **326**, 535 (2006).

[143] J. N. Cutler, G. M. Bancroft, and K. H. Tan, J. Chem. Phys. **97**, 7932 (1992).

[144] K. Mertens, N. Gerken, S. Klumpp, M. Braune, and M. Martins, J. Mod. Opt **63**, 383 (2016).

[145] F. Penent, J. Palaudoux, P. Lablanquie, L. Andric, R. Feifel, and J. H. D. Eland, Phys. Rev. Lett. **95** (2005).

[146] A. I. Kuleff, N. V. Kryzhevoi, M. Pernpointner, and L. S. Cederbaum, Phys. Rev. Lett. **117**, 093002 (2016).

[147] P. F. Barbara, T. J. Meyer, and M. A. Ratner, J. Chem. Phys. **100**, 13148 (1996).

[148] M. Delor, P. A. Scattergood, I. V. Sazanovich, A. W. Parker, G. M. Greetham, A. J. H. M. Meijer, M. Towrie, and J. A. Weinstein, Science **346**, 1492 (2014).

[149] P. Lablanquie, L. Andric, J. Palaudoux, U. Becker, M. Braune, J. Viefhaus, J. H. D. Eland, and F. Penent, J. Electron. Spectrosc. Relat. Phenom. Electronic Spectroscopy and Structure: ICESS-10, **156–158**, 51 (2007).

[150] R. Guillemin, P. Decleva, M. Stener, C. Bomme, T. Marin, L. Journel, T. Marchenko, R. K. Kushawaha, K. Jänkälä, N. Trcera, K. P. Bowen, D. W. Lindle, M. N. Piancastelli, and M. Simon, Nat. Commun **6**, 6166 (2015).

[151] R. K. Singh, G. S. Lodha, V. Sharma, I. A. Prajapati, K. P. Subramanian, and B. Bapat, Phys. Rev. A **74**, 022708 (2006).

[152] E. Wang, X. Shan, Z. Shen, M. Gong, Y. Tang, Y. Pan, K.-C. Lau, and X. Chen, Phys. Rev. A **91** (2015).

[153] P. Bhatt, R. Singh, N. Yadav, and R. Shanker, Phys. Rev. A **85** (2012).

[154] B. Wales, É. Bisson, R. Karimi, S. Beaulieu, A. Ramadhan, M. Giguère, Z. Long, W.-K. Liu, J.-C. Kieffer, F. Légaré, and J. Sanderson, J. Electron. Spectrosc. Relat. Phenom. **195**, 332 (2014).

[155] L. Hua, W.-B. Lee, M.-H. Chao, B. Zhang, and K.-C. Lin, J. Chem. Phys. **134**, 194312 (2011).

[156] D. Murdock, S. J. Harris, J. Luke, M. P. Grubb, A. J. Orr-Ewing, and M. N. R. Ashfold, Phys. Chem. Chem. Phys. **16**, 21271 (2014).

[157] C. Bordas, F. Paulig, H. Helm, and D. L. Huestis, Rev. Sci. Instrum. **67**, 2257 (1996).

[158] G. A. Garcia, L. Nahon, and I. Powis, Rev. Sci. Instrum. **75**, 4989 (2004).

[159] J. R. Gascooke, S. T. Gibson, and W. D. Lawrance, The Journal of Chemical Physics **147**, 013924 (2017).

[160] WIENER GmbH, *Universal low and high voltage power supply system*.

Appendix A

TOF jitter correction in the VMI experiments

In the operation of the double-sided VMI spectrometer used in the synchrotron experiments at the ALS for conducting coincidence ion-ion-electron experiments, it is the signal from the electron MCP that triggers the whole data acquisition system. The reason for using the electron TOF signal as trigger is that the synchrotron beam at the ALS has high (e.g. 500MHz) repetition rate in the multi-bunch mode, meaning synchrotron pulses are 2 ns away from each other. And if, instead, the synchrotron light signal (e.g. a signal generated from a photodiode when the synchrotron pulse hits) or the electronic "bunchmarker" signal provided by the facility are used as trigger, then it is impossible to achieve event by event data collection due to possible mixing of photoionization events caused by different pulses. Thus, the electron TOF signal was used to trigger the data acquisition and provide the timing reference. The TOF of electrons in the double-sided VMI is around 5 ns, which is the time it takes for an electron to travel from the interaction region to the surface of the MCP.

During one of the experiments reported in this thesis, an operator error caused the detectors to be flooded with a very high count rate of ions and electrons, which cause one of the resistors in the signal outcoupling of the electron detector to burn. This technical failure resulted in the experiment not having the fast electron MCP signals to trigger the

data acquisition system. Instead, one of the position signals from the electron detector, i.e. one of the four position signals picked up at the end of the delay line wires, was used as the trigger for the coincidence system. However, the arrival time of the position signals picked from one end of the delay-line wires can vary between 0 to 40 ns in time compared to the MCP signal, depending on the spot where the particle hit on the wire. Thus, the whole series of time and position signals on both electron and ion side detectors will depend on the position of the electrons. This effect, which we named time-jittering, will smear out the time resolution for the ions, distorting the correlation between coincidence signals and making it impossible to conduct high-resolution momentum imaging analysis.

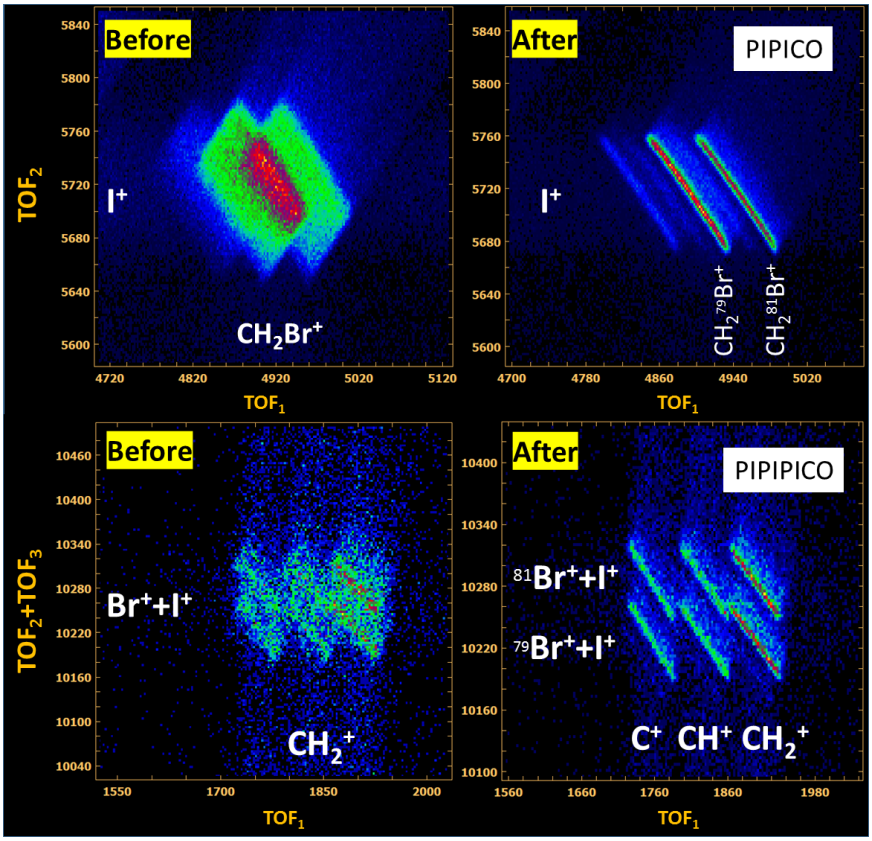

Figure A.1: PIPICO and PIPIPICO maps showing the two- and three-body coincidence channels, CH_2Br^++I^+ and CH_2^++Br^++I^+ after photoionization of CH_2IBr molecule using 107-eV synchrotron photons. (Left) Raw spectra with a position signal acted as trigger. (Right) A time-jitter corrected spectra.

Figure A.1 shows both the raw PIPICO map (left) and the time-jitter corrected PIPICO map (right). The PIPICO map is zoomed into the two-body breakup channel after pho-

toionization of 1,2-$C_2H_2Br_2$ with 120-eV synchrotron photons. In order to correct the time-jittering for the ion TOF signals, the "lost" electron MCP signal has to be reconstructed. According to the "time-sum" condition, the electron time signal T_e (from the electron ejection to the time of impact on the MCP) can be expressed as

$$T_e = \frac{(t_{x1} + t_{x2}) - C_x}{2}, \tag{A.1}$$

$$T_e = \frac{(t_{y1} + t_{y2}) - C_y}{2}. \tag{A.2}$$

where C_x and C_y are the constants representing the total time it takes for an electronic signal to propagate through the entire length of the x and y wires, t_{x1}, t_{x2} and t_{y1}, t_{y2} are the timing signals picked up from the two ends of the x and y wires. In this particular experiment conducted in April of 2015 at the ALS, the timing signal t_{y1} was used to trigger the entire data acquisition system after the electron MCP resistor was accidently burnt. In order to reconstruct the timing signal T_e for the electrons, the x position wire timing signals, t_{x1} and t_{x2}, are used. The corrected time signals for the ions, TOF_{ion}, can be expressed as

$$TOF_{ion} = TOF_{i\,recorded} - \frac{(t_{x1} + t_{x2} - C_x)}{2}. \tag{A.3}$$

In this equation, $TOF_{ion\,recorded}$ is the recorded time signal when the position time signal t_{y1} was used to trigger the system. C_x can be omitted since a constant shift on all ion time signals will not affect the correlation between coincidence ion TOF signals. So the equation in the data analysis system (e.g. the source code of COBOLDPC software in the analysis shown in Fig. A.1 (b)) can be written as

$$TOF_{ion} = TOF_{ion\,recorded} - \frac{(t_{x1} + t_{x2})}{2}. \tag{A.4}$$

Appendix B

VMI image circularization method

In VMI experiments, ions and electrons are produced from the light-matter interactions within a small volume and are accelerated toward their detectors by the electric field provided by the spectrometer. As the particles travel toward their detectors, they expand spherically due to the velocities gained through acceleration in the electric field. The two dimensional projection of such Newton sphere is projected onto the detector surface and position of each electron is measured and by applying electron inversion techniques such as Onion Peeling [76], BASEX [157] and Abel transformation [158], one can extract one dimensional radial distribution spectrum.

In an ideal measurment, a Newton sphere projected onto the detector surface appears as a perfect circle. However, in an actual experiment, electron position spectrum may be distorted and non-perfect circular images of electrons are measured. The distortion can be caused by external magnetic field, non-uniform detection efficiency of the detector surface or the slightly misalignment of the spectrometer. Such distortions will reduce the experimental resolution, e.g. electron velocity and energy resolution. In this Appendix, an image "circularization" method, is introduced to help remove or reduce the distortion from an otherwise circular electron images to help increase the electron energies.

Figure B.1 (a) shows the electron spectrum of neon after photoionization by 107-eV X-ray synchrotron beam. The dashed red line is a perfect red circle placed on the image to

distinguish distortions on 2s and 2p electron photo-lines. Figure B.1 (b) shows the same position spectrum of photoelectron lines after applying the image "circularization" method.

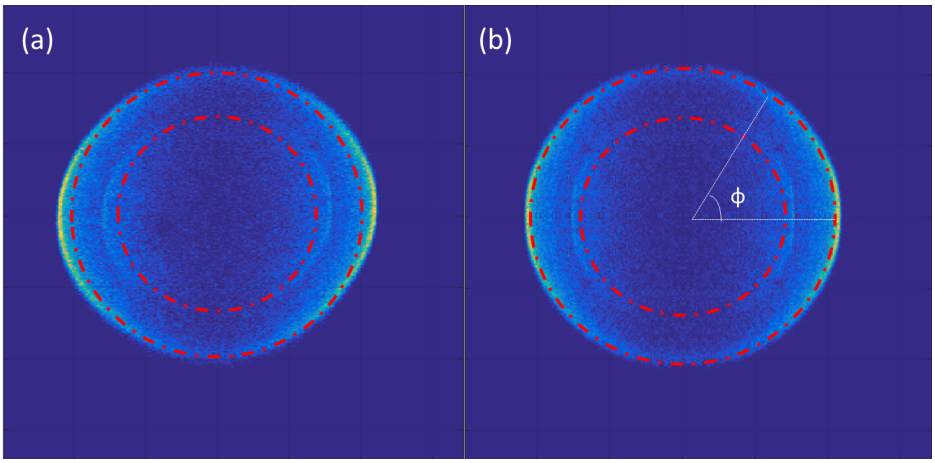

Figure B.1: A VMI image of the electron generated by photoionization of neon atom by 107eV X-ray photons. The dashed red circles are provided to guide the eye to distinguish the distortion of image. (a) distorted image (b) circularized image

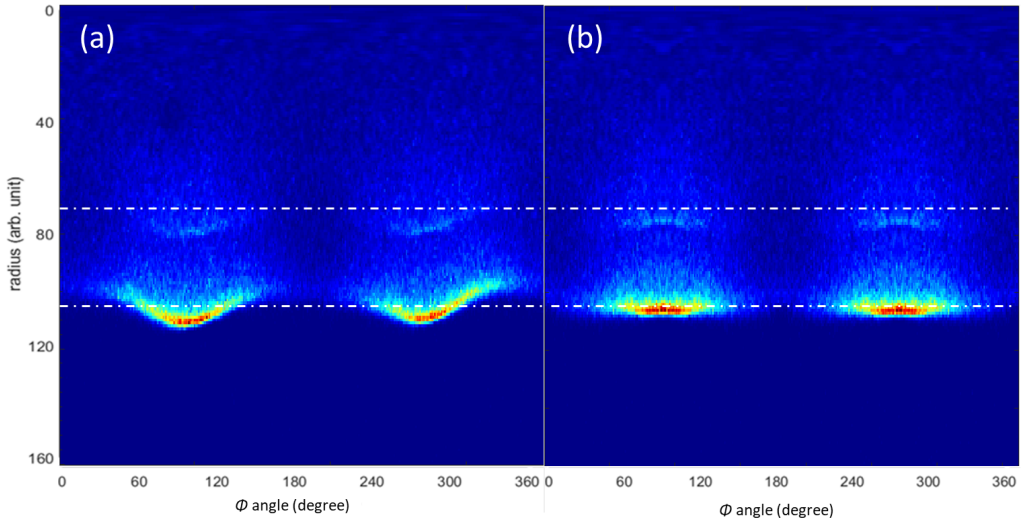

Figure B.2: (a) Radius vs. Phi angle distribution of raw VMI image (distorted) (b) Radius vs. Phi angle distribution of corrected VMI image

Figure B.2 shows the radial distribution as a function of ϕ angle, where ϕ is the symmetry angle labeled in Figure B.1 (b). It presents the distortion of radial photo-lines along ϕ angle in the entire 0-2π range. It is apparent in Figure B.1 (a) that the photo-lines change with respect to the angle ϕ due to the distortion. In order to reduce the distortion on the radial

photo-lines, there are two steps taken during the analysis. In first step, the "good" half of the raw radial distribution is selected. For example, in Figure B.2 (a), events fall between ϕ: (0-180) degree are selected and the data within the region are symmetrized to the other half, e.g. to (180-360) degrees. In the second step, the distortion of the radial photo-lines are corrected by removing the ϕ angle dependence from the radial distribution. The distorted radial photo-lines can be represented by a function of the form

$$Rd(\phi) = Rt + a \times cos(\frac{\pi \times (\phi - b)}{\omega}). \tag{B.1}$$

where Rd is the distorted radius that is a function of ϕ and Rt is the true un-distorted radius. a, b and ω are the fitting parameters that characterize the distortion.

It has to be noted that in this method, only the ϕ angle dependence from the distorted radial line Rt are removed and distortion parameters are assumed to be same for all photo-lines. This means, the parameter "a" is a constant and does not change by radius. It is assumed that a distortion that can be fitted well with a cosine distribution has same effect on all radial photo-lines regardless of their value. This crude assumption may work for photoelectron images that contain electrons with large energy values and with less difference in between. However, in experiments that involve measurment of electrons that result in large range of radial distribution, different radial regions containing photo-lines needs to be extracted and fitted separately to obtain specific radial dependent fitting parameter, e.g. a(Rt). In this Appendix, for brevity, "a" only presumed to be a constant number. For more sophisticated image circularization, one can refer to the method introduced by Gascooke *et al* [159].

By fitting the equation B.2 to the real data, a, b and ω are determined. The un-distorted true radial distribution Rt is obtained by subtracting the distortion curve from the experimental data,

$$Rt = Rd(\phi) - a \times cos(\frac{\pi \times (\phi - b)}{\omega}). \tag{B.2}$$

Appendix C

VMI Spectrometer Voltages

In synchrotron measurments using the double-sided VMI apparatus, voltages for the spectrometer as well as ion/electron detectors are provided through the WIENER universal power supply system [160], shown in Fig. D.4. The VMI spectrometer parts are labeled in C.2. Typically, a simulation is, first, conducted using the SIMION 8.1 software [67] to find optimal voltage parameters, then in the real experiment, mild modifications are made to those voltages to achieve optimized focusing conditions for both electrons and ions. The voltages applied to the ions and electron detectors, e.g. MCP, delay-line wires and meshes are chosen to optimize the coincidence detection condition in each experiment. In this appendix, the table of voltages used during the experiments are provided.

Figure C.1: Picture of the universal power supply system used in the double-sided VMI experiments.

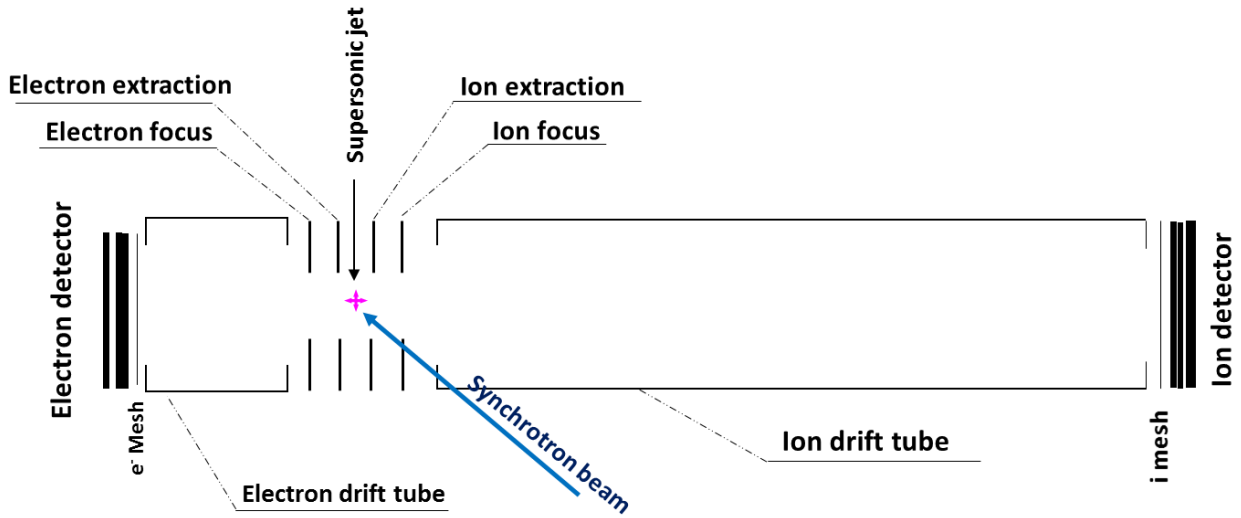

Figure C.2: The schematic figure of double-sided VMI spectrometer.

Molecules	1,2-$C_2H_2Br_2$ [V]	1,2-$C_2H_2Cl_2$ [V]	2,6- & 3,5-DFIB [V]
Time of the experiment [V]	May-2016	May-2016	August-2014
Electron drift tube [V]	3100	5580	3300
Electron focus [V]	600	1080	1000
Electron extraction [V]	100	180	500
Ion extraction [V]	-100	-180	-500
Ion focus [V]	-700	-1260	0
Ion drift tube [V]	-2650	-4770	-3300
Electron delay-line [V]	2950	2950	2908
Electron MCP front [V]	500	500	500
Electron mesh [V]	550	550	780
Ion ANODE [V]	-100	-100	200
Ion MCP front [V]	-2650	-2650	-2500
Ion mesh [V]	-2750	-2750	-2700
Ion reference wire [V]	100	100	300
Ion signal wire [V]	150	150	350

Appendix D

Coulomb Explosion Model Simulation Matlab Scripts

This appendix contains scripts used for the Coulomb explosion model simulation. The scripts help solve the equation of motion for individual ions produced from the dissociation of a molecule via Coulomb repulsion among ionic fragments. The numerical simulation presented in this thesis includes two and three-body fragmentation of isomeric molecules, thus in the following code, Coulomb explosion of two-body ion fragmentation channel $CH_3^+ + I^+$, and the Coulomb explosion of three-body channel $F^+ + C_6HF^+ + I^+$ are presented.

D.1 Coulomb explosion simulation: 2-body

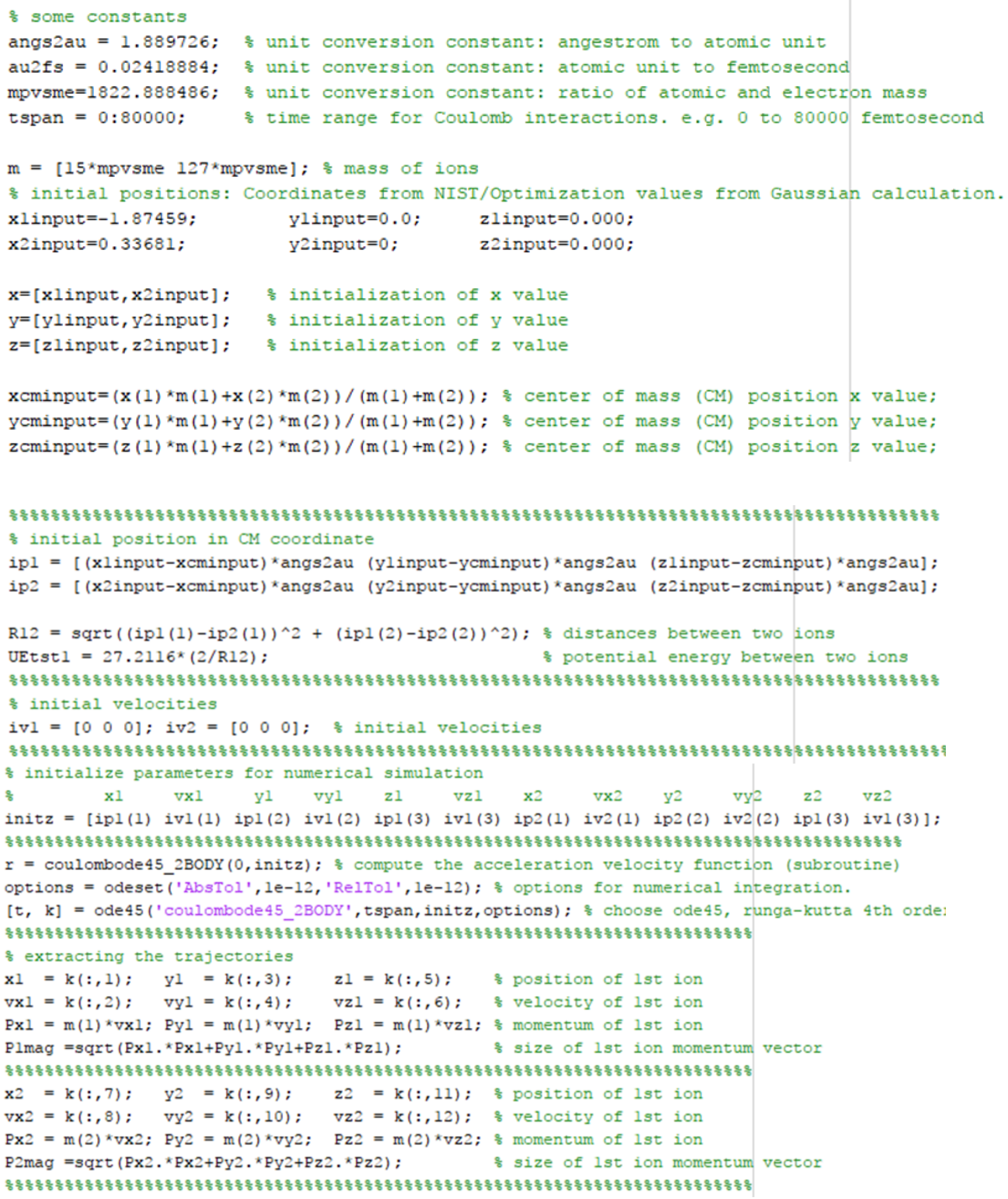

```
% some constants
angs2au = 1.889726;  % unit conversion constant: angestrom to atomic unit
au2fs = 0.02418884;  % unit conversion constant: atomic unit to femtosecond
mpvsme=1822.888486;  % unit conversion constant: ratio of atomic and electron mass
tspan = 0:80000;     % time range for Coulomb interactions. e.g. 0 to 80000 femtosecond

m = [15*mpvsme 127*mpvsme]; % mass of ions
% initial positions: Coordinates from NIST/Optimization values from Gaussian calculation.
x1input=-1.87459;         y1input=0.0;     z1input=0.000;
x2input=0.33681;          y2input=0;       z2input=0.000;

x=[x1input,x2input];   % initialization of x value
y=[y1input,y2input];   % initialization of y value
z=[z1input,z2input];   % initialization of z value

xcminput=(x(1)*m(1)+x(2)*m(2))/(m(1)+m(2)); % center of mass (CM) position x value;
ycminput=(y(1)*m(1)+y(2)*m(2))/(m(1)+m(2)); % center of mass (CM) position y value;
zcminput=(z(1)*m(1)+z(2)*m(2))/(m(1)+m(2)); % center of mass (CM) position z value;


%%%%%%%%%%%%%%%%%%%%%%%%%%%%%%%%%%%%%%%%%%%%%%%%%%%%%%%%%%%%%%%%%%%%%%%%%%%%%%%%%%%%%%%%%
% initial position in CM coordinate
ip1 = [(x1input-xcminput)*angs2au (y1input-ycminput)*angs2au (z1input-zcminput)*angs2au];
ip2 = [(x2input-xcminput)*angs2au (y2input-ycminput)*angs2au (z2input-zcminput)*angs2au];

R12 = sqrt((ip1(1)-ip2(1))^2 + (ip1(2)-ip2(2))^2); % distances between two ions
UEtst1 = 27.2116*(2/R12);                           % potential energy between two ions
%%%%%%%%%%%%%%%%%%%%%%%%%%%%%%%%%%%%%%%%%%%%%%%%%%%%%%%%%%%%%%%%%%%%%%%%%%%%%%%%%%%%%%%%%
% initial velocities
iv1 = [0 0 0]; iv2 = [0 0 0];  % initial velocities
%%%%%%%%%%%%%%%%%%%%%%%%%%%%%%%%%%%%%%%%%%%%%%%%%%%%%%%%%%%%%%%%%%%%%%%%%%%%%%%%%%%%%%%%%%
% initialize parameters for numerical simulation
%         x1     vx1     y1     vy1     z1     vz1     x2     vx2     y2     vy2     z2     vz2
initz = [ip1(1) iv1(1) ip1(2) iv1(2) ip1(3) iv1(3) ip2(1) iv2(1) ip2(2) iv2(2) ip1(3) iv1(3)];
%%%%%%%%%%%%%%%%%%%%%%%%%%%%%%%%%%%%%%%%%%%%%%%%%%%%%%%%%%%%%%%%%%%%%%%%%%%%%%%%%%%%%%%%%%
r = coulombode45_2BODY(0,initz); % compute the acceleration velocity function (subroutine)
options = odeset('AbsTol',1e-12,'RelTol',1e-12); % options for numerical integration.
[t, k] = ode45('coulombode45_2BODY',tspan,initz,options); % choose ode45, runga-kutta 4th orde
%%%%%%%%%%%%%%%%%%%%%%%%%%%%%%%%%%%%%%%%%%%%%%%%%%%%%%%%%%%%%%%%%%%%%%%%%%%
% extracting the trajectories
x1  = k(:,1);   y1  = k(:,3);    z1 = k(:,5);    % position of 1st ion
vx1 = k(:,2);   vy1 = k(:,4);    vz1 = k(:,6);   % velocity of 1st ion
Px1 = m(1)*vx1; Py1 = m(1)*vy1;  Pz1 = m(1)*vz1; % momentum of 1st ion
P1mag =sqrt(Px1.*Px1+Py1.*Py1+Pz1.*Pz1);         % size of 1st ion momentum vector
%%%%%%%%%%%%%%%%%%%%%%%%%%%%%%%%%%%%%%%%%%%%%%%%%%%%%%%%%%%%%%%%%%%%%%%%%%%
x2  = k(:,7);   y2  = k(:,9);    z2  = k(:,11);  % position of 1st ion
vx2 = k(:,8);   vy2 = k(:,10);   vz2 = k(:,12);  % velocity of 1st ion
Px2 = m(2)*vx2; Py2 = m(2)*vy2;  Pz2 = m(2)*vz2; % momentum of 1st ion
P2mag =sqrt(Px2.*Px2+Py2.*Py2+Pz2.*Pz2);         % size of 1st ion momentum vector
%%%%%%%%%%%%%%%%%%%%%%%%%%%%%%%%%%%%%%%%%%%%%%%%%%%%%%%%%%%%%%%%%%%%%%%%%%%
```

```
KER = 27.2116*(0.5*Px1.*Px1/m(1) + 0.5*Px2.*Px2/m(2) + 0.5*Py1.*Py1/m(1) + 0.5*Py2.*Py2/m(2)...
+ 0.5*Pz1.*Pz1/m(1) + 0.5*Pz2.*Pz2/m(2));
KE1 = 27.2116*(0.5*Px1.*Px1/m(1) + 0.5*Py1.*Py1/m(1) + 0.5*Pz1.*Pz1/m(1));
KE2 = 27.2116*(0.5*Px2.*Px2/m(2) + 0.5*Py2.*Py2/m(2) + 0.5*Pz2.*Pz2/m(2));
%%%%%%%%%%%%%%%%%%%%%%%%%%%%%%%%%%%%%%%%%%%%%%%%%%%%%%%%%%%%%%%%%%%%%%%%%%%%
dx12 = x1 - x2; sdx12 = dx12.^2; % distance between two ions in x axis
%%%%%%%%%%%%%%%%%%%%%%%%%%%%%%%%%%%%%%%%%%%%%%%%%%%%%%%%%%%%%%%%%%%%%%%%%%%%
dy12 = y1 - y2; sdy12 = dy12.^2; % distance between two ions in y axis
%%%%%%%%%%%%%%%%%%%%%%%%%%%%%%%%%%%%%%%%%%%%%%%%%%%%%%%%%%%%%%%%%%%%%%%%%%%%
dz12 = z1 - z2; sdz12 = dz12.^2; % distance between two ions in z axis
%%%%%%%%%%%%%%%%%%%%%%%%%%%%%%%%%%%%%%%%%%%%%%%%%%%%%%%%%%%%%%%%%%%%%%%%%%%%
UE = 27.2116*(1./sqrt(sdx12+sdy12+sdz12));  % potential energy between two ions
CONvergence = UE(end);

figure
hold on
plot(tspan*au2fs,KER,'*');  % plot time vs total KER
plot(tspan*au2fs,KE1,'g');  % plot time vs KE of 1st ion
plot(tspan*au2fs,KE2,'r');  % plot time vs KE of 2nd ion
```

Figure D.1: 2-body ion Coulomb explosion simulation Matlab script

```
function r =coulombode45_2BODY(t,k)
% defining the three masses
mpvsme=1822.888486424682;
q1=1; q2=1;  % charges on the ions;
% initial positions
m = [15*mpvsme 127*mpvsme]; % mass of CH3 and I (amu);
% m = [1 1 1]; % for equal masses
r = zeros(12,1);
% relabel input vector z
x1 = k(1);  u1 = k(2);  y1 = k(3);  v1 = k(4);  z1 = k(5);  w1 = k(6);
x2 = k(7);  u2 = k(8);  y2 = k(9);  v2 = k(10); z2 = k(11); w2 = k(12);
% u and v are first derivatives of x and y
r(1)  = u1;  r(3)  = v1;  r(5)  = w1;
r(7)  = u2;  r(9)  = v2;  r(11) = w2;
% compute squared distances
dx12 = x1 - x2; sdx12 = dx12^2;
dx21 = x2 - x1;
dy12 = y1 - y2; sdy12 = dy12^2;
dy21 = y2 - y1;
dz12 = z1 - z2; sdz12 = dz12^2;
dz21 = z2 - z1;
% just distance powered
d12 = (sdx12 + sdy12 + sdz12)^(3/2);
% second order:  accelerations
r(2)  = (q1*q2*dx12/d12)/m(1);   % acc_x for 1st
r(4)  = (q1*q2*dy12/d12)/m(1);   % acc_y for 1st
r(6)  = (q1*q2*dz12/d12)/m(1);   % acc_z for 1st
r(8)  = (q1*q2*dx21/d12)/m(2);   % acc_x for 2st
r(10) = (q1*q2*dy21/d12)/m(2);   % acc_y for 2st
r(12) = (q1*q2*dz21/d12)/m(2);   % acc_z for 2st
```

Figure D.2: Numerical integration function using Runge-Kutta 4th order method: 2-body

D.2 Coulomb explosion simulation: 3-body

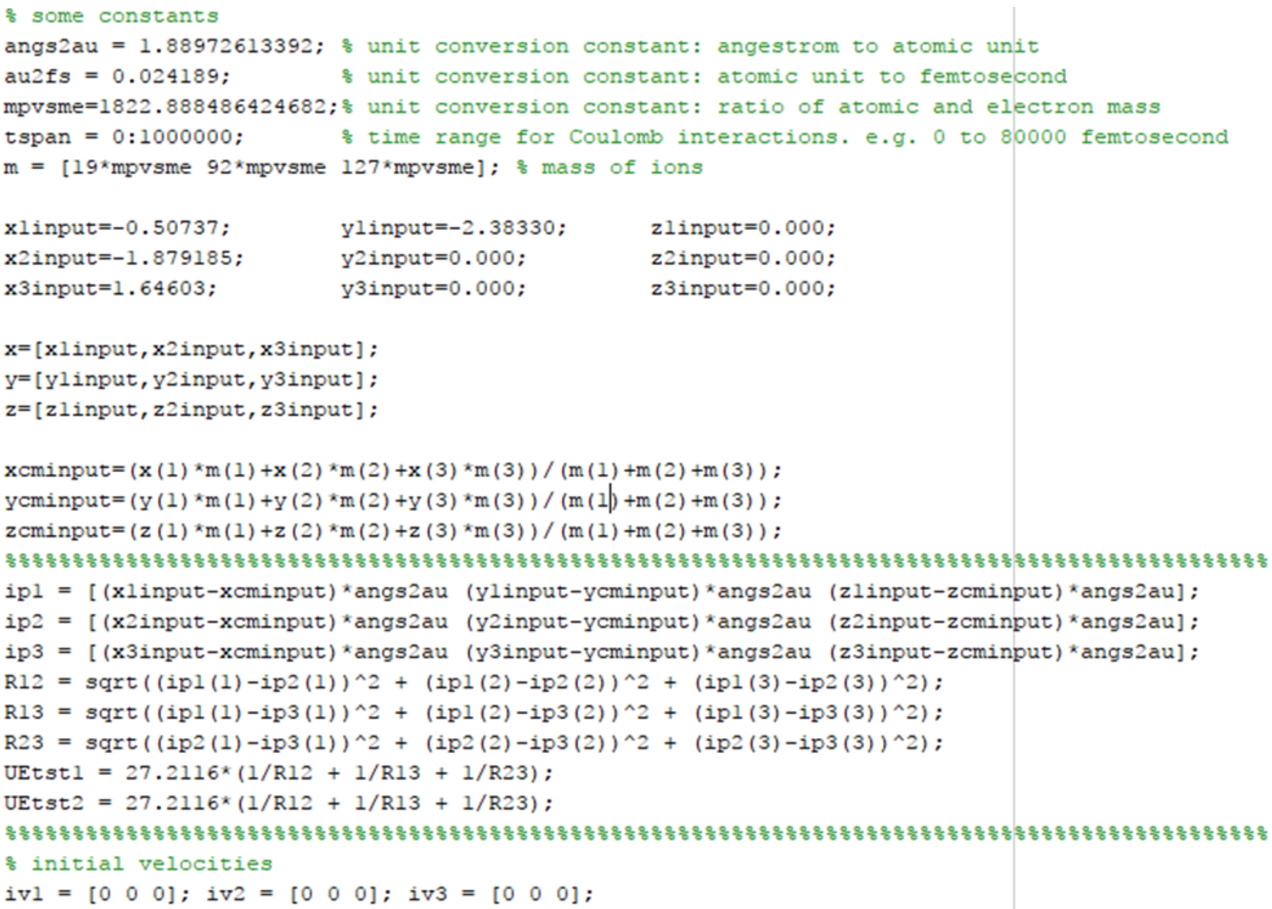

```
% some constants
angs2au = 1.88972613392; % unit conversion constant: angestrom to atomic unit
au2fs = 0.024189;        % unit conversion constant: atomic unit to femtosecond
mpvsme=1822.888486424682;% unit conversion constant: ratio of atomic and electron mass
tspan = 0:1000000;       % time range for Coulomb interactions. e.g. 0 to 80000 femtosecond
m = [19*mpvsme 92*mpvsme 127*mpvsme]; % mass of ions

x1input=-0.50737;        y1input=-2.38330;      z1input=0.000;
x2input=-1.879185;       y2input=0.000;         z2input=0.000;
x3input=1.64603;         y3input=0.000;         z3input=0.000;

x=[x1input,x2input,x3input];
y=[y1input,y2input,y3input];
z=[z1input,z2input,z3input];

xcminput=(x(1)*m(1)+x(2)*m(2)+x(3)*m(3))/(m(1)+m(2)+m(3));
ycminput=(y(1)*m(1)+y(2)*m(2)+y(3)*m(3))/(m(1)+m(2)+m(3));
zcminput=(z(1)*m(1)+z(2)*m(2)+z(3)*m(3))/(m(1)+m(2)+m(3));
%%%%%%%%%%%%%%%%%%%%%%%%%%%%%%%%%%%%%%%%%%%%%%%%%%%%%%%%%%%%%%%%%%%%%%%%%%%%%%%%%%%%%%%%%%%%%%%
ip1 = [(x1input-xcminput)*angs2au (y1input-ycminput)*angs2au (z1input-zcminput)*angs2au];
ip2 = [(x2input-xcminput)*angs2au (y2input-ycminput)*angs2au (z2input-zcminput)*angs2au];
ip3 = [(x3input-xcminput)*angs2au (y3input-ycminput)*angs2au (z3input-zcminput)*angs2au];
R12 = sqrt((ip1(1)-ip2(1))^2 + (ip1(2)-ip2(2))^2 + (ip1(3)-ip2(3))^2);
R13 = sqrt((ip1(1)-ip3(1))^2 + (ip1(2)-ip3(2))^2 + (ip1(3)-ip3(3))^2);
R23 = sqrt((ip2(1)-ip3(1))^2 + (ip2(2)-ip3(2))^2 + (ip2(3)-ip3(3))^2);
UEtst1 = 27.2116*(1/R12 + 1/R13 + 1/R23);
UEtst2 = 27.2116*(1/R12 + 1/R13 + 1/R23);
%%%%%%%%%%%%%%%%%%%%%%%%%%%%%%%%%%%%%%%%%%%%%%%%%%%%%%%%%%%%%%%%%%%%%%%%%%%%%%%%%%%%%%%%%%%%%%%
% initial velocities
iv1 = [0 0 0]; iv2 = [0 0 0]; iv3 = [0 0 0];
```

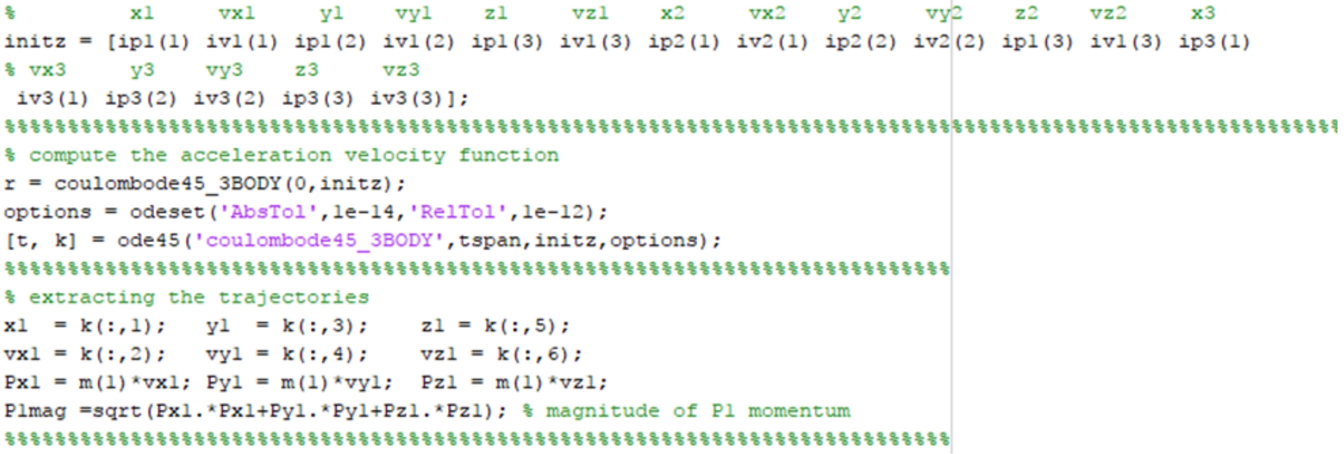

```
%        x1     vx1     y1     vy1    z1     vz1    x2     vx2    y2     vy2    z2     vz2    x3
initz = [ip1(1) iv1(1) ip1(2) iv1(2) ip1(3) iv1(3) ip2(1) iv2(1) ip2(2) iv2(2) ip1(3) iv1(3) ip3(1)
% vx3     y3     vy3    z3     vz3
 iv3(1) ip3(2) iv3(2) ip3(3) iv3(3)];
%%%%%%%%%%%%%%%%%%%%%%%%%%%%%%%%%%%%%%%%%%%%%%%%%%%%%%%%%%%%%%%%%%%%%%%%%%%%%%%%%%%%%%%%%%%%%%%%%%%%
% compute the acceleration velocity function
r = coulombode45_3BODY(0,initz);
options = odeset('AbsTol',1e-14,'RelTol',1e-12);
[t, k] = ode45('coulombode45_3BODY',tspan,initz,options);
%%%%%%%%%%%%%%%%%%%%%%%%%%%%%%%%%%%%%%%%%%%%%%%%%%%%%%%%%%%%%%%%%%%%%%%
% extracting the trajectories
x1  = k(:,1);   y1  = k(:,3);    z1 = k(:,5);
vx1 = k(:,2);   vy1 = k(:,4);    vz1 = k(:,6);
Px1 = m(1)*vx1; Py1 = m(1)*vy1;  Pz1 = m(1)*vz1;
P1mag =sqrt(Px1.*Px1+Py1.*Py1+Pz1.*Pz1); % magnitude of P1 momentum
%%%%%%%%%%%%%%%%%%%%%%%%%%%%%%%%%%%%%%%%%%%%%%%%%%%%%%%%%%%%%%%%%%%%%%%
```

```
x2  = k(:,7);   y2  = k(:,9);    z2  = k(:,11);
vx2 = k(:,8);   vy2 = k(:,10);   vz2 = k(:,12);
Px2 = m(2)*vx2; Py2 = m(2)*vy2;  Pz2 = m(2)*vz2;
P2mag =sqrt(Px2.*Px2+Py2.*Py2+Pz2.*Pz2); % magnitude of P2 momentum
%%%%%%%%%%%%%%%%%%%%%%%%%%%%%%%%%%%%%%%%%%%%%%%%%%%%%%%%%%%%%%%%%%%%%%%%%%%%%%%
x3  = k(:,13);  y3  = k(:,15);  z3 = k(:,17);
vx3 = k(:,14);  vy3 = k(:,16);  vz3 = k(:,18);
Px3 = m(3)*vx3; Py3 = m(3)*vy3; Pz3 = m(3)*vz3;
P3mag =sqrt(Px3.*Px3+Py3.*Py3+Pz3.*Pz3); % magnitude of P3 momentum
%%%%%%%%%%%%%%%%%%%%%%%%%%%%%%%%%%%%%%%%%%%%%%%%%%%%%%%%%%%%%%%%%%%%%%%%%%%%%%%
angtheta1 = (180/pi)*acos(( Px2.*Px3 + Py2.*Py3 + Pz2.*Pz3 )./(P2mag.*P3mag+1e-15));% angle between P2,P3
angtheta2 = (180/pi)*acos(( Px1.*Px2 + Py1.*Py2 + Pz1.*Pz2 )./(P1mag.*P2mag+1e-15));% angle between P1,P2
angtheta3 = (180/pi)*acos(( Px1.*Px3 + Py1.*Py3 + Pz1.*Pz3 )./(P1mag.*P3mag+1e-15));% angle between P1,P3
ang1 = cos(angtheta1(end)*pi/180);% angle between P2,P3 (cosine)
ang2 = cos(angtheta2(end)*pi/180);% angle between P1,P2 (cosine)
ang3 = cos(angtheta3(end)*pi/180);% angle between P1,P3 (cosine)
angsum = ang1+ang2+ang3; % angle sum to see if it peaks at 360 degree
KER = 27.2116*(0.5*Px1.*Px1/m(1) + 0.5*Px2.*Px2/m(2) + 0.5*Px3.*Px3/m(3) + 0.5*Py1.*Py1/m(1)
+ 0.5*Py2.*Py2/m(2) + 0.5*Py3.*Py3/m(3) + 0.5*Pz1.*Pz1/m(1) + 0.5*Pz2.*Pz2/m(2) + 0.5*Pz3.*Pz3/m(3));%KER
KE1 = 27.2116*(0.5*Px1.*Px1/m(1) + 0.5*Py1.*Py1/m(1) + 0.5*Pz1.*Pz1/m(1));% KE of 1st ion
KE2 = 27.2116*(0.5*Px2.*Px2/m(2) + 0.5*Py2.*Py2/m(2) + 0.5*Pz2.*Pz2/m(2));% KE of 2nd ion
KE3 = 27.2116*(0.5*Px3.*Px3/m(3) + 0.5*Py3.*Py3/m(3) + 0.5*Pz3.*Pz3/m(3));% KE of 3rd ion
%%%%%%%%%%%%%%%%%%%%%%%%%%%%%%%%%%%%%%%%%%%%%%%%%%%%%%%%%%%%%%%%%%%%%%%%%%%%%%%
dx12 = x1 - x2; sdx12 = dx12.^2;
dx13 = x1 - x3; sdx13 = dx13.^2;
dx23 = x2 - x3; sdx23 = dx23.^2;
%%%%%%%%%%%%%%%%%%%%%%%%%%%%%%%%%%%%%%%%%%%%%%%%%%%%%%%%%%%%%%%%%%%%%%%%%%%%%%%
dy12 = y1 - y2; sdy12 = dy12.^2;
dy13 = y1 - y3; sdy13 = dy13.^2;
dy23 = y2 - y3; sdy23 = dy23.^2;
%%%%%%%%%%%%%%%%%%%%%%%%%%%%%%%%%%%%%%%%%%%%%%%%%%%%%%%%%%%%%%%%%%%%%%%%%%%%%%%
dz12 = z1 - z2; sdz12 = dz12.^2;
dz13 = z1 - z3; sdz13 = dz13.^2;
dz23 = z2 - z3; sdz23 = dz23.^2;
%%%%%%%%%%%%%%%%%%%%%%%%%%%%%%%%%%%%%%%%%%%%%%%%%%%%%%%%%%%%%%%%%%%%%%%%%%%%%%%
% Potential energies
UE = 27.2116*(1./sqrt(sdx12+sdy12+sdz12) + 1./sqrt(sdx13+sdy13+sdz13) + 1./sqrt(sdx23+sdy23+sdz23));
% Final potential energy, to see if is zero at infinite distance
CONvergence = UE(end);
% Plot energies with respect to time;
figure
hold on
plot(tspan*au2fs,KE1,'g');
plot(tspan*au2fs,KE2,'r');
plot(tspan*au2fs,KE3,'k');
```

Figure D.3: 3-body ion Coulomb explosion simulation Matlab script

```
function r =coulombode45_3BODY(t,k)
% defining the three masses
mpvsme=1822.888486424682;
% initial positions
m = [19*mpvsme 94*mpvsme 127*mpvsme];
% m = [1 1 1]; % for equal masses
r = zeros(18,1);
% relabel input vector z
x1 = k(1);  u1 = k(2);  y1 = k(3);  v1 = k(4);  z1 = k(5);  w1 = k(6);
x2 = k(7);  u2 = k(8);  y2 = k(9);  v2 = k(10); z2 = k(11); w2 = k(12);
x3 = k(13); u3 = k(14); y3 = k(15); v3 = k(16); z3 = k(17); w3 = k(18);
% u and v are first derivatives of x and y
r(1)  = u1;  r(3)  = v1;  r(5)  = w1;
r(7)  = u2;  r(9)  = v2;  r(11) = w2;
r(13) = u3;  r(15) = v3;  r(17) = w3;
% compute squared distances
%%%%%%%%%%%%%%%%%%%%%%%%%%%%%%%%%%%%%%%%%%%%%%%%%%%%%%%%%%%%%%%%%%%%%%%%%%%%%%%
dx12 = x1 - x2; sdx12 = dx12^2; dx21 = x2 - x1; sdx21 = dx21^2;
dx13 = x1 - x3; sdx13 = dx13^2; dx31 = x3 - x1; sdx31 = dx31^2;
dx23 = x2 - x3; sdx23 = dx23^2; dx32 = x3 - x2; sdx32 = dx32^2;
%%%%%%%%%%%%%%%%%%%%%%%%%%%%%%%%%%%%%%%%%%%%%%%%%%%%%%%%%%%%%%%%%%%%%%%%%%%%%%%
dy12 = y1 - y2; sdy12 = dy12^2; dy21 = y2 - y1; sdy21 = dy21^2;
dy13 = y1 - y3; sdy13 = dy13^2; dy31 = y3 - y1; sdy31 = dy31^2;
dy23 = y2 - y3; sdy23 = dy23^2; dy32 = y3 - y2; sdy32 = dy32^2;
%%%%%%%%%%%%%%%%%%%%%%%%%%%%%%%%%%%%%%%%%%%%%%%%%%%%%%%%%%%%%%%%%%%%%%%%%%%%%%%
dz12 = z1 - z2; sdz12 = dz12^2; dz21 = z2 - z1; sdz21 = dz21^2;
dz13 = z1 - z3; sdz13 = dz13^2; dz31 = z3 - z1; sdz31 = dz31^2;
dz23 = z2 - z3; sdz23 = dz23^2; dz32 = z3 - z2; sdz32 = dz32^2;
%%%%%%%%%%%%%%%%%%%%%%%%%%%%%%%%%%%%%%%%%%%%%%%%%%%%%%%%%%%%%%%%%%%%%%%%%%%%%%%
% just distance powered
d12 = (sdx12 + sdy12 + sdz12)^(3/2); d21 = (sdx21 + sdy21 + sdz21)^(3/2);
d13 = (sdx13 + sdy13 + sdz13)^(3/2); d23 = (sdx23 + sdy23 + sdz23)^(3/2);


% second order:  accelerations
r(2)  = (dx12/d12 + dx13/d13)/m(1);    % acc_x for 1st
r(4)  = (dy12/d12 + dy13/d13)/m(1);    % acc_y for 1st
r(6)  = (dz12/d12 + dz13/d13)/m(1);    % acc_z for 1st
r(8)  = (dx21/d12 + dx23/d23)/m(2);    % acc_x for 2st
r(10) = (dy21/d12 + dy23/d23)/m(2);    % acc_y for 2st
r(12) = (dz21/d12 + dz23/d23)/m(2);    % acc_z for 2st
r(14) = (dx31/d13 + dx32/d23)/m(3);    % acc_x for 3st
r(16) = (dy31/d13 + dy32/d23)/m(3);    % acc_y for 3st
r(18) = (dz31/d13 + dz32/d23)/m(3);    % acc_z for 3st
```

Figure D.4: Numerical integration function using Runge-Kutta 4th order method: 3-body